

ESCOLA POLITÉCNICA DA UNIVERSIDADE DE SÃO PAULO

DEPARTAMENTO DE ENGENHARIA MECÂNICA

BRUNO CESAR MUSSULINI

**Modelamento e caracterização de atrito para aplicações de  
segurança veicular**

SÃO PAULO

2023



ESCOLA POLITÉCNICA DA UNIVERSIDADE DE SÃO PAULO  
DEPARTAMENTO DE ENGENHARIA MECÂNICA

BRUNO CESAR MUSSULINI

**Friction modeling and characterization for crashworthiness  
applications**

Thesis presented to the Mechanical Engineering Department at Escola Politécnica da Universidade de São Paulo, Brazil, in order to obtain the title of Doctor of Mechanical Engineering. Corrected version.

Concentration area: Mechanical Engineering.

Advisor: Prof. Dr. Marcilio Alves

SÃO PAULO

2023

Autorizo a reprodução e divulgação total ou parcial deste trabalho, por qualquer meio convencional ou eletrônico, para fins de estudo e pesquisa, desde que citada a fonte.

Este exemplar foi revisado e corrigido em relação à versão original, sob responsabilidade única do autor e com a anuência de seu orientador.

Assinatura do autor:



Assinatura do orientador:

---

### Catálogo-na-publicação

Mussulini, Bruno Cesar

Friction modeling and characterization for crashworthiness applications /  
B. C. Mussulini -- versão corr. -- São Paulo, 2023.  
181 p.

Tese (Doutorado) – Escola Politécnica da Universidade de São Paulo.  
Departamento de Engenharia Mecânica.

1. Modeling and Simulation 2. Friction 3. Crashworthiness 4. Finite  
Element Analysis 5. Mechanical Design I. Universidade de São Paulo. Escola  
Politécnica. Departamento de Engenharia Mecânica II.t.

## ABSTRACT

Crashworthiness is a crucial and complex design consideration in the automotive industry. It involves multiple disciplines and intricate energy absorption and dissipation phenomena. Numerical analysis using the finite element method has become a widely adopted approach for studying vehicle safety. This method offers cost and time efficiency, as it typically requires only one physical test for result validation.

One specific aspect that needs investigation is the role of friction in impact events and its influence on structural stability. This study aims to evaluate the impact of friction in a crash test through numerical analysis using the finite element method. Additionally, it will explore existing devices for measuring friction under impact conditions and propose a new testing rig based on available literature and functional requirements for friction tests. A data acquisition system will be designed, and data obtained through the proposed methodology will be presented.

To capture a broader range of tribological phenomena that affect the friction coefficient, a new constitutive equation will be proposed based on a review of relevant literature. Finally, a comparative analysis will be conducted, comparing the friction models proposed in this work with commonly used approaches in the industry. This analysis will emphasize the significance of incorporating slip velocity and pressure dependence when modeling the friction coefficient.

**Keywords:** Modeling and Simulation, Friction, Crashworthiness, Finite Element Analysis, Mechanical design



## **ACKNOWLEDGEMENTS**

I would like to dedicate this work to the loving memory of my greatest supporter, teacher, and dear mother, Sueli. She provided me with immeasurable love, comfort, and hope during the most challenging moments of my life, teaching me the significance of living with passion and pursuing our dreams. In immense sadness, she was not able to witness the realization of this dream in life, but I know that her strength, courage, and guidance have illuminated my path during this journey and will continue to do so for the rest of my life.

To my father, Paulo, whose admirable intelligence, dedication, and resilience have guided me along the paths of life until this moment, supporting me on the toughest decisions and leading me towards the wiser paths.

To my grandparents, Alayde and Archanjo, for their constant companionship, unwavering support, and invaluable teachings throughout all my life. Thank you for the title, sirs.

To my bride, Ariana, for the faithful companionship, gentle support and shared strength, both in the good times and when I needed it the most.

To the professors and members of the Solid Mechanics and Impact on Structures Group, I would like to express my gratitude for the invaluable teachings, friendships, and enjoyable shared moments on this long journey. These experiences have been instrumental in shaping my professional development.

To BMW, for proposing and financing this challenging and groundbreaking project.

*In memory of my beloved mother, Sueli Aparecida Michelan Mussulini.*



# SUMMARY

<b>1. INTRODUCTION</b> .....	<b>1</b>
<b>2. LITERATURE REVIEW</b> .....	<b>5</b>
2.1. TRAFFIC ACCIDENTS .....	5
2.2. CRASHWORTHINESS .....	8
2.2.1. <b>Crash Management Systems</b> .....	<b>8</b>
2.2.2. <b>Vehicular structure</b> .....	<b>8</b>
2.2.3. <b>Buckling of thin wall structures</b> .....	<b>12</b>
2.2.4. <b>Regulations</b> .....	<b>14</b>
2.2.5. <b>Independent institutions crash tests</b> .....	<b>24</b>
2.2.6. <b>Small overlap crash test protocol</b> .....	<b>26</b>
2.2.7. <b>Friction in crashworthiness</b> .....	<b>28</b>
2.3. TRYBOLOGY .....	34
2.3.1. <b>Friction</b> .....	<b>37</b>
2.3.2. <b>Engineering surfaces</b> .....	<b>40</b>
2.3.3. <b>Wear maps</b> .....	<b>42</b>
2.4. FRICTION TESTING.....	44
2.4.1. <b>Pin on Disk (ASTM G-99)</b> .....	<b>46</b>
2.4.2. <b>Reciprocating test apparatus (ASTM G133)</b> .....	<b>47</b>
2.4.3. <b>Standard Test Method for Static and Kinetic Coefficients of Friction of Plastic Film and Sheeting (ASTM D1894 – 001)</b> .....	<b>48</b>
2.4.4. <b>Strip Drawing test method</b> .....	<b>49</b>
2.4.5. <b>Friction rigs for impact applications</b> .....	<b>50</b>
2.5. NUMERICAL MODELING OF FRICTION .....	65

2.5.1.	<b>Coulomb friction model</b> .....	66
2.5.2.	<b>Smooth Coulomb friction model</b> .....	67
2.5.3.	<b>Exponential decay</b> .....	68
2.5.4.	<b>Velocity Based Model</b> .....	70
2.5.5.	<b>Dahl model</b> .....	71
2.5.6.	<b>Piecewise linear</b> .....	72
3.	<b>MATERIALS AND METHODS</b> .....	73
3.1.	FINITE ELEMENT MODEL .....	73
3.2.	FRICION RIG DESIGN .....	74
3.2.1.	<b>Sliding bearing</b> .....	75
3.2.2.	<b>Tangential Load Actuation</b> .....	77
3.2.3.	<b>Normal load actuation</b> .....	79
3.2.4.	<b>Sample holding</b> .....	81
3.2.5.	<b>Load decomposition Mechanism</b> .....	82
3.3.	FINITE ELEMENT ANALYSIS .....	86
3.4.	PROTOTYPE .....	90
3.4.1.	<b>Data acquisition system</b> .....	91
3.4.2.	<b>Software</b> .....	92
3.4.3.	<b>Impact hammer</b> .....	95
3.4.4.	<b>Samples</b> .....	95
3.5.	CONSTITUTIVE EQUATION .....	98
3.5.1.	<b>Current Approach</b> .....	98
3.5.2.	<b>Proposed Approach</b> .....	99
4.	<b>RESULTS</b> .....	104
4.1.	CRASH TEST SENSITIVITY ANALYSIS .....	104

4.1.1.	<b>Overall Analysis</b> .....	104
4.1.2.	<b>Structural Analysis</b> .....	107
4.1.3.	<b>Biomechanical Analysis</b> .....	112
4.1.4.	<b>Contact pressure and slip velocity evaluation</b> .....	120
4.2.	<b>FRICTION MODELS</b> .....	121
4.2.1.	<b>Steel – Aluminum</b> .....	123
4.2.2.	<b>Dummy skin – Airbag</b> .....	124
4.2.3.	<b>Airbag – Dummy shirt</b> .....	125
4.2.4.	<b>Dummy shirt – Leather</b> .....	126
4.2.5.	<b>Seatbelt – Dummy shirt</b> .....	127
4.2.6.	<b>Dummy shirt – Dummy skin</b> .....	128
<b>5.</b>	<b>FRICTION COEFFICIENT MODELS ASSESSMENT</b> .....	<b>130</b>
5.1.	STEEL – ALUMINUM.....	130
5.2.	DUMMY SKIN – AIRBAG.....	131
5.3.	AIRBAG – DUMMY SHIRT .....	132
5.4.	DUMMY SHIRT – LEATHER .....	133
5.5.	SEATBELT – DUMMY SHIRT.....	134
5.6.	DUMMY SHIRT – DUMMY SKIN .....	135
<b>6.</b>	<b>DISCUSSIONS AND CONCLUSIONS</b> .....	<b>139</b>
<b>7.</b>	<b>REFERENCES</b> .....	<b>144</b>
<b>APPENDIX A – INJURY CRITERIA</b> .....		<b>151</b>
A.1.	HEAD INJURY CRITERIA (HIC) .....	151
A.2.	CHEST SEVERITY INDEX (CSI) .....	151
A.3.	TIBIA AXIAL LOAD.....	152
A.4.	NECK INJURY CRITERIA .....	152

<b>APPENDIX B – COMPONENTS AND SENSORS SELECTION.....</b>	<b>154</b>
B.1. LINEAR GUIDE .....	154
B.2. LOAD CELLS .....	155
B.3. LINEAR ENCODER.....	159
<b>APPENDIX C – RESULTS METRICS .....</b>	<b>162</b>
C.1. STEEL – ALUMINUM.....	162
C.2. DUMMY SKIN – AIRBAG .....	162
C.3. AIRBAG – DUMMY SHIRT.....	163
C.4. DUMMY SHIRT – LEATHER.....	163
C.5. SEATBELT – DUMMY SHIRT .....	164
C.6. DUMMY SHIRT – DUMMY SKIN .....	164
<b>APPENDIX D – CONTACT MECHANICS COMPLEMENTS .....</b>	<b>165</b>
D.1. CONTACT MECHANICS.....	165
D.2. FRICTION .....	169
<b>D.2.1. Metallic friction .....</b>	<b>169</b>
<b>D.2.2. Friction in Polymers.....</b>	<b>172</b>
<b>D.2.3. Rubber friction.....</b>	<b>173</b>
<b>APPENDIX E – WEDGE TEST RIG PROPOSAL .....</b>	<b>175</b>
<b>APPENDIX F – LABVIEW BLOCK DIAGRAM .....</b>	<b>181</b>

## FIGURE INDEX

Figure 1 – Decrease of road traffic fatalities in Europe (Statista, 2020, Eurostat 2020).....	6
Figure 2 – Fatality rate per 100,000 inhabitants (IPEA, 2023). ....	7
Figure 3– Typical Body in White of a commercial vehicle (Duddek, 2016). ...	9
Figure 4 – Typical anatomy of an automotive front structure. (Duddek, 2016). .....	10
Figure 5 – Passenger Cabin typical structure (Duddek, 2016).....	11
Figure 6 – Progressive folding and plastic hinge (or global bending) buckling mechanisms (Duddek, 2016). ....	13
Figure 7 – Force response of progressive folding and global bending buckling mechanisms (Duddek, 2016) .....	13
Figure 8 – Deformation triggers typically used on crash boxes. (Kumar <i>et al.</i> , 2014.).....	14
Figure 9 – Full frontal impact crash test protocol ABNT NBR 15300-2 (Safety Companion, 2023). ....	16
Figure 10 – 40% offset frontal impact crash test protocol ABNT NBR 15300-3 (Safety Companion, 2023) .....	17
Figure 11 – Side impact crash test protocol (a – ABNT NBR 16204-2; b – 16204-3) .....	18
Figure 12 – Side pole impact crash test protocol as per a – FMVSS 214 and b – ECE R135 (Safety Companion, 2023) .....	19
Figure 13 – Rear impact test as per FMVSS 301 (Safety Companion, 2023). .....	20
Figure 14 – Ejection mitigation test as per FMVSS 226 (Safety Companion, 2023).....	21
Figure 15 – Roof crush resistance test as per FMVSS 216 (Safety Companion, 2023).....	21
Figure 16 – Pedestrian protection tests as per ECE R127 (Safety Companion, 2023).....	22
Figure 17 – Rules and regulations on occupant protection around the world (Safety Companion, 2023) .....	23

Figure 18 – Principal vehicle safety tests performed by independent institutions on Americas and Europe (Safety Companion, 2023).....	25
Figure 19 – Small overlap crash test protocol (IIHS,2021).....	26
Figure 20 – Mercedes C250 2012 small overlap crash test (IIHS, 2021).....	27
Figure 21 – Infinity G25 2012 small overlap crash test (IIHS, 2021). ....	28
Figure 22 – The influence of friction on the impact of a commercial vehicle against a road barrier (Stanislawek, Dziewulski, and Kedzierski, 2019). ....	29
Figure 23 – Pickup Chevrolet C 1500 behavior on the impact against CSB under different friction coefficients (Trajkovski, Ambrož and Kunc, 2018)....	30
Figure 24 – contact of the headform with side curtain airbag (Mihora, Friedman and Hutchinson, 2011).....	31
Figure 25 – Dummy head – airbag oblique impact test (Erikson and Piroti, 2018).....	32
Figure 26 – Front and side view of dummy’s head with grease paint applied to the side that is expected to be in contact with the airbag (Erikson and Piroti, 2018).....	33
Figure 27 – Friction coefficients comparison between Dummy Sking and Human Skin for different airbag samples. Dong <i>et al.</i> (2020). ....	34
Figure 28 – A time-length scales map of models developed in tribology, highlighting the intrinsic link between multiscale physics that needs to be captured in order to provide predictive tools for engineering applications (Vakis <i>et al.</i> , 2018).....	35
Figure 29 – The multifaceted nature of tribological interactions (Vakis <i>et al.</i> , 2018).....	36
Figure 30 – Different behaviors of the coefficient of friction on normal load variation (a – Steel sliding over aluminum in air; b – Copper sliding over copper in air; c – Stainless steel sliding over NiAl alloy in air) (Hutchings, 2017). ...	38
Figure 31 – Behavior of the friction coefficient on apparent area variation during slip between steel and wood (Hutchings, 2017).....	39
Figure 32 – (a) Coefficient of friction behavior as a function of the sliding velocity for titanium sliding on titanium at 3 N normal load; b) Behavior of the	

coefficient of friction as a function of the slip speed for copper and bismuth on themselves at 3 N normal load (Hutchings, 2017). .....	40
Figure 33 – Basic friction and wear mechanisms (Holmberg, 2007).....	41
Figure 34 – Main parameters influencing the friction in engineering contact situation (Holmberg, 2007).....	42
Figure 35 – Wear mechanism map for steel-on-steel sliding (Lim and Ashby,1987).....	43
Figure 36 – Frictional map for sliding of steel on steel under various normalized pressures and slip velocities (Lim and Ashby, 1987). .....	44
Figure 37 – Pin on disk apparatus (Tribonet, 2023) .....	46
Figure 38 – Reciprocating test apparatus (ASTM G133). .....	48
Figure 39 – Friction measurement by ASTM D1894 – 001. ....	49
Figure 40 – Strip drawing test concept with two side fabric samples. (Kruse <i>et al.</i> , 2022).....	50
Figure 41 –Impact friction rig scheme (Lai <i>et al.</i> , 2012). .....	51
Figure 42- Slip velocity dependence of friction coefficient (Lai <i>et al.</i> , 2012). ..	52
Figure 43 – Pressure dependence of friction coefficient (Lai <i>et al.</i> , 2012). ..	52
Figure 44 – Slip velocity path dependence due to surface and tribosystem modifications during testing (Lai <i>et al.</i> , 2012).....	53
Figure 45 – Friction force vs. sliding velocity characteristics for various driving velocities and natural frequencies of the system Oden and Martins (1984). .....	54
Figure 46 – Devices used by (a) Sutter and Ranc (2010) and (b) List, Sutter and Arnoux (2013) to measure the friction coefficient at very high speeds. .	55
Figure 47 – Asperities collision model for ballistic friction testing (List, Sutter and Arnoux, 2013). .....	56
Figure 48 – Interfacial compressive stress, shear stress, and friction coefficient histories (Lin <i>et al.</i> , 2014).....	56
Figure 49 – Friction model fitted from slip velocity, pressure and temperature data (Klocke <i>et al.</i> 2015). .....	58
Figure 50 – Local coefficients of friction on finite simulation model (Klocke <i>et al.</i> 2015).....	59

Figure 51 – Contour plots of friction coefficient during a deep drawing process of a dishwasher indoor panel (Klocke <i>et al.</i> , 2015). .....	60
Figure 52 – Evolution of the friction coefficient at a sliding speed of 10 mm/s, a pressure of 550 MPa, and a lubricant density of 0.2 mg/mm <sup>2</sup> between a disk made of AA6082 Aluminum alloy and a Tungsten carbide ball (Hu <i>et al.</i> , 2017). .....	62
Figure 53 – A comparison of modeling and experiment friction models in Hu <i>et al.</i> (2017) as function of lubricant density (a), contact pressure (b) and sliding speed (c).....	62
Figure 54 – Stribeck curve (adopted from Hamrock, Schmid, and Jacobson, 2004).....	63
Figure 55 – Map of pressure and slip velocity capabilities of literature available friction rigs.....	64
Figure 56 – The Coulomb friction model (Pennestri <i>et al.</i> , 2016).....	67
Figure 57 – The Smooth Coulomb friction model (Pennestri <i>et al.</i> , 2016)....	68
Figure 58 – Benson exponential friction model (Pennestri <i>et al.</i> , 2016). .....	69
Figure 59 – Velocity Based friction model (Pennestri <i>et al.</i> , 2016).....	70
Figure 60 – The bristle analogy in the Dahl model (Pennestri <i>et al.</i> , 2016)..	71
Figure 61- Toyota Yaris 2010 Finite Element Model (NCAC, 2014).....	73
Figure 62 – Linear Motion Guide (THK, 2018) .....	76
Figure 63 – Tangential load actuation system proposals (a – Spring accumulator, b – Impact hammer, c – Pneumatic Actuator). .....	78
Figure 64 – Normal load actuation system proposals (a – Threaded Joint, b – Spring based, c – Pneumatic). .....	80
Figure 65 – Fixed side sample holders (a – fabric sample holder, b – thin sheet sample holder). .....	81
Figure 66 – Moving side sample holder with the vise mechanism. ....	82
Figure 67 – Schematics of the proposed test rig.....	84
Figure 68 – Movable tangential load cell base.....	85
Figure 69– Rig final CAD concept.....	86
Figure 70 – Finite element model of friction rig on LS-Dyna. ....	87
Figure 71- Stress over time in most critical element of test rig.....	88



Figure 72 – Stress contour plots of test rig under operation. ....	88
Figure 73 – Finite element output of the load cell measurements.....	89
Figure 74 – Frequency domain analysis of load cell signals outputted by finite element analysis (a) Tangential load cell HBM U93 and (b) Normal load cells HBM C9C.....	90
Figure 75 – Final test rig prototype. ....	91
Figure 76 – National Instruments USB-6356. ....	91
Figure 77 – Fylde FE 579 bridge Amplifier.....	92
Figure 78 – User interface of LabView based data acquisition software.....	93
Figure 79 – Low Energy Impact Hammer with friction test rig.....	95
Figure 80 – Samples of tested materials.....	97
Figure 81 – Reference constitutive equation parameters influence on function response.....	98
Figure 82 – Cumulative Density Function for $\gamma = 3$ . ....	100
Figure 83 – Proposed constitutive equation parameters influence on function response.....	101
Figure 84 – Influence of friction on the overall behavior of a crash test. Friction of $\mu=0.0$ , $\mu=0.4$ and $\mu=0.8$ – Full vehicle deformations. ....	104
Figure 85 – Front left wheel behavior for friction coefficients of $\mu=0.0$ , $\mu =0.4$ and $\mu=0.8$ – side view. ....	106
Figure 86 – Center of gravity resultant acceleration.....	107
Figure 87 – Influence of friction on the structural behavior of Toyota Yaris 2010. Friction coefficients of $\mu=0.0$ , $\mu =0.4$ and $\mu=0.8$ – BIW Plastic strain.....	108
Figure 88- Influence of friction on the structural behavior of Toyota Yaris 2010. Friction coefficients of $\mu=0.0$ , $\mu =0.4$ and $\mu=0.8$ – BIW Plastic strain.....	109
Figure 89 – Left front rail normal forces for different overall friction coefficients. ....	109
Figure 90 – Left front rail energy for different overall friction coefficients... ..	110
Figure 91 – Left A-pillar normal forces for different overall friction coefficients. ....	111
Figure 92 – Left Rockwell normal forces for different overall friction coefficients. ....	112

Figure 93 – Influence of friction on dummy-airbag and vehicle interior interaction. Friction coefficients of $\mu=0.0$ , $\mu =0.4$ and $\mu=0.8$ . .....	113
Figure 94 – Head Injury Criteria (HIC) for different overall friction coefficients. ....	114
Figure 95 – Neck resultant forces for different overall friction coefficients. ....	115
Figure 96 – Neck resultant moment for different overall friction coefficients. ....	116
Figure 97 – Chest Severity Index (CSI) for different overall friction coefficients. ....	117
Figure 98 – Left femur normal force for different overall friction coefficients. ....	118
Figure 99 – Left tibia normal forces for different overall friction coefficients. ....	118
Figure 100 – Overall biomechanical parameters expressed as a percentage of the ECE R94 standard for different friction coefficients.....	119
Figure 101 – Ranking of residuals for Dummy shirt – Dummy Skin contact pair. ....	122
Figure 102 – Steel – Aluminum friction model.....	124
Figure 103 – Dummy skin – Airbag friction model.....	125
Figure 104 – Airbag – Dummy shirt friction model. ....	126
Figure 105 – Dummy shirt – Leather friction model. ....	127
Figure 106 – Seatbelt – Dummy shirt friction model. ....	128
Figure 107 – Dummy shirt – Dummy skin friction model.....	129
Figure 108 – Steel – Aluminum friction coefficient comparison.....	131
Figure 109 – Dummy Skin – Airbag friction coefficient comparison. ....	132
Figure 110 – Airbag – Dummy Shirt friction coefficient comparison.....	133
Figure 111 – Dummy shirt leather friction coefficient comparison.....	134
Figure 112 – Seatbelt – Dummy shirt Friction coefficient comparison. ....	135
Figure 113 – Dummy skin – Dummy shirt friction coefficient comparison. .	136
Figure 114 – RMS Error to reference of constant friction coefficient model. ....	137

Figure 115– RMS Error to reference of proposed friction coefficient model. .....	137
Figure 116 – full Bridged load cell scheme (800 load cell, 2019). .....	156
Figure 117 – Piezoelectric load cell anatomy (source: HBM, 2019).....	157
Figure 118 – HBM U93 (left) and C9C (right) Load cells (source: HBM, 2018). .....	158
Figure 119 – Incremental optical encoder working principle (Renishaw,2019). .....	159
Figure 120 – Magnetic encoder working principle (Domajnko and Križaj, 2018). .....	160
Figure 121 – Incremental optical (a) and magnetic (b) encoder scales (Renishaw, 2018). .....	161
Figure 122 – Steel – Aluminum friction model.....	162
Figure 123 – Dummy skin – Airbag friction model.....	162
Figure 124 – Airbag – Dummy shirt friction model. ....	163
Figure 125 – Dummy Shirt – Leather friction model.....	163
Figure 126 – Seatbelt – Dummy Shirt friction model. ....	164
Figure 127 – Dummy Shirt – Dummy Skin friction model.....	164
Figure 128 – Schematic demonstration of real and apparent contact area (Santana, 2009). .....	165
Figure 129 – Contact representation between a smooth surface and a rough surface (Johnson, 1985). ....	167
Figure 130 – Representation of the average roughness of a surface (Johnson, 1985).....	167
Figure 131 – Gaussian distribution of depths of a real surface (Johnson, 1985). .....	168
Figure 132 – Theoretical modelling of the adhesion effect during contact between a nickel indenter (upper body) and an initially plane gold surface in perfect vacuum (Hutchings, 2017). .....	170
Figure 133 – Model for the ploughing component of friction, in which a conical asperity with a semi-angle $\alpha$ indents and slides through the surface of a softer material (Hutchings, 2017). .....	171

Figure 134 – Effect of polymer layer transfer on the coefficient of friction of high-density polyethylene (HDPE) against glass (Kawakame and Bressan, 2000).....	173
Figure 135 – Adhesion and hysteresis friction mechanisms on rubber block sliding with constant velocity $v$ over a rough surface (Meyer and Kummer, 1962).....	174
Figure 136 – Design of wedge test rig. ....	176
Figure 137 – Static analysis on the circlip.....	178
Figure 138– Operation map of the proposed rig. ....	179
Figure 139 – Sensitiveness analysis of indenter vertical displacement to dynamic friction coefficient.....	180
Figure 140 – Friction rig LabView block diagram of test rig setup.....	181



## TABLE INDEX

Table 1 – Comparison of sheet thickness determined by experimental forming and FEA analysis using different friction modeling approaches (Klocke <i>et al.</i> , 2015).....	60
Table 2 – Summary of literature available rigs and their capabilities. ....	65
Table 3 – Sample carrier design decision matrix. ....	76
Table 4 – Tangential load actuation decision matrix. ....	78
Table 5 – Normal load actuation decision matrix. ....	80
Table 6 – Load decomposition mechanism decision matrix.....	83
Table 7 – Contact pairs and tests conditions. ....	96
Table 8 – Pressure levels during a crash test for different contacting parts	121
Table 9 – Slip velocity levels during a crash test for different contacting parts .....	121
Table 10 – Constitutive equation coefficients for all contact pairs.....	123
Table 11 – Contact pairs average friction coefficient. ....	130
Table 12 – RMS error reduction from constant to proposed friction model.	138
Table 13 – HIC allowable values for different dummy models .....	151
Table 14 – Linear guide selection table. ....	155



## 1. INTRODUCTION

Crashworthiness is currently one of the most important and challenging design considerations in the automotive industry. This is a multidisciplinary field where energy absorption mechanisms, materials engineering, friction, and biomechanics are coupled, playing crucial roles during a vehicle impact.

Energy absorption mechanisms encompass a range of strategies employed to dissipate and distribute impact forces, thereby reducing the severity of deceleration experienced by the vehicle and its occupants. To enhance vehicular safety for occupants, these mechanisms can include crumple zones, deformation patterns, engineered structural elements, and materials designed to collapse in a controlled manner.

Occupant restraint systems such as seatbelts and airbags have also drastically reduced the fatality rate of crashes since they maintain the driver in the correct position during the impact and avoid contact of passengers with the hard parts of the vehicle.

Finite element analysis (FEA) has revolutionized the automotive industry's approach to crashworthiness design. By creating virtual models of vehicles and their components, engineers can simulate and predict the dynamic behavior and structural response during impact events. This simulation process considers various factors, such as material properties, geometry, and boundary conditions to generate highly accurate representations of real tests.

The increasing accuracy of finite element models has numerous benefits for the automotive industry. Firstly, it reduces the number of needed physical prototypes and experimental crash tests, thereby saving both time and resources in the product development cycle. Through virtual simulations, engineers can iteratively refine designs, evaluate various scenarios, and optimize vehicle structures for crash performance.

In recent times there has been a significant focus on investigating the influence of friction on vehicle and occupant behavior in the field of crashworthiness research. While friction may not directly contribute significantly to energy absorption during a crash, it plays an important role in determining the



mechanical behavior of structures under critical conditions, such as buckling and occupant positioning.

Friction profoundly affects the overall response of a vehicle during a crash event. When structures experience high forces and deformations, the presence of friction can affect the distribution and transfer of energy within the system. It influences the interaction between different components, such as the vehicle's body and its restraint systems, leading to changes in the mechanical behavior of the entire structure.

One important aspect where friction plays a critical role is in determining the buckling behavior of vehicle components. Friction at the contact interfaces between different components can affect the initiation and progression of buckling, thereby influencing the collapse pattern and overall deformation of the structure. Understanding the frictional effects in these scenarios is crucial for accurately predicting the failure modes and optimizing the crashworthiness performance of vehicles.

Friction also influences the positioning of occupants during a crash. It affects the interaction between occupants and their restraint systems, such as seat belts and airbags. The frictional forces between the occupant and these safety devices can affect the timing and effectiveness of occupant restraint and reduce the risk of injury. Proper modeling and characterization of friction in occupant simulations is essential for accurately predicting their motion, interaction with restraints, and overall injury risk assessment.

It is interesting to note that the impact dynamics of a crash test can be significantly affected by the dependence of friction on pressure and velocity. This makes the measurement of friction under high speeds and pressures very challenging. A better understanding of friction behavior and its modeling could lead to improved finite element crash test models.

This research has as its main objective the study of friction on crashworthiness and the development of a test rig and methodology to impact conditions, as well as defining a modeling approach to capture slip velocity and pressure dependent friction coefficient from a large set of experimental data.

Among various pairs of materials, the development of a friction rig capable of measuring friction coefficients under impact conditions will be described. The primary objective is to generate accurate input friction models for finite element simulations of crash tests and apply them to dynamic loading scenarios.

The study will cover various aspects, including the CAD concept of the friction rig, dimensioning of components, selection of sensors, and comprehensive finite element analysis. These elements collectively form a framework for examining and understanding the behavior of friction during crash events.

The CAD concept phase involves designing the friction rig with attention to detail, ensuring its structural integrity and compatibility with experimental requirements. Advanced computer-aided design techniques will be employed to create a functional and robust prototype.

Dimensioning the rig's components is an important step that involves determining the optimal sizes and specifications of various elements within the system. Calculations and considerations will be made to ensure that the rig's performance aligns with the objective of capturing friction coefficients under impact conditions. Then, various types of sensors will be evaluated to ensure accurate measurement of parameters such as forces, pressures, and velocities during crash events.

Additionally, finite element analysis will be conducted to validate and optimize the performance of the friction rig. This computational simulation technique allows for virtual testing and assessment of the behavior of the rig under different impact scenarios. Numerical models and algorithms will be used to refine the design of the rig and improve its effectiveness in generating accurate friction models for finite element crash test simulations.

Furthermore, the data acquisition system will be described, with a focus on the LabView program used to interface with the end user. This program facilitates the acquisition of high-frequency data and enables the triggering of tests. Details of the system's configuration and functionality will be provided.

Then, a Matlab based software will be described for automated data treatment and analysis using a regression method. This regression will be based on a novel constitutive equation that depends on pressure and slip velocity. A new parameter has been introduced to capture nonlinear frictional behaviors. An acceptance criterion was also considered to ensure the reliability, repeatability, and convergence of the data modeling.

Is worth mentioning that the proposed approach aims to input friction models in table format in finite element software to avoid the use of computationally expensive sub-routines.

The proposed friction models were then applied to the finite element simulation of the friction rig machine, and the results were compared with the averaged friction coefficient of each contact pair, representing the most used approach in the industry. As an outcome, one noticed a drastic difference over the measured forces on the tangential direction between models, especially on the low and high pressures. A mean error reduction of 69% was achieved with the use of the proposed friction model.

These findings highlight the potential of the proposed methodology to enhance the understanding and prediction of frictional behavior, thereby contributing to the overall accuracy and realism of crash test simulations.

It is worth noting that further research and validation are necessary to ensure the robustness and generalizability of the regression model across various crash scenarios and material combinations. The promising agreement observed in this study lays a solid foundation for future advancements and optimizations in the field of friction modeling for crashworthiness analysis.

## **2. LITERATURE REVIEW**

### **2.1. TRAFFIC ACCIDENTS**

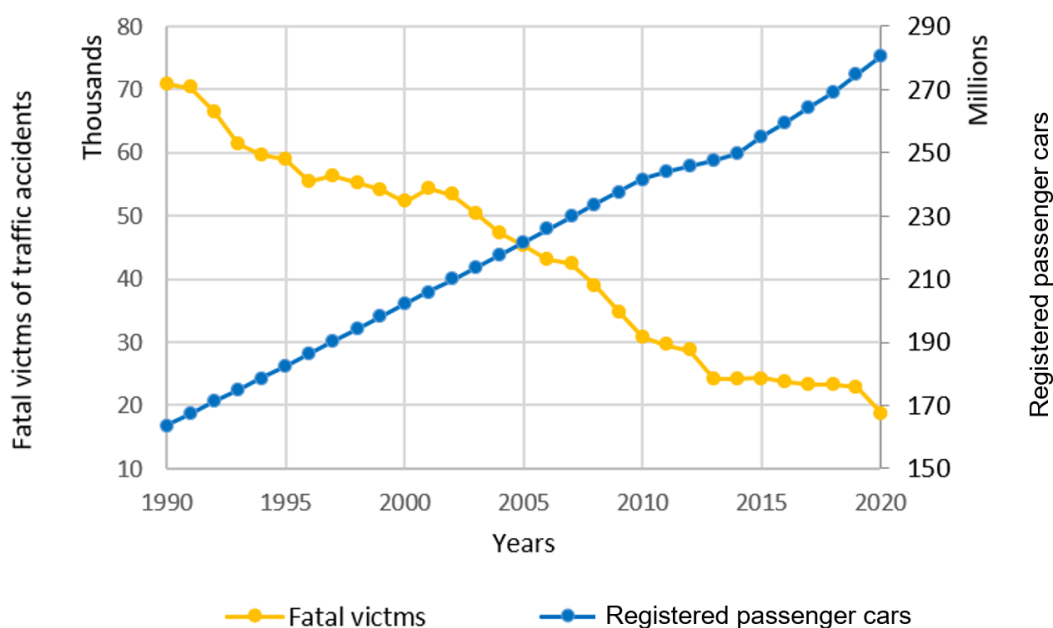
According to the World Health Organization (2023), there were 1.24 million road deaths when the world population was approximately 6.79 billion, resulting in 18 deaths per 100,000 inhabitants. In Brazil, the numbers are even more alarming. According to sources from the Department of Information Technology of the Unified Health System, in 2013, the death rate was 21 deaths per 100,000 inhabitants. This reality is accountable for significant personal and economic losses for victims, families, and countries, considering the expenses of treatment and the required time away from work.

A significant effort has been made in recent years by society, industry, and government to address the issue of traffic accident victims. This effort has focused on implementing safety legislation and developing new technologies that aim to prevent vehicle accidents (active safety) and minimize injuries for occupants in unavoidable collisions (passive safety).

The mandatory use of safety belts and the heightened political dedication to road safety were crucial factors in the decline of road fatalities across Europe starting from the 1970s. According to the World Health Organization (2023), using safety belts by front-seat passengers reduces the risk of fatal injuries by around 50%, and the risk of death and serious injuries among back-seat occupants by 25%.

Figure 1 shows the reduction in fatalities over the years in Europe with the introduction of these measures, despite a significant increase in the number of vehicles on the road.

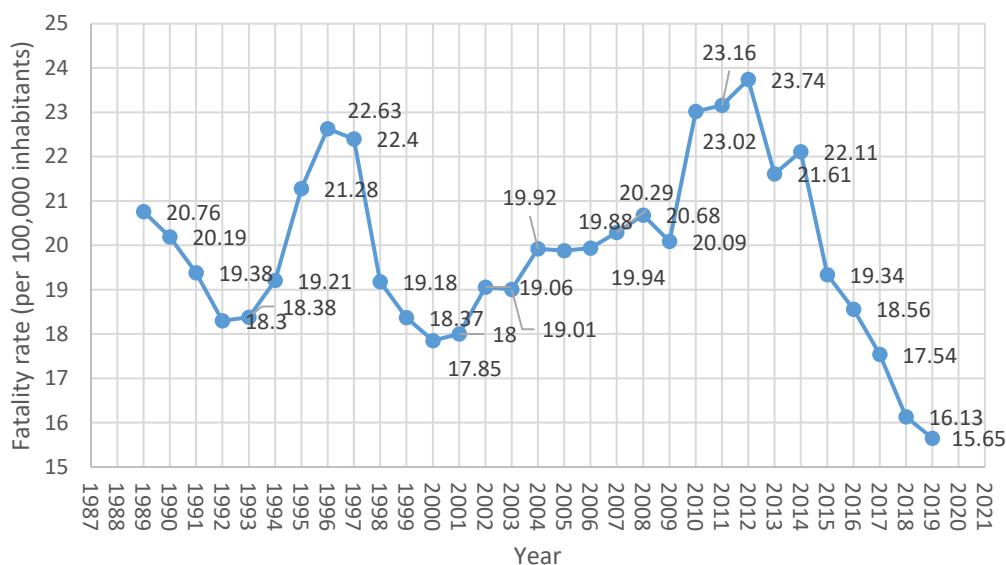
Figure 1 – Decrease of road traffic fatalities in Europe (Statista, 2020, Eurostat 2020)



In Brazil alone, according to Andrade *et al.* (2014), more than 43,000 people were killed in road traffic crashes in 2010, which accounted for 3.86% of the total deaths in the country.

A reliable source of information on the fatality of traffic accidents in Brazil is the Institute of Applied Economic Research (IPEA). This institute releases annual data on violence in the country, including deaths related to traffic accidents. Figure 2 shows the fatality rate per 100,000 inhabitants during the period from 1989 to 2019.

Figure 2 – Fatality rate per 100,000 inhabitants (IPEA, 2023).



It is interesting to note two significant peaks of fatalities during this period. The first occurred in 1996, prior to the rigorous 1997 traffic legislation update (Law 9.503/1997). However, the level of violence in traffic reached a new record in 2012 when the so-called "dry law," number 12.270/2012, increased the severity of penalties for drunk drivers. The trend of reducing violence in traffic was confirmed after 2014 when Law 11.910/2009 came into effect, making airbags and Anti-lock Braking System (ABS) mandatory in all new vehicles.

Another justification for the reduction of fatalities is the continuous improvement of the efficiency of vehicle active and passive safety systems. Active safety refers to technology that assists in the prevention of a crash, such as ABS, Electronic Stability Control (ESC), Autonomous Emergency Braking (AEB), Lane Departure Warning (LDW), etc. Passive safety includes all components of the vehicle that help to reduce the severity of a crash event, such as seatbelts, airbags, and structural elements.

Passive safety systems have shown significant improvement over the last few decades, primarily due to the increasing accuracy and fidelity of crash test finite element analysis to real-world scenarios. These models have gained crucial importance in new car development programs, as they significantly

reduce the number of physical prototypes, thereby shortening development times and costs. The environment of this process is specially treated in the field of crashworthiness.

## 2.2. CRASHWORTHINESS

### 2.2.1. Crash Management Systems

The term “Crash Management System” is generally used to describe the structural module consisting of the bumper and the related attachments that connect to the longitudinal beams of the car. Front bumpers are normally connected to the front longitudinal beam by a separate deformation element (“crash box”). Rear bumpers are, however, mounted directly to the rear longitudinal beam. However, the bumper system can’t be considered as an isolated structural module. Its design must be optimized taking into account the crashworthiness of the overall body structure, in particular the deformation characteristics of the safety cell and the crumple zones.

These components are designed not only to ensure occupant and pedestrian protection and meet legislative requirements but also to improve the repairability of the vehicle.

The analysis of real-world accidents determined that more than 85% of all frontal impacts occur at velocities below 9 mph (15 km/h), resulting in one of the primary crash safety requirements for the front structure of cars (Leimbach and Kiebach, 2013). Ensuring both damageability and repairability enhancements in vehicles is crucial, but it must be done without compromising the safety of vehicle occupants or pedestrians.

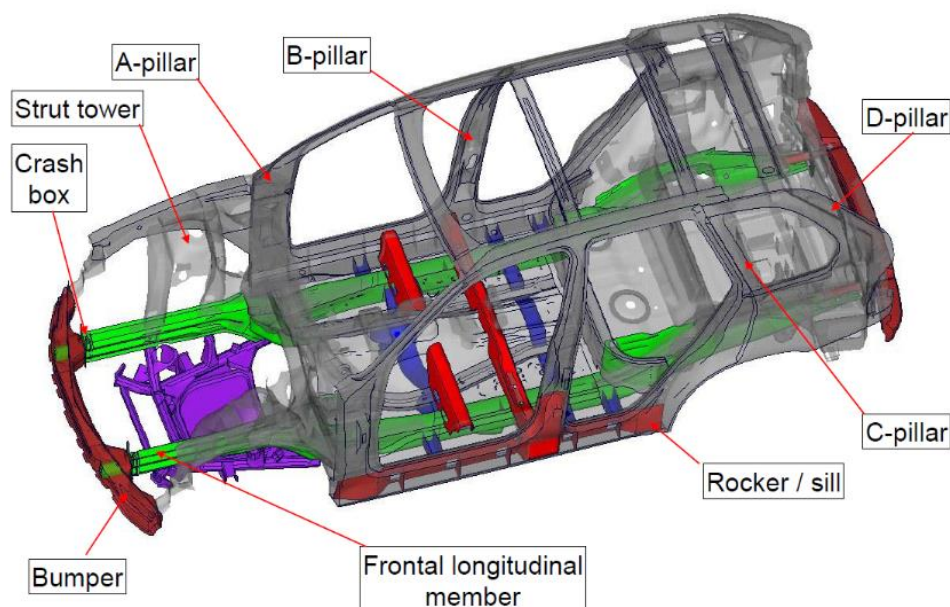
### 2.2.2. Vehicular structure

A vehicle structure, commonly referred to as the Body in White (BIW), is designed to withstand various loading conditions throughout the vehicle's lifespan, while also ensuring occupant safety during a crash. The BIW needs to possess specific characteristics, such as stiffness, lightweight construction, and compatibility with conventional manufacturing processes and materials.

These attributes are essential not only for meeting performance requirements but also for minimizing production costs.

The stiffness of the BIW is crucial as it provides structural integrity and resistance to deformation. A rigid structure helps distribute loads efficiently, preventing excessive bending or twisting during normal driving conditions and crash events. By maintaining structural integrity, the BIW can effectively protect the vehicle occupants and ensure their safety. A common BIW and its components are shown in Figure 3.

Figure 3– Typical Body in White of a commercial vehicle (Duddek, 2016).



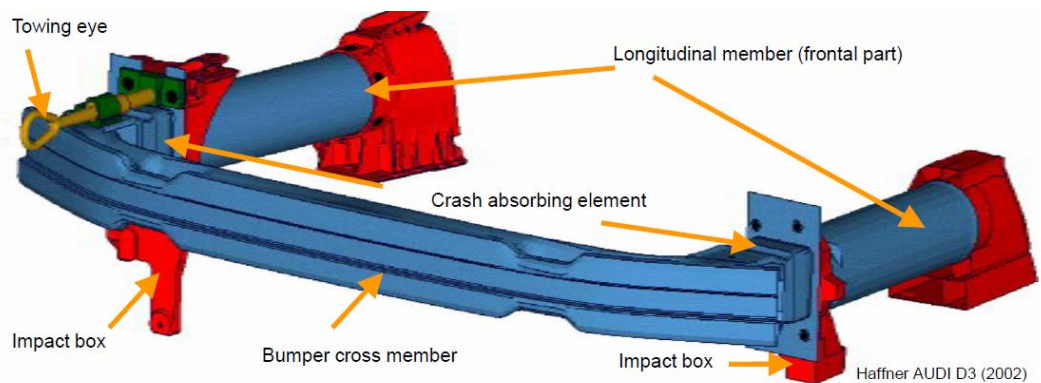
One can divide the BIW in three sections: front structure, rear structure and passenger compartment (Lima, 2016).

#### 2.2.2.1. Front Structure

During a frontal vehicular impact, the front bumper cross member, crash box, and longitudinal members play crucial roles in ensuring the safety and structural integrity of the vehicle. Figure 31 illustrates the typical anatomy of an automotive front structure.



Figure 4 – Typical anatomy of an automotive front structure. (Duddek, 2016).



The main functions and considerations of each of these will be discussed below.

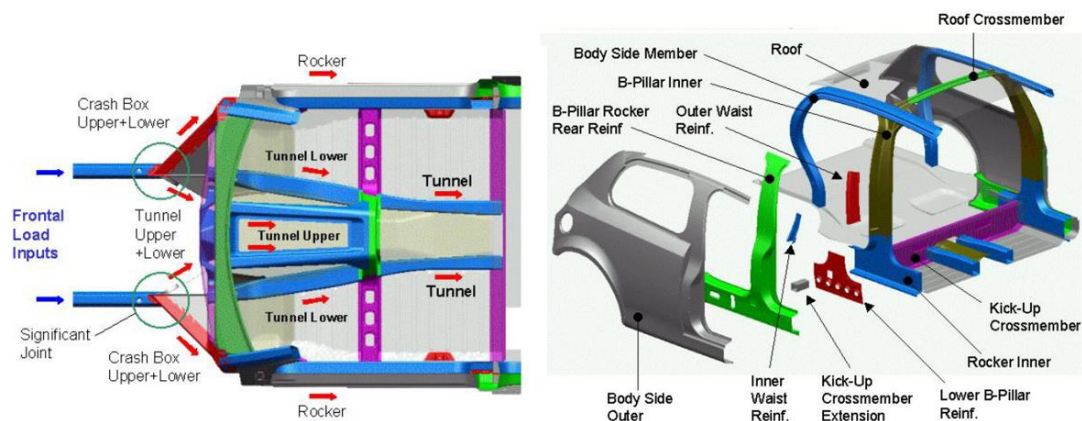
- **Front Bumper Cross Member:** The front bumper cross member, also known as bumper reinforcement or bumper beam, is a structural component located behind the front bumper cover. Its primary function is to absorb and distribute impact forces during a collision. The cross member is typically made of high-strength steel or aluminum. It helps prevent or minimize damage to the vehicle's front body structure and other critical components, such as the engine, radiator, and headlights. Its strength is particularly crucial in cases of offset or oblique frontal impacts, where the force is not evenly distributed throughout the vehicle structure.
- **Crash Box:** The crash box, also known as the energy absorber element, is typically integrated into the front bumper system. The crash box is typically constructed using foam, honeycomb structures, or deformable materials with crush initiators. This design ensures maximum energy absorption in various situations, including oblique impacts.
- **Longitudinal Members:** The longitudinal members are elements that run along the length of the vehicle's body frame. During a collision, the longitudinal members serve as the primary load-bearing structures, transferring impact forces from the front or rear of the vehicle to other parts of the chassis. Generally, each front longitudinal member absorbs

25% of the impact energy in the event of a frontal collision with a rigid wall.

#### 2.2.2.2. Passenger cabin

The passenger cabin plays a crucial role in ensuring maximum stiffness and preventing intrusion in the event of a frontal, rear, or side crash. It is designed with a tunneling structure located above the floor, which transfers the forces from a front or rear impact to the rest of the vehicle. Additionally, the cabin must be specifically engineered to provide protection against side impacts, as there are no designated zones for absorbing the energy. This can be achieved by using high-strength materials on structural elements such as the B-pillar, roof, and kick-up cross members, as well as ensuring the correct distribution of load paths. Figure 5 illustrates the passenger cabin frame.

Figure 5 – Passenger Cabin typical structure (Duddek, 2016).



In addition to its role in frontal, rear, and side crashes, the passenger compartment also plays a critical role in protecting occupants during rollover scenarios. The pillars, such as the A-pillars, B-pillars, and C-pillars, are strengthened to withstand the forces experienced during rollovers. They provide vertical support to the roof, helping to prevent it from collapsing inward and reducing the risk of head and neck injuries to occupants (Duddek, 2016).

#### 2.2.2.3. Rear structure

When it comes to rear impacts, vehicles usually show the following structural elements to withstand these collisions.

- **Rear Frame Rails or Cross Members:** The rear frame rails or cross members are structural components that extend along the rear of the vehicle's frame or chassis. They provide strength and rigidity to the rear structure. During a rear impact, these elements help distribute the forces throughout the vehicle's body, minimizing deformation and protecting the occupants.
- **Rear Energy Absorbing Structures:** Rear energy absorbers, similar to crash boxes, are often integrated into the rear structure of the vehicle. These structures are designed to absorb and dissipate energy during a rear impact. They are typically made of deformable materials or foam that can compress and crumple, reducing the severity of the forces transmitted to the occupants.
- **Rear Longitudinal Rails:** Rear longitudinal rails have the same function as front longitudinal rails. When a rear crash occurs, rear rails shall transmit the loads to the rest of the vehicle structure with minimum collapsing as possible. Although most cars have a crumple zone at their rear ends to reduce acceleration on the occupants, there are legal requirements to avoid fuel tank damages and leakages that could cause fire after the crash. Parenteau *et al.* (2020).

### **2.2.3. Buckling of thin wall structures**

Modern vehicular structures are mainly built of stamped and welded steel thin wall sheets due to the good stiffness, strength, low weight, and low costs that this process offers to vehicle manufacturers. The front and rear regions of vehicles typically utilize thin-walled closed section structures, which can demonstrate significant energy absorption values during buckling when exposed to frontal impact.

Structures involved in vehicular impacts can exhibit two distinct modes of buckling: progressive folding and global bending. Progressive folding involves consecutive plastic deformations, which result in a higher mean crushing force and, consequently, higher energy absorption. On the other hand, global bending is characterized by a single force peak followed by a sudden decrease

in axial load, indicating a lower energy absorption capacity. Figure 6 and Figure 7 illustrate these buckling modes.

Figure 6 – Progressive folding and plastic hinge (or global bending) buckling mechanisms (Duddek, 2016).

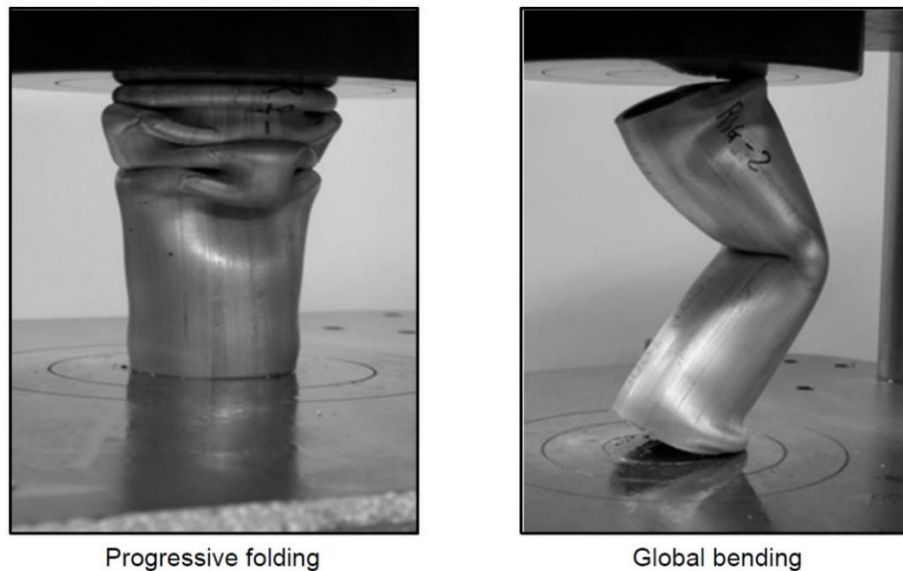
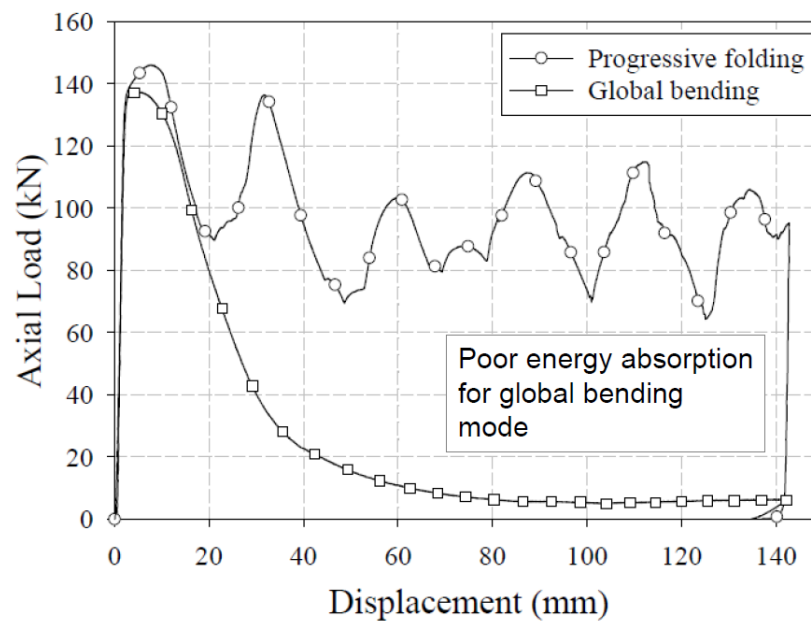


Figure 7 – Force response of progressive folding and global bending buckling mechanisms (Duddek, 2016)

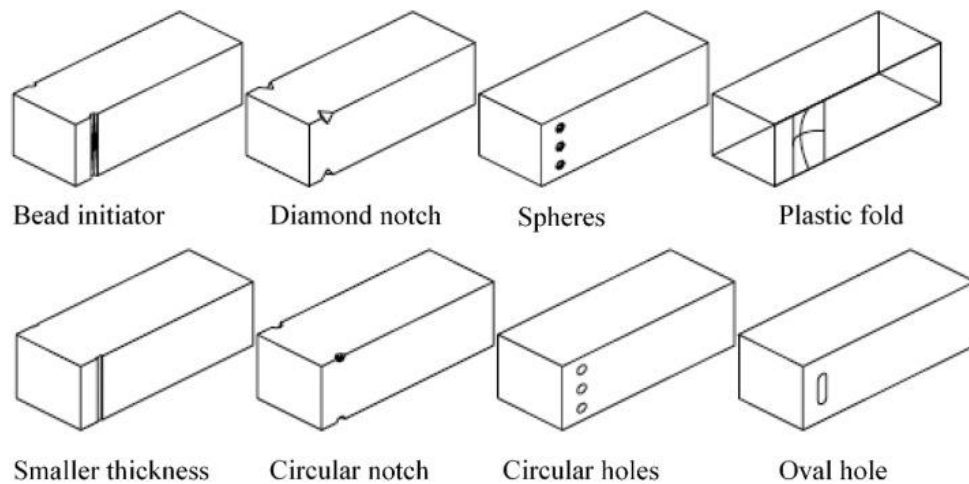


The symmetry of both the geometry of a structure and load distribution plays a crucial role in determining its deformation behavior. It affects whether the structure will exhibit progressive folding or global bending when subjected to

external forces. In the case of an asymmetrical structure or significant shear load, the development of global bending regions can result in reduced energy absorption during impact events. To overcome this limitation, practical applications often employ triggers that promote progressive folding, as shown in Figure 7, even if it leads to a slight decrease in the mean crushing force.

By favoring progressive folding through the use of triggers, engineers can increase the overall energy absorption capacity of the structure, thereby improving its crashworthiness. Although there may be a trade-off in terms of a small decrease in the mean crushing force, the ability to sequentially engage plastic deformations allows for higher levels of energy dissipation and improved occupant safety. Figure 8 illustrates various types of deformation triggers applied to a thin-walled square cross-section structure.

Figure 8 – Deformation triggers typically used on crash boxes. (Kumar *et al.*, 2014.)



#### 2.2.4. Regulations

In the realm of vehicular safety, manufacturers are obligated to subject their vehicles to rigorous testing procedures mandated by regulatory agencies. These tests serve to assess the crashworthiness of vehicles and ensure that they meet or exceed the specified standards set by the respective regulatory bodies. In the United States, the National Highway Traffic Safety Administration (NHTSA) establishes guidelines and requirements for vehicle crashworthiness. Similarly, Europe follows the standards outlined by the

United Nations (UN), while China adheres to the GB Standards (National Standards of the People's Republic of China).

Regarding vehicle safety around the globe, there are different types of legislation.

- International
  - ECE (United Nations Economic Commission for Europe)
  - EU (EG Directives)
- National
  - United States/Canada (Federal Motor Vehicle Safety Standard, or FMVSS)
  - Australia (Australian Design Rules, or ADR)
  - Japan
  - India (Automotive Industry Standards, or AIS)
- State / Provincial
  - Canada
  - United States
  - Australia

In addition to standards and regulations concerning occupant protection in vehicles, there are also specific standards and regulations in place to address pedestrian protection. These standards, known as Global Technical Regulations (GTRs), are developed and implemented by the United Nations. One significant GTR in this area is GTR No. 9, which specifically focuses on pedestrian protection. Its aim is to enhance the safety of pedestrians in the event of a collision with a vehicle and consider various factors such as the design of the vehicle's front end, its interaction with pedestrians, and the mitigation of potential injuries.

In Brazil, the National Traffic Council (CONTRAN) is the highest normative and advisory body of the national traffic system. It establishes guidelines for the national traffic policy and coordinates all entities within the National Traffic System. In the context of crashworthiness, CONTRAN establishes the national

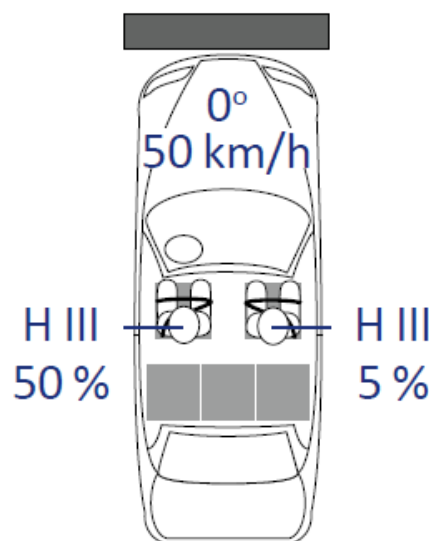
protection requirements for vehicle occupants under different impact scenarios.

Furthermore, the Brazilian Association of Technical Standards (ABNT) also plays a role in establishing technical standards related to vehicle safety. ABNT develops and publishes voluntary standards that are often adopted as regulations by CONTRAN.

These regulatory standards serve as benchmarks to ensure that vehicles provide sufficient protection to occupants in the event of a crash, thereby reducing the risk of injuries and fatalities. The main types of crash tests and their respective standards are mentioned below.

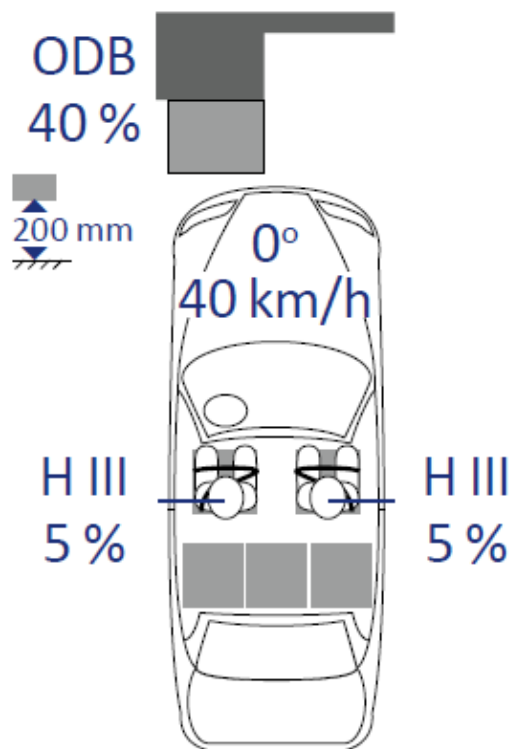
- Frontal Impact Tests:
  - Full Frontal Impact Test: This test simulates a head-on collision between two vehicles of the same weight, traveling at a speed of 50 km/h. It evaluates the vehicle's ability to absorb and distribute the impact forces evenly across the front structure, which is usually critical for dummy acceleration levels and HIC. Brazilian standards ABNT NBR 15300-1 and ABNT NBR 15300-2 describe the conditions for this test in an equivalent manner to ECE R94.

Figure 9 – Full frontal impact crash test protocol ABNT NBR 15300-2 (Safety Companion, 2023).



- Offset Frontal Impact Test: In this test, the vehicle is impacted on one side of the front structure, simulating a real-world scenario where only 40% of the front end is involved in a collision against an offset deformable barrier (ODB). It assesses the vehicle's ability to protect occupants when the impact is not directly centered and is usually critical for firewall intrusions and deformations on the A-pillar. In Brazil, this test can be considered for frontal impact according to the manufacturer's criteria, as per the standards ABNT NBR 15300-1 and ABNT 15300-3. This test is equivalent to FMVSS 208.

Figure 10 – 40% offset frontal impact crash test protocol ABNT NBR 15300-3 (Safety Companion, 2023)

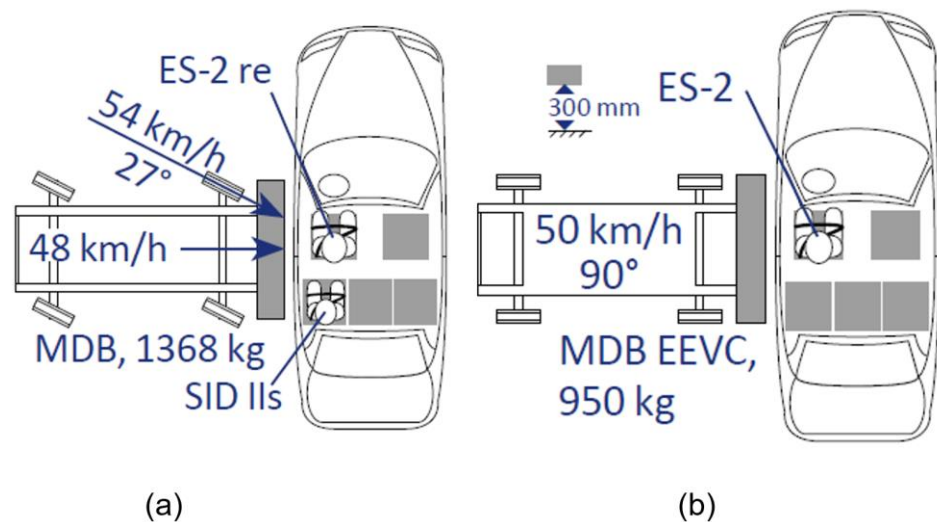


- Side Impact Tests
  - Side Impact Crash Test: This test evaluates a vehicle's protection for occupants during a side collision. A deformable barrier or a moving trolley impacts the side of the vehicle, simulating the force experienced in a typical side-impact crash. The standard ABNT 16204-1 describes the procedures for side impact tests and should be used in conjunction with ABNT NBR 16204-2 or ABNT NBR 16204-3, according to the



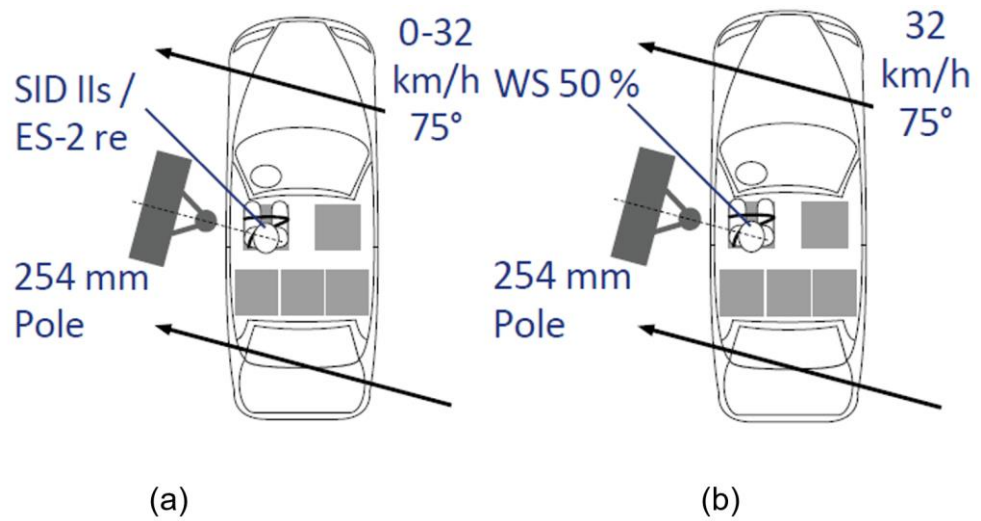
manufacturer's criteria. The first scenario is very similar to FVMSS 214, in which a 950 kg sled impacts the car laterally at a 90° angle and a speed of 50 km/h. The second scenario is similar to ECE 95, where a 1368 kg sled impacts the side of the car at a 27° angle and a speed of 54 km/h.

Figure 11 – Side impact crash test protocol (a – ABNT NBR 16204-2; b – 16204-3)



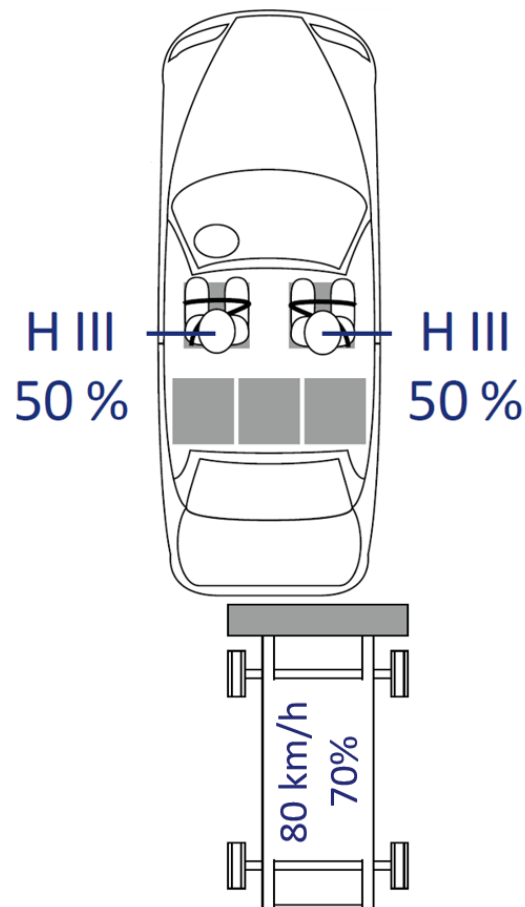
**Side Pole Impact Test:** This test simulates a vehicle striking a rigid pole or tree on its side. It assesses the protection offered to the head and chest of occupants, as pole impacts can be particularly severe. CONTRAN Resolution 949, dated 28/03/2022, establishes the requirements for side pole impact crash tests. These tests can be conducted in accordance with either FVMSS 214 or ECE R135, depending on the automaker's preference.

Figure 12 – Side pole impact crash test protocol as per a – FMVSS 214 and b – ECE R135 (Safety Companion, 2023)



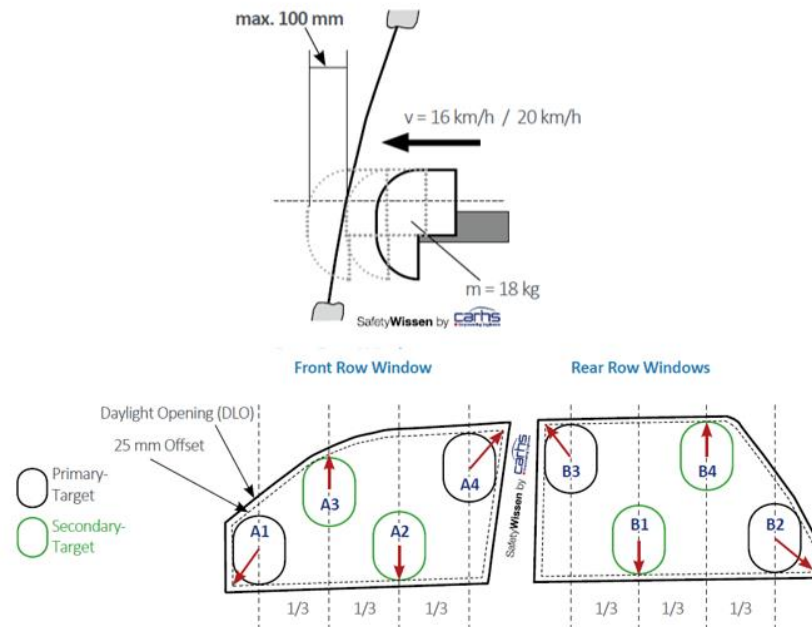
- Rear Impact tests
  - FMVSS 202a – Head Restraints: This standard sets requirements for head restraints in passenger vehicles. It aims to reduce the risk of neck injuries, particularly whiplash, in rear-end collisions. It is based on a dynamic test to evaluate head restraint performance during a rear impact.
  - FMVSS 301 – Fuel System Integrity: This standard addresses the integrity of a vehicle's fuel system in a 70% Overlap Deformable Barrier (ODB) of 1368 kg at 80 km/h rear impact. It aims to reduce the risk of fuel leakage and fuel-related fires in rear-end collisions. It requires vehicles to undergo a rear impact test to evaluate fuel system integrity. Mandates that the fuel system must remain intact and free from major fuel leaks during and after the test.

Figure 13 – Rear impact test as per FMVSS 301 (Safety Companion, 2023).



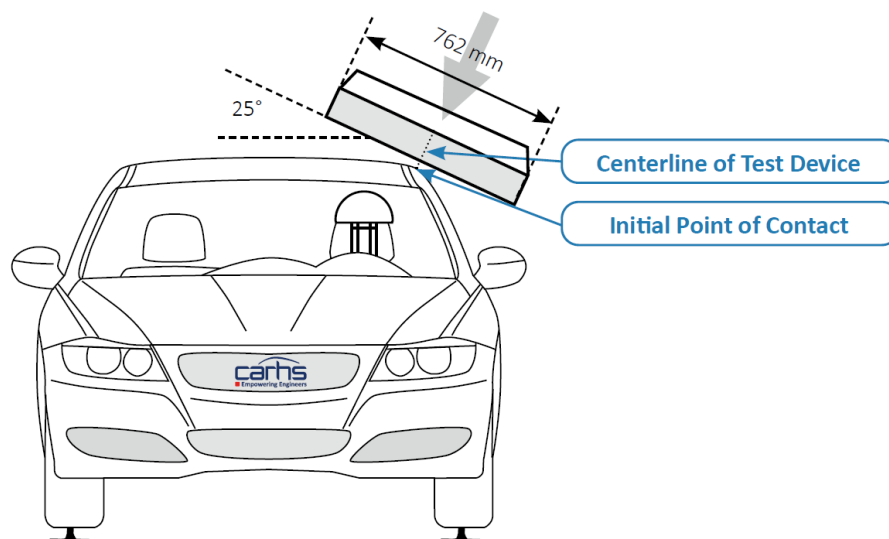
- Rollover tests
  - Ejection Mitigation Test: This test establishes requirements for ejection mitigation systems to reduce the likelihood of ejections of vehicle occupants through side windows during rollovers or side impact events. The standard is based on the impact of an 18 kg headform on up to 4 impact test locations on each side window, which head excursion may not exceed 100 mm. It applies to the side windows next to the first three rows of seats, and to a portion of the cargo area behind the first or second rows. It is defined by the standard FMVSS 226 and is illustrated in Figure 14.

Figure 14 – Ejection mitigation test as per FMVSS 226 (Safety Companion, 2023).



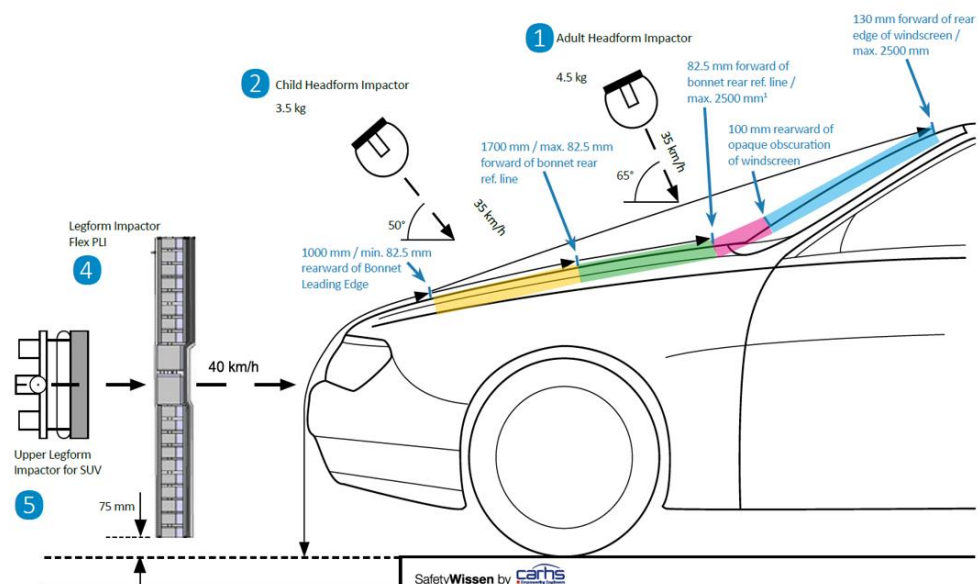
- Roof Crush Resistance Test: The purpose of this test is to assess the strength of vehicle roofs to prevent or minimize injuries and fatalities in rollover accidents. The roof crush resistance is specifically evaluated by applying a load that is 1.5 times the weight of the unloaded vehicle and it must not deform beyond a predetermined level. The test specification is defined in the FMVSS 216 standard.

Figure 15 – Roof crush resistance test as per FMVSS 216 (Safety Companion, 2023)

















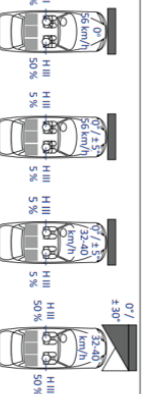
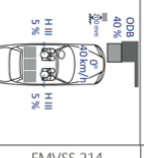
- Pedestrian Protection Tests:
  - Adult Headform Impact Test: This test evaluates the vehicle's front-end design in terms of pedestrian safety. A headform impacts various areas of the vehicle's front surface to assess the potential for head injuries in the event of a collision.
  - Child Head Impact Test: This test evaluates the protection provided to a child's head in the event of a collision. It involves impacts with different vehicle surfaces to assess potential head injuries.
  - Legform Impact Test: This test assesses the risk of leg injuries to pedestrians. It involves the impact of a legform on the vehicle's front bumper and bonnet to evaluate the protection offered to a pedestrian's lower limbs.
  - Upper Legform Impact Test: Equivalent to the legform impact test, this test focuses on the upper leg area. It assesses the protection provided to the upper legs of pedestrians during a collision.

Figure 16 – Pedestrian protection tests as per ECE R127 (Safety Companion, 2023).



A broader picture of the different types of crash tests in different regions of the world, their respective standards and main characteristics can be seen illustratively in Figure 17.

Figure 17 – Rules and regulations on occupant protection around the world (Safety Companion, 2023)

	Australia	S. Korea	India	China	Japan	Europe	USA
	 	 	 	 	 	 	 
	ADR 69/00 <small>Safety Witness by CERTS</small>	KMVSS 102-3	AIS-201 (Draft)	GB 11551-2014	Art. 18	UN R137 <sup>1</sup>	FMVSS 208 
	ADR 73/00 <small>NBR 15300-3</small>	KMVSS 102	AIS-098	GB/T 20913-2007	Art 18	UN R94	FMVSS 208 
	ADR 72/00	KMVSS 102 <small>ES-1/ES-2 50 km/h 90° MDB EVC 950 kg</small>	AIS-099 <small>ES-1/ES-2 50 km/h 90° MDB EVC 950 kg</small>	GB 20071-2006 <small>ES-2 50 km/h 90° MDB EVC 950 kg</small>	Art. 18 <small>ES-2 50 km/h 90° MDB EVC 950 kg</small>	UN R95 <small>ES-2 50 km/h 90° MDB EVC 950 kg</small>	FMVSS 214 <small>ES-1 re ES-2 re 48 km/h 90° MDB 1368 kg SID 16</small>
	ADR 85/00 <small>32 km/h 75° WS 50% Pole 54 mm</small>	KMVSS 102-4 <small>WS 50% 254 mm Pole 32 km/h 75°</small>		GB/T 37337-2019 <small>ES-1 re ES-2 re WS 50% 254 mm Pole 32 km/h 75°</small>	Art. 18 <small>32 km/h 75° WS 50% Pole 54 mm</small>	UN R135 <sup>1</sup> <small>WS 50% 254 mm Pole 32 km/h 75°</small>	FMVSS 214 <small>ES-1 re ES-2 re WS 50% 254 mm Pole 0.32 m/s 75°</small>
		KMVSS 102-2	AIS-100	GB/T 24550-2009	Article 18	UN R127 R (EU) 2019/2144 <sup>4</sup> R (EU) 2021/535	Pedestrian
		KMVSS 91 KMVSS 91-2 KMVSS 91-3	AIS-101	GB 20072-2006	Article 22-4	UN R34 UN R153	Rear
	ADR 21	KMVSS 88	IS15223	GB11552-2009	Article 20	UN R21	Head Impact
	<small>Safety Witness by CERTS</small>			Roof Crush: GB6134-2010			Rollover <small>Roof Crush: FMVSS 216a Ejection Mitigation: FMVSS 226</small>

### **2.2.5. Independent institutions crash tests**

Due to the great importance of improving vehicle safety on a global scale, several independent institutions, such as the IIHS (Insurance Institute for Highway Safety) and NCAP (New Car Assessment Program), voluntarily publish safety reports and assign star ratings to new cars based on their performance in various tests. These tests evaluate both active safety systems such as Anti-lock Braking Systems (ABS), Electronic Stability Control (ESC), Autonomous Emergency Braking (AEB), Lane Departure Warning, and more, as well as passive safety systems like seatbelts, airbags, energy absorption capacity, and structural integrity. These programs are not mandatory for vehicle commercialization, but they impose quality checks on new cars in the market. They have stricter specifications and regularly publish a detailed analysis of their crash results, which encourages manufacturers to construct safer vehicles. A comprehensive list of vehicle safety tests conducted by each of the main independent institutions in America and Europe is shown in Figure 18.

Figure 18 – Principal vehicle safety tests performed by independent institutions on Americas and Europe (Safety Companion, 2023)

	Euro NCAP / ANCAP	U.S. NCAP	IIHS	Latin NCAP
Full-width	<p>Sled Test 56 km/h</p> <p>50/35 km/h</p> <p>H III 5% TH 50% H III 5%</p> <p>2026 modifications are preliminary</p>	<p>56 km/h</p> <p>H III THOR 50% H III 5%</p>		
ODB / SOB	<p>MPDB 1400 kg</p> <p>0°, 50 km/h</p> <p>THOR 50% Q6 H III 50/5% Q10</p>	<p>OMDB, 2486 kg</p> <p>15°, 35 km/h</p> <p>THOR 50% THOR 50%</p>	<p>SOB 25%</p> <p>0° 64 km/h</p> <p>H III 50% H III 5%</p>	<p>ODB 40%</p> <p>0° 64 km/h</p> <p>H III 50% Q3 H III 50% Q1.5</p>
MDB	<p>AE-MDB, 1400 kg</p> <p>60 km/h 90°</p> <p>Q10 Q6</p> <p>■ Far Side Occupant Protection</p>	<p>ES-2 re WS 50%</p> <p>55 km/h 27°</p> <p>MDB, SID IIS 1368 kg</p>	<p>SID IIS</p> <p>90° 60 km/h</p> <p>1900 kg</p> <p>SID IIS</p>	<p>ES-2</p> <p>MDB EVC</p> <p>50 km/h 90°</p> <p>950 kg Q1.5 Q3 Q1.5</p>
Pole	<p>WS 50%</p> <p>32 km/h 75°</p> <p>254 mm Pole</p> <p>■ Far Side Occupant Protection</p>	<p>SID IIS WS 50%</p> <p>32 km/h 75°</p> <p>254 mm Pole</p>		<p>ES-2</p> <p>29 km/h 90°</p> <p>254 mm Pole</p>
Rollover		<p>■ SSF</p>		
VRU	<ul style="list-style-type: none"> <li>■ aPLI</li> <li>■ Upper Legform</li> <li>■ Headforms</li> <li>■ AEB/AES Ped., Cyclist, PTW, PSS</li> <li>■ AEB Reverse Pedestrian</li> </ul>	<ul style="list-style-type: none"> <li>■ Flex PLI</li> <li>■ Upper Legform</li> <li>■ Headforms</li> <li>■ AEB Pedestrian</li> <li>■ Rear Automatic Braking</li> </ul>	<ul style="list-style-type: none"> <li>■ AEB Pedestrian</li> </ul>	<ul style="list-style-type: none"> <li>■ Flex PLI</li> <li>■ Upper Legform</li> <li>■ Headforms</li> <li>■ AEB VRU</li> </ul>
Child Safety	<ul style="list-style-type: none"> <li>■ Frontal MPDB</li> <li>■ Side MDB</li> <li>■ CRS - Installation</li> <li>■ Veh. Based Assessment, CPD</li> </ul>		<ul style="list-style-type: none"> <li>■ LATCH (Lower Anchors and Tethers for Children)</li> <li>■ Booster Seat Rating</li> </ul>	<ul style="list-style-type: none"> <li>■ Frontal ODB</li> <li>■ Side MDB</li> <li>■ CRS - Installation</li> <li>■ Veh. Based Assessment</li> </ul>
Whiplash	<ul style="list-style-type: none"> <li>■ Static Front / Rear</li> <li>■ Dynamic (2 Pulses)</li> </ul>			<ul style="list-style-type: none"> <li>■ Static</li> <li>■ Dynamic (1 Pulse)</li> <li>■ AEB City</li> </ul>
Other	<ul style="list-style-type: none"> <li>■ SBR, SAS, AEB, LSS, AEB, Occupant Status, AES, Rescue, Pedal Misapplication, AD</li> </ul>	<ul style="list-style-type: none"> <li>■ FCW, LDW, AEB, DBS, BSD, Headlights</li> </ul>	<ul style="list-style-type: none"> <li>■ AEB, FCW, SBR</li> <li>■ Headlights</li> </ul>	<ul style="list-style-type: none"> <li>■ SBR, ESC, SAS, BSD, LSS, AEB, e-Call, Rescue Sheet, Rear Impact: UN R32</li> </ul>

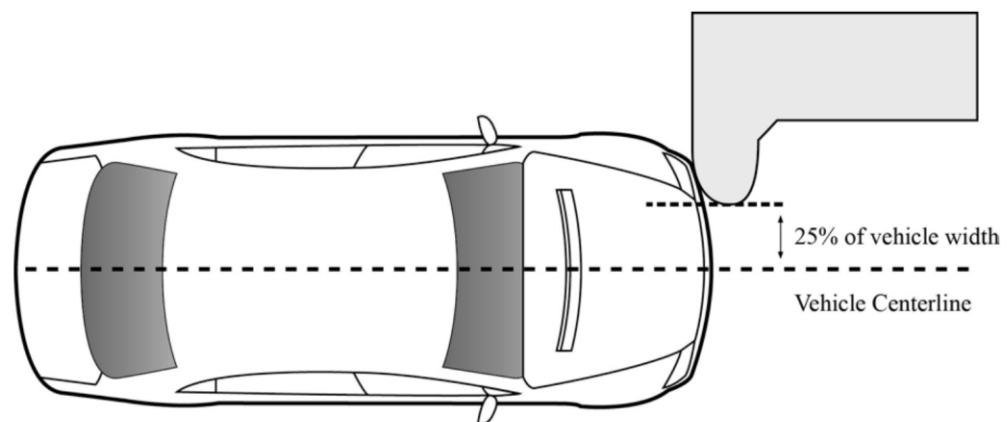
One of the most challenging crash test protocols adopted by most of these associations is the small overlap frontal impact, which is of particular interest in this work.



### 2.2.6. Small overlap crash test protocol

Over the years, vehicles have consistently achieved top ratings in both the IIHS and NCAP, prompting these institutions to explore additional test configurations for frontal impacts. One such protocol introduced by the IIHS in the late 2000s is the Small Overlap Crash Test Protocol, as discussed by Brumbelow and Zuby (2009). This test involves a frontal crash at 64.4 km/h with a 25% overlap on the driver's side, directed towards a rigid barrier. Its purpose is to evaluate vehicle safety under crash conditions where the front rails are not fully engaged. The rating protocol includes analyzing the responses of a 50th percentile male Hybrid III dummy, intrusion of the dash, steering column, and floor pan into the passenger compartment, as well as the effectiveness of the airbag, (Prasad, Dalmotas and German, 2014). Figure 19 provides an illustration of the small overlap test protocol.

Figure 19 – Small overlap crash test protocol (IIHS,2021).



The specific test configuration described above holds significant interest in this thesis due to the potential influence of friction on various aspects. Load eccentricity and shearing forces within the vehicle structure can greatly impact the occurrence of progressive buckling or the formation of plastic hinges, ultimately affecting the effectiveness of energy absorption during the crash event.

Furthermore, the driver-side small overlap frontal test presents notable challenges concerning dummy kinematics and airbag interaction. The impact-generated force often propels the dummy towards the A-pillar direction,

leading to the dummy's head sliding over the frontal airbag. Gaining an understanding of friction's role in this particular test configuration is crucial for advancing our knowledge of the complex interactions among the vehicle structure, dummy kinematics, and airbag performance.

To compare the stability of the dummy against airbag during the crash, two specific cases will be presented and analyzed.

Figure 20 showcases a poor interaction between the frontal airbag and the dummy during a small overlap crash test of a 2012 Mercedes C250. Initially, the airbag effectively supported the head, but as the crash progressed the dummy moved laterally and was thrown beyond the airbag's intended protection region. The lack of side curtain airbags contributed to this movement. As a consequence, the dummy's head contacted the roof rail during the rebound phase, resulting in a high acceleration peak.

Figure 20 – Mercedes C250 2012 small overlap crash test (IIHS, 2021).

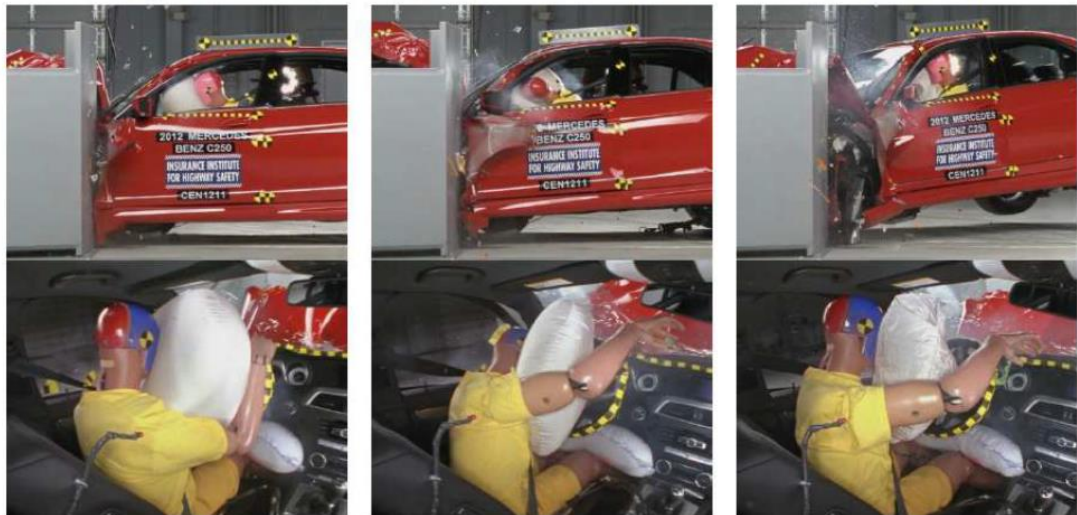
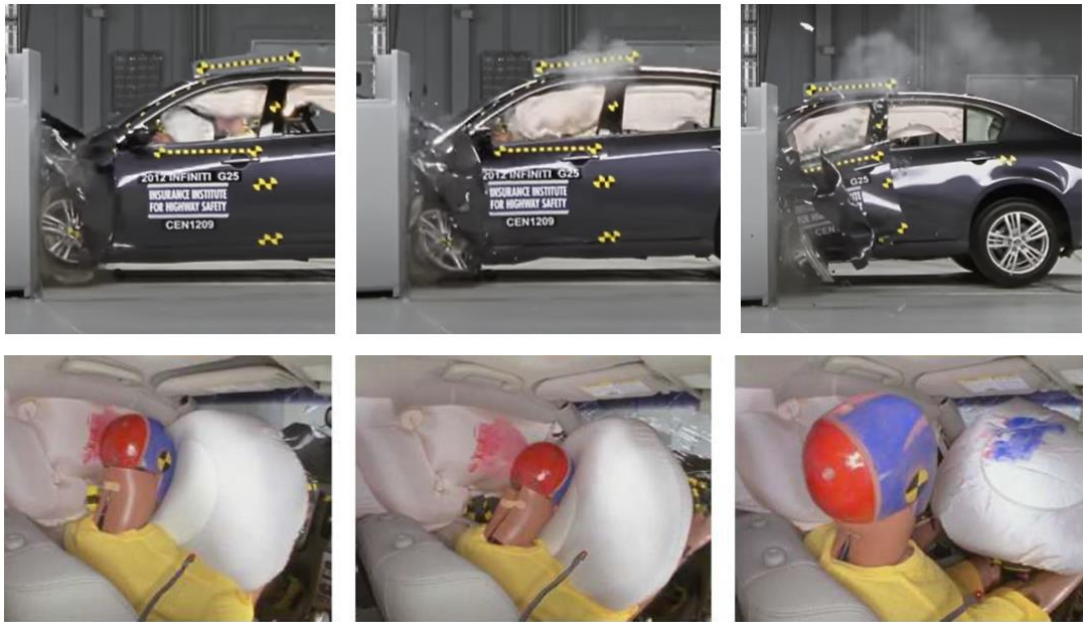


Figure 21 shows a crash test of the 2012 Infiniti G25, which effectively controlled the dummy's motion during the small overlap impact test. The summation of the effects of front and side curtain airbags was crucial in this case, as evidenced by dummy paint residue on their surfaces after the contact. It was also observed that the rebound phase was much more controlled than in former example, since the dummy was thrown back through the seat direction and no hard contact with the vehicle structure was noticed.

Figure 21 – Infinity G25 2012 small overlap crash test (IIHS, 2021).



### 2.2.7. Friction in crashworthiness

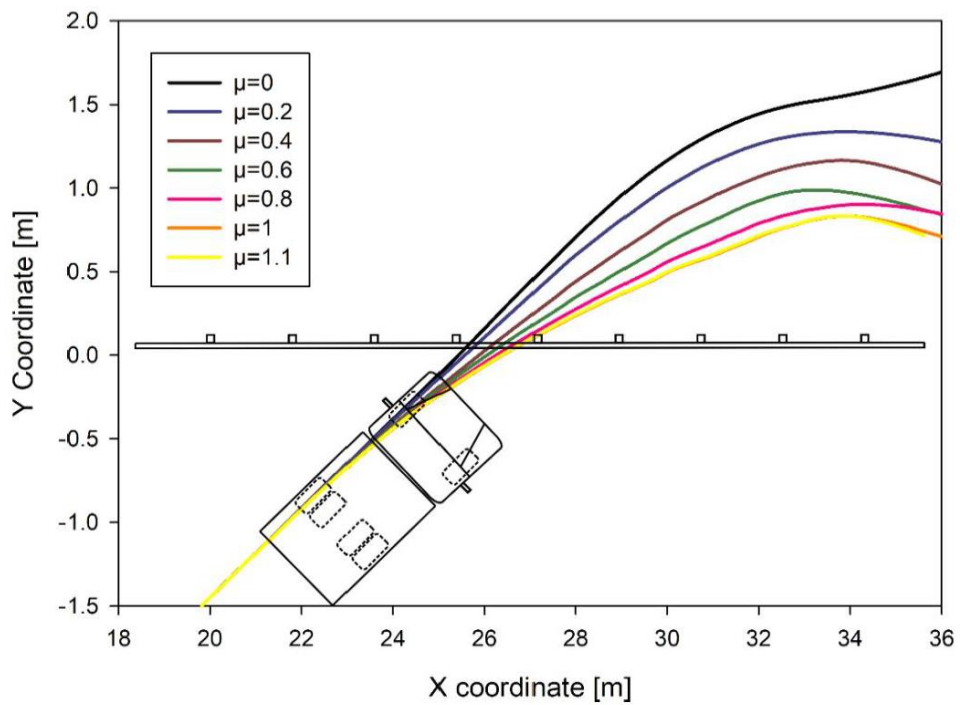
Friction plays a significant role in vehicular crashes, as it affects the interaction between surfaces that come into contact at high speeds and pressures. While friction itself may not be the primary mechanism for energy dissipation during a collision, it can greatly influence the deformation mode of vehicle components, thereby directly affecting their energy absorption capacity (Nia and Hamedani, 2010).

In the context of structural buckling analyses and vehicular impacts, the coefficient of friction is often determined based on user experience, relying on literature references (that are often simplified for low-pressure and low-velocity cases), or by using a single calibration parameter for a decay exponent. Surprisingly, only a limited number of studies have been conducted in this field, despite the well-established influence of friction on real-world crash scenarios.

For example, Stanislawek, Dziejewski, and Kedzierski (2019) have demonstrated that the trajectory of a vehicle is affected by the friction coefficient between tires and the ground during a crash. A series of numerical tests were conducted to investigate the influence of the friction coefficient over the normative EN 1317 specifications. The results obtained demonstrate that

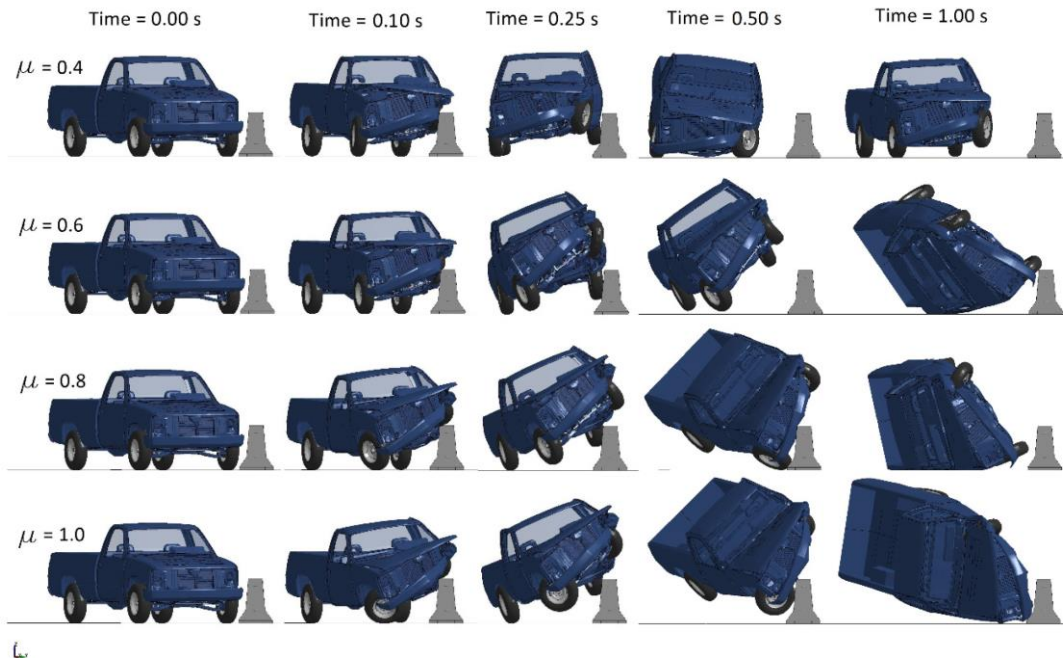
the trajectory of a vehicle is significantly affected by friction, as shown in Figure 22.

Figure 22 – The influence of friction on the impact of a commercial vehicle against a road barrier (Stanislawek, Dziewulski, and Kedzierski, 2019).



Trajkovski, Ambrož and Kunc (2018) found that the coefficient of friction has a crucial effect on vehicle rollover scenarios. In this study, different vehicles have been evaluated regarding rollover behavior on the oblique impacts on a concrete safety barrier (CSB). The study considered different levels of friction coefficient between the tires and the concrete, as shown in Figure 23.

Figure 23 – Pickup Chevrolet C 1500 behavior on the impact against CSB under different friction coefficients (Trajkovski, Ambrož and Kunc, 2018).

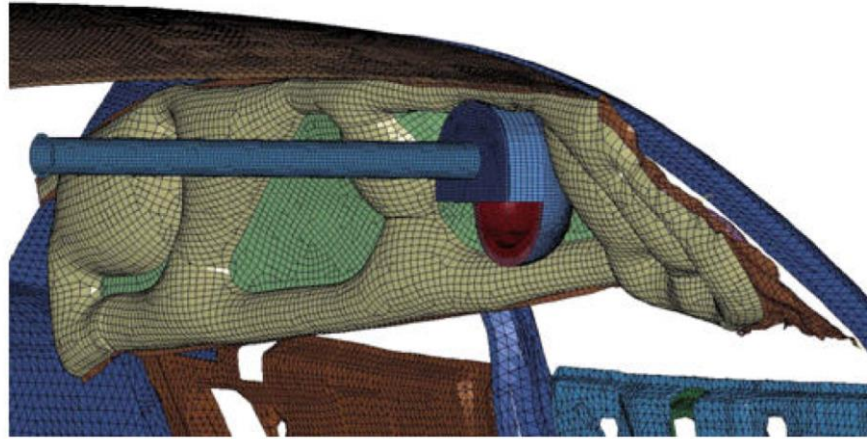


In the study, it was observed that when a vehicle collides with a barrier at an angle, the resulting lateral forces can create a moment around the vehicle's vertical axis, which has the potential to cause a rollover. The coefficient of friction between the tires and the road surface plays a significant role in determining the magnitude of these lateral forces and, consequently, the vehicle's behavior.

The findings of the study revealed that the value of the friction coefficient can either induce or prevent a vehicle rollover. Through simulations, it was demonstrated that when the tire-concrete safety barrier (CSB) coefficient of friction was low ( $\mu = 0.4$ ), the Chevrolet C 1500 successfully redirected itself back into its driving lane. However, in all other cases with different friction coefficients, a vehicle rollover occurred.

Friction is also a key element in the vehicle's interior, particularly in the contact between occupants against airbags, seatbelt, and internal coverings. Mihora, Friedman, and Hutchinson (2011) demonstrated that the friction between the head and the airbag can affect the effectiveness of this component, particularly when a lateral impact occurs at the borders of the airbag.

Figure 24 – contact of the headform with side curtain airbag (Mihora, Friedman and Hutchinson, 2011)



Authors found that in some cases, the high friction between the headform and the lateral curtain airbag prevents the sliding of the fabric upward and off the headform. This friction creates a rebound effect, ensuring that there is no hard contact between the parts. This is important because hard contact could result in severe accelerations and increase the risk of injury for the occupant. Further, friction was found to be especially important for oblique impacts due to the longer sliding distances along the curtain. An important finding of this study is that human-like skin was found to have a significantly lower friction coefficient against airbag fabric compared to dummy skin (vinyl plastisol). This could result in more slippery and unstable behaviors than the ones found on crash tests.

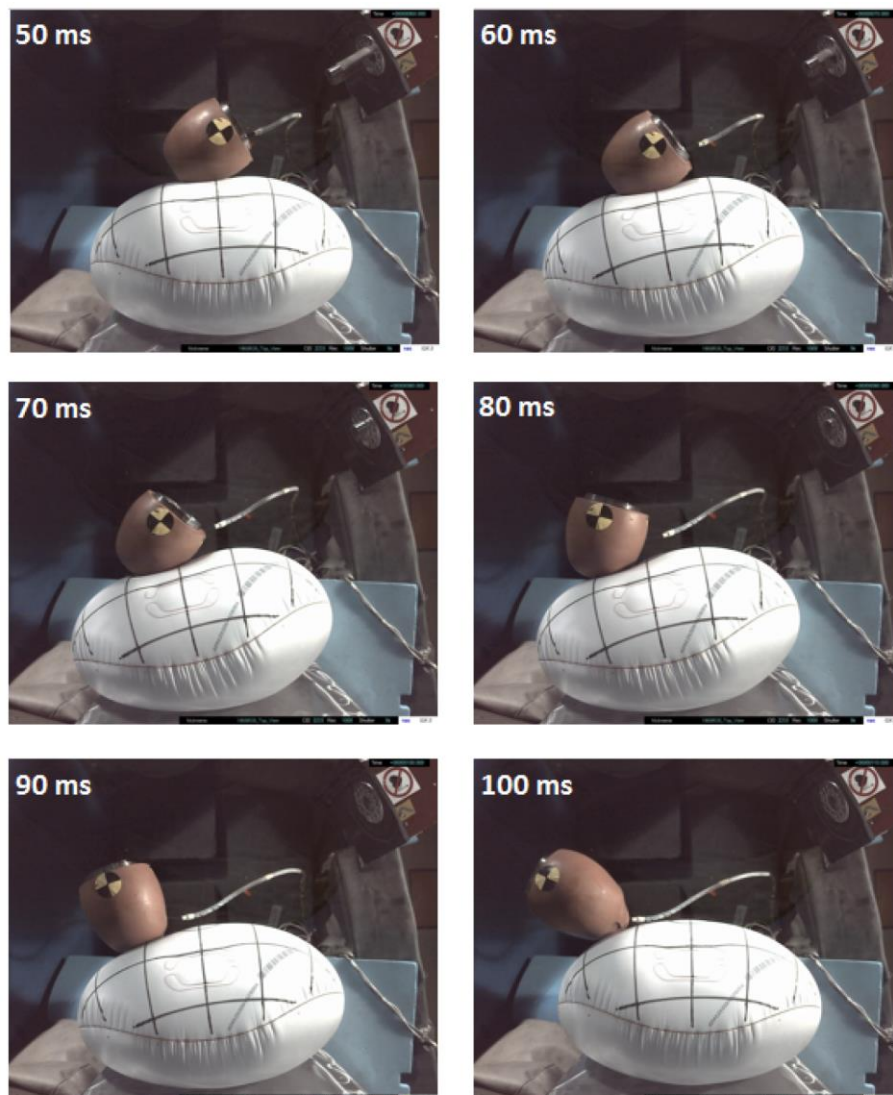
The study conducted by Eriksson and Piroti (2018) provides valuable insights into the influence of friction on crash tests, with a specific focus on the oblique collision of a dummy's head against an airbag. The rotational brain injury mechanisms are evaluated in this type of test, and one of the metrics used is the Brain Injury Criteria (BrIC), which has been proposed for potential inclusion in future New Car Assessment Program (NCAP) rating criteria.

The authors of the study investigated several parameters that affect the test results, including impact velocity, airbag pressure, and surface conditions.

They also examined the impact of surface conditions, such as the paint that is typically applied to the dummy's face during a crash test.

Understanding the role of friction in these crash tests is crucial for assessing the potential for brain injuries. By analyzing various parameters and surface conditions, the researchers aimed to gain a better understanding of how friction influences rotational brain injury mechanisms and the resulting BrIC values. An illustration of the experimental apparatus used in this work is shown in Figure 25.

Figure 25 – Dummy head – airbag oblique impact test (Erikson and Piroti, 2018).



The authors tested a wide range of parameter combinations in a Design of Experiments study. They examined three impact velocities (4.0, 5.4, and 6.7

m/s), three impact angles (45°, 60° and 70°), two airbag internal pressures (15 and 20 kPa), and three dummy surface conditions (clean rubber, dummy shirt fabric, and with grease paint, this last showed in Figure 26).

Figure 26 – Front and side view of dummy's head with grease paint applied to the side that is expected to be in contact with the airbag (Erikson and Piroti, 2018).



It was found that the rotational velocity of the head is heavily dependent on the friction force between the airbag and the dummy's head. Furthermore, the results of numerical simulations in LS-Dyna are enhanced when incorporating pressure and slip velocity dependence in the friction model.

One important observation of this work is that friction shows a significant reduction in regions where paint was applied. This is a very common technique in crashworthiness to create marks on the contact regions of a dummy with other parts such as the airbag and vehicle panel. This can be interpreted as a lubricated system rather than a dry friction mechanism. No references were found in the literature that considers paint as a lubricant in the dummy's interaction with the airbag and the vehicle's interior.

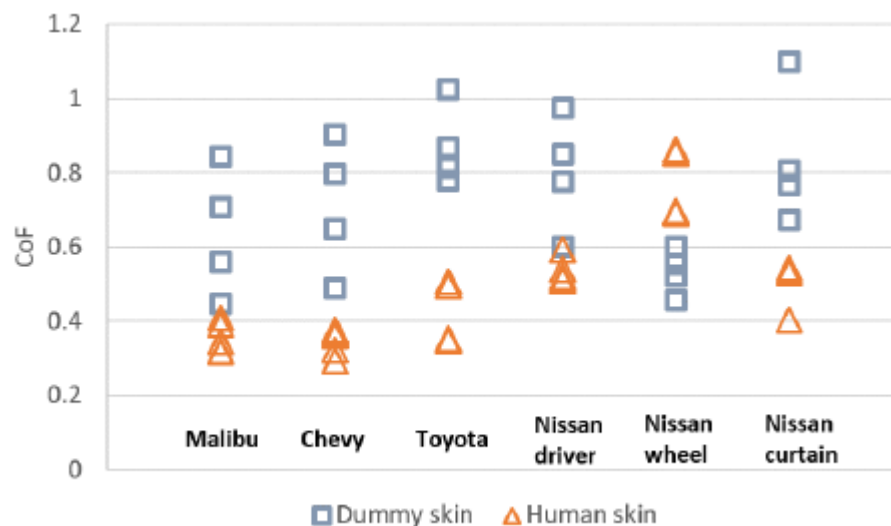
The authors also stated that the friction force and its modeling have a significant impact on the rotation of a dummy head during impact with the airbag. This influence is even greater than that of internal airbag pressure. Therefore, the improvement of friction models between these contact pairs can



be a step towards improving vehicle safety and consequently reducing traffic-related injuries.

Dong *et al.* (2020) experimentally characterized the friction coefficient between human skin from post-mortem human subjects (PMHS) and airbag fabrics. The authors also compared the results with different dummy skin samples made of vinyl plastisol at different slip velocities and pressures. The authors found that the difference between human and dummy skin friction with the airbag samples varied significantly among different airbags.

Figure 27 – Friction coefficients comparison between Dummy skin and Human skin for different airbag samples. Dong *et al.* (2020).



### 2.3. TRYBOLOGY

Before describing any tribological phenomena one must keep in mind that a tribological system has multiscale and multidisciplinary interaction. According to Holmberg (2007), a tribological problem can be divided into three scales: nanotribology, microtribology and macrotribology.

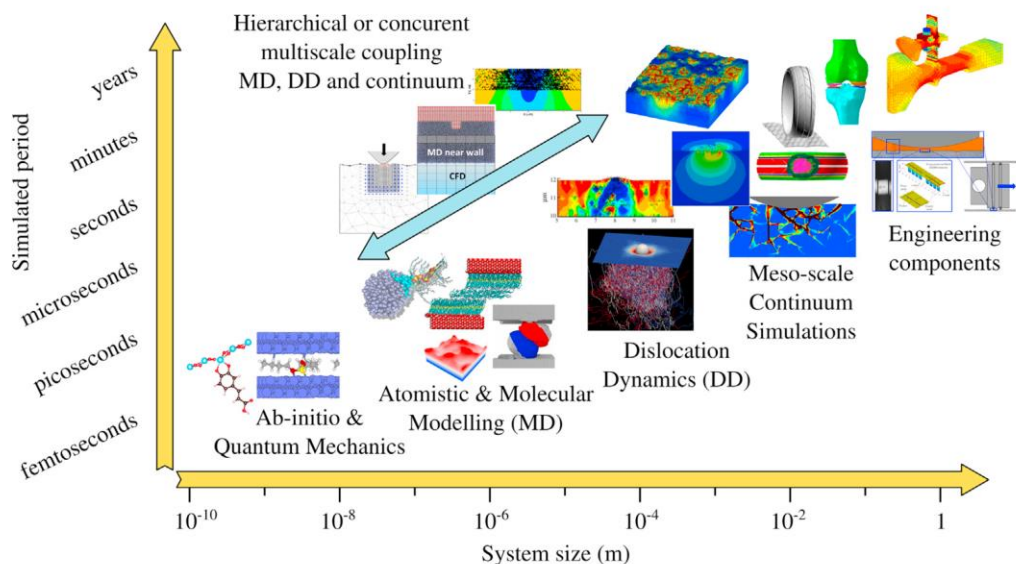
- **Nanotribology:** At this scale, intermolecular interactions between surfaces occur, such as van der Waals forces, which are responsible for the phenomenon of surface adhesion. It ranges between 0.1nm to 100nm.
- **Microtribology:** In this field, one studies small surface irregularities that can lead to discontinuities in contact between two surfaces. These irregularities

characterize the roughness of the material and may cause local variations in contact pressure as well as influence the static and dynamic tangential behavior of the pair. In addition, other phenomena of great importance to tribology occur at this scale, such as the formation of surface layers, debris, and surface plastic deformations. Micro-scale phenomena can be considered as those that occur within a range of 0.1  $\mu\text{m}$  to 100  $\mu\text{m}$ .

- Macrotribology: at this scale, superficial conformations determine the initial contact geometry, as well as the stress fields arising from the contact between the pair. These stress fields may extend for considerable distances depending on the transmitted force. It is generally considered within the scale of 0.1 mm to 100 mm.

In addition, according to Vakis *et al.* (2018), a wide range of phenomena occur across different length and time scales that can play an important role in tribology, as illustrated in Figure 28.

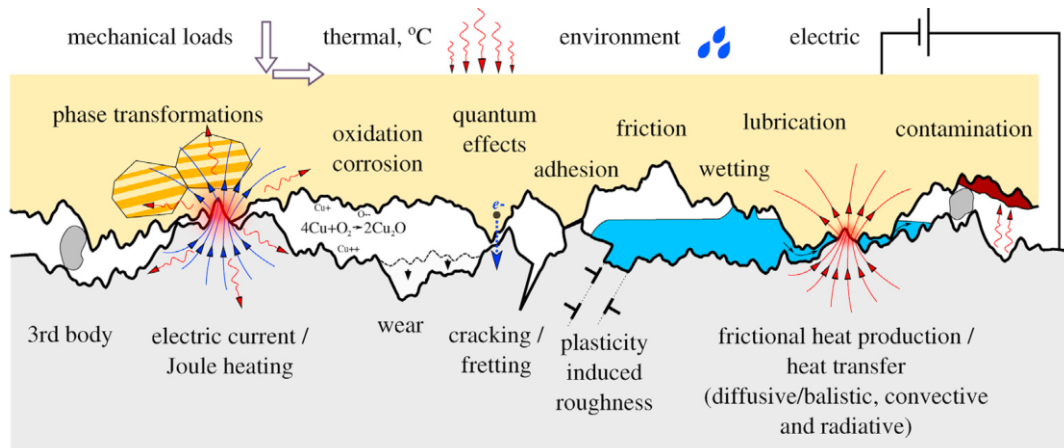
Figure 28 – A time-length scales map of models developed in tribology, highlighting the intrinsic link between multiscale physics that needs to be captured in order to provide predictive tools for engineering applications (Vakis *et al.*, 2018).



All tribological phenomena occurring near interfaces between solids are determined by the atomic interactions within and between solids, as well as those between atoms of the substances present at the interface. Since these

interactions give rise to various physics phenomena, which are described at the macroscale by different theories and models, the tribological interface can be considered a "paradise" of multiphysics, as shown in Figure 29. The diagram illustrates the multifaceted nature of tribological interactions. It depicts two distinct solids with rough surfaces and their corresponding material microstructures. These solids come into mechanical contact and are subjected to different types of loads, including mechanical, thermal, electric, and environmental forces (Vakis *et al.*, 2018).

Figure 29 – The multifaceted nature of tribological interactions (Vakis *et al.*, 2018).



Mechanical phenomena refer to the deformation of solids and their contact interactions. The process of material removal or surface deterioration, such as micro-cracking, abrasive wear, and adhesive wear, can also be included within this type. Thermal phenomena are related to heat transfer from one solid to another, as well as heat generation resulting from interfacial friction or dissipation within the bulk. Heat exchange can be either ballistic or diffusive, depending on the size of the contact spots. The local heating of contacting asperities up to the point of local melting, recognized in early tribological studies and known as flash-heating, has significant implications for friction, particularly in dry contacts. Metallurgical phenomena occurring in near-interface layers encompass a range of microstructural changes. These changes can be induced by temperature variations (such as Joule or frictional heating) or by severe deformations. They include dynamic recrystallization and various phase transformations in metals. An example is the formation of the so-called "white layer," which is a fine-grained and rather brittle martensitic

layer. For materials undergoing glass transition, the localized increase in temperature can have a significant impact on their mechanical performance. In general, mechanical properties are highly influenced by temperature, making the thermo-mechanical problem one of the most inherent and strongly coupled multiphysical problems in tribology, particularly in dry contact or in the mixed lubrication regime. Because of excessive local heating, the solids can reach their melting or sublimation point and experience phase transition. A complex interaction of the aforementioned physics with a fluid present at the interface creates a strongly coupled multiphysical problem, particularly in the context of Elasto Hydrodynamic Lubrication (EHL). Because of the complexity of direct experimental measurements and the inseparability of various physical mechanisms in real interfaces, a big challenge is to construct reliable and precise models that have predictive power while, at the same time, being verifiable and sufficiently comprehensive (Vakis *et al.*, 2018).

Although all of these concepts are important to keep in mind, due to the complexity of this subject, this work will aim to focus only on the most relevant fundamentals of physics for the current application.

### 2.3.1. Friction

According to Hutchings (2017) “The force known as friction may be defined as the resistance encountered by one body in moving over another” and “The ratio between this frictional force  $F_{at}$  and the normal load  $W$  is known as the coefficient of friction”, as defined by Equation (1).

$$\mu = \frac{F_{at}}{W} \quad (1)$$

This relation depends on a series of interfacial mechanical behaviors and surface interactions, and the study of the involved phenomena and their related patterns has been known to be studied since the 15th century.

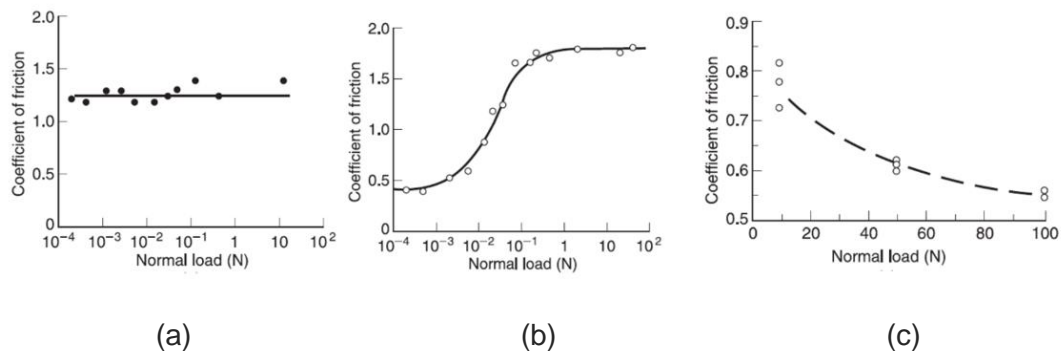
In 1493 Leonardo Da Vinci was considered to first understand the fundamentals of this phenomena. Two hundred years later Guillaume Amontons is credited to describe the three laws of friction. Although these laws

may not be considered valid nowadays, they preceded multiple discoveries in tribology field.

#### 2.3.1.1. 1<sup>st</sup> Friction Law: Frictional force is proportional to load.

Despite the first works affirmed this relation was true for most pure metal cases, as shown in Figure 30 – a, in contact between ceramics, polymers and in situations where surfaces are coated with surface oxide films (Figure 30 – b) this law is not true, since increased load may break the interfacial film and change the contact system. Another important example is that on rough metal surfaces of similar hardness, there is a tendency for the wear of these irregularities generate so-called debris, which can increase or reduce the friction coefficient as in the case of Figure 30 – c.

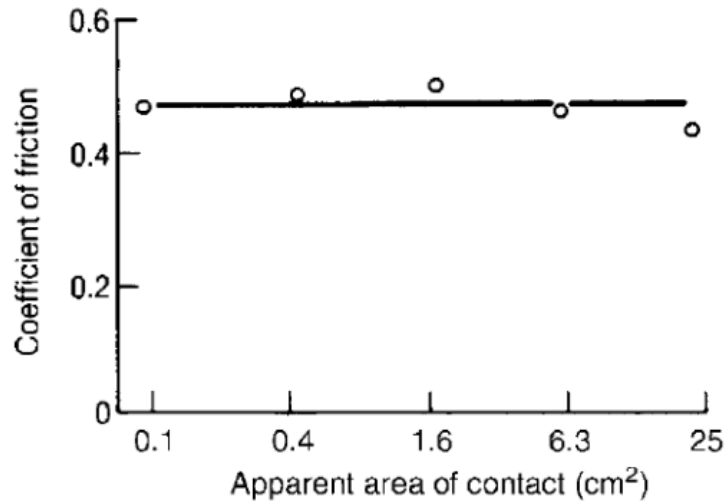
Figure 30 – Different behaviors of the coefficient of friction on normal load variation (a – Steel sliding over aluminum in air; b – Copper sliding over copper in air; c – Stainless steel sliding over NiAl alloy in air) (Hutchings, 2017).



#### 2.3.1.2. 2<sup>nd</sup> Friction Law: Frictional force is independent of apparent area.

Although less explored than the first law, the second law is nevertheless well attested for most materials, with the exception of polymers.

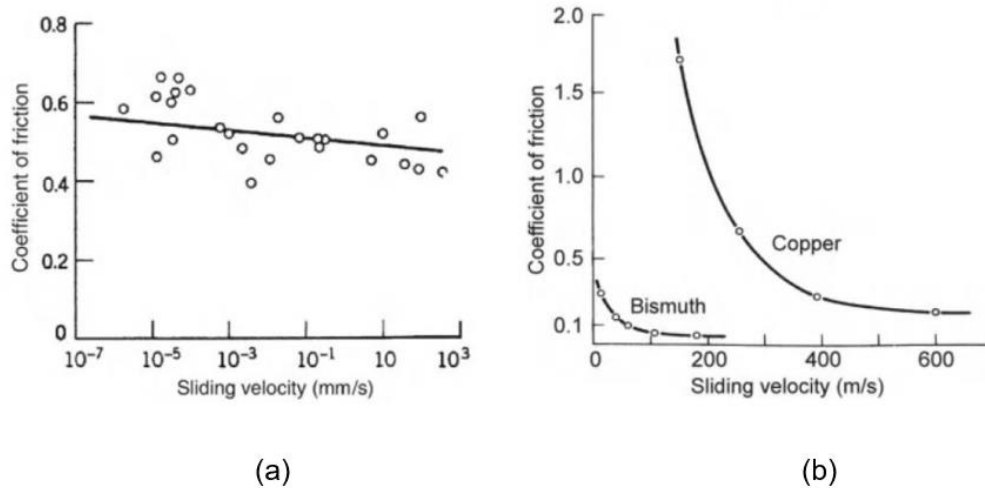
Figure 31 – Behavior of the friction coefficient on apparent area variation during slip between steel and wood (Hutchings, 2017).



2.3.1.3. 3<sup>rd</sup> Friction law: Frictional force is independent of sliding speed.

The third law of friction is less grounded than the first two, as slip velocity involves factors such as wear, interface temperature, and various other phenomena that can strongly influence a tribosystem. These factors range from the generation of debris to the phase change of materials in contact. However, for many contact pairs, the dynamic friction coefficient is independent within a certain range of speeds and may depend on this magnitude only for speeds above tens of m/s. In general, there is a drop in the dynamic coefficient of friction with increasing sliding velocity, as shown in the case of Figure 31. In (a), a linear drop of about 30% is noted, while in (b) it is more noticeable. A nonlinear variation of about twenty times was observed for copper, indicating the predominance of different friction mechanisms between the contact pairs.

Figure 32 – (a) Coefficient of friction behavior as a function of the sliding velocity for titanium sliding on titanium at 3 N normal load; b) Behavior of the coefficient of friction as a function of the slip speed for copper and bismuth on themselves at 3 N normal load (Hutchings, 2017).



When the temperature of a sliding metal increases, several effects occur: its mechanical properties change, the rate of oxidation and other chemical reactions at the surface increases, and phase transformations may take place. All of these factors will influence its frictional behavior (Hutchings, 2017).

### 2.3.2. Engineering surfaces

Engineering surfaces are often composed of different layers of materials, which can be formed naturally through the oxidation of the bulk material, electrochemical deposition such as galvanization, or even mechanical deposition such as coat paintings. These coatings are essential for the tribomechanics of contact pairs because their mechanical properties are the primary factors that govern friction behavior, and they can increase the strength of the interface when compared to the properties of the bulk material.

From Holmberg (2007), friction of engineering surfaces is the force that opposes motion and can be defined by three fundamental phenomena.

- Adhesion – Is the breaking of adhesive bonds between two surfaces.
- Ploughing – Is the resistance that arises from elastic and plastic deformation.

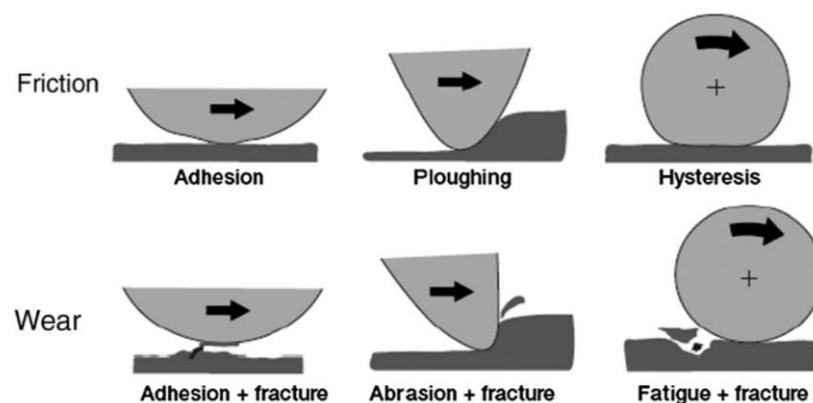
- Hysteresis – Resistance originating from continuous elastic deformation within one of the moving surfaces.

These phenomena cause stress on contact regions and are often associated with fracture mechanisms and material removal, resulting in what is known as wear. The same author classifies wear into three mechanisms associated with the aforementioned friction.

- Adhesion + Fracture – Adhesive lifting of shearing force causes stresses that exceed the material strength, resulting in crack growth and material detachment.
- Abrasion + Fracture – A hard countersurface moves across a softer surface, causing deformation. The high shear stresses cause crack growth and material detachment.
- Fatigue + Failure – Compressive cyclic loading on a surface causes shear stresses that exceed the material's endurance limit, resulting in crack growth and material detachment.

A representation of these phenomena can be seen in Figure 33.

Figure 33 – Basic friction and wear mechanisms (Holmberg, 2007).



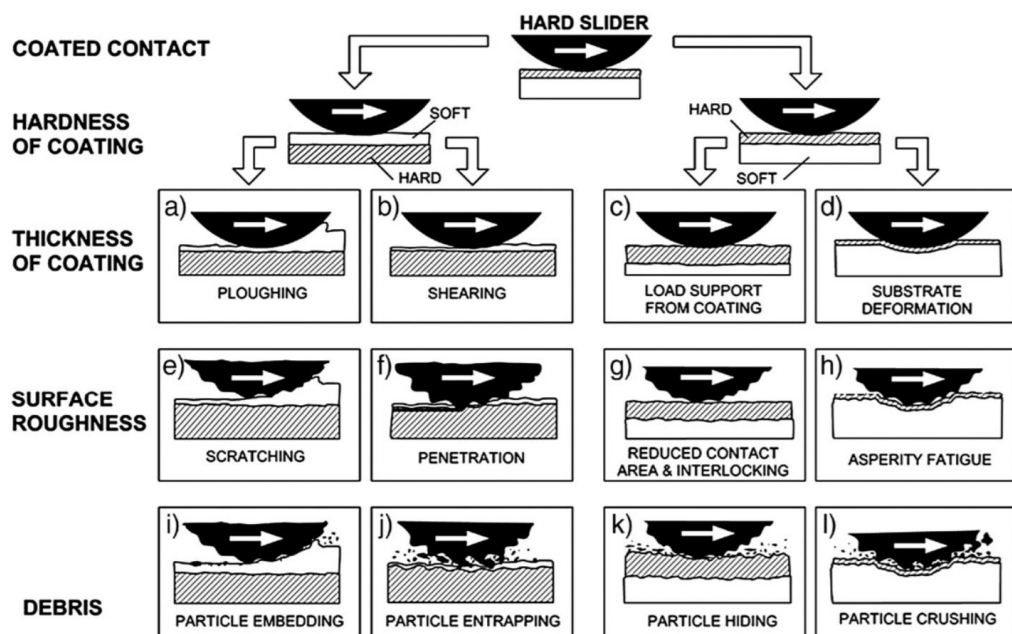
It is important to remember that the basic mechanisms of friction and wear are typically combined in a complex manner. This complexity arises from various factors, such as intricate contact geometries or conditions, which involve roughness and debris, as well as inhomogeneous surface materials. Additionally, mass and heat transfer, transient loads, and other multiphysics



phenomena contribute to the complexity. During sliding contact, several parameters undergo changes. Surface layers are formed, strain hardening occurs, local temperature increases, material properties changes, and after this transient stage a new set of parameters will govern friction and wear, consecutively.

In a contact situation, there are typically a limited number of around five to ten parameters that significantly influence the friction and wear behavior. Some of the dominant parameters include the relationship between coating and substrate hardness, coating thickness, roughness, and debris during contact. An illustrative example of these relations is shown in Figure 34.

Figure 34 – Main parameters influencing the friction in engineering contact situation (Holmberg, 2007).

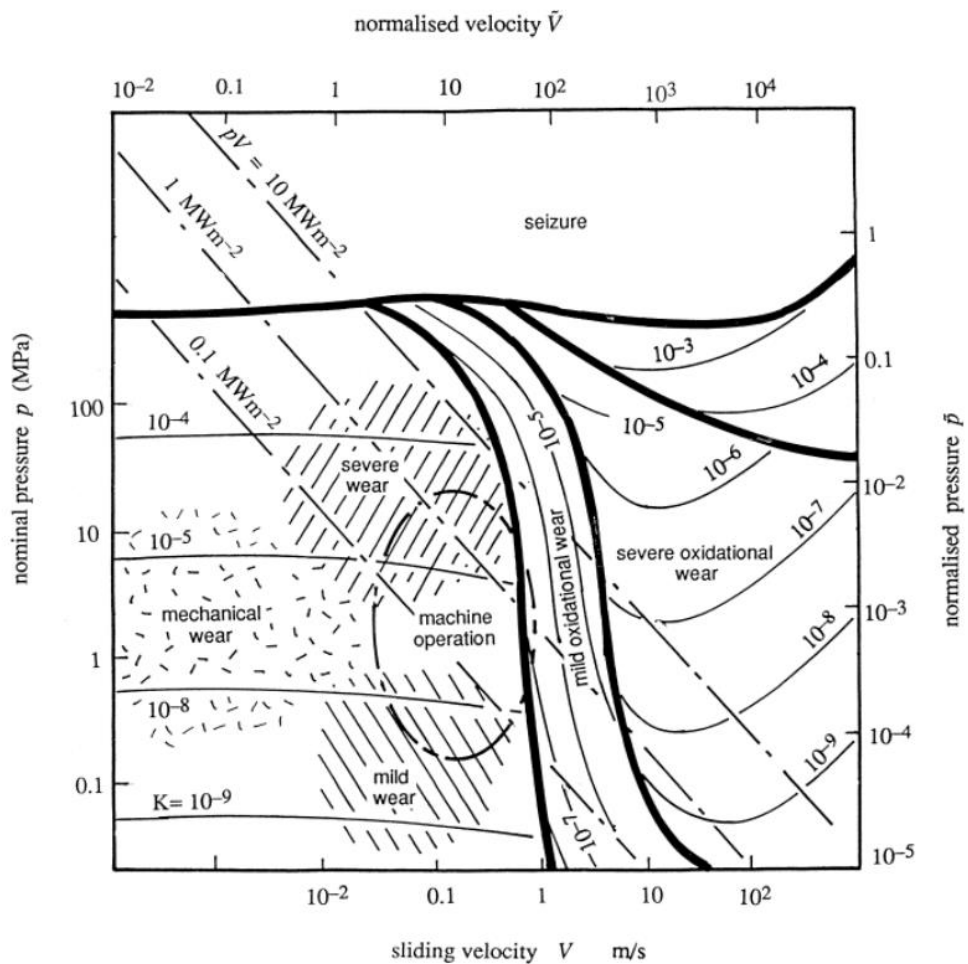


### 2.3.3. Wear maps

Lim and Ashby (1987) have performed substantial amounts of laboratory tests and introduced wear maps where the wear coefficient is plotted as a function of sliding velocity and pressure. The wear map corresponding to medium carbon steel, based largely on pin-on-disc data, is generally divided into two main regions of mechanical and chemical wear. Mechanical wear occurs at low sliding velocities where the wear coefficient is more a function of nominal

pressure than the velocity. The chemical mechanism occurs at higher sliding velocities (above 1 m/s). The mechanical part contains three regions of mild and severe wear together with a transition area in between. The chemical part of the map, however, contains two regions: mild and severe oxidative wear. As seen in the figure, mild oxidation could even be protective as at a given level of pressure and high sliding speed the wear coefficient drops to low values. This mild oxide material behaves like a lubricant in between the surfaces (Nia, 2017). Figure 35 shows a wear mechanism map for steel-on-steel sliding under various pressures and slip velocities.

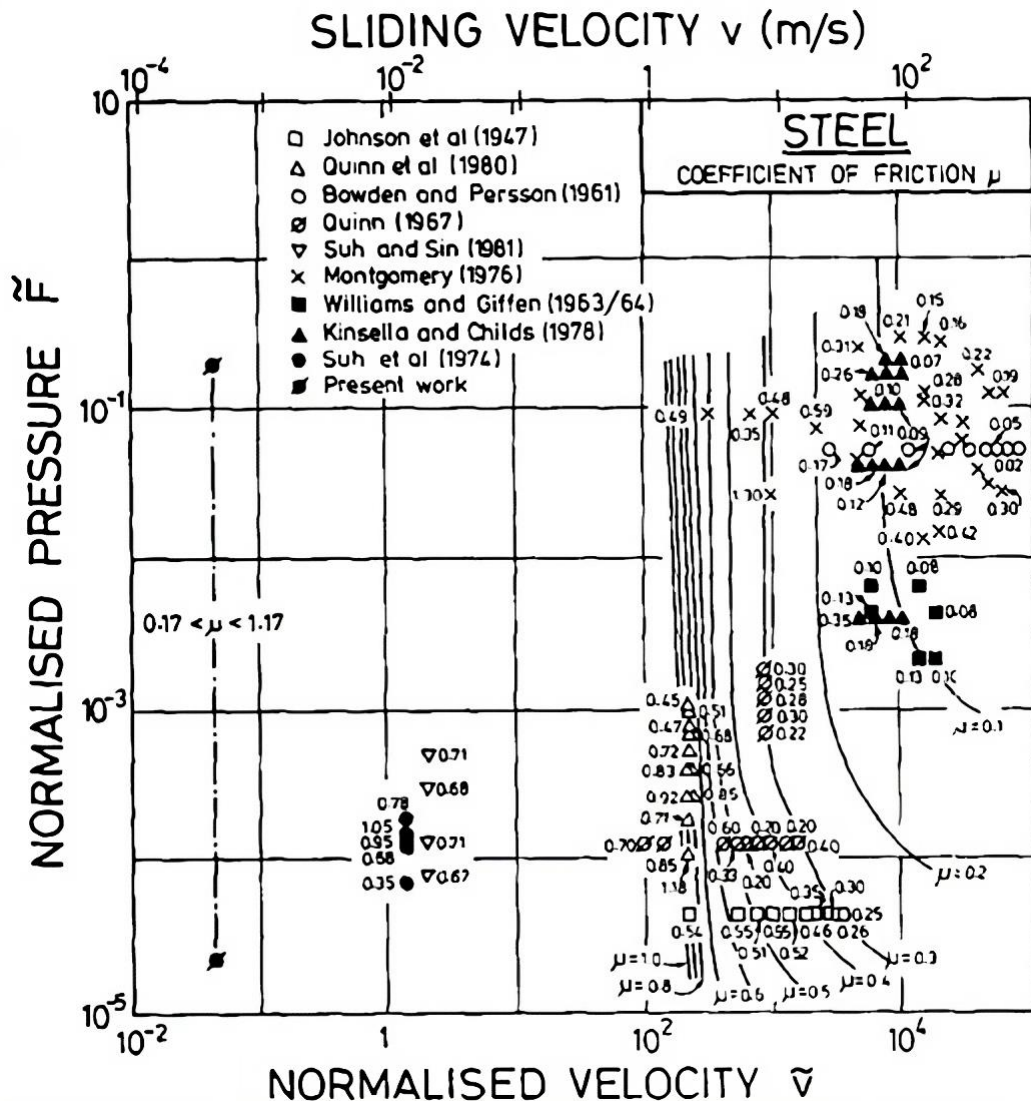
Figure 35 – Wear mechanism map for steel-on-steel sliding (Lim and Ashby, 1987).



These two mentioned areas of the map also affect the behavior of the friction coefficient. Although at low sliding speeds friction appears to be independent of slip velocity, significant variations in friction are observed when different wear mechanisms are present. Figure 36 presents an equivalent map for the

friction coefficient where similarity with Figure 35 can be observed. This reinforces the importance of correctly interpreting the relationship between friction mechanisms, wear rate, and friction coefficient.

Figure 36 – Frictional map for sliding of steel on steel under various normalized pressures and slip velocities (Lim and Ashby, 1987).



Although this example illustrates steel-to-steel sliding, the friction and wear coefficients dependence on pressure and slip velocity may also be found in other contact pairs as well.

#### 2.4. FRICTION TESTING

Many different experimental methods have been used to study sliding friction and wear. Laboratory investigations are typically conducted to either examine

the mechanisms by which wear occurs or to simulate practical applications and provide valuable design data on wear rates and coefficients of friction. For both purposes, selection, control, and measurement of all variables that may influence friction and wear are very important, since they are often highly dependent on the sliding conditions, and even apparently minor changes in these conditions can lead to radical changes in the primary mechanism and the rate of wear. Careful choice of test conditions and their close control and monitoring are essential, regardless of whether the results are being used for the simulation of a practical application or for scientific purposes or not. In a sliding tribological test, the main aspects that should be considered are mentioned below.

- The materials of the two bodies in contact and their method of surface preparation.
- The test geometry, including both the shape and dimensions of the samples.
- The applied load and contact pressure.
- The sliding velocity.
- The test environment (the nature of the environment surrounding the contact, including its temperature and humidity).

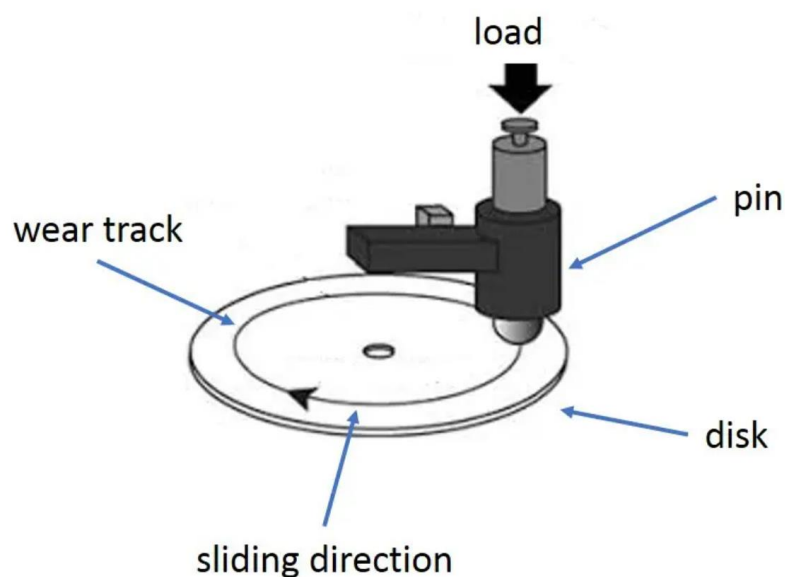
In designing a test, each of these factors needs to be considered and justified. It is important to remember that the behavior of a tribological contact is related to the behavior of the whole system and not just of a material pair, and that one can never define the tribological behavior of a material without a full description of the system. Due to this, understanding the underlying physical mechanisms of damage and wear is essential, as it may allow the conclusions to be extrapolated beyond the strict range of the test condition (Hutchings, 2017).

### 2.4.1. Pin on Disk (ASTM G-99)

This method is one of the most well-known tribomechanical tests and describes a laboratory procedure for determining the wear of materials during sliding using a pin-on-disk apparatus. Materials are tested in pairs under nominally non-abrasive conditions. The principal areas of experimental focus in using this type of apparatus to measure wear are described. The coefficient of friction may also be determined.

For the pin-on-disk wear test, two specimens are required. A pin with a rounded tip is positioned perpendicular to a flat circular disk. A rigidly held ball is often used as the pin specimen. The testing machine causes either the disk specimen or the pin specimen to rotate around the center of the disk. In either case, the sliding path forms a circle on the surface of the disk. The pin specimen is pressed against the disk at a specified load, typically using an arm or lever with attached weights. Other loading methods have been used, such as hydraulic or pneumatic. Figure 37 shows a schematic drawing of a typical pin-on-disk wear test system, as well as photographs of two apparatuses with different designs.

Figure 37 – Pin on disk apparatus (Tribonet, 2023)



Rotating speeds are typically in the range of 0.3 to 3 rad/s (60 to 600 RPM). Although there is no radius limit according to the standard, pin-on-disk machines usually allow discs with a diameter no larger than 200 mm. Also, normal forces are typically less than 200 N, with pin or ball diameters not exceeding 5 mm. This often results in slip velocities of less than 0.3 m/s and contact pressures of less than 100 MPa under steady-state conditions, which is not suitable for impact scenarios.

#### **2.4.2. Reciprocating test apparatus (ASTM G133)**

This test method covers laboratory procedures for determining the sliding wear of ceramics, metals, and other candidate wear-resistant materials using a linear, reciprocating ball-on-flat plane geometry, as shown in Figure 38. The direction of the relative motion between sliding surfaces reverses periodically, causing the sliding to occur back and forth in a straight line. The primary quantities of interest are the volumes of wear in the ball and flat specimen materials that come into contact. Indeed, the coefficient of kinetic friction can also be measured. This test method encompasses both unlubricated and lubricated testing procedures. It is designed to simulate the geometry and motions experienced in many types of rubbing components. These components undergo periodic reversals in the direction of relative sliding during normal operation.

Friction forces are measured during the test and can be used to evaluate variations in the contact conditions or the kinetic friction coefficient over time.

Figure 38 – Reciprocating test apparatus (ASTM G133).

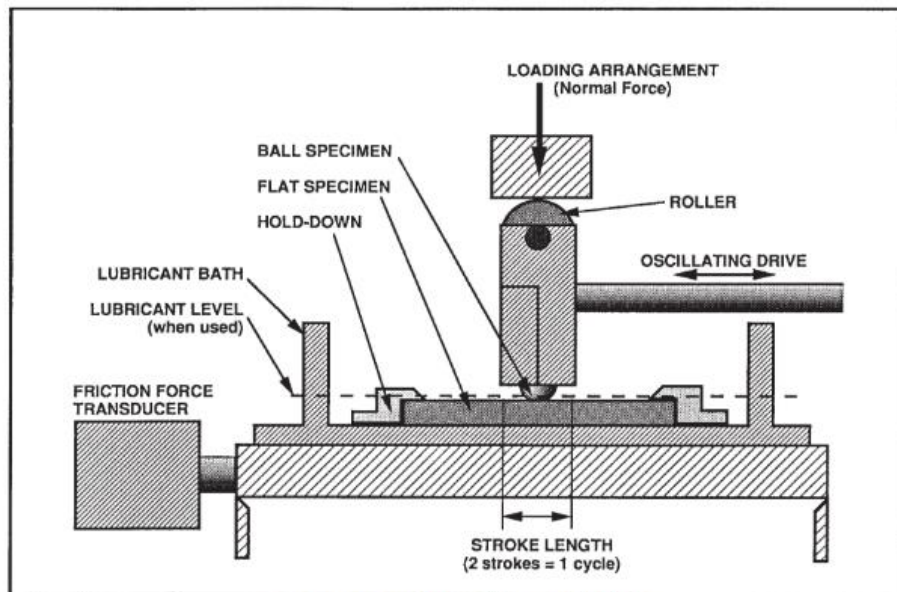


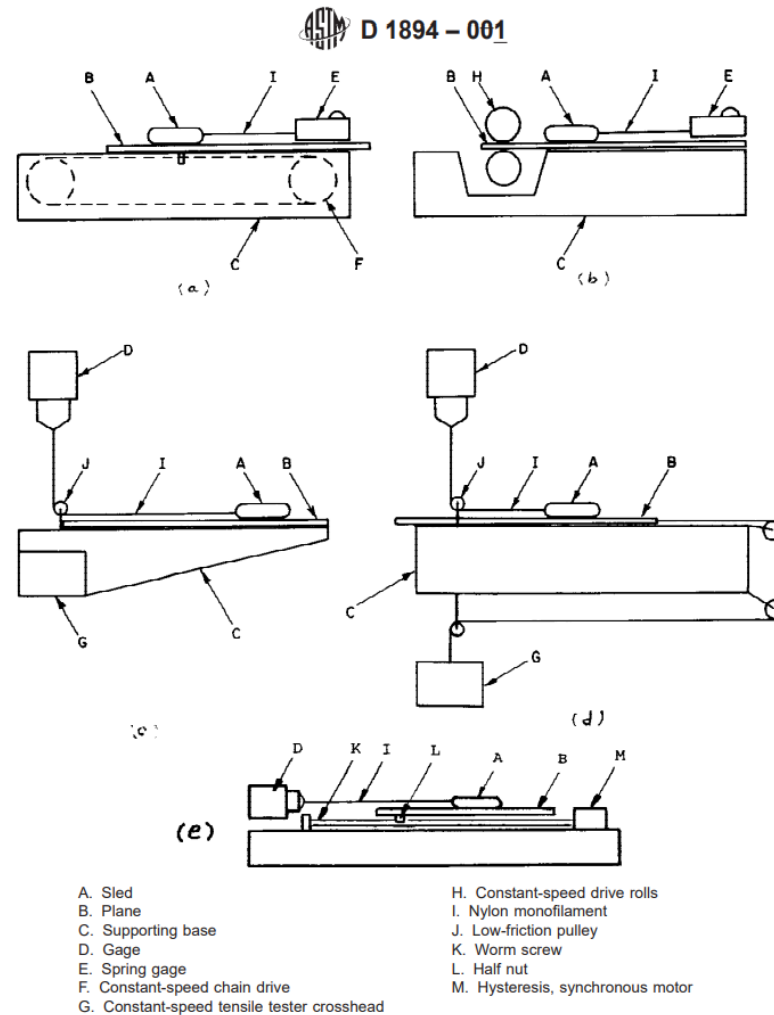
FIG. 1 Reciprocating Test—Schematic Diagram

According to this standard, the oscillation frequency should not exceed 10 Hz, with a stroke length of 10 mm. The recommended pin tip radius is 4.76 mm, and the maximum normal force is 200 N. This test setup ensures that the maximum contact pressures for metallic Hertzian contact are on the order of 100 MPa, and that slip velocities do not exceed 0.1 m/s. So, similar to ASTM G-99, this test is not suitable for capturing the transition from static to dynamic events that occur during impact events.

#### **2.4.3. Standard Test Method for Static and Kinetic Coefficients of Friction of Plastic Film and Sheeting (ASTM D1894 – 001)**

This test method covers the determination of the coefficients of starting and sliding friction of plastic film and sheeting when sliding over itself or other substances under specified test conditions. The procedure allows the use of either a stationary sled with a moving plane or a moving sled with a stationary plane. Both procedures yield the same coefficients of friction values for a given sample. The standard states that tests shall occur at constant slip velocities ranging from 120 mm/min to 180 mm/min and pressures ranging from 70 kPa to 100 kPa. Figure 39 illustrates the test procedures and assembly process.

Figure 39 – Friction measurement by ASTM D1894 – 001.



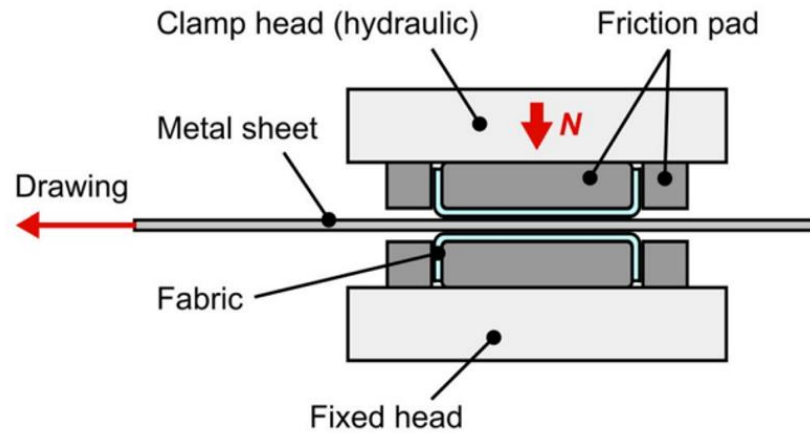
Although this test setup design is closer to the objective of this work, it does not reference high speed and pressure tests, nor does it address friction modeling as a function of pressure and slip velocity. The methodology shown in this standard will be considered as a motivation for the development of a new device for friction measurement.

#### 2.4.4. Strip Drawing test method

The principle of the strip drawing test is similar to ASTM D1894 test rig, where normal force is applied by a clamp head instead of weights. Due to this, two contacting surfaces are necessary to ensure the force equilibrium in the normal direction. Figure 40 illustrates the concept in the work developed by (Makhkamov, 2021).



Figure 40 – Strip drawing test concept with two side fabric samples. (Kruse *et al.*, 2022)



The greatest advantage of this concept is the compact and simple design of normal actuators, which allows normal pressures ranging from Pa up to MPa magnitude orders. Thus, it also allows low normal force application, for low pressure measurements. Further, the drawing force can be applied in multiple forms, such as electric motors, pneumatic or hydraulic actuators as well as impact hammers, allowing the slip velocities from  $\mu\text{m/s}$  up to  $\text{m/s}$  magnitude orders. This concept makes this design well suited for the role in this work.

One of the disadvantages of the strip drawing test is that both contacting sides are assumed to have the same friction coefficient, thus the clamping heads must possess the same materials. Depending on the sample count and material properties, the test operation might also be work intensive, since the assembling and disassembling of samples is doubled.

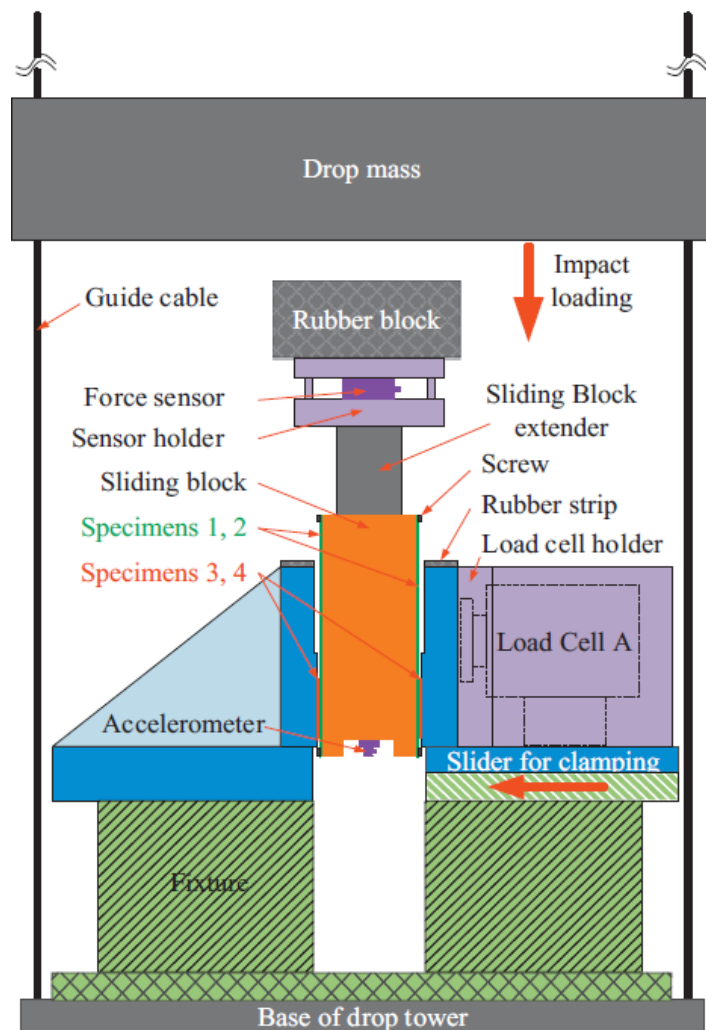
#### 2.4.5. Friction rigs for impact applications

Lai *et al.* (2012) stated that contact friction can impact the mode of structural deformation and the capacity for absorbing kinetic energy during a vehicle crash. Due to the lack of information on friction modeling for crashworthiness applications and the unavailability of suitable test devices, the authors developed a friction rig. This rig enabled the measurement of friction on metallic samples under dry friction and impact conditions, with pressures of up to 100 MPa and slip velocities of 6 m/s. These high pressures and slip velocities can occur both in contact between different components and in self-

contact during a vehicle crash, especially during the progressive buckling of front rails.

The primary objective of the rig proposed in this study is to replicate the conditions found in a vehicle crash event. This includes simulating not only high pressure and slip velocities but also considering the specific characteristics of such crashes, namely short time durations (approximately 10 ms) and limited sliding distances (less than 35 mm) in a single pass slide. These parameters are strategically chosen to prevent significant surface modifications resulting from wear, heating, and their subsequent effects. By accurately replicating these crash conditions, the proposed rig enables researchers to investigate and analyze the behavior of materials and interfaces in realistic crash scenarios. The proposed test rig can be found in Figure 41.

Figure 41 –Impact friction rig scheme (Lai *et al.*, 2012).



It has been found that, in the ranges of contact pressure and sliding velocity tested in this study, the friction coefficient of dry contact of steel-vs-steel can exhibit significant dependence on the applied contact pressure and sliding velocity, as shown in Figure 42 and Figure 43.

Figure 42- Slip velocity dependence of friction coefficient (Lai *et al.*, 2012).

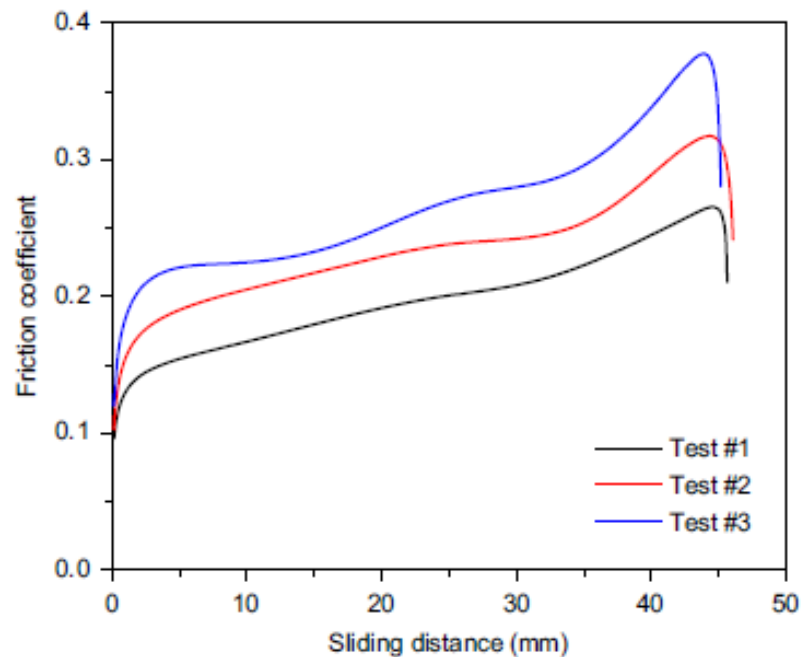
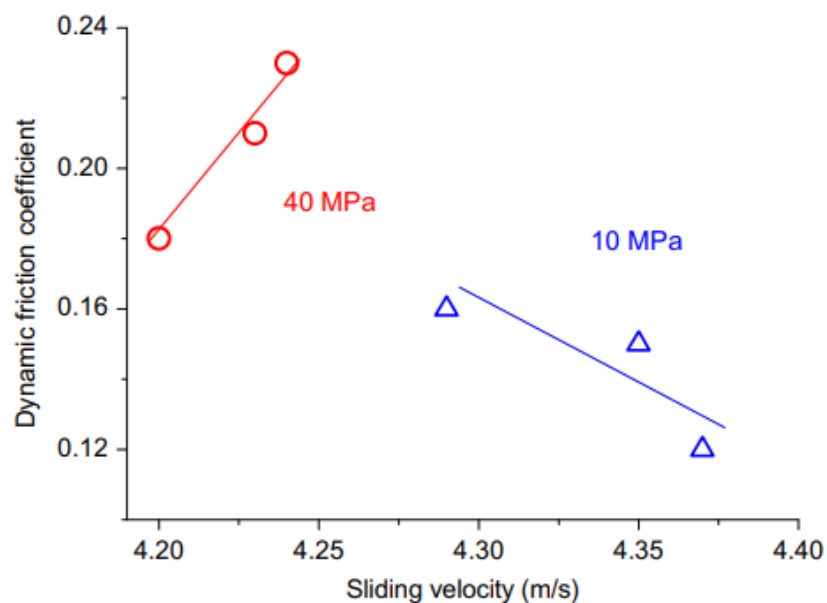


Figure 43 – Pressure dependence of friction coefficient (Lai *et al.*, 2012).



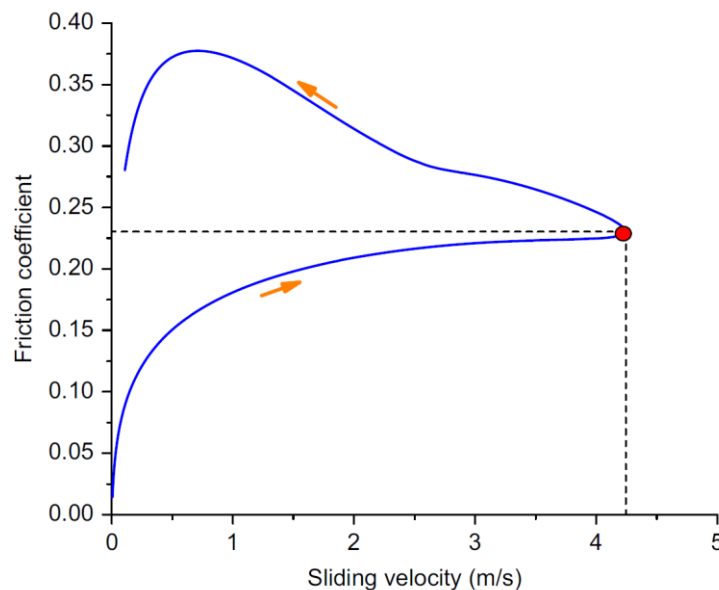
Following the tests, the authors conducted a detailed surface analysis, which revealed important findings. At a low contact pressure of 10 MPa, the dominant

tribological mechanisms observed were plowing and abrasion. These mechanisms were responsible for causing scratching and polishing effects on the surfaces of the specimens that were tested.

However, under higher contact pressure conditions of 40 MPa, a different set of tribological mechanisms became prominent. Adhesion between the surfaces resulted in severe plastic deformation, which caused the formation of cold welds and the transfer of material between the contacting surfaces. The adhesion mechanism played a significant role in this pressure range and contributed to the surface modifications that were observed.

Furthermore, the authors observed a significant phenomenon related to the dependence of slip velocity, even in cases with short durations and limited sliding distances. This effect was illustrated in Figure 44, where the friction coefficient exhibited path-dependent behavior in relation to the slip velocity. The friction coefficient increased almost monotonically throughout the test, emphasizing the cumulative effect of surface and tribosystem modifications that took place during the test period.

Figure 44 – Slip velocity path dependence due to surface and tribosystem modifications during testing (Lai *et al.*, 2012).

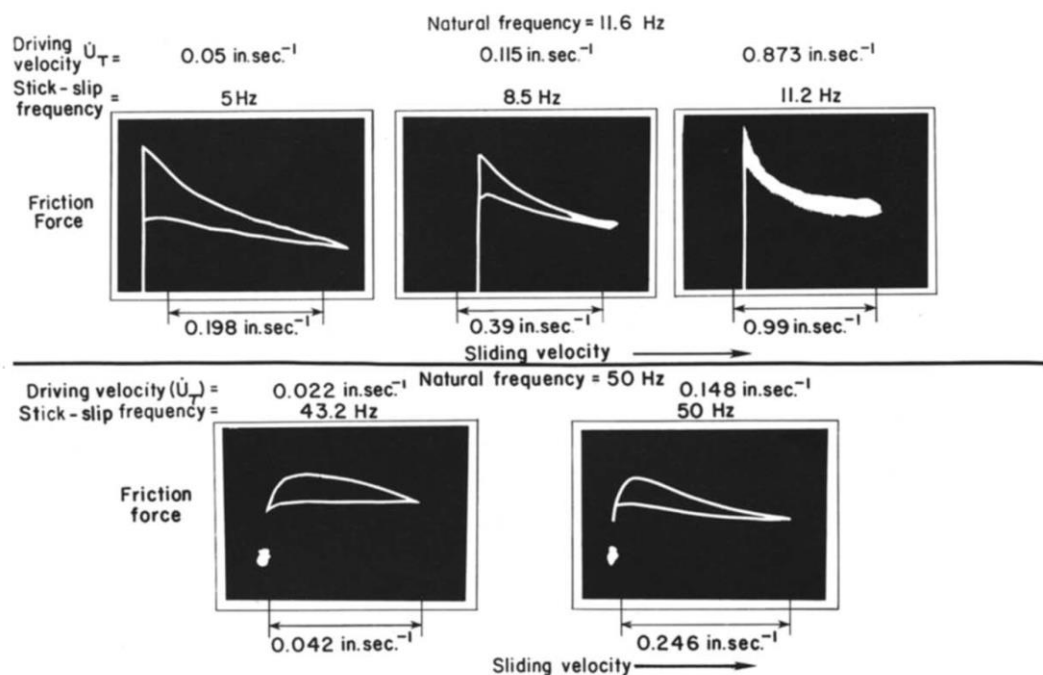


One further comment on this work is that dynamic friction was considered as the value at maximum velocity, as shown in Figure 44. The present author

believes that these phenomena should be considered in friction modeling for crashworthiness applications, as they are expected to play their roles during a vehicle collision.

Interestingly, this path-dependence behavior was noticed by Oden and Martins (1984), who also noticed friction coefficient dependence of system natural frequency when two metals are subjected to unlubricated sliding. This implies that the experimental friction-sliding velocity curve is not defined uniquely by the nature of the surfaces in contact, but it is a consequence of all the dynamic variables involved. Figure 45 shows the different behaviors of friction force vs. sliding velocity depending on the system's natural frequency.

Figure 45 – Friction force vs. sliding velocity characteristics for various driving velocities and natural frequencies of the system Oden and Martins (1984).

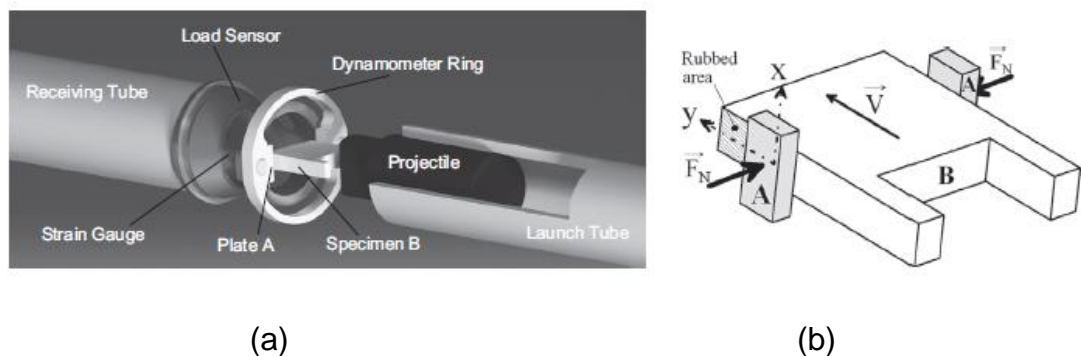


The same authors also mention the influence of the time of stationary contact on the value of the static coefficient of friction, since creep deformation and variation of real contact area in material as polymers could become a relevant variable.

Sutter and Ranc (2010) developed a rig based on a ballistic device to measure the friction coefficient at high sliding velocities, in local instantaneous temperatures (flash temperatures) in the contact pair exceeding 1100°C.

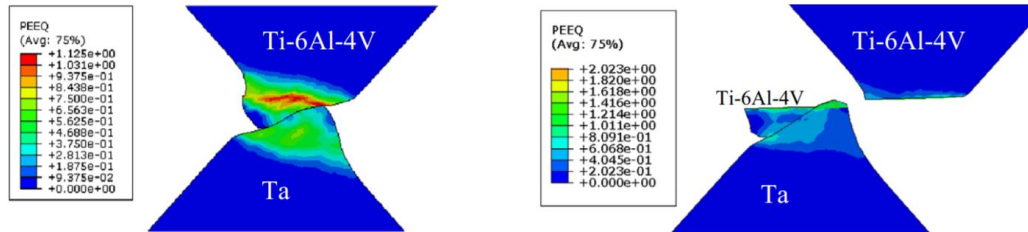
These high temperatures are mainly caused by energy dissipation during plastic deformation in the near-surface layers, within  $5\mu\text{m}$  of the contact surfaces, which is then transformed into heat. They were found to strongly influence the mechanical behavior of the materials involved in dry friction. They are responsible for oxide formation, spot weld regions, thermoelastic instabilities, thermomechanical failure, and wear.

Figure 46 – Devices used by (a) Sutter and Ranc (2010) and (b) List, Sutter and Arnoux (2013) to measure the friction coefficient at very high speeds.



List, Sutter and Arnoux (2013) also worked with a test apparatus similar to that used by previous authors. In their work, they also point out the relevance of material transfer between contact surfaces for the overall behavior of tribosystems and the friction force caused by the shear or breakage of asperities. They considered that during asperities interlocking, there is competition between strain hardening, strain rate hardening, and thermal softening processes. This is due to the very high flash temperatures, which result in oxidation processes and changes in oxide mechanical properties. A microscale asperity finite element model has been developed in Abaqus to demonstrate an asperity collision model under the conditions previously presented by Sutter and Ranc (2010), and is illustrated in Figure 47.

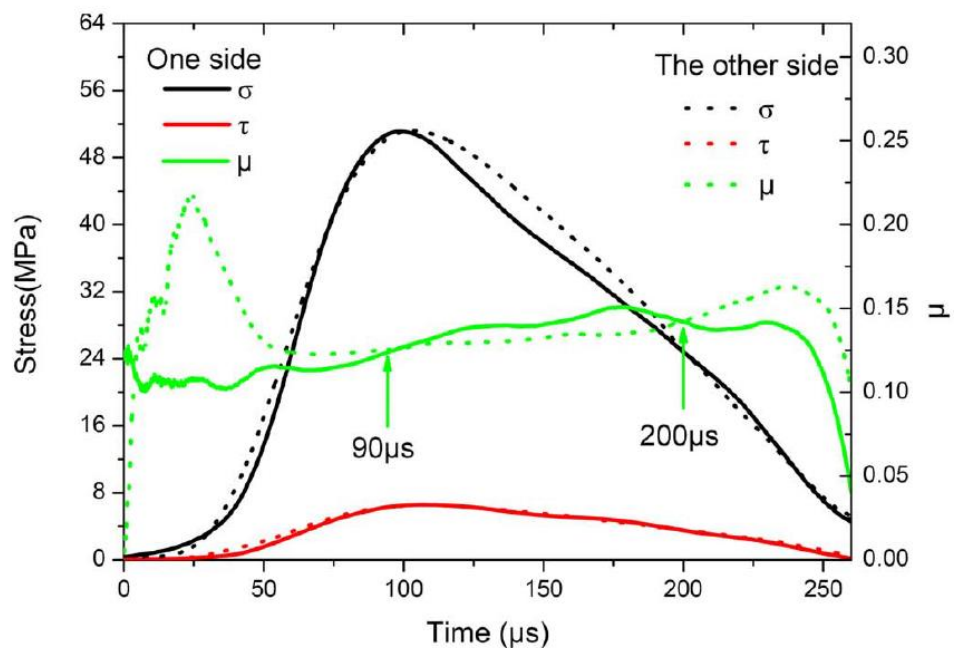
Figure 47 – Asperities collision model for ballistic friction testing (List, Sutter and Arnoux, 2013).



Lin *et al.* (2014) developed a novel setup based on the Split Hopkinson bar technique (Alves *et al.*, 2012) to test the dynamic friction coefficient under impact loading. In the setup, a wedge-shaped geometry was used to apply a combined compressive normal and shear frictional loading.

Interestingly, the authors considered two shear sensors for measuring and correlating the results, one on each contact side. They found that although the results are similar, some intrinsic differences due to the dynamic nature of the event can be found, as shown in Figure 48.

Figure 48 – Interfacial compressive stress, shear stress, and friction coefficient histories (Lin *et al.*, 2014).



In a counterintuitive manner, although the average values can be considered similar between the contact sides, one side exhibits a constant friction

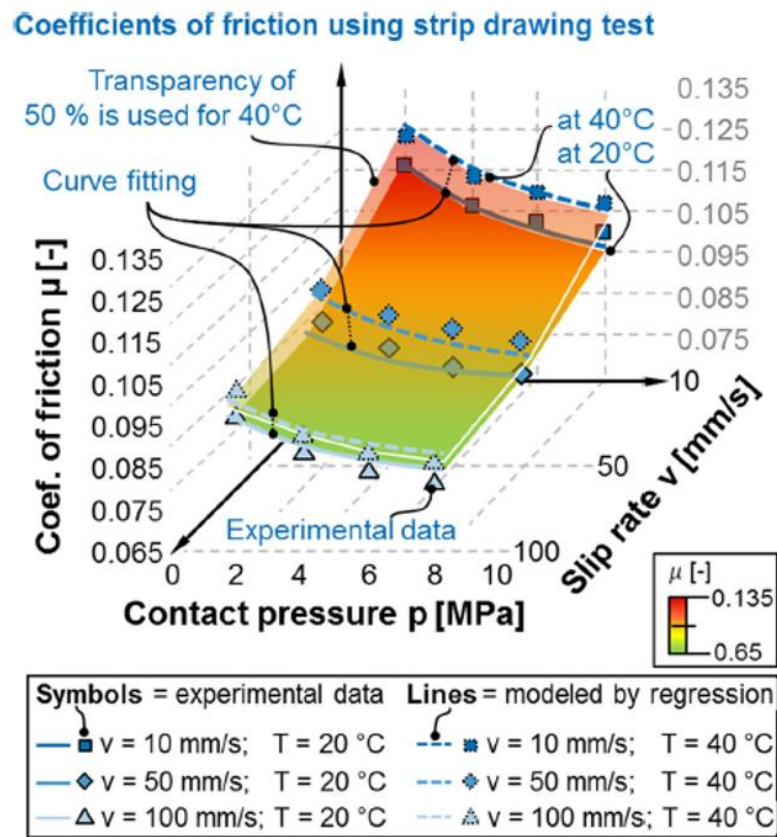
coefficient while the other side appears to have a transient behavior in the first 50  $\mu$ s. In conclusion, the authors remark that the behavior of the friction coefficient between pairs changes throughout the test and is often very unstable. This is due to the complex nature of both the tribosystem behavior and the highly dynamic process.

Shi *et al.* (2017) also developed a friction rig for forming applications in aluminum. This rig enabled tests with a variation of slip velocity ranging from 25 to 150 mm/s, contact pressures ranging from 3.3 MPa to 12.8 MPa, and temperatures up to 300°C. Although temperature was found to be very significant to friction, no relevant effect on the friction coefficient was found due to slip velocity and pressure variation.

Klocke *et al.* (2015) developed a methodology for modeling friction in forming applications, which considers the dependence of slip velocity, pressure, and temperature. This methodology is based on strip drawing tests. To develop a phenomenological friction model, the authors conducted a strip drawing test at pressures of 2 MPa, 4 MPa, and 6 MPa, and slip velocities of 10 mm/s, 50 mm/s, and 100 mm/s. They utilized a non-linear least square regression model in Matlab to analyze the experimental data. A brief overview of the fitted results can be seen in Figure 49.

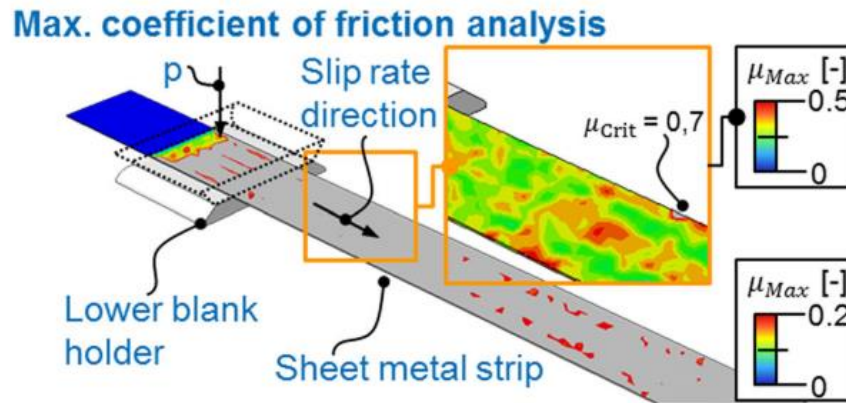


Figure 49 – Friction model fitted from slip velocity, pressure and temperature data (Klocke *et al.* 2015).



Furthermore, the authors have also developed a subroutine in Abaqus that enables the visualization of local coefficients of friction on a finite simulation model for each contact node. This allows for the identification of critical frictional regions in situ of the die tool in real-time, facilitating design optimization that considers tribological aspects during forming. This visualization can be seen in Figure 50.

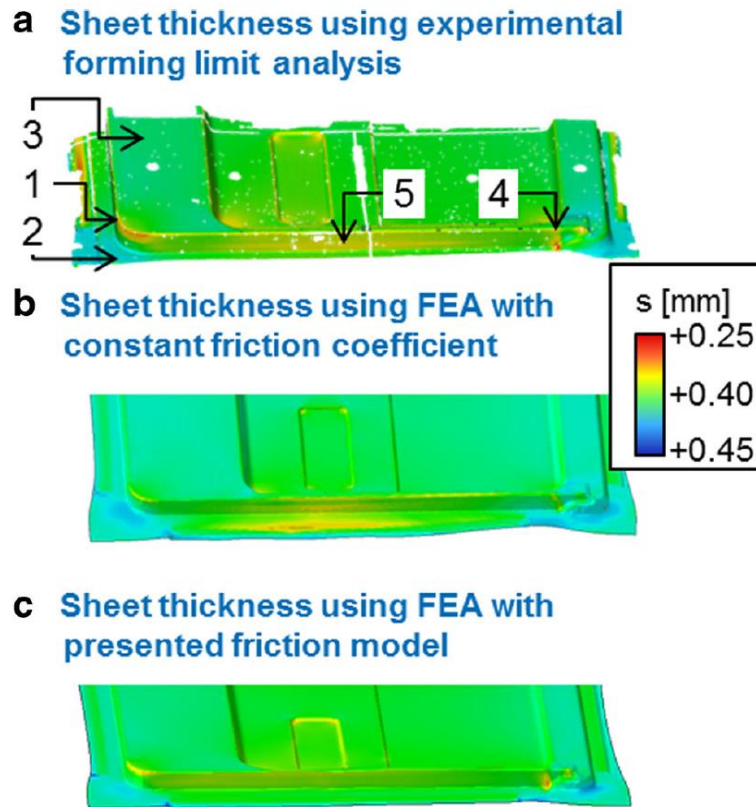
Figure 50 – Local coefficients of friction on finite simulation model (Klocke *et al.* 2015).



Besides, the authors have also compared the final thickness of the stamped part after the process at 5 different positions, considering Coulomb constant coefficient of friction and using the proposed model. The contours can be seen in

Figure 51.

Figure 51 – Contour plots of friction coefficient during a deep drawing process of a dishwasher indoor panel (Klocke *et al.*, 2015).



In the previous figure, five positions were considered to validate the friction model in correlation with experimental results. These regions' thicknesses were measured and compared with finite element models, considering  $\mu=0.1$ ,  $\mu=0.05$  and  $\mu = f(p, v, T)$ . Results are shown in Table 1.

Table 1 – Comparison of sheet thickness determined by experimental forming and FEA analysis using different friction modeling approaches (Klocke *et al.*, 2015).

STH $s$ [mm]	Exp.	FEA $\mu = 0.1$	FEA $\mu = 0.05$	FEA $\mu = f(p, v, T)$
Pos. 1	0.26	0.31	0.30	0.29
Pos. 2	0.40	0.43	0.41	0.40
Pos. 3	0.38	0.40	0.40	0.39
Pos. 4	0.26	0.33	0.31	0.29
Pos. 5	0.32	0.40	0.38	0.34

According to

Figure 51 and Table 1, it can be concluded that the simulation using the proposed friction model is more realistic and provides more accurate results, particularly in the regions near the draw beads (Position 5), given that the deviations with the variable friction model are smaller than the deviations with a constant friction coefficient.

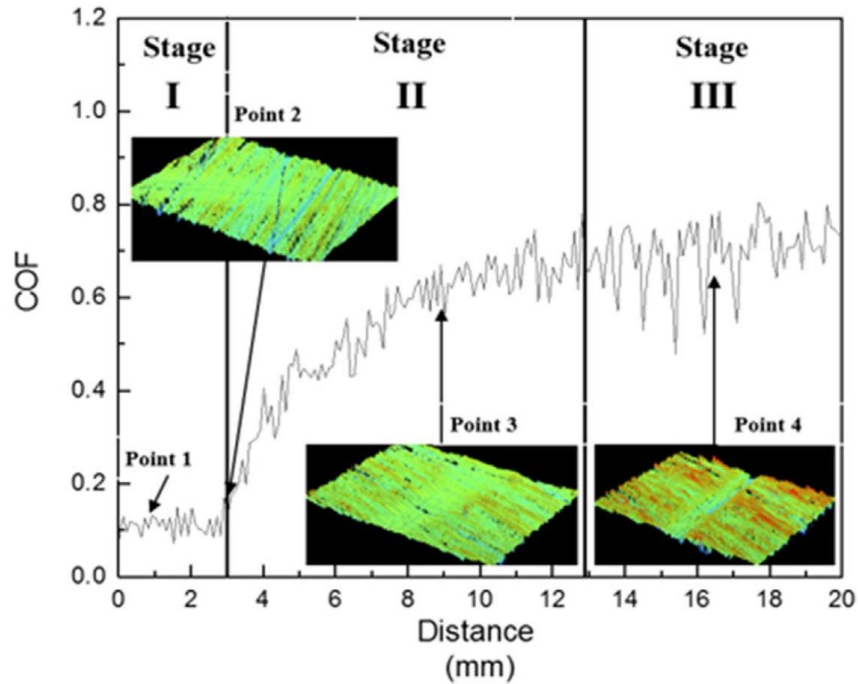
Hu *et al.* (2016) studied the frictional behavior of an interactive friction-lubricant system under different lubricant quantities, pressures, and slip velocities. The system involved a Tungsten Carbide ball sliding against a disc made from AA6082 Aluminum alloy. Their work focused on metal forming applications. The authors state that current finite element models often utilize constant friction coefficients, which can result in inaccuracies in the results. The proposed model herein depends on contact pressure, slip velocity, time, initial lubricant amount, lubricant, and surface topography parameters.

Through a pin-on-disk test procedure, partially based on ASTM G99, the authors found that a three-stage friction behavior can occur in lubricated systems.

- Stage I: The coefficient of friction is low and stable (approximately 0.1), with no scars on the surfaces. This suggests that the two surfaces were fully separated by the lubricant film.
- Stage II: The thickness of the lubricant decreases to the height of the peaks on the counter surface. The normal force is supported by the residual lubricant trapped between the contact surfaces and the surface asperities.
- Stage III: The friction coefficient reaches a plateau with a higher average value (0.65) and exhibits instabilities, which are consistent with the characteristics of dry friction in a contact pair. In this stage, the lubricant is almost completely removed from the contact interface, and therefore ploughing friction plays an important role in the overall friction force.

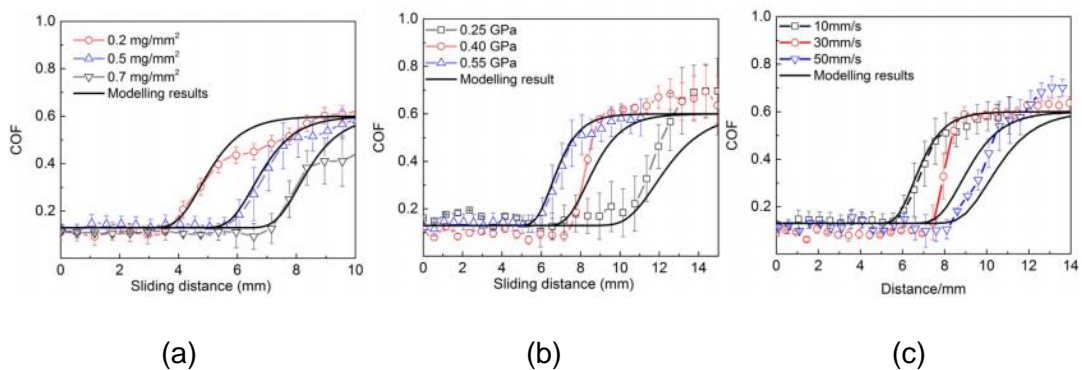
The stages of evolution of the friction coefficient are shown in Figure 52, using measurement data and wear track images. through the measurement data and wear track images.

Figure 52 – Evolution of the friction coefficient at a sliding speed of 10 mm/s, a pressure of 550 MPa, and a lubricant density of 0.2 mg/mm<sup>2</sup> between a disk made of AA6082 Aluminum alloy and a Tungsten carbide ball (Hu *et al.*, 2017).



A comparison of the modeling and experimental results of the coefficient of friction under various lubricant quantities, contact pressures, and sliding speeds, as well as the behavior of the lubricant for breakdown distance, where lubricant thickness has same height as the highest asperity of the surface, is shown in Figure 53.

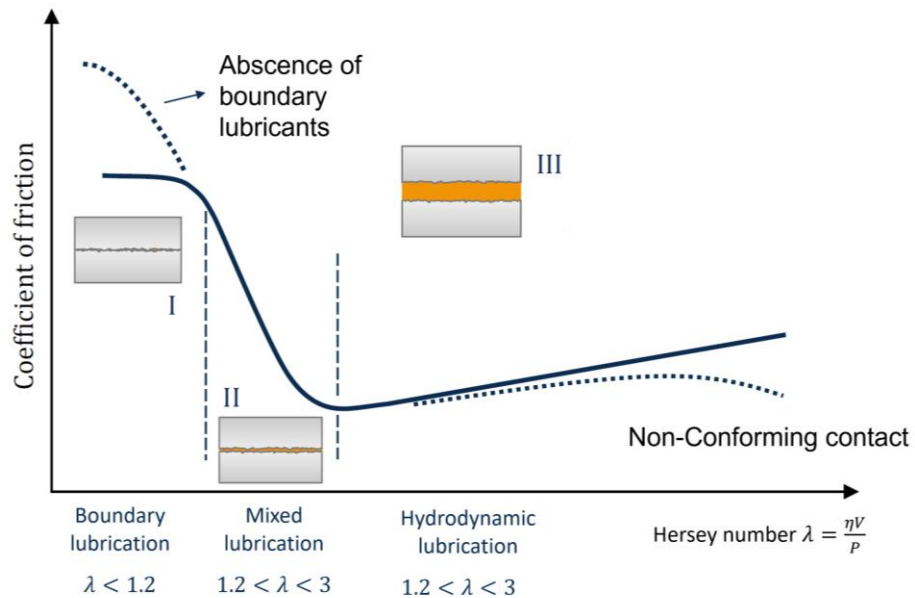
Figure 53 – A comparison of modeling and experiment friction models in Hu *et al.* (2017) as function of lubricant density (a), contact pressure (b) and sliding speed (c).



This breakdown phenomenon agrees with the trend predicted from the generalized Stribeck curve and the Hersey number,  $\frac{\eta v}{P}$  (where  $\eta$  is the viscosity

of lubricant,  $v$  is the sliding velocity and  $P$  is the load), that is, the increasing load will result in thinner lubricant film and thus premature breakdown. Figure 54 shows the Stribeck curve with the three mentioned lubrication regimes.

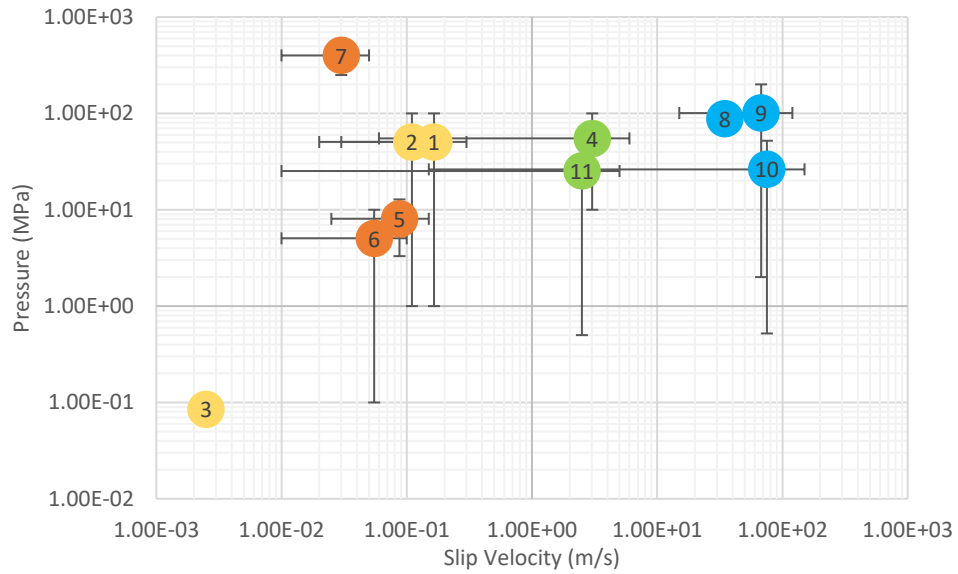
Figure 54 – Stribeck curve (adopted from Hamrock, Schmid, and Jacobson, 2004)



Despite the focus of the current work is the modeling of friction coefficient in dry contact situations, the Hersey number dependence of friction coefficient for lubricated contacts might be considered when developing a general friction coefficient modeling equation.

A brief overview of the reviewed literature is provided, focusing on contact pressure, slip velocity and the application of each type of friction test is shown in Figure 55.

Figure 55 – Map of pressure and slip velocity capabilities of literature available friction rigs.



● Crashworthiness    ● Ballistics    ● Metal forming    ● General friction and wear

Table 2 provides a summary of the available rigs and their capabilities, including information about the rig concept, reference, application, and objectives.

Table 2 – Summary of literature available rigs and their capabilities.

Rig	Reference	Application	
		Rig concept	Objective
1	ASTM G-99	Pin on disk	General friction and wear
2	ASTM G133	Reciprocating Test Apparatus	General friction and wear
3	ASTM D 1894 – 001	Sliding sheet by weight actuator	General friction and wear
4	Shi <i>et al.</i> (2017)	Strip drawn	Metal forming
5	Klocke <i>et al.</i> (2015)	Strip drawn	Metal forming
6	Hu <i>et al.</i> (2017)	Pin on disk	Metal forming
7	Sutter and Ranc (2010)	Sliding sheet by Ballistic (gas gun) actuator	Ballistics
8	List, Sutter and Arnoux (2013)	Sliding sheet by Ballistic (gas gun) actuator	Ballistics
9	Lin <i>et al.</i> (2014)	Sliding sheet by ballistic actuator	Ballistics
10	Lai <i>et al.</i> (2012)	Sliding sheet by impact vertical hammer actuator	Crashworthiness
11	Present work	Sliding sheet by impact vertical hammer actuator	Crashworthiness

## 2.5. NUMERICAL MODELING OF FRICTION

Finite element software provides several approaches for modeling frictional contact, ranging from simple frictionless models to more complex cases that take into account variables such as pressure, slip velocity, temperature, surface roughness, and others.

The selection of an appropriate friction model depends on the specific physical and operating conditions of the system. When selecting a friction formulation, it is important to take into account characteristics such as the capability to reproduce stiction, slip velocity dependence, and pre-sliding displacements. These features play an important role in accurately representing real-world friction phenomena.

In mechanical systems, where fast and responsive dynamic computations are required, computational efficiency is a critical consideration. The efficiency of



the algorithm used to model friction is essential in ensuring efficient simulations.

Data inputs in friction modeling are often described as functions of equation parameters or as piecewise linear tabular data. These input representations allow for flexibility in capturing the behavior of friction under different conditions.

In the following section, traditional approaches to friction modeling will be discussed, exploring their strengths and limitations. By examining these approaches, valuable insights can be gained into the advancements made in the field of friction modeling.

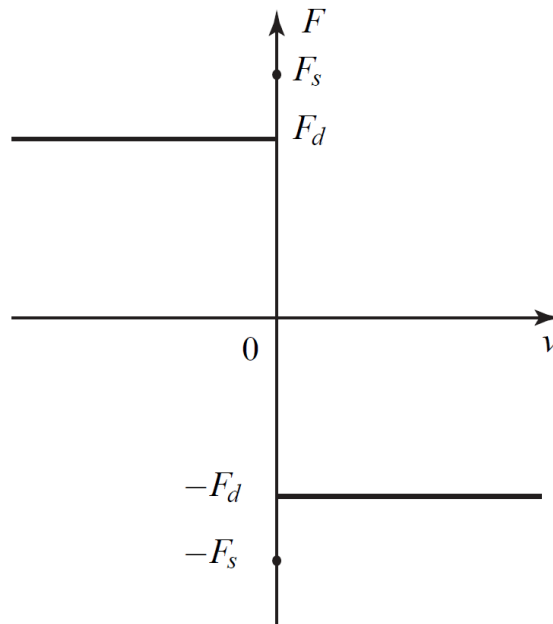
### 2.5.1. Coulomb friction model

The classic Coulomb friction is used as an example in the discussion about the macroscopic effects of friction. This model appears elementary from a mathematical standpoint and is straightforward to implement in a dynamic simulation environment. In particular, the friction force, which is tangent to the contacting surface, is analytically expressed by Equation (2) (Pennestri *et al.*, 2016).

$$F_T \begin{cases} \leq \mu_s F_N & v = 0 \\ = -\mu_d F_N \text{sign}(v) & v \neq 0 \end{cases} \quad (2)$$

Where:

- $F_T$  is the frictional force exerted by each surface on the countersurface; It is parallel to the surface, in a direction opposite to the applied force;
- $\mu_s$  is the static coefficient of friction;
- $\mu_d$  is the dynamic coefficient of friction;
- $F_N$  is the normal force exerted by each surface on the other;
- $v$  is the slip velocity.

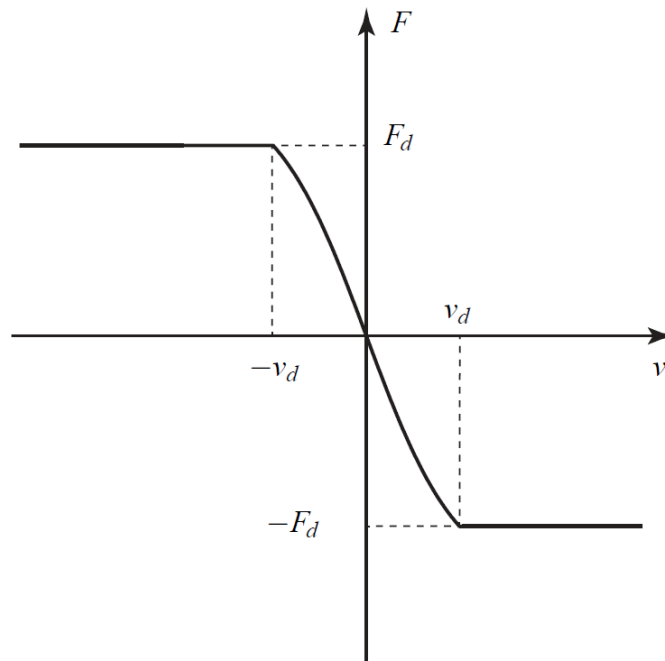
Figure 56 – The Coulomb friction model (Pennestri *et al.*, 2016).

In order to simplify the Coulomb model, it is possible to eliminate the static friction force, resulting in a simplified friction coefficient as presented in equation 1.

Notice in Figure 56 that while the friction coefficient remains constant and continuous, the force is discontinuous. This discontinuity can lead to convergence issues in numerical environments.

### 2.5.2. Smooth Coulomb friction model

The smooth Coulomb friction model, also known as the continuous model, is a variation of the classic Coulomb model. It has been introduced to avoid the computational burden caused by the discontinuity in forces. As shown in Figure 57, a smooth curve replaces the discontinuity around  $v = 0$ .

Figure 57 – The Smooth Coulomb friction model (Pennestri *et al.*, 2016).

Several smoothing functions can be utilized to achieve the desired effect, including linear, exponential, or trigonometric functions. However, the focus will solely be on investigating the hyperbolic tangent smoothing function. Therefore, the smooth Coulomb model can be formulated as demonstrated in Equation (3).

$$F = -F_d \tanh\left(\frac{v}{v_d}\right) \quad (3)$$

From it, it is also possible to deduce the value of the friction coefficient using Equation (4).

$$\mu(v) = \frac{F_d}{N} \tanh\left(\frac{v}{v_d}\right) \quad (4)$$

Where  $v_d$  is the velocity tolerance. Since the force is null at zero velocity, this model cannot reproduce stiction. The main advantage is the improvement in computational stability, which now depends on the chosen value of  $v_d$ .

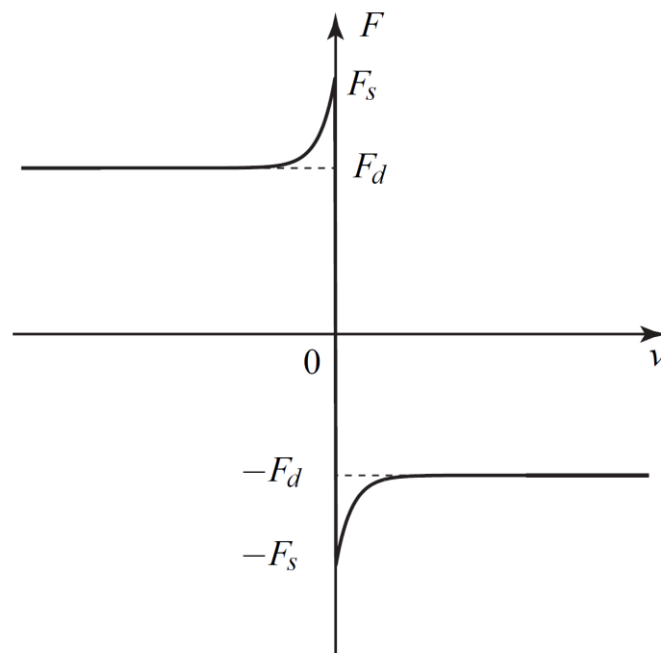
### 2.5.3. Exponential decay

As observed by experimental evidence (Hutchings, 2017), the friction force varies with the relative velocity. This variation can be divided into three main regions when plotting the friction force. The first region, characterized by low

values, can be accurately approximated using the Coulomb model. However, beyond a certain velocity limit and within a finite interval, a decrease in force is observed. Outside of this interval, there is a slight increase in the friction force with speed. While the classic Coulomb model results in stiff equations of motion and can be inaccurate, experimental observations demonstrate a more intricate relationship between friction force and velocity.

One of the most used functions in this role is the Benson exponential friction model. This model was first described by Benson and Hallquist (1989) and is shown in Figure 58, apud Pennestri *et al.* (2016). The model is by Equation (6)

Figure 58 – Benson exponential friction model (Pennestri *et al.*, 2016).



$$F = -Fd - (Fs - Fd)e^{-c|v|} \operatorname{sgn}(v) \quad (5)$$

$$\mu(v) = \mu_D + (\mu_S - \mu_D)e^{-c|v|} \quad (6)$$

This function assumes that friction varies from static to dynamic values according to an exponential decay, given by a constant  $c$ . It returns the friction coefficient as a function of slip velocity  $v$ , and depends on:

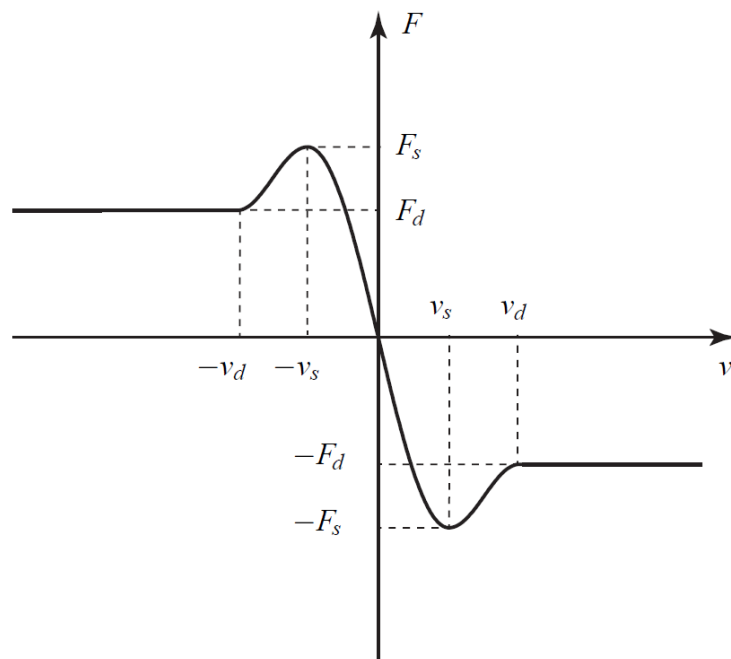
- $\mu_S$  Static friction coefficient;
- $\mu_D$  Dynamic friction coefficient;
- $c$  Decay constant.

At this stage, the following discussion proves to be necessary. Usually, the transition from static to dynamic friction coefficient is considered to be non-continuous, since the surfaces that were previously stuck are now sliding. Although large values of decay constant  $c$  may represent these behaviors, one shall notice that friction coefficients in dynamic conditions can vary for different slip velocities, due to very complex interfacial phenomena.

#### 2.5.4. Velocity Based Model

The velocity-based friction model shares a similar approach with the Smooth Coulomb Model. There is only a variation in the friction force with respect to velocity. Within the interval that includes zero velocity, an additional curve is introduced in an effort to mimic stiction. Figure 59 depicts the plot of the friction force versus velocity.

Figure 59 – Velocity Based friction model (Pennestri *et al.*, 2016).



Some authors (e.g., Wang and Rui, 2000) hinted the use of the single expression.

$$F = -F_s \sin[C \tan^{-1}(Bv) - E\{(Bv) - \tan^{-1}(Bv)\}] \quad (7)$$

or, in terms of friction coefficient, it can be rewritten as:

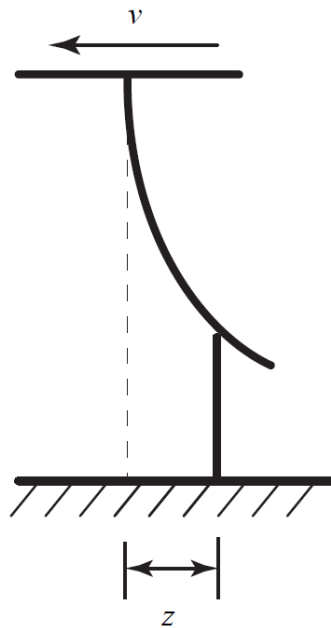
$$\mu(v) = \frac{F_s}{N} \sin[C \tan^{-1}(Bv) - E\{(Bv) - \tan^{-1}(Bv)\}] \quad (8)$$

The shape of the function can be adjusted by varying the parameters  $C$ ,  $B$  and  $E$  in order to match experiments.

### 2.5.5. Dahl model

The Dahl friction model is essentially a Coulomb friction model with a delay in the transition of the friction force when the direction of motion changes. The Dahl model is commonly described as a bristle model, as shown in Figure 60. Within a given applied load, the bristle undergoes elastic deformation, adding compliance, and returns to its original position after the load is removed. Once the elastic resistance is overcome, the entire brush moves and a permanent displacement is produced. The Dahl model incorporates a lag when the velocity changes sign.

Figure 60 – The bristle analogy in the Dahl model (Pennestri *et al.*, 2016).



### 2.5.6. Piecewise linear

Another common modeling approach is to discretize a continuous function using piecewise linear data through numerical interpolation. In this case, more complex functions can be used instead of the aforementioned models, as the hypothesis of monotonic continuity is considered for the friction coefficient. This approach can be very useful and versatile, and details will be shown later in this work.

The concept of a piecewise linear function involves representing a continuous curve using a composition of discrete straight-line segments. This approach allows for approximating any curved shape by using a combination of straight lines. It enables the function to have any real value and can accommodate a wide range of curve configurations.

To approximate a known curve using this method, the curve is sampled at specific points, and linear interpolation is performed between these points. This discretization process ensures that curves with abrupt changes in slope are accurately fitted by using appropriately sized straight-line segments. By minimizing the residuals between the piecewise fitted function and the original continuous shape, one can achieve a close approximation to the curve.

One major advantage of this approach is its versatility, as it can effectively approximate any curved shape described by constitutive equations from third-party software. This eliminates the need to directly implement complex formulations into the software's code using user-defined subroutines, thereby simplifying the implementation process.

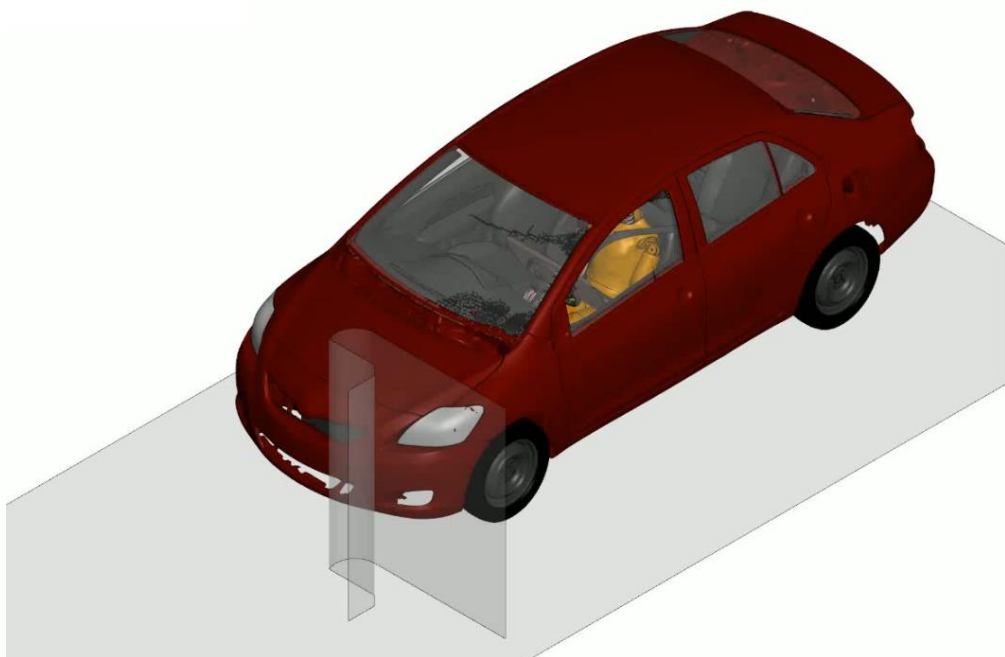
Furthermore, this method supports interpolation in multidimensional arrays, enabling the implementation of complex constitutive models for friction coefficients that may depend on multiple variables such as pressure, slip velocity, temperature, and more. This multidimensional capability enhances the flexibility and applicability of the approach, making it suitable for modeling and analyzing a wide range of complex systems and phenomena.

### 3. MATERIALS AND METHODS

#### 3.1. FINITE ELEMENT MODEL

A preliminary numerical crash test was performed as a starting point for the present work, following the guidelines of the IIHS small overlap crash protocol. The reason for choosing this protocol is that the off-center forces in this type of crash test typically pose a challenge for restraint systems. Additionally, varying levels of friction can lead to significantly different outcomes in terms of vehicle structure stability and the interaction between the dummy and airbag. The vehicle used was the 2010 Toyota Yaris, which was made available by NCAC at George Washington University, and its relevant information is described by Marzougui *et al.* (2014). Inside, a Hybrid III 50th Percentile dummy, detailed by Kan, Marzougui, and Bedewi (2003), was positioned in the driver's seat, and secured by a three-point seat belt attached to the vehicle frame. Also, an airbag was installed on the steering wheel of the vehicle, allowing for the pressures and speeds between the airbag and the dummy's clothing or skin. Figure 61 shows the finite element model used in the test. All preprocessing, processing, and postprocessing were performed in LS-Dyna.

Figure 61- Toyota Yaris 2010 Finite Element Model (NCAC, 2014)





This model was developed for two main purposes. The first objective is to assess the impact of friction on a finite element crash test model. For this, three simulations were run considering different friction coefficient levels among all parts,  $\mu=0.0$ ,  $\mu=0.4$ , and  $\mu=0.8$ . The following parameters were analyzed:

- Chest peak acceleration;
- Chest Severity Index (CSI);
- Head peak acceleration;
- Head Injury Criteria (HIC);
- Left femur normal force;
- Left tibia normal force;
- Neck resultant forces;
- Neck resultant moment.

A detailed explanation of each variable can be found In Appendix A.

The second purpose of this model was to determine the level of contact pressure in specific regions, in order to design the machine appropriately to withstand the required test conditions. They are:

- Steel – Aluminum;
- Dummy skin – Airbag;
- Airbag – Dummy shirt;
- Leather – Dummy shirt;
- Seatbelt – Dummy shirt;
- Dummy shirt – Dummy skin.

### 3.2. FRICTION RIG DESIGN

After conducting a careful literature review, various design concepts for rigs have been evaluated to address the concerns related to friction testing at different pressures and sliding velocities.

The rig designed here is based on the concept of strip test drawing, which is the most suitable method for friction coefficient during the initial moments of contact. The focus is on the transient condition, where there is no accumulated

wear from previous events. The measurement starts from a static condition and reaches maximum velocity after a few milliseconds. As the phenomenon is highly transient, of short duration, and occurs at high pressure and high speed, it is important to note that the sliding distance should be as small as possible. Larger sliding distances could result in different behaviors of the tribosystem due to wear and the accumulation of debris. The rig structure also must endure the test conditions with no damage and high stiffness. Due to this, thick structures of SAE 1020 steel have been considered for the role on structural elements.

After these initial considerations, the selection of the best solution was done step by step using decision matrices. The proposals were graded between 1 and 9 for each design step, as shown in Table 3 to Table 6.

### **3.2.1. Sliding bearing**

Considering that dynamic friction is associated with moving parts, it is expected that one of the contact sides should be kept stationary while the other one (herein called sample carrier) moves in a single direction. Three proposals have been compared in this sense. The first one is a double-sided sample carrier, similar to the one used by Lai *et al.* (2012) and shown in Figure 41. The second and third sample carriers are single-sided, allowing for the choice of a linear bearing or roller bearing guide on the opposite side of the sample to ensure motion, as illustrated in Figure 62.

Figure 62 – Linear Motion Guide (THK, 2018)

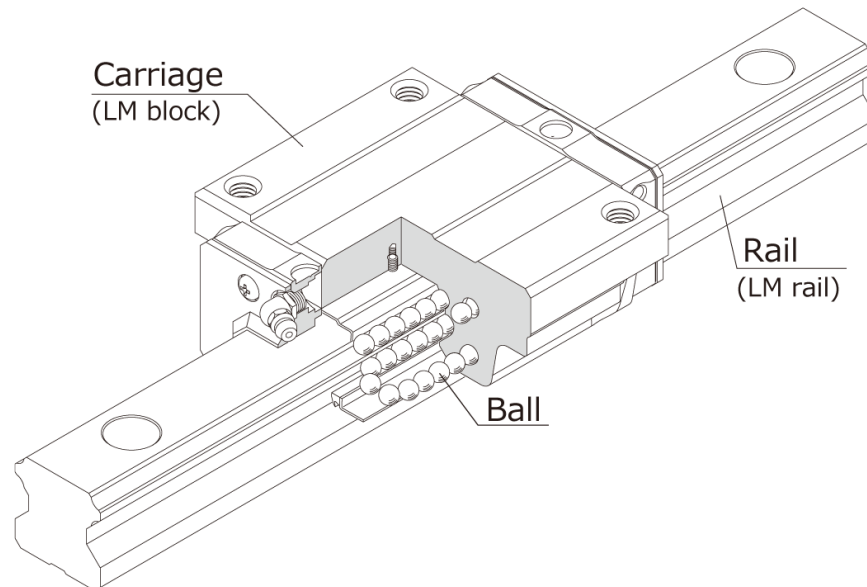


Table 3 – Sample carrier design decision matrix.

Solution criteria	weights	Averaged weights	Double sided sample	Linear motion guide	Linear roller motion guide
Cost	9	0.28	1	7	5
Easy to implement	1	0.03	3	9	7
Easy to use	3	0.09	1	7	7
Expected stability	5	0.16	1	9	7
Speed range	7	0.22	9	5	5
Force range	7	0.22	9	5	7
<b>Total</b>	<b>32</b>	<b>1</b>	<b>4.56</b>	<b>6.50</b>	<b>6.00</b>

In the decision matrix of Table 3, it has been considered that using double-sided samples could lead to significant test instabilities. This is because the only forces acting on the carrier are friction forces, which could result in lateral movements and tilt angles of the carrier during the test. The bearings restrict these degrees of freedom, but they have the disadvantage of limited normal force capacity. Also, using double-sided samples would result in a more

laborious operation, as each test would require twice the amount of sample preparation (as noticed in Figure 40). Finally, this would also result in high sensor costs. If the load cells are placed on stationary sample holders, two load cells would be required for tangential measurements. Alternatively, if the load cells are placed on the movable sample holder, a single load cell and an accelerometer would be needed.

Considering the availability on the market and the recommendations of the bearing manufacturer regarding expected stability and force capabilities for the given application, the linear bearing guide has been chosen for the role.

### **3.2.2. Tangential Load Actuation**

The tangential loading actuation is responsible for accelerating the sample carrier up to approximately 5 m/s within a range of about 0.01 s. This results in accelerations of up to 50 g and significant energy levels. To reach such conditions, three tangential load actuation mechanisms were proposed.

The first concept considered is a spring energy actuator, where this element would be loaded until the desired energy level is reached and then released, causing the sample carrier to accelerate instantaneously.

The second proposed solution involves using a vertical drop impact hammer. This hammer would strike a rod connected to the sample holder, and any remaining energy would be absorbed by a foam block located on top of the rig.

For the last part, a pneumatic actuator was considered. This solution is used in Hopkinson bar experiments and can achieve high energy levels in very short response times.

Figure 63 shows the three proposed mechanisms for tangential load actuation.

Figure 63 – Tangential load actuation system proposals (a – Spring accumulator, b – Impact hammer, c – Pneumatic Actuator).

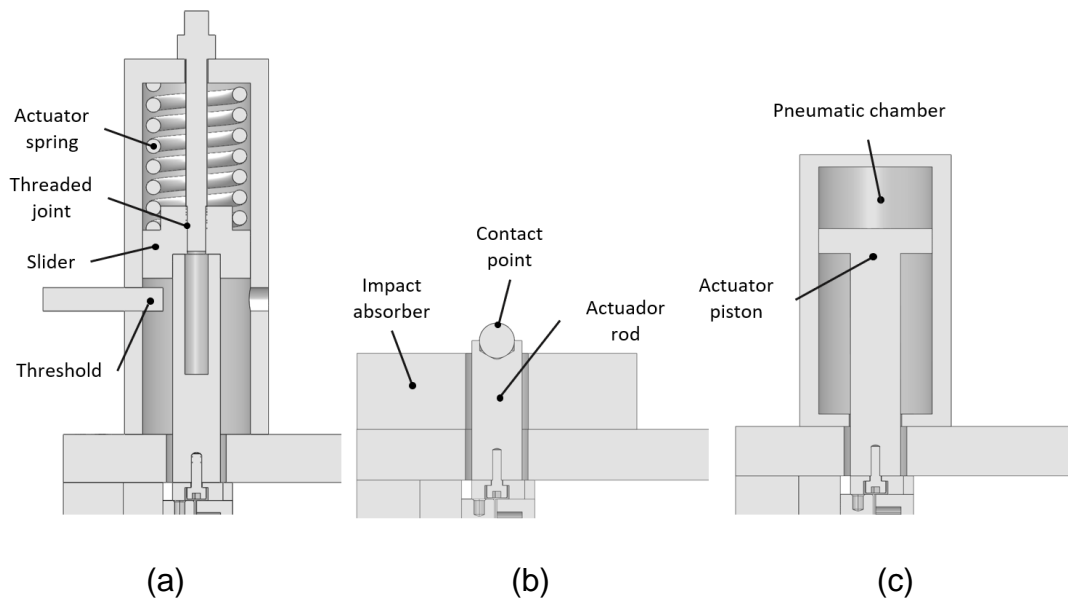


Table 4 – Tangential load actuation decision matrix.

Solution criteria	Weights	Averaged weights	Spring accumulator	Impact hammer	Pneumatic actuator
Cost	9	0.28	3	9	1
Easy to implement	1	0.03	7	7	1
Easy to use	3	0.09	7	3	7
Expected stability	5	0.16	3	3	3
Potential Energy storage Capacity	7	0.22	5	9	7
Acceleration Capacity	7	0.22	3	7	7
<b>Total</b>	<b>32</b>	<b>1</b>	<b>3.94</b>	<b>7.00</b>	<b>4.50</b>

In Table 4, it was considered that although spring energy accumulators are relatively easy to use and implement, and they eliminate the need for an external device as the impact hammer, they are expected to provide slower acceleration compared to other solutions due to the spring release time. Also, the dimensioning of a mechanism to compress and release the spring would be necessary, since that high forces are expected. On the other hand, pneumatic actuators are well-suited for the role, but they are more expensive and complex to implement than the impact hammer. An impact hammer easily

achieves the desired acceleration levels with considerable simplicity, and it is available at the GMSIE laboratory.

However, the impact between two metallic bodies can generate a high load peak and reduce the lifespan of the rig. So, to ensure smoother load actuation a thin sheet of rubber damper component is placed between the hammer and the rig.

Further, to transmit axial load only and avoid misalignments between the contact components, a good approach is to place a semi-sphere on top of the actuator hammer. Considering these decision criteria and the available alternatives, the impact hammer was chosen for the role.

### **3.2.3. Normal load actuation**

To evaluate the transition behavior of the friction coefficient from static to dynamic under various pressures, the rig must be equipped with an adjustable actuator that applies force in the direction of the normal force on the samples. The force applied may range from 100 N to 5000 N. It is also desirable to keep the pressure as constant as possible during the test. Then, three actuators are considered for the role: a threaded joint, a spring-based mechanism, and a pneumatic actuator.

Figure 64 – Normal load actuation system proposals (a – Threaded Joint, b – Spring based, c – Pneumatic).

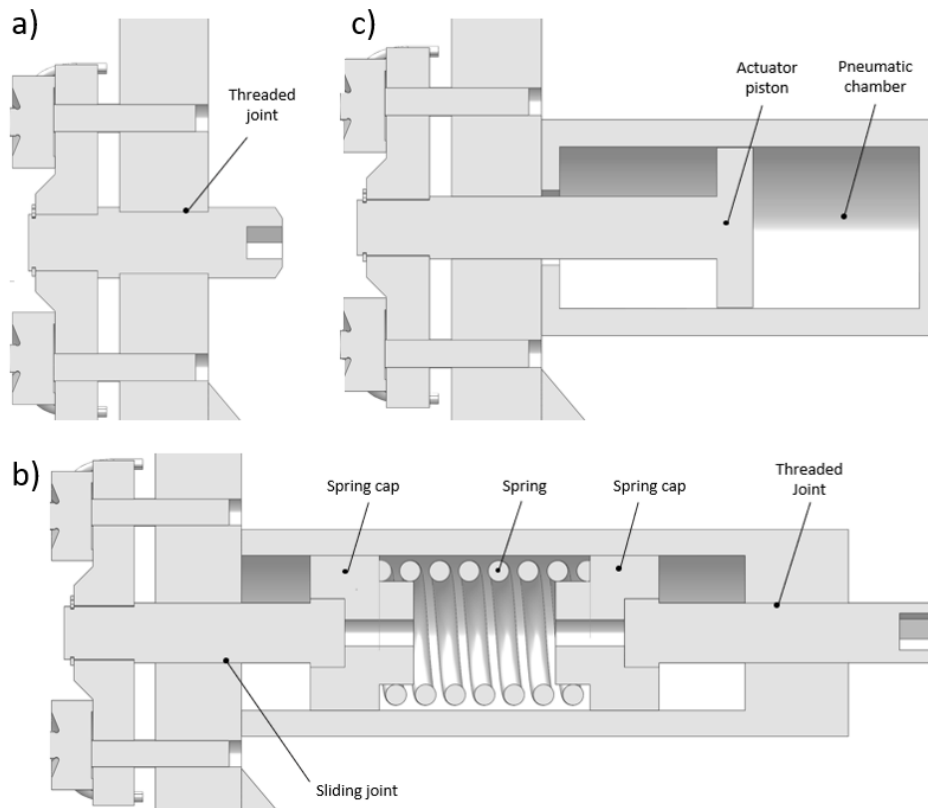


Table 5 – Normal load actuation decision matrix.

Solution criteria	Weights	Averaged weights	Threaded Joint	Spring based	Pneumatic actuator
Cost	9	0.36	9	7	1
Easy to implement	1	0.04	9	4	1
Easy to use	3	0.12	3	1	9
Expected stability	5	0.20	5	1	9
Force range	7	0.28	9	5	7
<b>Total</b>	<b>25</b>	<b>1</b>	<b>7.48</b>	<b>4.40</b>	<b>5.24</b>

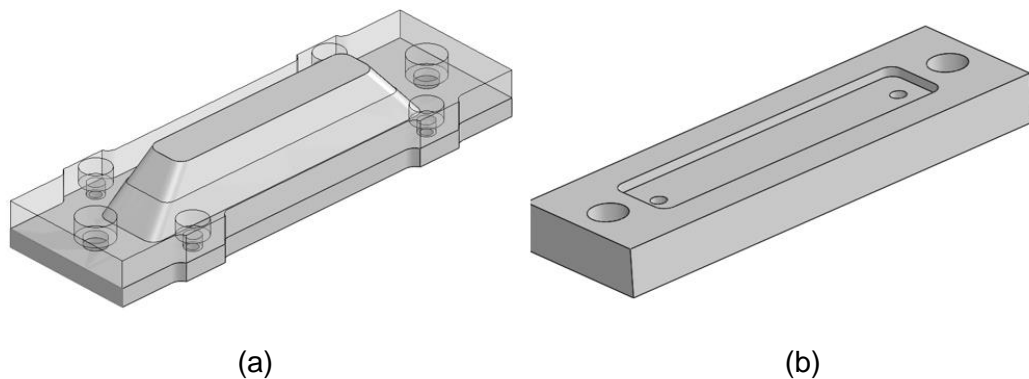
The threaded joint is the simplest mechanism for actuation in this role. Although it brings high stiffness to the system, where any clearance or dimensional variation could result in significant pressure oscillation, this approach is a good candidate since minimal wear is expected during the tests.

An alternative to consider for improved performance in handling pressure variations and excessive stiffness is a spring-based actuator. However, it is important to note that this type of actuator may cause the normal force to bounce due to system vibrations. Another option that has been considered is a pneumatic actuator, which has the potential to address both high stiffness and vibration concerns. However, similar complexities and cost considerations raised in relation to tangential actuation also apply to normal actuation. So, the threaded joint was selected for the role.

### 3.2.4. Sample holding

Different types of materials are expected to be tested on the rig, such as sheet metal, airbag fabric, dummy shirt fabric, and leather. In order to properly accommodate all types of materials, two sample holders were developed for the fixed side of the rig. One holder was designed to accommodate elastic fabric materials, while the other was designed to accommodate solid sheets. They are shown in Figure 65.

Figure 65 – Fixed side sample holders (a – fabric sample holder, b – thin sheet sample holder).



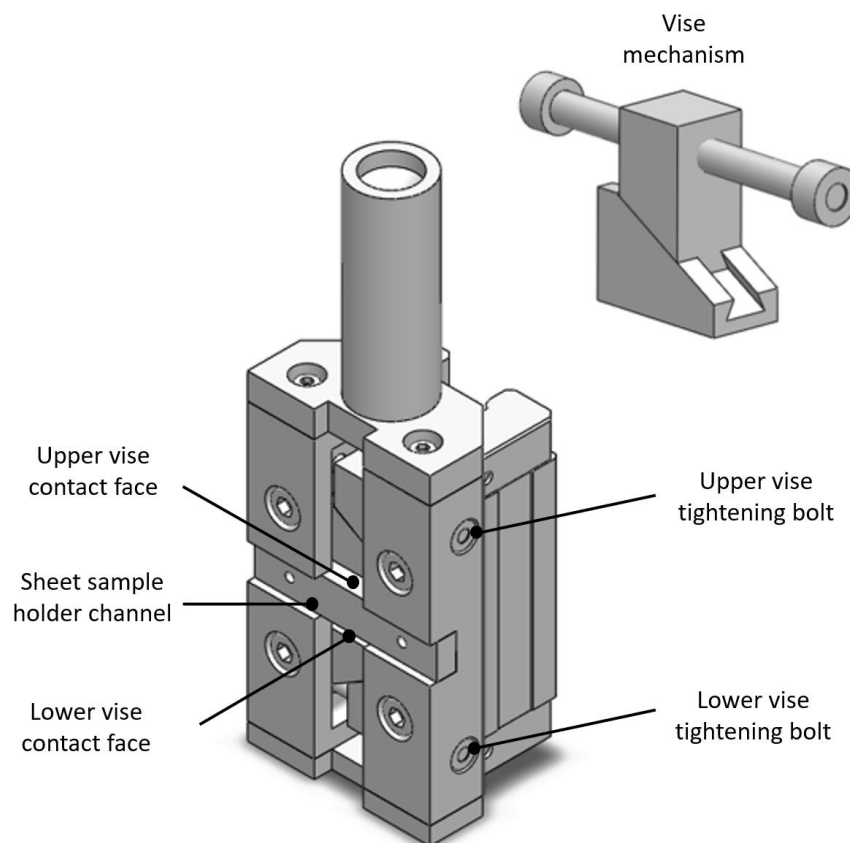
The fixed side sample needs to have a narrow and long proportion, as sliding will occur over its surface. Elastic fabric materials are very complicated to accommodate properly for frictional tests. If they are not pre-stretched correctly, the friction results can be influenced by ploughing and other phenomena associated with their deformation. The fabric sample holder is designed to minimize these undesired effects.



The sheet sample holder is much simpler and consists of fixture bolts and a recessed face to ensure sample stability during the test. Metal and polymeric sheets are compatible with this holder.

On the other side of the rig, a versatile sample holder has been developed. It can hold sheet samples horizontally or flexible samples with the help of a vise system. The vise can be tightened or loosened by turning a bolt on the side of the sample holder, and a slanted plane feature will be used to move a small block up and down, securing the sample in place. Figure 66 shows the moving side sample holder with the vise mechanism.

Figure 66 – Moving side sample holder with the vise mechanism.



### 3.2.5. Load decomposition Mechanism

One of the most challenging steps in rig development is properly decomposing the normal and tangential forces while minimizing errors caused by their interactions. So, three proposals have been considered and are shown in Table 6.

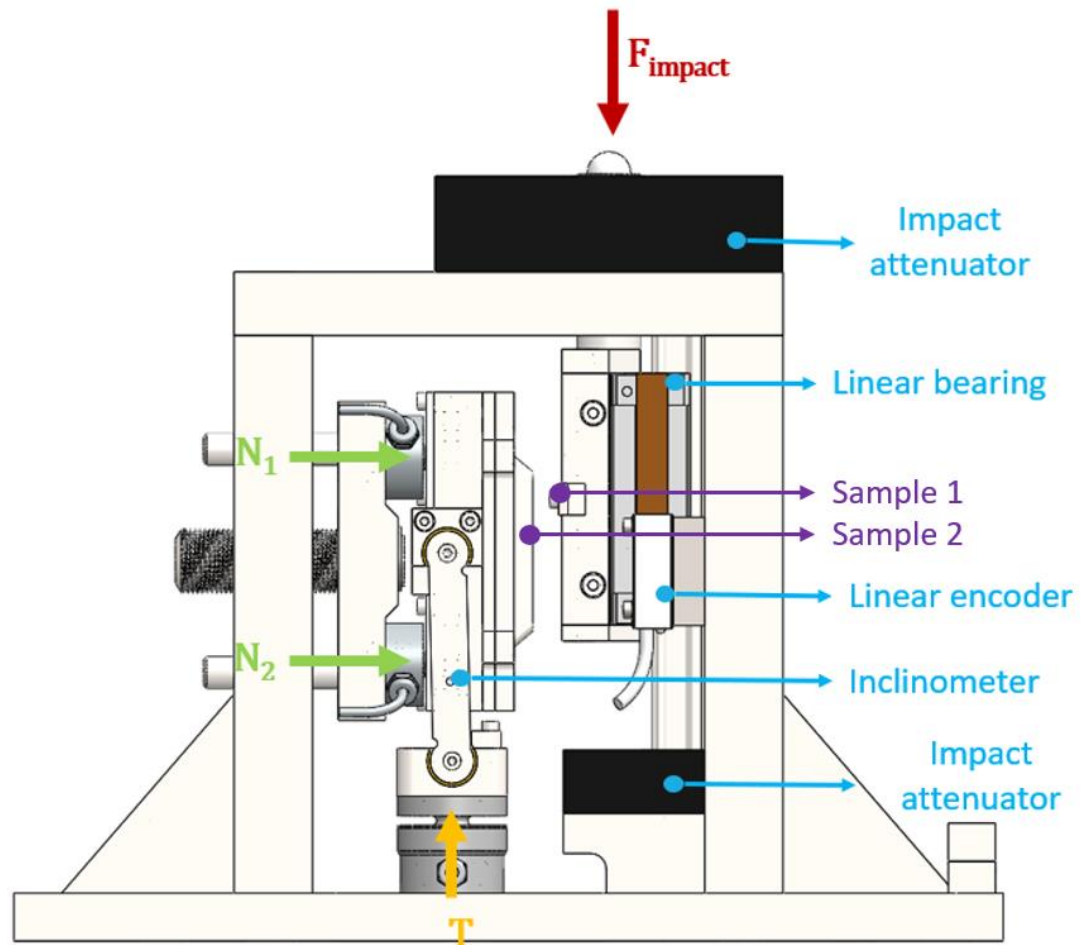
Table 6 – Load decomposition mechanism decision matrix

Solution Criteria	Weights	Averaged weights	Biaxial load cell	3 uniaxial load cells
<b>Cost</b>	<b>9</b>	<b>0.33</b>	1	7
<b>Easy to implement</b>	<b>1</b>	<b>0.04</b>	9	3
<b>Easy to use</b>	<b>3</b>	<b>0.11</b>	7	3
<b>Expected stability</b>	<b>5</b>	<b>0.19</b>	7	5
<b>Accuracy</b>	<b>9</b>	<b>0.33</b>	7	9
<b>Total</b>	<b>27</b>	<b>1</b>	<b>5.07</b>	<b>6.70</b>

First, a biaxial load cell has been considered because this sensor can measure the force on two orthogonal axes and is suitable for the role. One of the principal drawbacks of this equipment is its high cost and limited availability of commercial options. Additionally, there is a variation in the force actuation point during the test, and it is expected that a significant moment load will be transmitted to the sensor.

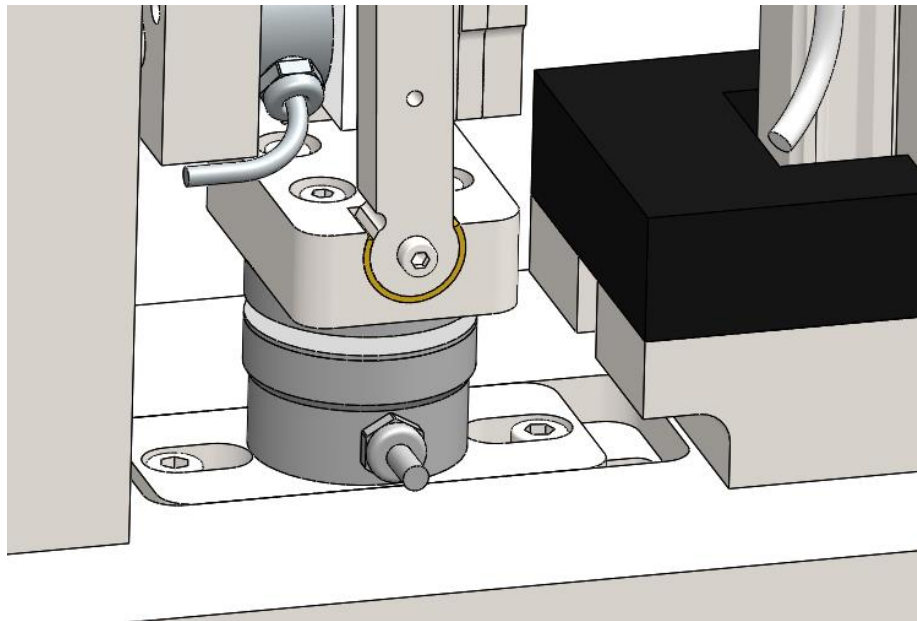
The second proposal suggests using two uniaxial sensors to measure normal loads and one sensor to measure the tangential force. This setup would eliminate the issue of moment load, as the sliding range would be centralized and limited between the two sensors. Figure 67 shows the referenced design, the sensor positioning, and the main rig components.

Figure 67 – Schematics of the proposed test rig.



However, this design creates a side effect of a force decomposition angle on the system. This angle might cause the loads to decompose and result in measurement errors if not taken into account in the final result. To resolve this, a movable base was considered, which can be adjusted to keep the rod angles negligible in every situation. Figure 68 shows the design of the movable base.

Figure 68 – Movable tangential load cell base.



With this device, the friction coefficient can be calculated by Equation (9).

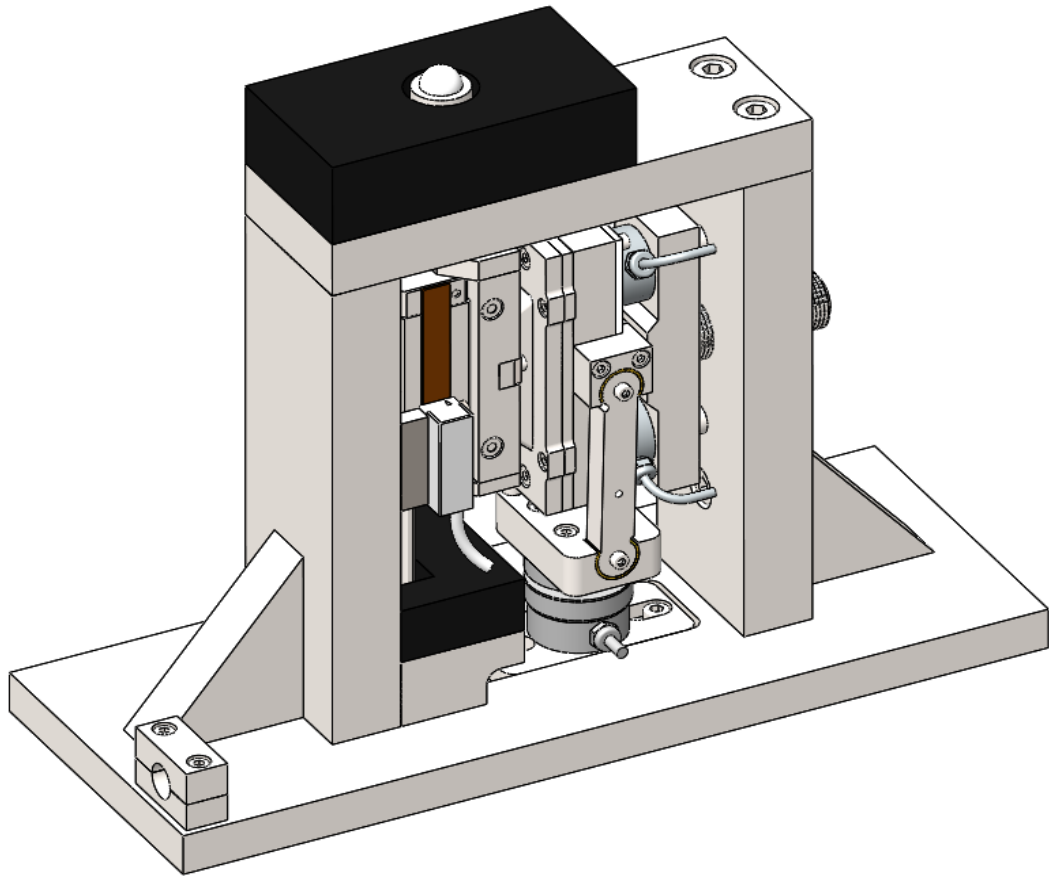
$$\mu = \frac{T}{N_1 + N_2 - T \sin(\theta)} \quad (9)$$

Considering a small angle of less than  $5^\circ$  where  $\sin(\theta) \cong 0$ , the maximum error on the signal due to force decomposition is 0.44%. For this reason, and to avoid introducing additional noise on signal acquisition, the inclinometer will only be utilized to verify that the test angle is small. Consequently, the simplified Equation (10) will be employed.

$$\mu = \frac{T}{N_1 + N_2} \quad (10)$$

The final version of the rig concept can be seen in Figure 69.

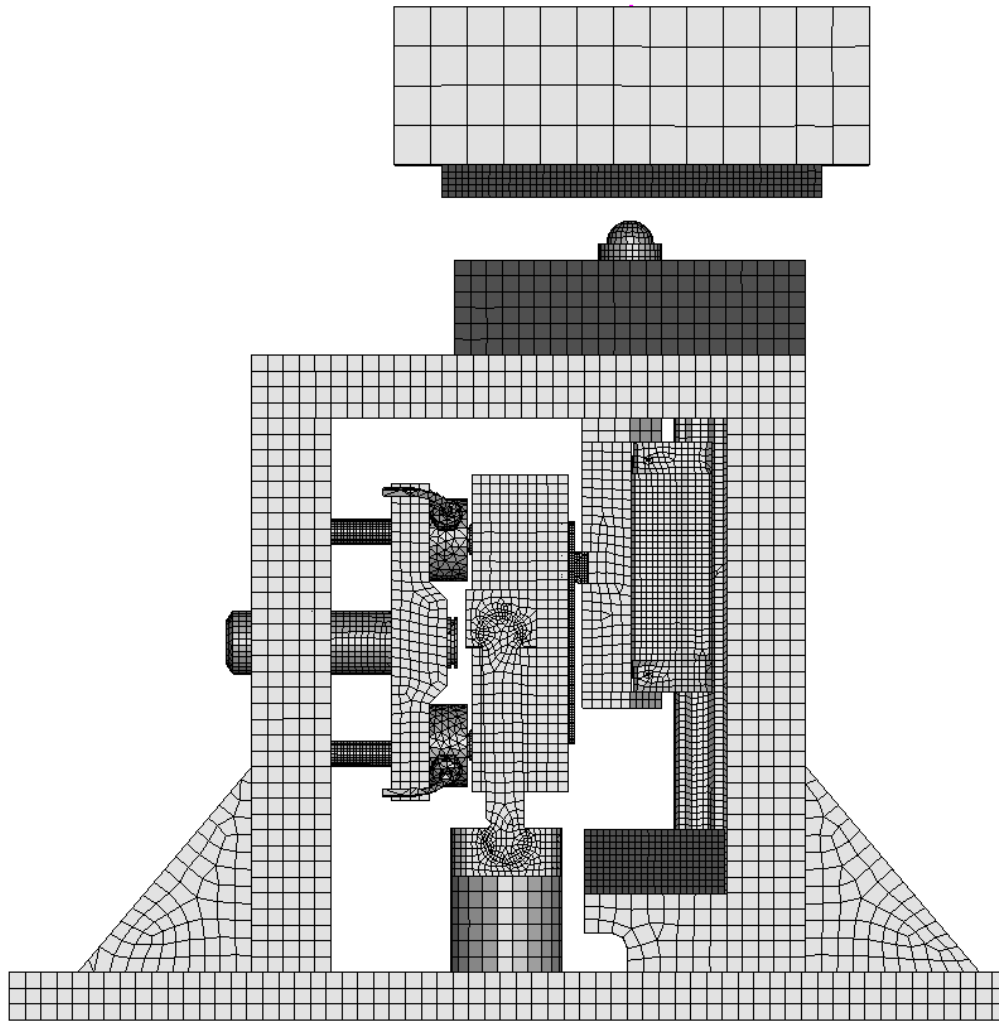
Figure 69– Rig final CAD concept.



### 3.3. FINITE ELEMENT ANALYSIS

To ensure that the rig would withstand the tests and produce accurate results, a finite element analysis of the model was conducted using LS-Dyna. The objective of this analysis was to determine whether the stresses are below the material's yield stress and if the loads passing through the load cells accurately replicate the friction model applied to the contacting surface. A 5 kN normal load was applied, and an initial velocity of 5 m/s was assigned to the drop mass of 10 kg.

Figure 70 – Finite element model of friction rig on LS-Dyna.



In the initial 2.5 ms, a preload was applied to the threaded joint until the desired pressure level of the samples was achieved. Following this, the impact hammer made contact with the rod, initiating the test.

The model was built with 152151 first order elements and the total simulation time was set to 0.016 s. All parts were modeled as linear elastic SAE 1020 steel, where a yielding strength of 330 MPa was considered as the design limit. The foam material on energy absorbers was modeled as described by Mussulini and Driemeier (2017). The stress on the most critical element and the contour plot frames of rig simulation

Figure 71- Stress over time in most critical element of test rig.

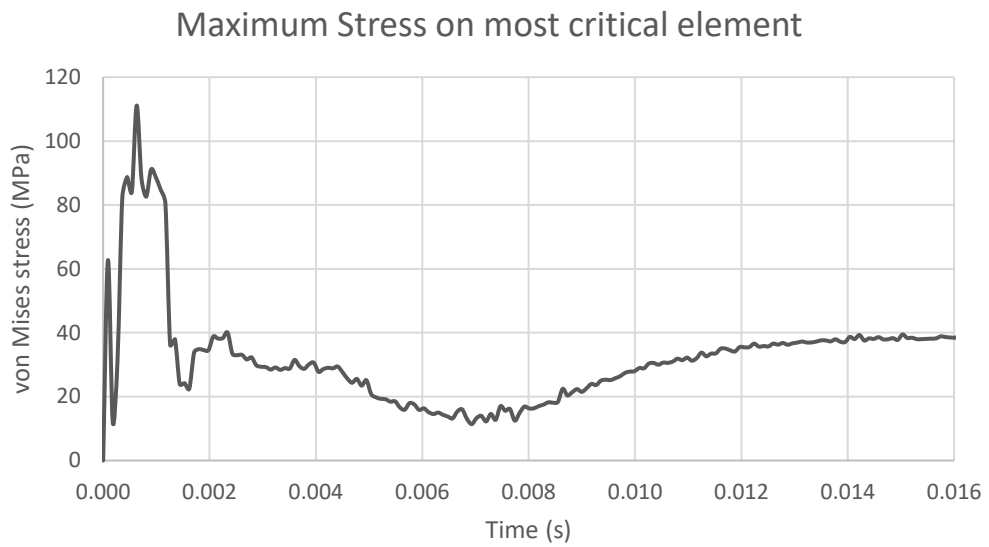
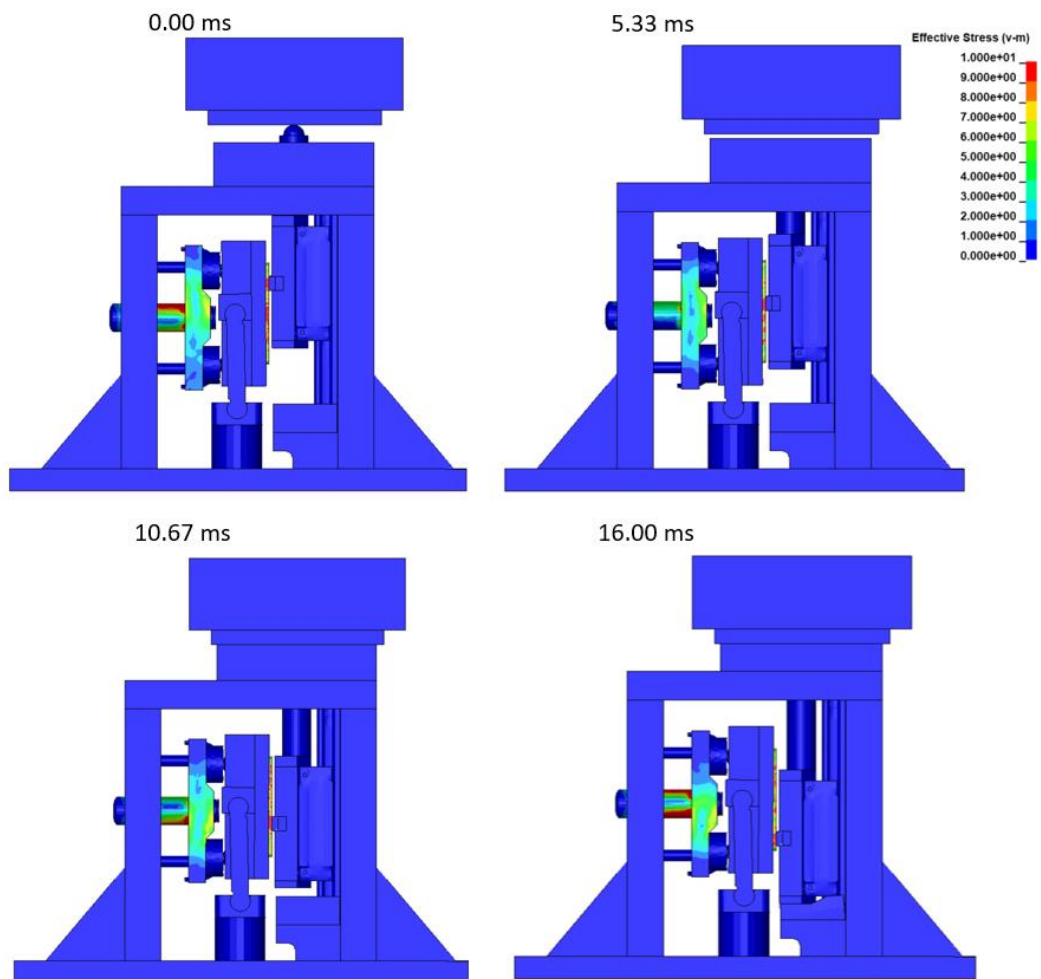


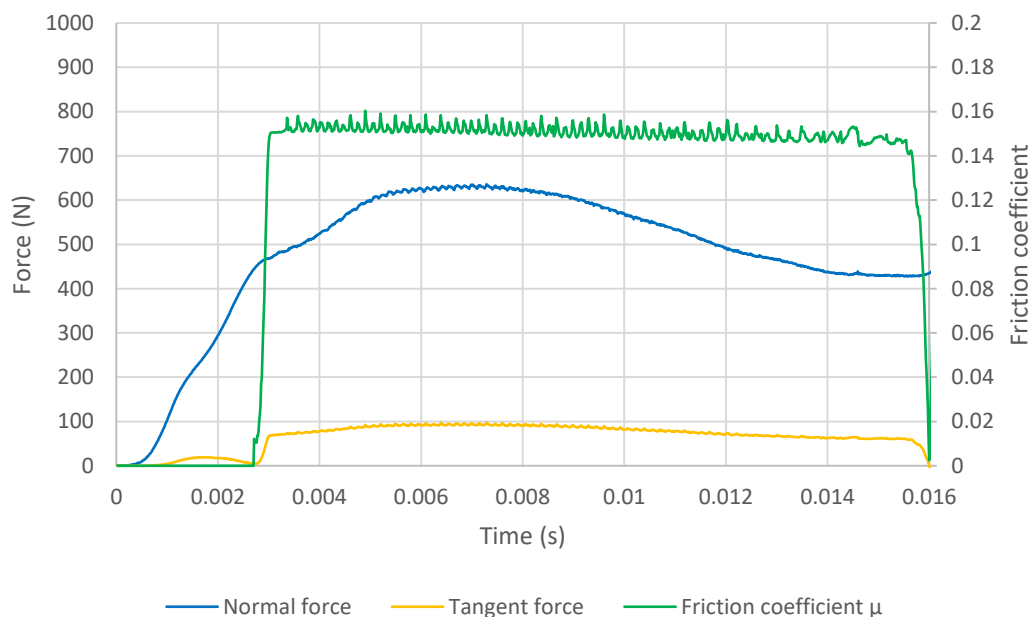
Figure 72 – Stress contour plots of test rig under operation.



From simulation results, it is noticeable that the rig operates in a safe stress range even in the worst scenario, ranging below 40 MPa during operation. One relevant comment in Figure 71 is that the high stress peak at the beginning of the simulation arises artificially from the pre-load setting in a very short period of time and must be neglected since this preload will be applied gradually during normal operation.

The rig's general behavior was also assessed and the profile of acquired signals was examined. To simulate real-world conditions, a constant friction coefficient of 0.15 was applied to the testing surfaces as input. The primary objective was to determine the measured friction by analyzing sensor forces. The measured loads on the sensor and the acquired friction coefficient of the numerical model are presented in Figure 73

Figure 73 – Finite element output of the load cell measurements.



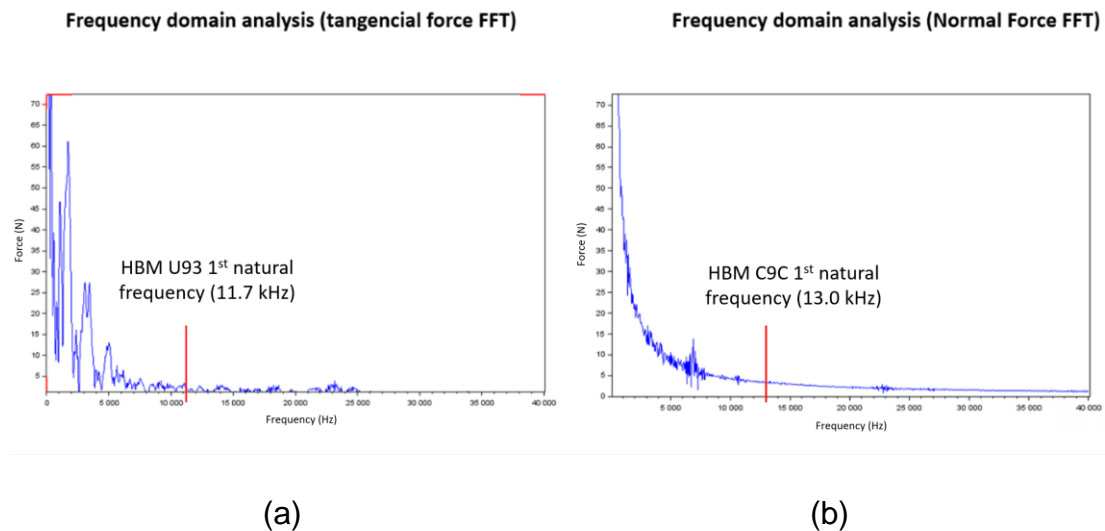
During the test, it was observed that there was approximately a 20% variation in the normal load. This variation was attributed to the movement of the contacting samples in relation to the load cells. However, it is worth noting that this minor fluctuation will be accounted for during the regression of constitutive



equation parameters, as it takes into consideration the pressure variations throughout the tests.

To ensure the accuracy and reliability of the acquired sensor data, a frequency domain analysis has been conducted. This approach needs to ensure that excitation frequencies on the neighbors of 1<sup>st</sup> sensor's natural frequency are small. This analysis involves applying a Fast Fourier Transform (FFT) to the virtual load measurements. By analyzing the frequency components of the signals, any irregularities or noise can be identified and addressed.

Figure 74 – Frequency domain analysis of load cell signals outputted by finite element analysis (a) Tangential load cell HBM U93 and (b) Normal load cells HBM C9C.

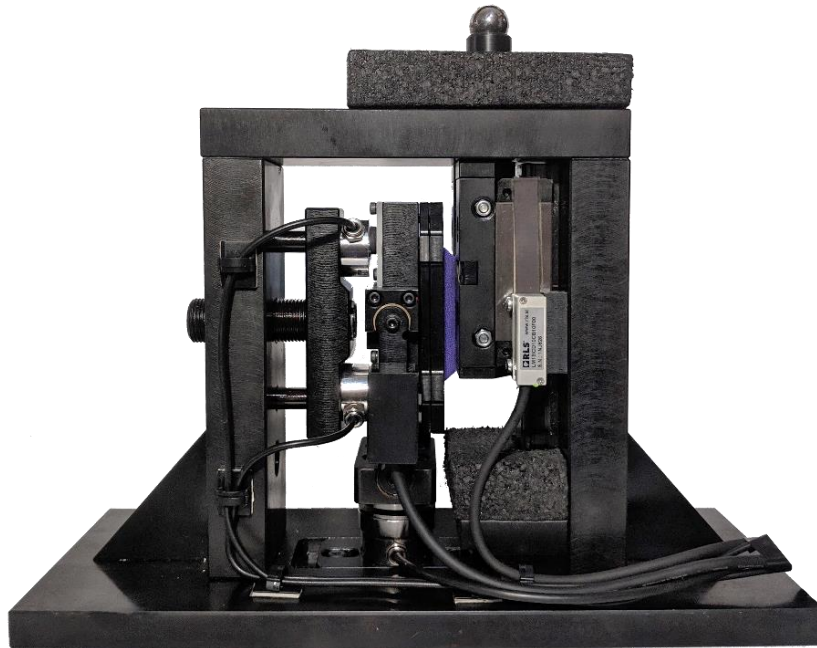


The load component around the natural frequency region of the sensors has been found to be less than 0.1% of the sensor's nominal load. This indicates that there is no significant vibration or resonance occurring within the system during the test.

### 3.4. PROTOTYPE

The final prototype was built as showed on Figure 75.

Figure 75 – Final test rig prototype.



### 3.4.1. Data acquisition system

The hardware for data acquisition was based on a National Instruments USB-6356, with a maximum frequency of 1.25 MHz, 8 analog inputs, 24 digital inputs, and a 16-bit AD converter, as shown in Figure 76.

Figure 76 – National Instruments USB-6356.



Additionally, a Fylde FE 579 bridge amplifier is used for amplifying and filtering the load cell signal. This apparatus plays a crucial role in the data acquisition process, allowing accurate measurements and analysis of load cell output.

Load cells are transducers that convert mechanical force or weight into an electrical signal. However, the signals generated by load cells are typically weak and require amplification to enhance their strength and quality for subsequent processing. The apparatus is shown in Figure 77.

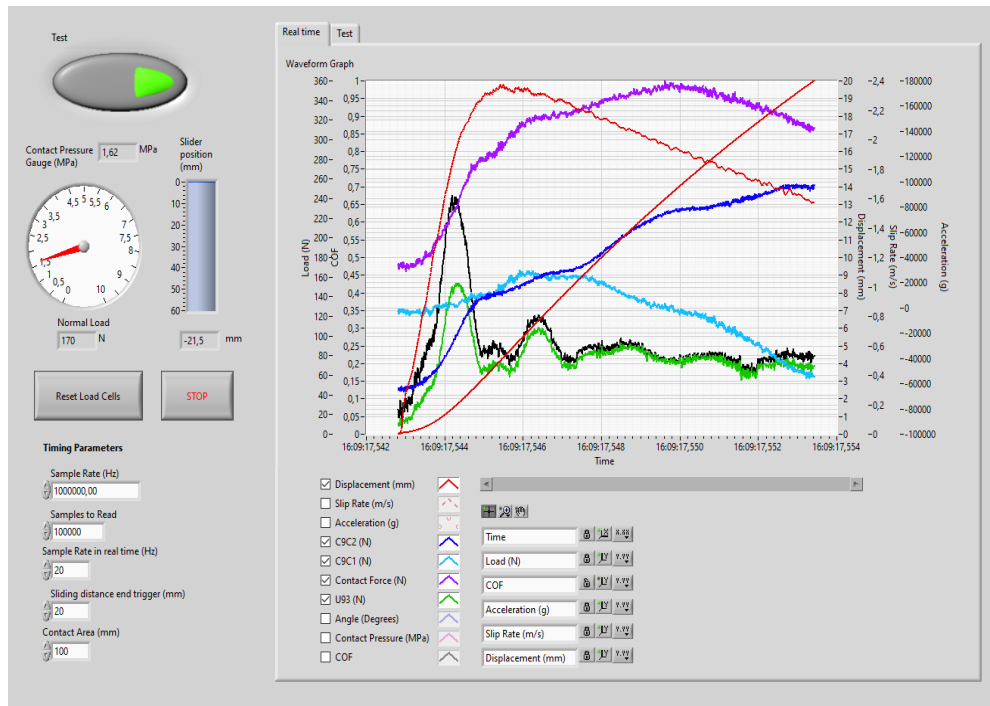
Figure 77 – Fylde FE 579 bridge Amplifier



### 3.4.2. Software

The data acquisition process was facilitated by a user interface developed in LabVIEW, which provided a user-friendly platform for controlling and monitoring the test setup. A sample of the raw data obtained from the contact pair between a dummy shirt and skin is presented in Figure 78

Figure 78 – User interface of LabView based data acquisition software.



In the data plot, the friction coefficient is represented by the black line. It can be observed that the friction coefficient experiences a significant increase, followed by a subsequent decrease and stabilization. The characteristic behavior described is commonly known as the static-dynamic transition. This transition occurs when the displacement sensor detects sliding between the contact surfaces. It is important to consider that there might be shearing of soft samples during the initial stage of the test, which can affect the actual contact surface. Therefore, the displacement is considered to start at this transition point because it signifies the beginning of significant sliding.

In cases where no distinct peak is observed in the data, an offset is considered to be the highest value among the first 20% of data points. This approach ensures that the displacement measurement accurately reflects the contact behavior and avoids underestimating the true contact displacement.

Given the rapid nature of the test, with a duration of less than 0.01 ms in some cases, and the relatively short duration of the transition from static to dynamic friction (less than 10% of the test time), it is necessary to acquire data at

frequencies exceeding 100 kHz. To achieve this, a triggering system is implemented to initiate and terminate the data acquisition process.

The test is initiated upon detecting the first movement of the encoder sensor, which serves as a reliable indicator of contact onset and the test's start. Once the test is triggered, the system begins acquiring data at a high-frequency sampling rate.

To prevent unnecessary data recording, the test is programmed to stop once a specified displacement of 30 mm is reached. This displacement threshold serves as an appropriate endpoint for the test, enabling adequate data capture while also maintaining control over the test duration.

By implementing this triggering system, it is possible to accurately capture the relevant data during the test period, allowing for a thorough analysis of friction behavior and contact dynamics.

A block diagram of the LabView based developed software is shown in Appendix F.

The software offers two distinct modes of operation to cater to different measurement requirements.

The first mode is the real-time measurement mode, which is designed to give users instant access to the most up-to-date measured data. This mode proves particularly valuable for tasks such as calibrating contact pressure and debugging signals before conducting tests. Operating at a lower frequency, it allows users to observe and analyze the data in real time, aiding in the fine-tuning and optimization of measurement parameters.

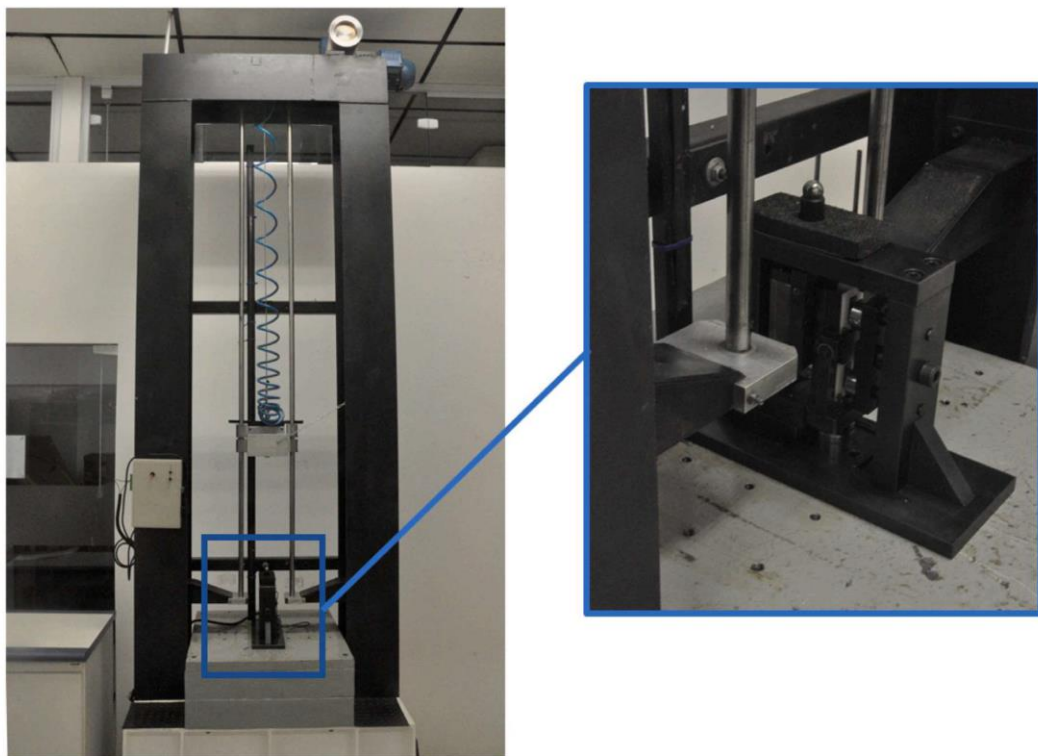
The second mode, on the other hand, offers start-stop trigger functionality. This feature is specifically designed to facilitate high-frequency measurements during tests while minimizing unnecessary data storage. By utilizing the start and stop triggers, users can precisely control the data acquisition process, ensuring that only relevant data is recorded. This feature helps to save storage space and streamline data analysis.

Upon completion of the test, the software presents the test results on the screen, providing users with immediate feedback and insights. Furthermore, the software automatically saves the test results in a convenient text file format for future reference and analysis.

### 3.4.3. Impact hammer

The friction tests under impact conditions were performed on the Low Energy Impact Hammer at Group of Solid Mechanics and Structural Impact, which is shown in Figure 79. The test setup allows impact conditions of up to 5 m/s and 15 kg.

Figure 79 – Low Energy Impact Hammer with friction test rig.



### 3.4.4. Samples

The selection of contact pairs for this study was based on observation of the phenomena occurring in the frontal region of the vehicle during the virtual crash test. To represent the interactions between structural elements, one has chosen samples of the aluminum cross member and the steel crash box with the longitudinal element. This particular contact pair is crucial to evaluate at

higher contact pressures as it will demonstrate the measuring machine's capability under significant normal stresses.

Regarding internal vehicle components, it was considered contact pairs such as Dummy skin – Airbag, Airbag – Dummy shirt, Dummy shirt – Leather, Seatbelt – Dummy shirt, and Dummy skin – Dummy shirt. These contact pairs serve as excellent examples for data collection, showcasing the machine's efficiency and adaptability when dealing with different materials and lower pressures.

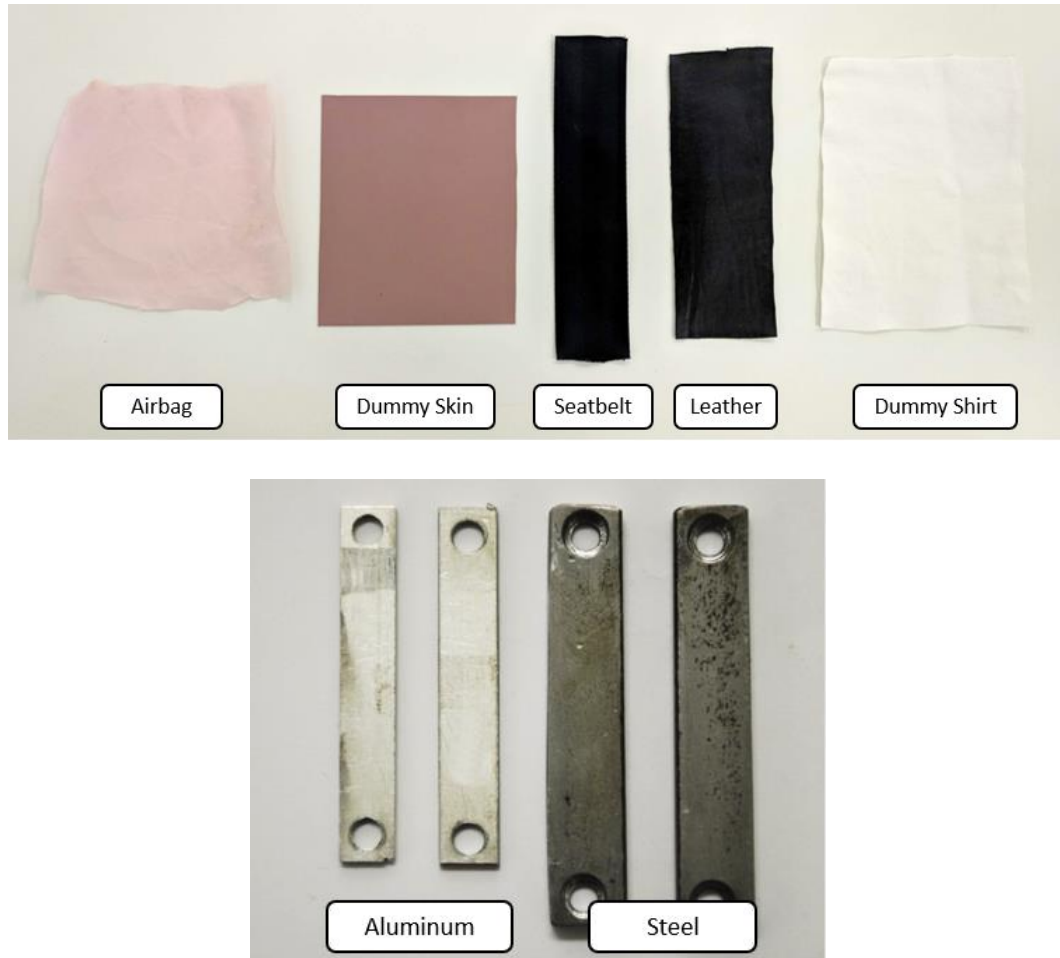
Table 7 shows the pressure and slip velocity levels considered for each contact pair and

Figure 80 shows the base materials for the mentioned samples.

Table 7 – Contact pairs and tests conditions.

Samples	Pressure (MPa)			Slip velocity (m/s)	
	Low	Medium	High	Low	High
<b>Steel – Aluminium</b>	1	5	10	1	5
<b>Dummy skin – Airbag</b>	0.5	1.5	3	1	5
<b>Airbag – Dummy Shirt</b>	0.5	1.5	3	1	5
<b>Dummy Shirt – Leather</b>	0.5	1.5	3	1	5
<b>Dummy Shirt – Seatbelt</b>	0.5	1.5	3	1	5
<b>Dummy skin – Dummy shirt</b>	0.5	1.5	3	1	5

Figure 80 – Samples of tested materials.



In order to accurately represent contact behavior in crashworthiness scenarios, various contact pairs were selected for testing. These pairs included the interaction between the airbag and the dummy's skin, the seatbelt and the dummy's shirt, the seat cover leather, and the dummy's shirt, as well as the bumper and the front rails (both made of aluminum and steel).

To capture the complexity of these contact interactions, six different test configurations were defined, resulting in a total of 18 tests conducted for each pair of contacts. In total, 126 tests were performed.

The contact pressures selected for these tests were chosen to closely replicate the conditions experienced during actual crash tests, within the mechanical limitations of the rig and without causing any visual degradation of the test samples.



### 3.5. CONSTITUTIVE EQUATION

#### 3.5.1. Current Approach

According to Equation (6) friction is expected to behave as an exponential function from  $\mu_s$  to  $\mu_d$ , controlled by the parameter  $c$ . In this study, the goal is to consider  $\mu$  as a function of both slip velocity  $v$  and pressure  $p$ . Thus, it was initially proposed an exponential decay for both parameters, as shown in Equation (11).

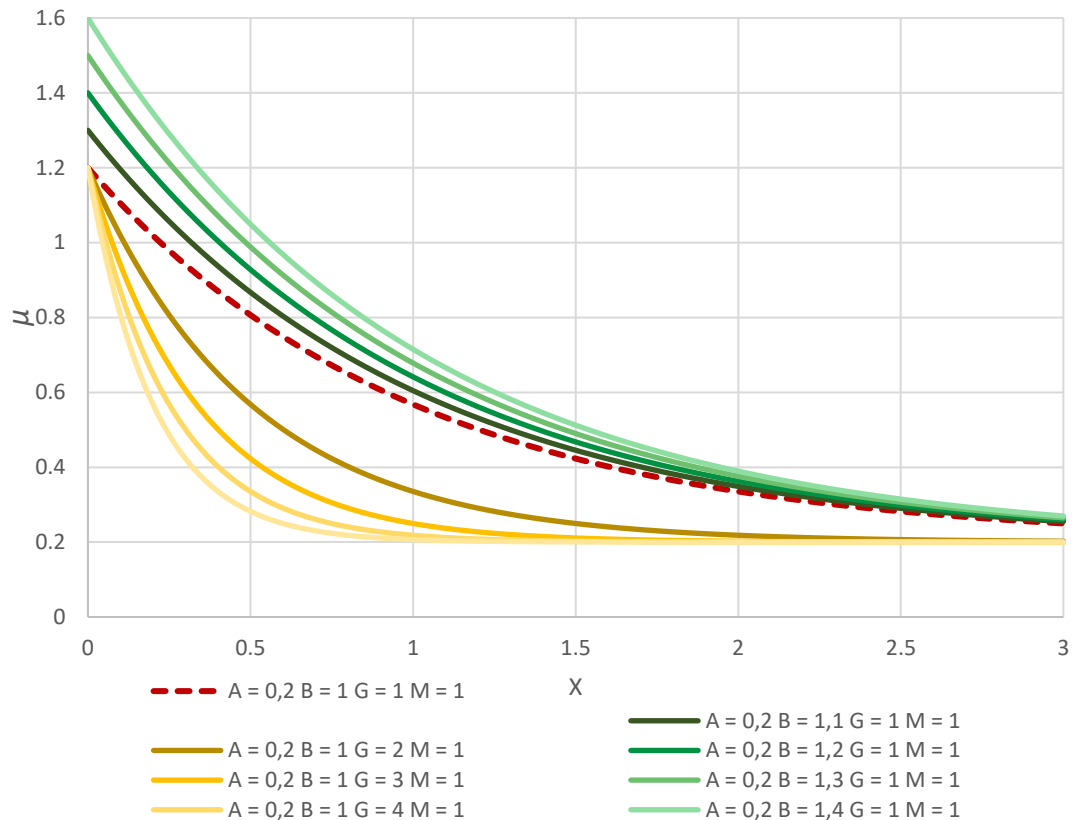
$$\mu(v, p) = A + B e^{-Gv} + C e^{-Hp} \quad (11)$$

Let's note, however, that this function assumes that friction only exponentially decays between two values, and it is not possible to represent different plateaus with smooth transition, as found in Figure 30 and Figure 53, especially for pressure dependence. So, this work proposes to consider an additional parameter to control the slope of the function, allowing the regression methodology to define the coefficients that best define the friction behavior of acquired data.

Starting with a simple example of the parameters of this equation and, considering only one exponential, as Equation (12), one can note the pattern shown in Figure 81.

$$\mu(x) = A + B e^{-Gx} \quad (12)$$

Figure 81 – Reference constitutive equation parameters influence on function response.



In Equation (12)  $A$  controls the dynamic friction coefficient (in this case, defined as 0.2),  $B$  defines the static friction coefficient, and  $G$  defines the transition slope between them. The coefficient  $M$  in this equation was kept constant and equal to unity.

### 3.5.2. Proposed Approach

To introduce an additional degree of freedom to the equation and achieve a closer approximation of the behavior illustrated in the aforementioned references (specifically, Figure 30 and Figure 53), one possible approach is to explore the characteristics of exponential functions observed in nature. Indeed, the Weibull distribution offers a flexible framework for modeling a wide range of phenomena, making it an invaluable tool for engineers seeking to analyze and understand complex systems. Its ability to capture a diverse range of shapes makes it an excellent candidate for the problem at hand and is described by Equation ((13) (Jhonson, Kotz and Balakrishnan, 1995). Its wide

application and adaptability make it a compelling choice for investigating desired properties.

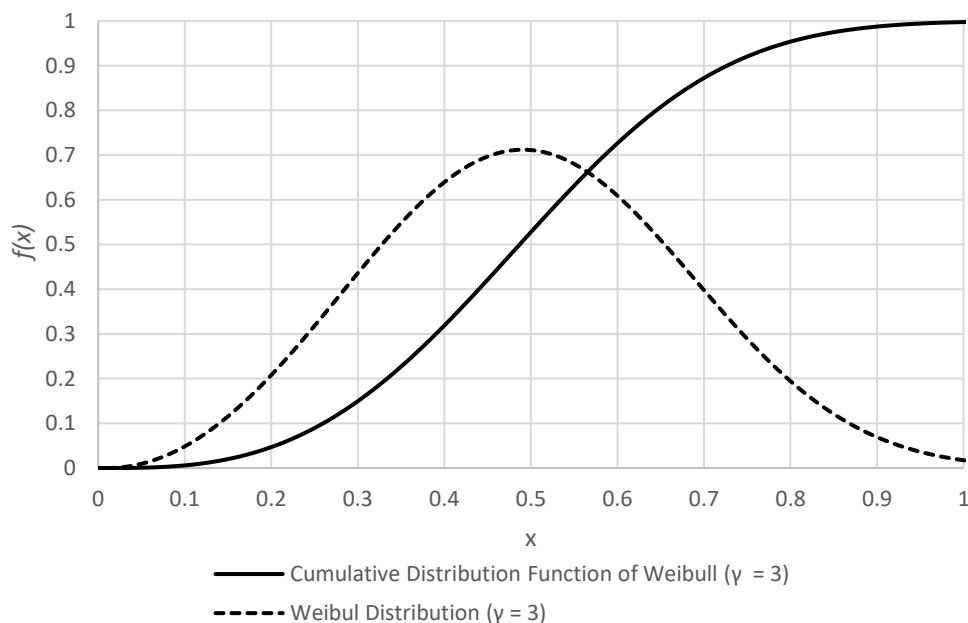
$$f(x) = \frac{\gamma}{\alpha} \left( \frac{x - \mu}{\alpha} \right)^{\gamma-1} \exp \left( -\frac{(x - \mu)^\gamma}{\alpha} \right) \quad x \geq \mu; \gamma, \alpha > 0 \quad (13)$$

When the value of  $\gamma$  equals 3, this function provides an approximation of the normal distribution, which assumes that the observed phenomena were generated by a random process. Based on this approximation, it is feasible to derive the cumulative distribution function (CDF).

$$F(x) = 1 - \exp(-x^\gamma) \quad (14)$$

Weibull distribution and its CDF are showed in Figure 82.

Figure 82 – Cumulative Density Function for  $\gamma = 3$ .



This exponent  $\gamma$  adds a gradient of friction decay with an intrinsic relation to tribological characteristics. The shape of the proposed equation can be adjusted to achieve different plateaus of the friction coefficient, which can represent different tribological mechanisms, as discussed in item 2.3.3 of this work and shown in Figure 35 and Figure 36. Interestingly, if a lubricated contact pair is tested and modeled with this approach, the different frictional plateaus seen in Stribeck curve in Figure 54 can be approximated using this

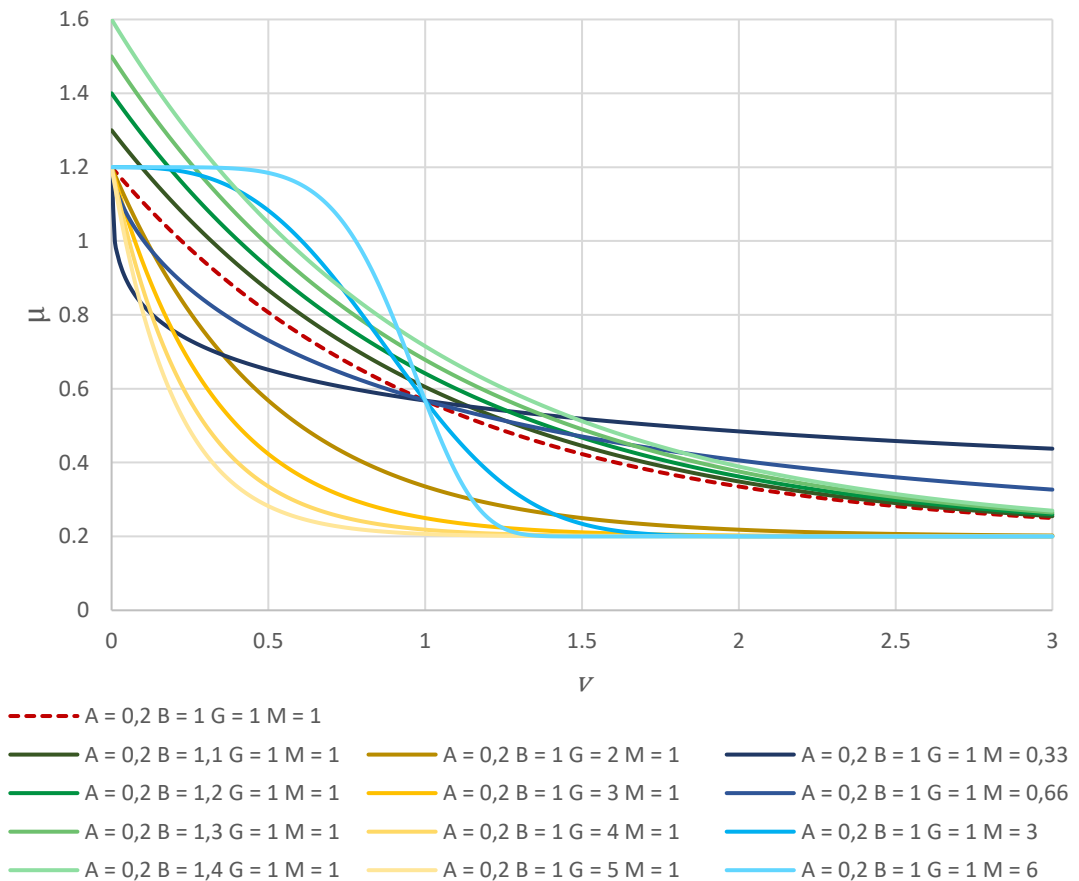
equation shape. This approach is one of the novelties of this work for literature since no similar modeling technique has been found.

The constitutive equation for friction modeling is given by Equation (15).

$$\mu(v, p) = A + B e^{-(Gv)^m} + C e^{-(Hp)^n} \quad (15)$$

It can also be considered that this proposed formulation improves the robustness of the method by adding a new shape control term to both velocity and pressure variables. The behavior of the proposed constitutive equation is shown in Figure 83.

Figure 83 – Proposed constitutive equation parameters influence on function response.



The coefficients  $A$ ,  $B$ ,  $C$ ,  $G$ ,  $H$ ,  $m$ ,  $n$  and variables  $v$  and  $p$  are, respectively:

- $A$  is the dimensionless independent coefficient that controls minimum overall  $\mu$ ;

- $B$  and  $C$  are the dimensionless linear coefficients associated with slip velocity and contact pressure, respectively. These parameters control the decay amplitude;
- $G$  and  $H$  are the exponential coefficients associated with slip velocity and contact pressure, respectively. These parameters control the decay rate. The dimensions are, respectively,  $m^{-1}s$  and  $MPa^{-1}$ ;
- $m$  and  $n$  are the dimensionless variables exponents that control the decay shape;
- $v$  is the slip velocity variable;
- $p$  is the contact pressure variable.

The parameters of this constitutive equation will be determined using a non-linear least squares regression routine in Matlab. This will involve inputting a cloud of points obtained from tests conducted with the proposed rig, under various contact pressures and slip velocities.

- `μModelEquation = 'a +b*exp(-(g*x)^m)+c*exp(-(h*y)^n)'`

This line defines the  $\mu$  model equation as a string. The equation includes variables 'x' and 'y', as well as parameters 'a', 'b', 'c', 'g', 'm', 'h', and 'n'. It represents the mathematical relationship between the `μModelEquation` (dependent variable 'z') and the independent variables 'x' and 'y'.

- `ft = fittype(μModelEquation , 'independent', {'x', 'y'}  
'dependent', 'z')`

The 'fittype' function is used to create a fitting type of object. The equation for the friction coefficient model is provided as the first argument (`μModelEquation`). The options 'independent' and 'dependent' specify the independent variables as 'x' and 'y', respectively, and the dependent variable as 'z'. The `fittype` function creates a fitting type object 'ft' that represents the model equation and the variables.

- `opts = fitoptions('Method', 'NonlinearLeastSquares');`

This line creates an options structure `opts` using the 'fitoptions' function. The option 'Method' is set to 'NonlinearLeastSquares', indicating that the fitting should be performed using the Nonlinear Least Squares method.

- `opts.StartPoint = [0.0 0.0 0.0 0.0 0.0 0.0 0.0]`

This line initializes the starting values for the fitting parameters. The values are specified as a numeric array [a b c g m h n]. These values represent the initial estimates for the parameters to begin the fitting process.

- `opts.Lower= [0 0.01 -10 0.05 0.05 0.05 1]` and  
`opts.Upper= [5 10 10 10 1 5 2]`

These lines define the lower and upper bounds for the fitting parameters. The arrays [a b c g m h n] are used to specify the lower and upper limits for each respective parameter, which were obtained through experimental exploration. This bounding has proven to be very important in adding constraints to the model and avoiding unrealistic values during the transition from static to dynamic. It also helps prevent sudden discontinuities that could result in numerical issues during simulation.

One of the limitations of this approach is that despite it provides a slip velocity dependence, there is no distinction of path-dependent behavior as pointed by Lai *et al.* (2012) in Figure 44 and Oden and Martins (1984) in Figure 45. This is because current commercial software inputs does not allow friction dependence of such variable, and its implementation would require complex subroutines usage drastically increasing the processing cost of the model.

## 4. RESULTS

### 4.1. CRASH TEST SENSITIVITY ANALYSIS

The crash test results for the 2010 Toyota Yaris impact simulation conducted on this work will be described in this section, which will be divided into:

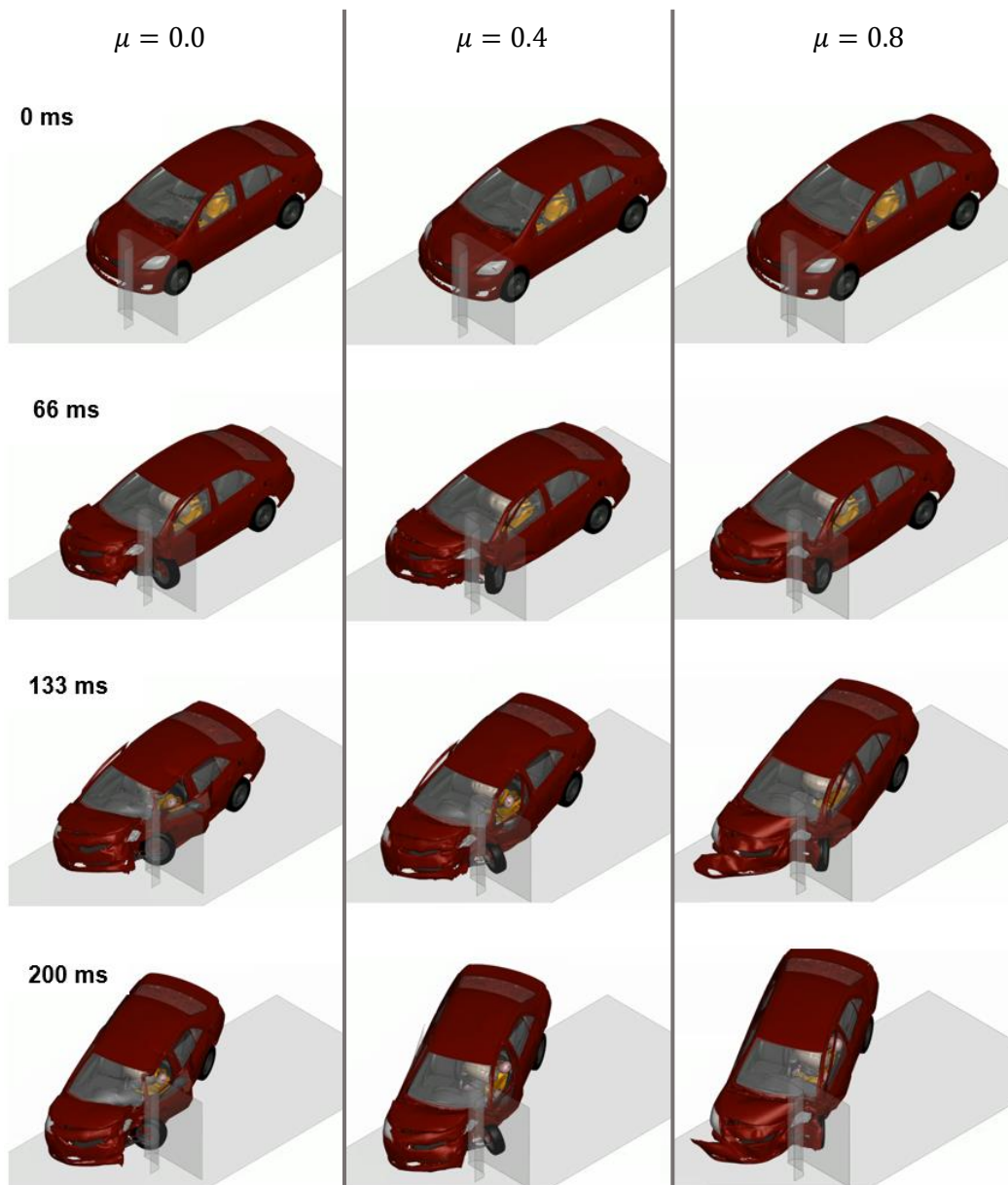
- Overall results, where the vehicle's behavior will be analyzed in a general sense, detailing major deformation patterns, interaction with barrier, and center of gravity acceleration;
- Structural results, where the behavior of the structure, forces, and energy absorption will be examined;
- Biomechanical analysis, where the interaction between the dummy and the vehicle's interior as well as the dummy's sensor analysis will be detailed.

The models with different friction coefficients will be compared, and their differences due to friction variation will be explained.

#### 4.1.1. Overall Analysis

It was found significant difference in overall behavior of the vehicle when the friction coefficient was changed. Figure 84 shows a comparative result of vehicle behavior during the impact with the small offset barrier for the three friction coefficient scenarios for all contacting surfaces.

Figure 84 – Influence of friction on the overall behavior of a crash test. Friction of  $\mu=0.0$ ,  $\mu=0.4$  and  $\mu=0.8$  – Full vehicle deformations.



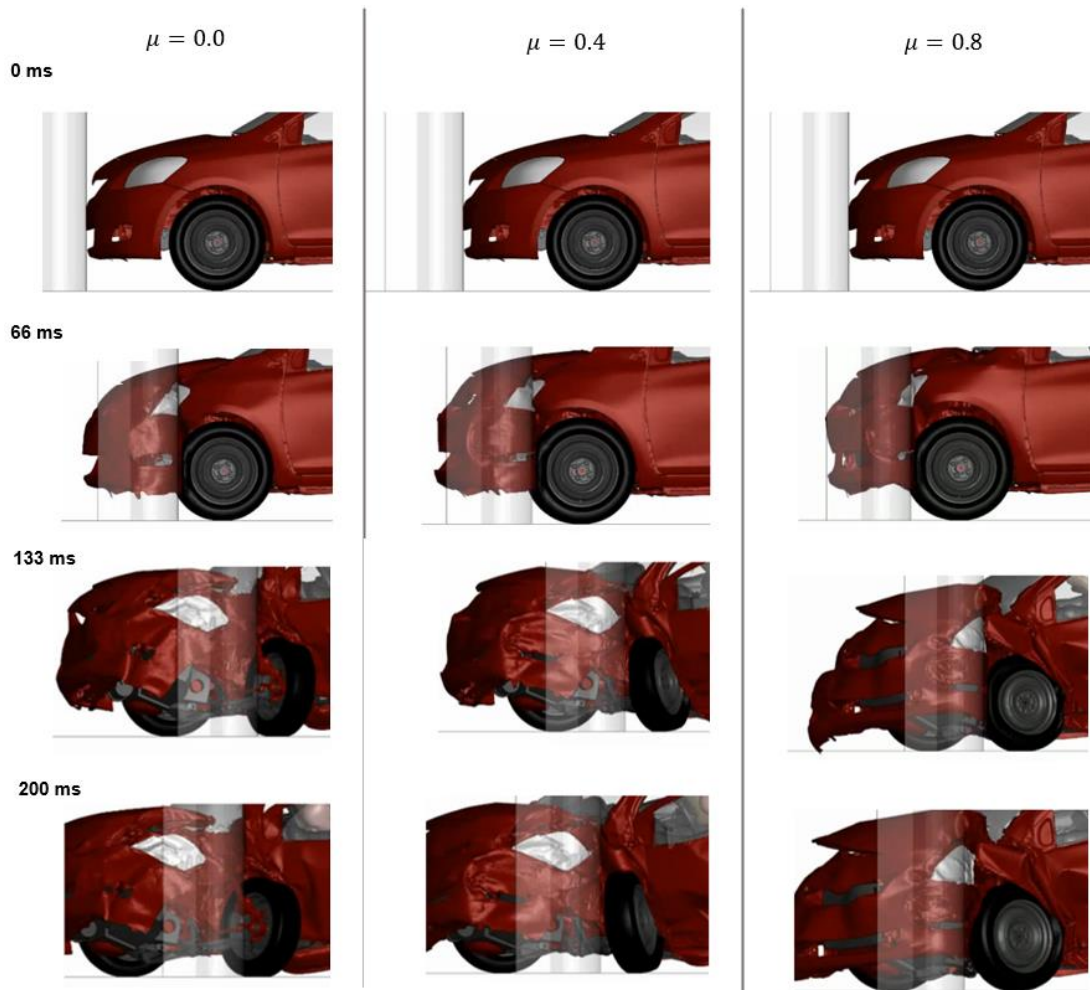
In the  $\mu=0.0$  simulation, the vehicle slid through the barrier, while in the  $\mu=0.4$  and  $\mu=0.8$  simulations it exhibited better stability. This played an important role in the load path. In the  $\mu=0.0$  model, a significant amount of impact force has been transmitted to the A-pillar, while in the  $\mu=0.8$  model this value was shown to be lower, given the smaller deformations of this component along the test.

Another significant difference was the interaction between the wheel and the barrier, which had numerous implications for structural and biomechanical analysis. Figure 85 shows the frontal and lateral views of the impact region, illustrating the rapid rotation of the wheel between instants 66 ms and 133 ms



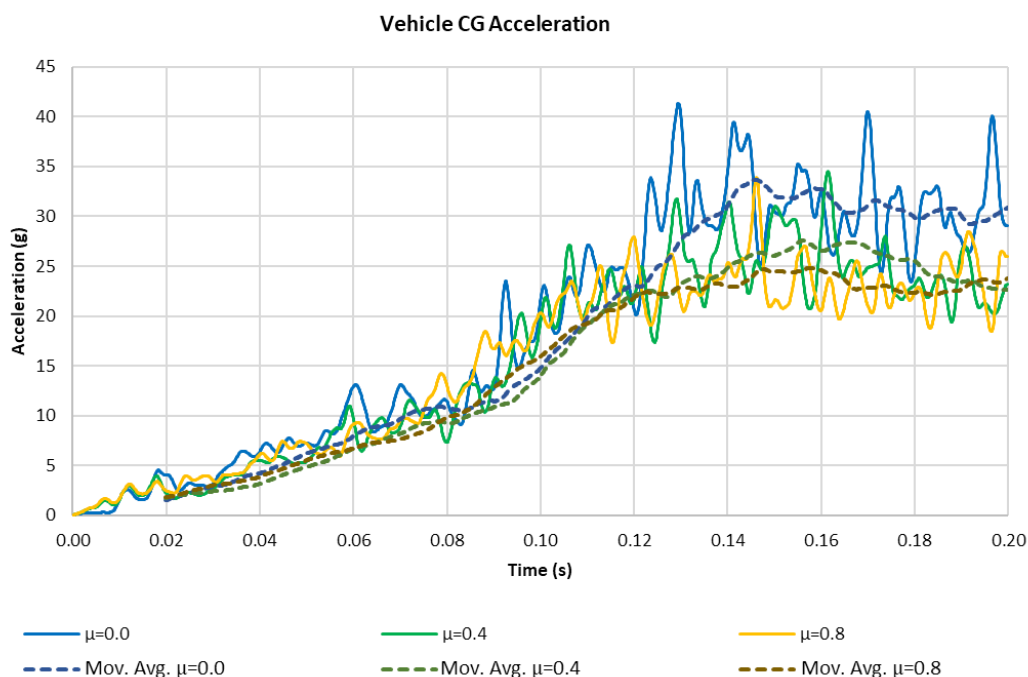
for the  $\mu=0.0$  case. Interestingly, the wheel rotation on case  $\mu=0.4$  took longer to overpass  $90^\circ$  with its original position, and on  $\mu=0.8$  wheel remained almost unrotated. The stability of the wheel justifies the minor deformation on the A-Pillar, as it allowed a stable transmission of the impact load to the right Rockwell column.

Figure 85 – Front left wheel behavior for friction coefficients of  $\mu=0.0$ ,  $\mu =0.4$  and  $\mu=0.8$  – side view.



Further, the differences caused by friction on structural elements also lead to different accelerations on the vehicle CG. Low friction coefficients implied in higher peak accelerations, as shown in Figure 86.

Figure 86 – Center of gravity resultant acceleration.

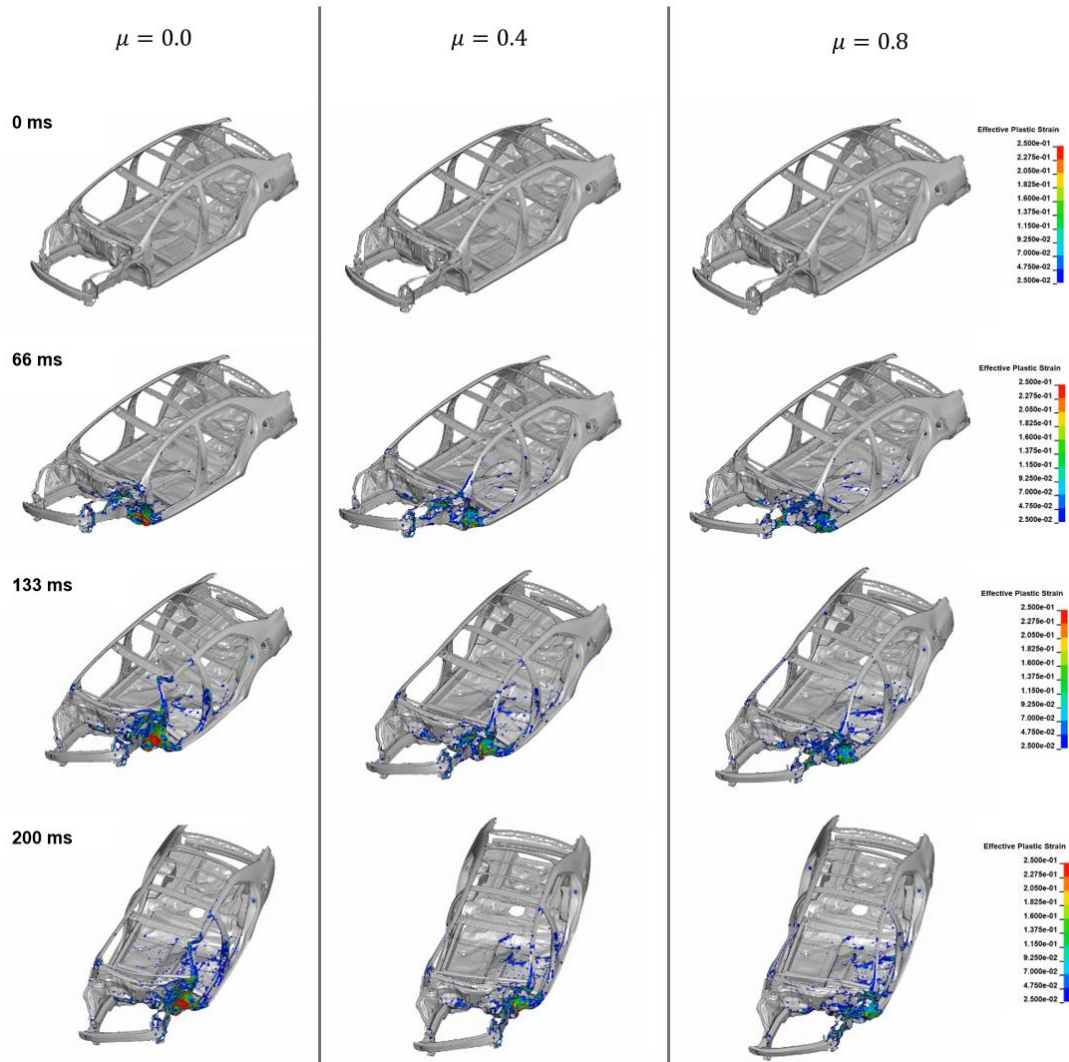


The acceleration of the center of gravity is an important metric for understanding the overall behavior of a vehicle, as this acceleration will be transferred to the occupants during an impact. Thus, manufacturers try to minimize these acceleration peaks as a measure to improve vehicle safety. From Figure 86 one can notice a reduction of 26% in maximum filtered acceleration from  $\mu=0.0$  to  $\mu=0.8$  cases.

#### 4.1.2. Structural Analysis

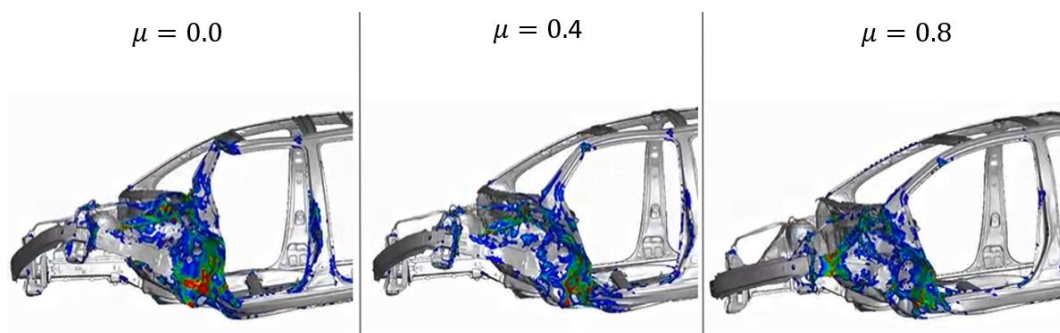
From the overall results, it is noticeable that the variation in the friction coefficient led to significantly different outcomes. One effective method for understanding the influence of friction on the crash from a structural point of view is to examine the plastic deformation patterns of the body in white. Additionally, it is important to examine the cross-sectional forces acting on three of the most important structural components in this crash scenario: the front rail, A-pillar, and Rockwell column.

Figure 87 – Influence of friction on the structural behavior of Toyota Yaris 2010. Friction coefficients of  $\mu=0.0$ ,  $\mu=0.4$  and  $\mu=0.8$  – BIW Plastic strain.



In Figure 87, it can be observed that in the case where  $\mu=0.0$ , there was a higher plastic strain near the wheel housing and firewall plate. This is intrinsically related to low energy absorption efficiency on the front rails, which has led to severe consequences for the A-pillar and Rockwell bar. It is also evident that the A-pillar of the low coefficient model has bent and experienced severe intrusions into the vehicle's passenger cabin. In contrast, the higher friction coefficients have enhanced energy absorption on the front rails and exhibited minimal bending on the A-pillar, particularly in the case of  $\mu=0.8$ .

Figure 88- Influence of friction on the structural behavior of Toyota Yaris 2010.  
Friction coefficients of  $\mu=0.0$ ,  $\mu=0.4$  and  $\mu=0.8$  – BIW Plastic strain.



This behavior is explained by the normal forces of the front rail force cross section during the crash. Figure 89 shows that a higher friction coefficient exhibited a different buckling behavior compared to other cases. It maintained a higher compressive force until 0.10 s, resulting in a significantly greater amount of energy absorbed, as shown in Figure 90.

Figure 89 – Left front rail normal forces for different overall friction coefficients.

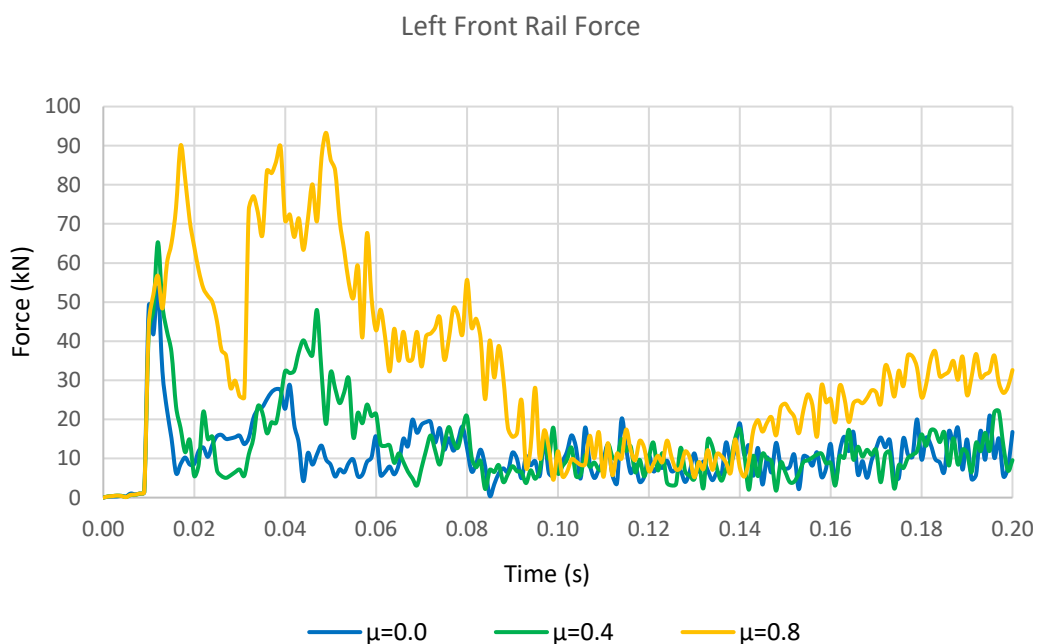
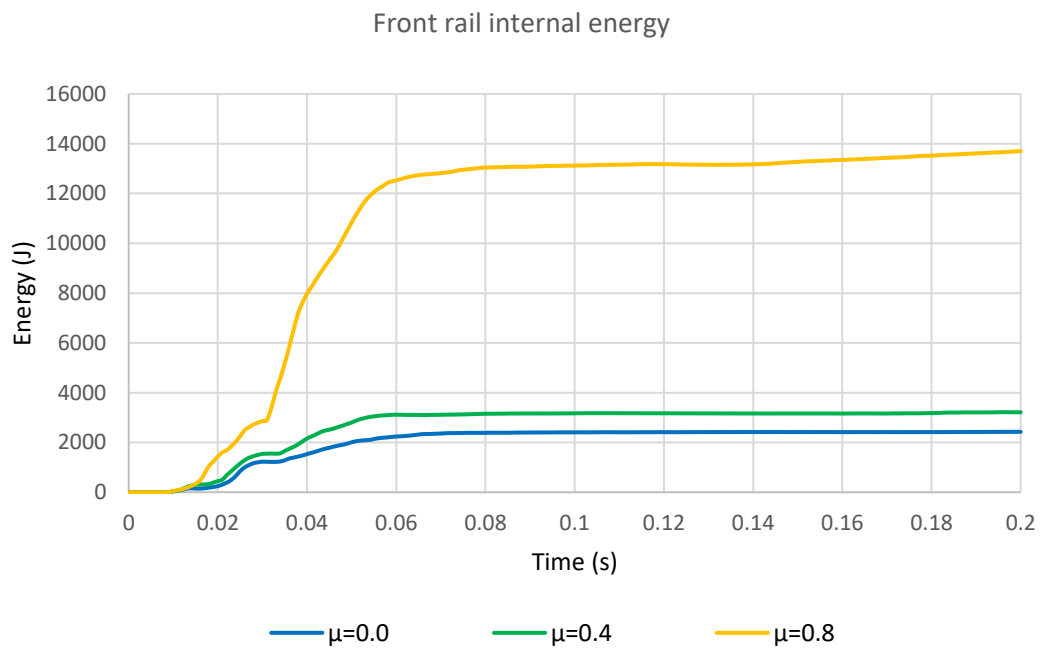


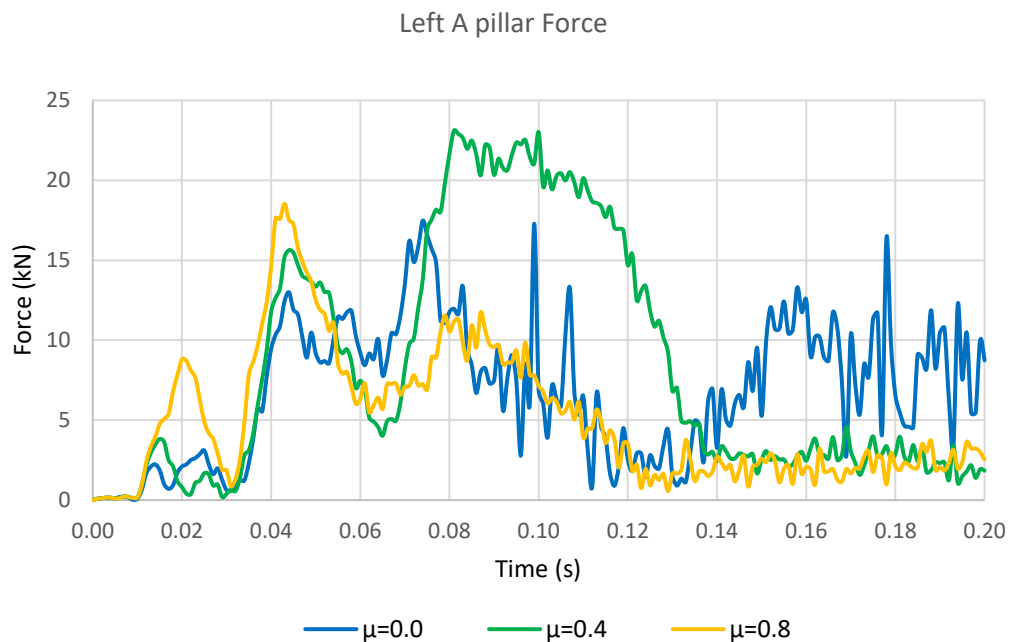
Figure 90 – Left front rail energy for different overall friction coefficients.



It was found an impressive increase of more than 560% in energy absorbed by  $\mu=0.8$  model than  $\mu=0.0$  case. This is associated with a greater axial force transmission through the front rail and to the more stable buckling phenomena detailed in Figure 6.

The greater engagement of the front rail during the crash was very important to the proper transmission of the impact loads to the rest of the structure during the test. This can be seen, for instance, by analyzing the cross-sectional forces of the A-pillar in Figure 91.

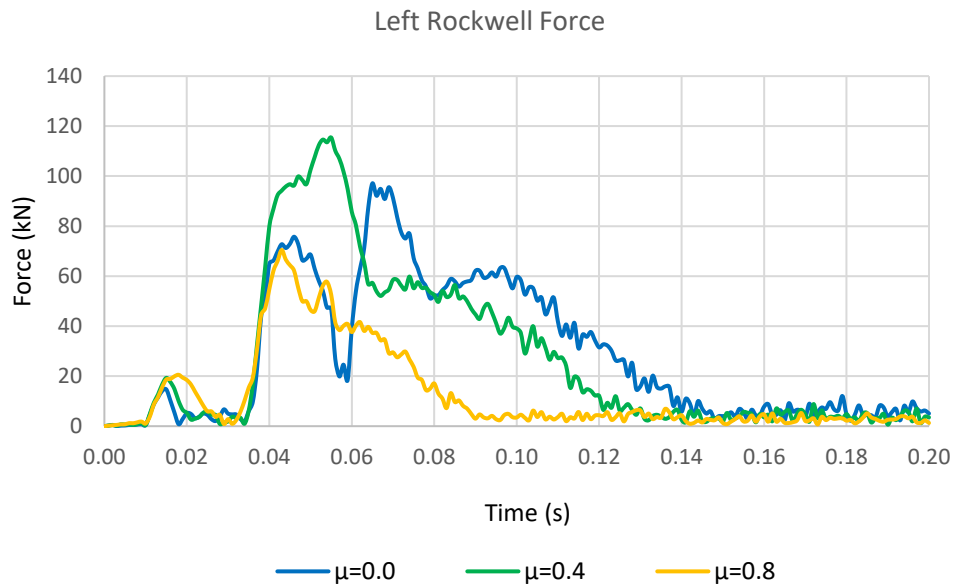
Figure 91 – Left A-pillar normal forces for different overall friction coefficients.



It is noticeable that friction coefficients led to higher initial force peaks at 0.04 s, but smaller friction cases showed a sudden increase at 0.07 s.  $\mu=0.0$ , this value continues to increase until 17 kN, at which point bending occurs and the transmitted axial force drops significantly. For  $\mu=0.4$  this value exceeds 20 kN, as the bending is significantly smaller. For  $\mu=0.8$  no peak was found after 0.07 s since impact energy has been absorbed by front rails.

A similar behavior is also found at the left Rockwell bar. Figure 83 shows that for  $\mu=0.8$ , there was a minimum overall peak force associated with better energy absorption of the front rails. For  $\mu=0.4$  case, it was found that there was a maximum force associated with poor energy absorption of the structure at the Rockwell bar. For the case of Friction case  $\mu=0.0$  an oscillating behavior is still present due to the bending of the Rockwell bar (as seen in Figure 88). This behavior is associated with more significant intrusions into the cockpit.

Figure 92 – Left Rockwell normal forces for different overall friction coefficients.

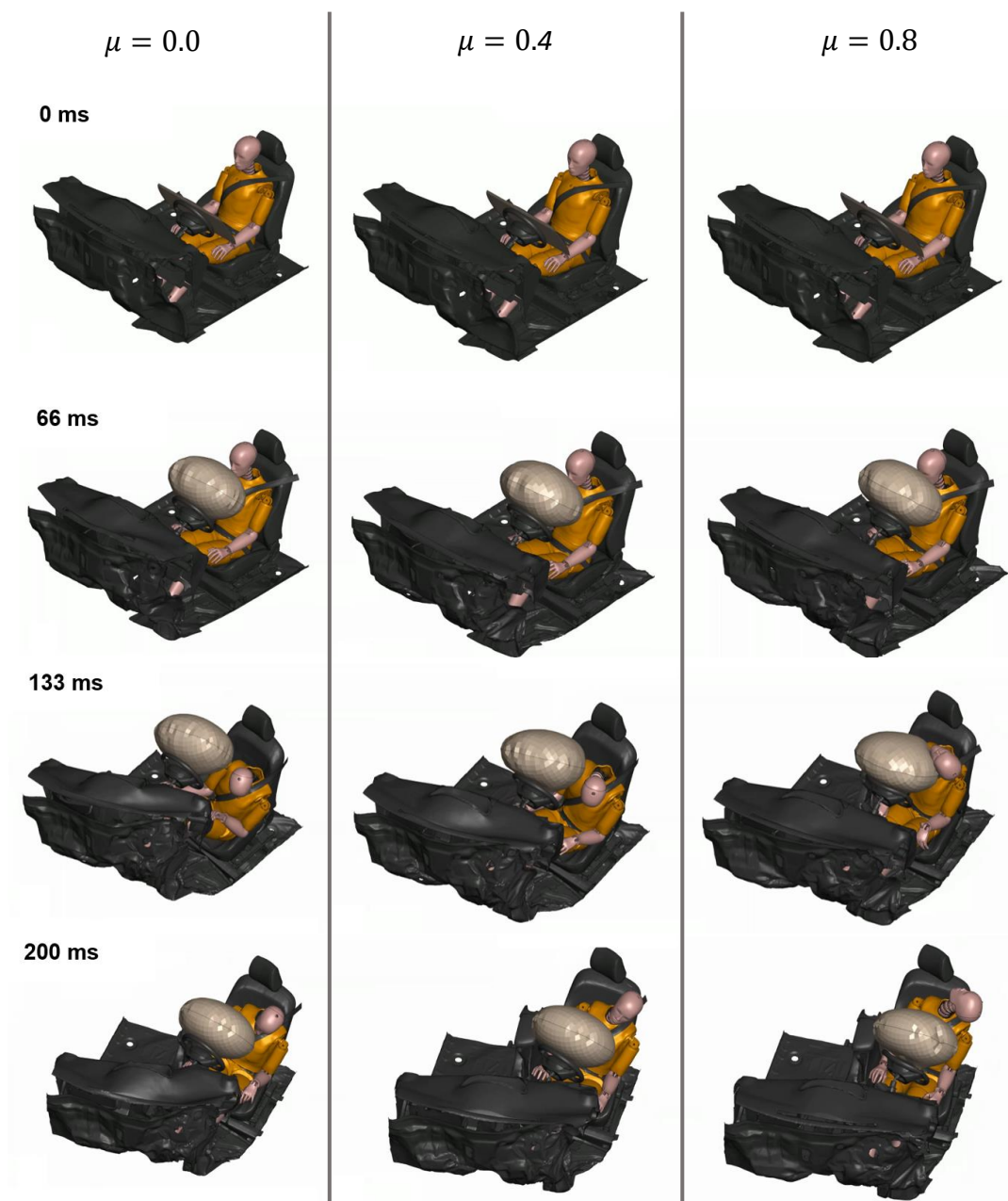


The previous findings show that the friction coefficients have a significant influence on the overall vehicle deceleration, front rail, A-pillar, and Rockwell bar normal forces, stability, and energy absorption efficiency. These findings are highly relevant to the performance of vehicles in small overlap crash tests, as they directly influence the integrity of the passenger cabin and the safety of both the driver and passengers during a crash.

#### 4.1.3. Biomechanical Analysis

All of the aforementioned behaviors will directly impact the safety of the driver and passengers. This safety can be quantified according to biomechanical parameters such as head peak acceleration, Head Injury Criteria (HIC), chest peak acceleration, Chest Severity Index (CSI), normal forces on the left femur and tibia, and neck forces and moments. The detailed meanings of these parameters can be found in Appendix A). This section will detail the results of the current simulation for the interaction between the dummy and airbag and the dummy and vehicle interior, as illustrated in Figure 93.

Figure 93 – Influence of friction on dummy-airbag and vehicle interior interaction.  
Friction coefficients of  $\mu=0.0$ ,  $\mu=0.4$  and  $\mu=0.8$ .

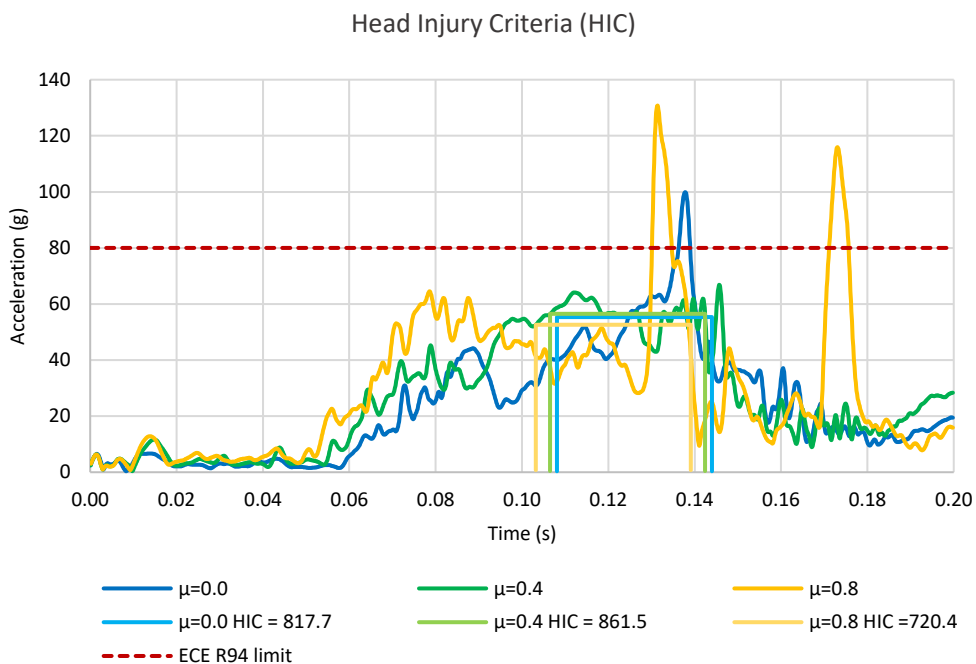


Following the structural response to friction in these scenarios, it was shown that friction has a strong influence on the contact between the dummy and the airbag, as well as other components such as the seatbelt. Figure 93 shows that for the case when  $\mu=0.0$ , the dummy has completely slid through the airbag, indicating a complete inefficiency of this component at such low friction levels. This was followed by contact with a hard part of the vehicle's door,



which caused an acceleration peak greater than allowed by the ECE R94 standard, as shown in Figure 94.

Figure 94 – Head Injury Criteria (HIC) for different overall friction coefficients.

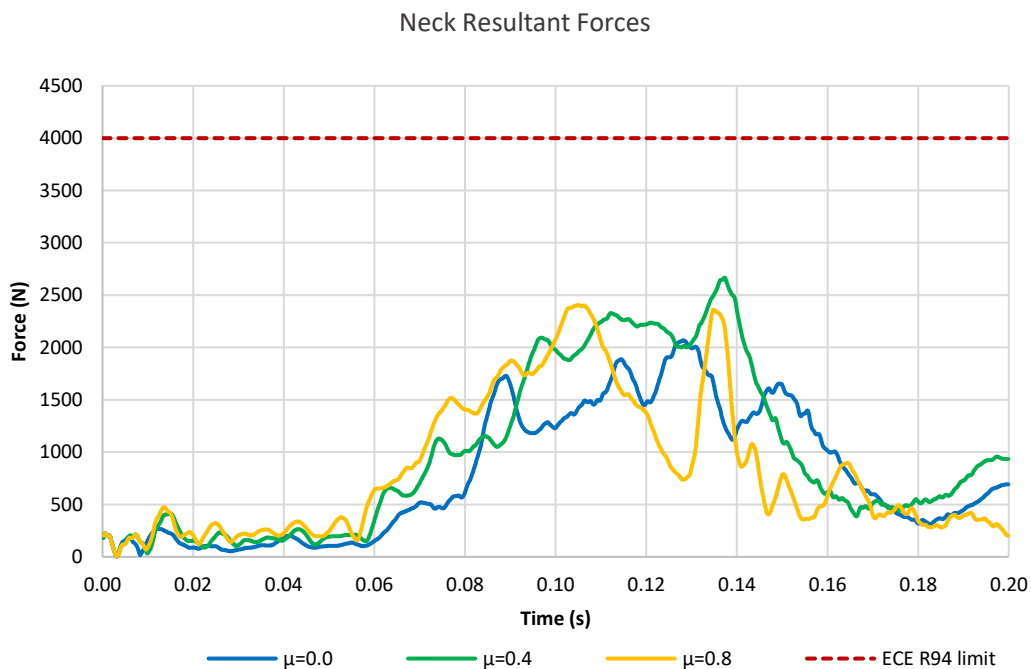


Although all HIC (Head Injury Criterion) values were below the standard requirement of 1000, a friction coefficient of  $\mu=0.8$  resulted in a severe rebound and a significantly high acceleration peak when the head contacted the airbag without sliding. This was followed by another forceful impact with the door B-pillar. On the other hand, in the case of a friction coefficient of  $\mu=0.4$ , where the head slid over the airbag, the best result was obtained due to the absence of hard impacts and peak accelerations. This sliding behavior is not uncommon in small overlap crash tests, and many vehicles, especially those without curtain airbags, may show inadequate performance due to the uneven distribution of loads during impact and diagonal movement of the dummy.

Furthermore, even if a friction coefficient of 0.8 did not cause a hard contact, this does not necessarily indicate that higher friction coefficients in airbags could improve vehicle safety. High friction coefficients could potentially cause burn injuries and wounds due to increased shearing forces on the driver's skin,

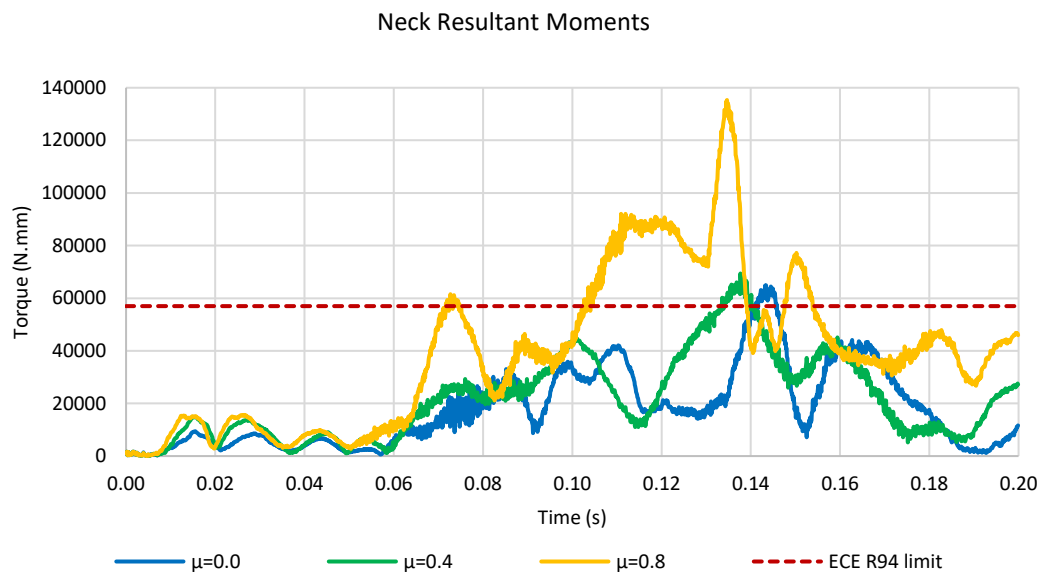
as well as greater moments on the dummy's neck. Accordingly, forces and moments are shown in Figure 95 and Figure 96.

Figure 95 – Neck resultant forces for different overall friction coefficients.



In the present study, neck resultant forces are within the limits set by ECE R94 for all cases and no significant difference is observed in this result. However, the measurement of moments shows a completely different scenario, as shown in Figure 96.

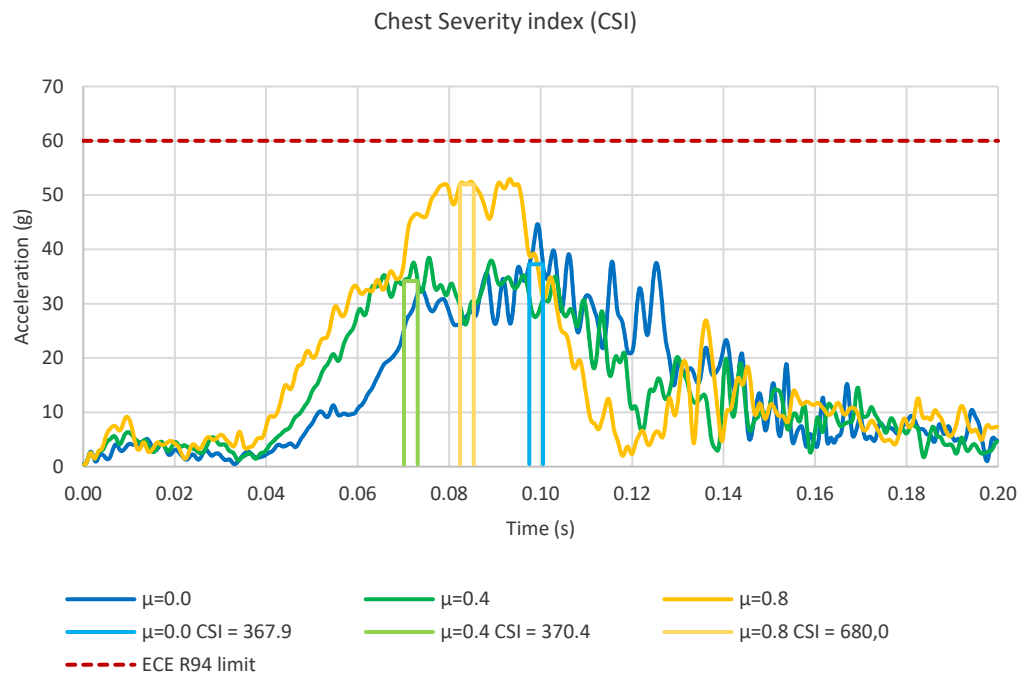
Figure 96 – Neck resultant moment for different overall friction coefficients.



While the friction coefficient of 0.0 implied on dummy's head sliding over the airbag and the lowest moment (even with the hard contact with the door panel), the  $\mu=0.4$  simulation had a slightly higher moment due to the partial sliding, and the  $\mu=0.8$  case had a very severe moment due to the low sliding condition with the airbag. This last condition is visible in Figure 84, where the head sticks to the airbag and undergoes severe rotation during the test. Although all conditions exceed the allowable limit according to ECE R94, while  $\mu=0.0$  and  $\mu=0.4$  would probably cause spinal damage, the  $\mu=0.8$  case could potentially be fatal for the driver due to the high torsional moment on the neck.

Another analysis is the chest acceleration and Chest Severity Index, whose data is shown in Figure 97.

Figure 97 – Chest Severity Index (CSI) for different overall friction coefficients.



This metric measures the amount of acceleration and deflection applied to the thoracic region, and high values could indicate damage to the ribs and internal organs. The test measures the interaction between the seatbelt and the dummy. It is noticeable that a higher friction coefficient led to a higher CSI, which exceeded the ECE R94 limit of 600. This result is particularly interesting since the 0.8 model had the lowest vehicle CG acceleration, as shown in Figure 86. This evidence led to the conclusion that the gripping behaviors between the seatbelt and the dummy's chest may not be beneficial, as seatbelt sliding could alleviate high pressures and chest deflections during a crash.

The next indicator to be analyzed is the dummy left femur. Figure 98 shows normal forces on this region for the three simulations.

Figure 98 – Left femur normal force for different overall friction coefficients.

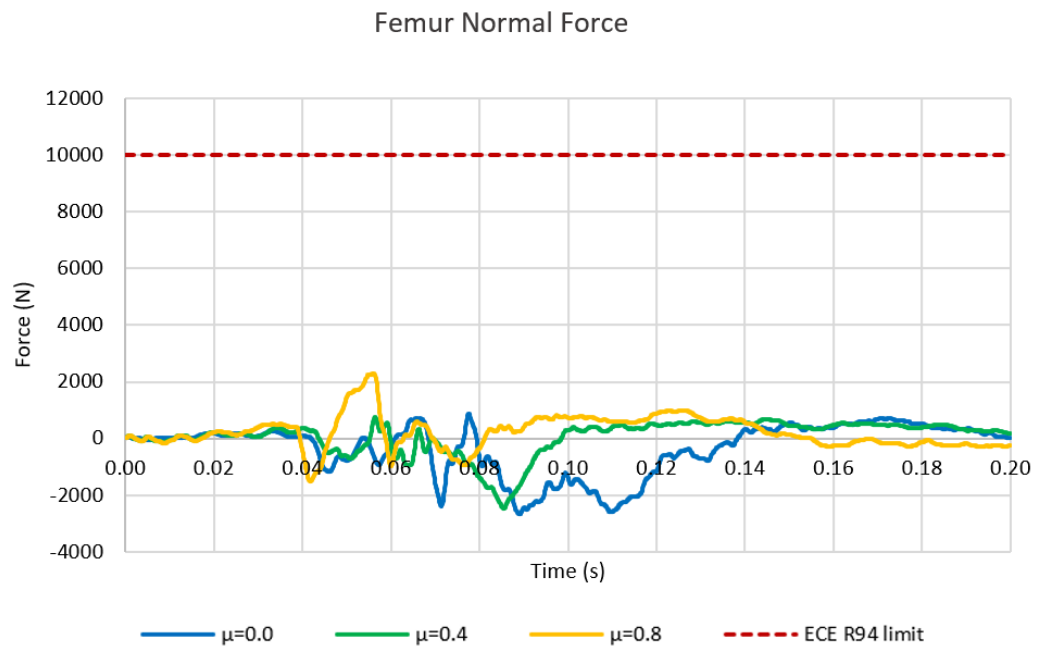
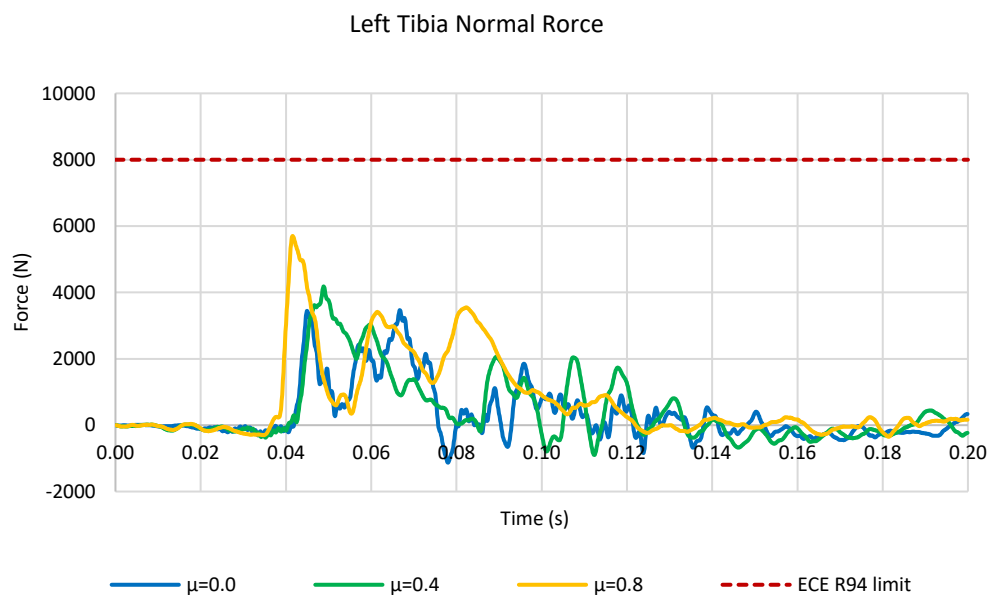


Figure 99 shows the normal forces on the left tibia, where a higher force is visible at  $\mu=0.8$  compared to the low friction cases. This result is associated with the higher force transmitted from the front rail to the vehicle structure, as the structural connection of these components is located very close to the footrest region.

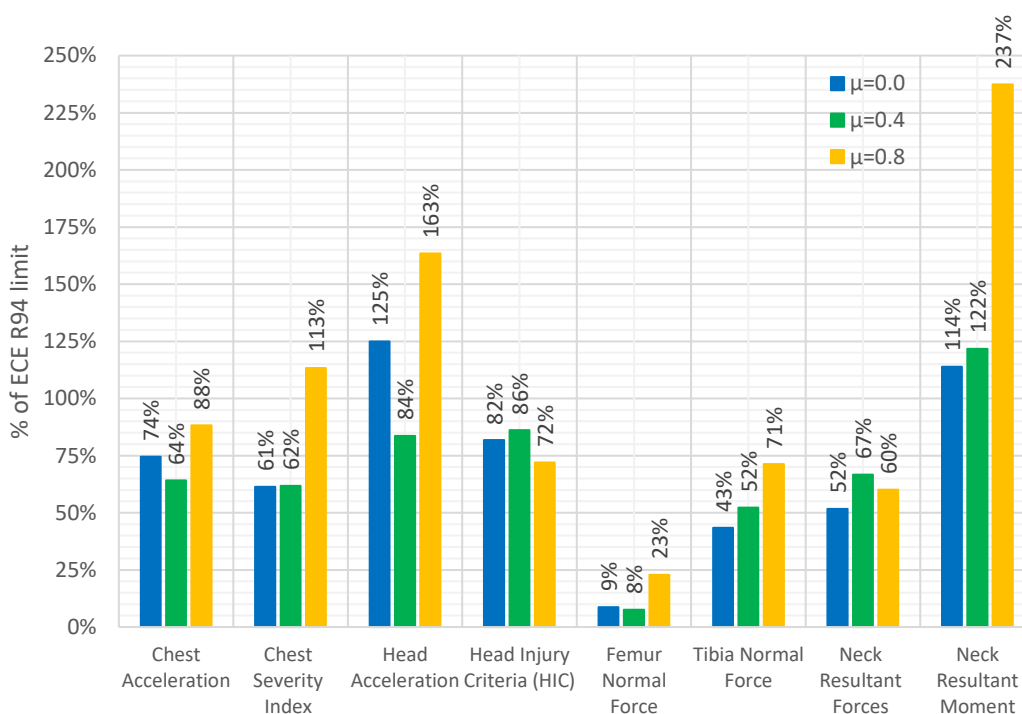
Figure 99 – Left tibia normal forces for different overall friction coefficients.



Despite the fact that a higher friction coefficient was found to be beneficial for energy absorption on the front rail, it is expected that higher forces on this component would result in greater displacements along the load path within the vehicle structure. Thus, it would be a clever decision to relocate the structural pathways away from regions where deformations could pose a risk to occupants.

Finally, all biomechanical data is compiled in Figure 100, where the values are shown in comparison to ECE R94.

Figure 100 – Overall biomechanical parameters expressed as a percentage of the ECE R94 standard for different friction coefficients.



This section demonstrated that while there is no clear trend between friction and vehicle safety, it is evident that it has a significant impact on the results. Further, some behaviors are noteworthy in this regard. First, the contact of the dummy head with the airbag showed a significant difference in behavior across the simulated scenarios, particularly for the friction coefficient levels of 0.8.

When the friction coefficient was 0.0, the airbag proved to be ineffective as the head slid directly over it, causing a whiplash effect on the dummy's neck and impacting a hard part of the vehicle. Conversely, with a friction coefficient of

0.8, the head was fully restrained in the center of the airbag, leading to higher acceleration and severe neck rotation. Notably, the simulation with an overall friction coefficient of 0.4 produced more favorable results compared to other tests, as illustrated in Figure 100.

The data demonstrated a high degree of non-linearity across different friction levels.

If any design considerations are intended to be made regarding changes in friction coefficients (such as finding the optimum friction coefficient for airbag and dummy skin), each phenomenon must be studied at both the component and system levels due to their interdependence.

This simulation is a good example of the complexity of crash test simulations and the importance of accurate friction models for both the structural and occupant restraint systems. Friction can cause different mechanical responses in different areas of the vehicle. It was also found that these triggers, such as tire rotation over the vertical axis, change the overall deceleration of the vehicle, which in turn influences occupant behavior during a crash.

#### **4.1.4. Contact pressure and slip velocity evaluation.**

It is important to note that the pressures between two contacting surfaces are not constant during the crash development, as well as the velocity between the contact pairs. Due to this reason, pressures have been obtained on different parts of the vehicle finite element model as a guide for rig development. The friction coefficient scenario of 0.4 was considered. Additionally, interest contact pairs have been considered for the analysis of relative slip velocity levels. Results are shown in Table 8 and Table 9.

Table 8 – Pressure levels during a crash test for different contacting parts

Pressure (MPa)	Steel – Aluminium	Dummy skin – Airbag (head)	Seatbelt – Dummy Shirt	Dummy Shirt – Leather	Dummy Shirt - Airbag
<b>Max</b>	405.09	3.48	15.31	12.25	2.59
<b>Mean</b>	106.64	0.34	6.76	3.54	0.26
<b>Std</b>	68.09	0.80	4.88	2.49	0.51
<b>Min</b>	0.02	0.00	0.00	0.00	0.00

In this analysis, the majority of contact pairs showed pressure averages below 10 MPa. This pressure is strongly influenced by material properties, as softer materials tend to have lower pressures while harder materials, such as aluminum bumper and front longitudinal rails, experience higher pressures.

Table 9 – Slip velocity levels during a crash test for different contacting parts

Slip velocity (m/s)	Steel – Aluminium	Dummy skin – Airbag (head)	Seatbelt – Dummy Shirt	Dummy Shirt – Leather	Dummy Shirt - Airbag
<b>Max</b>	2.55	40.87	5.12	5.55	0.55
<b>Mean</b>	1.12	18.98	0.92	2.52	0.19
<b>Std</b>	0.89	10.05	1.61	1.21	0.14
<b>Min</b>	0.00	4.35	0.00	0.26	0.04

As noted, all slip velocity averages are less than 5 m/s, except for the dummy head against the airbag. In this case, the high velocity was reached due to the whiplash effect on the dummy's neck and significant sliding over the airbag. This behavior indicates a low effectiveness of the airbag on this model. The airbag should effectively restrain the head during impact, keeping slip velocities similar to the contact with the dummy shirt. Due to this reason, the slip velocities considered in airbag-dummy skin friction tests will be assumed to be the same as those in airbag-dummy shirt tests.

#### 4.2. FRICTION MODELS

After completing all the tests, friction models were generated using nonlinear regression in Matlab. One important finding is the potential variation in pressure during the test due to surface changes, such as wear, debris formation, or fabric wrinkling. Initially, an initial pressure was applied to the



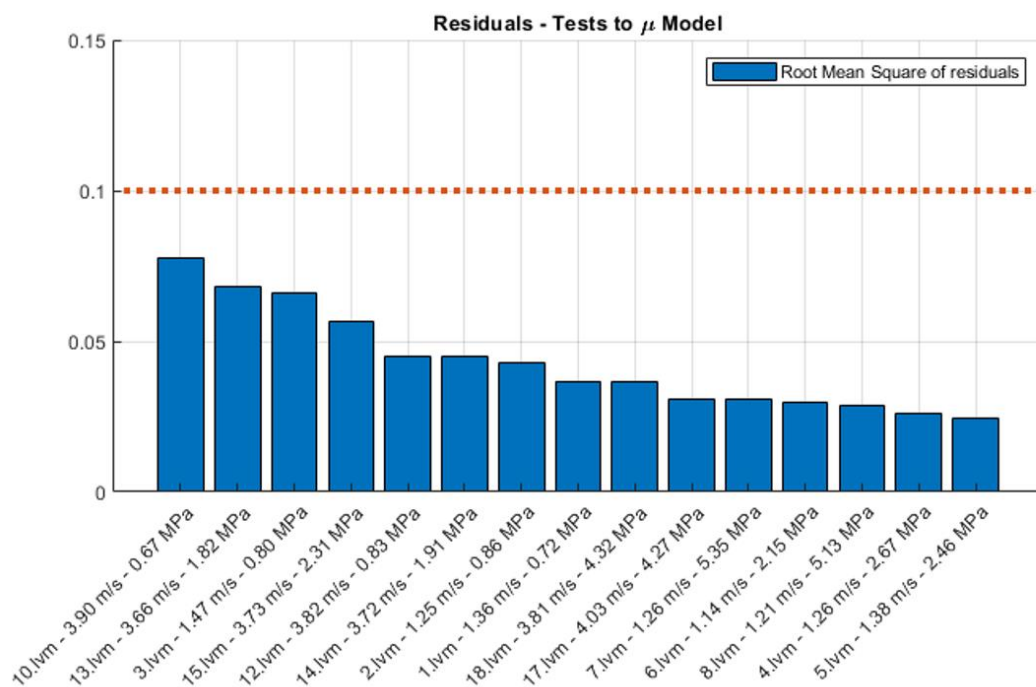
threaded joint, but as the test progresses, the pressure can vary due to these surface variations.

To ensure the repeatability and correlation of the test data with the numerical model, and to avoid unreliable test results, an approval criterion was established for the model. The criterion involved ranking the root mean square (RMS) residuals for each test and rejecting those that exceeded the empirically observed limit of 0.1. This approach aimed to evaluate the fit between the experimental data and the model.

Figure 101 illustrates the ranking of residuals for the Dummy Shirt – Dummy Skin tests. This ranking permits a visual assessment of the agreement between the experimental data and the model predictions.

By implementing this approval criterion, the reliability and accuracy of the friction model were enhanced, ensuring that only high-quality and representative data were used. This approach enhances the overall robustness of the model and reinforces the correlation between experimental and numerical results.

Figure 101 – Ranking of residuals for Dummy shirt – Dummy Skin contact pair.



The residuals from all contact pairs can be found in Appendix C.

The friction models coefficients according to Equation (15) are shown in Table 10

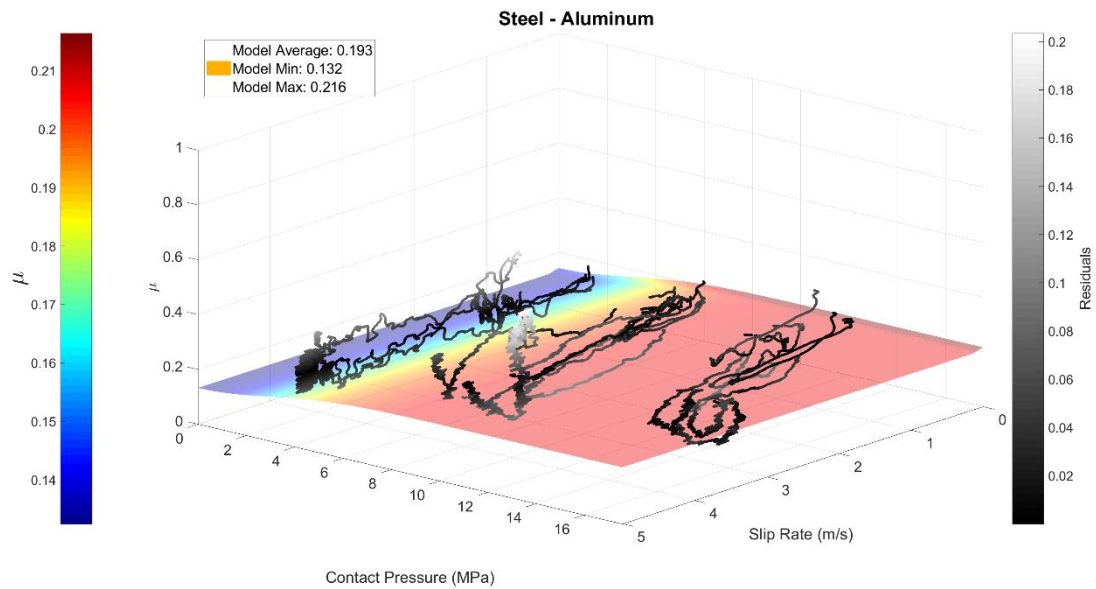
Table 10 – Constitutive equation coefficients for all contact pairs.

Contact Pair	A	B	C	G	H	M	N	R <sup>2</sup>
Steel – Aluminium	0.203	0.010	-0.074	10.000	0.240	2.509	2.000	0.182
Dummy skin – Airbag	0.000	0.596	0.358	0.477	0.905	0.326	1.000	0.588
Airbag – Dummy shirt	0.123	0.141	0.041	5.540	0.339	0.908	2.000	0.259
Dummy shirt – Leather	0.089	0.288	0.280	10.000	0.299	0.598	1.000	0.483
Seatbelt – Dummy shirt	0.158	0.091	0.089	10.000	1.000	1.000	2.000	0.190
Dummy skin – Dummy shirt	0.187	0.446	0.484	5.590	0.667	1.000	1.250	0.776

#### 4.2.1. Steel – Aluminum

During the Steel – Aluminum test, an intriguing trend was observed regarding the friction coefficients at different pressure levels. The results showed relatively low friction coefficients at low pressures and slightly higher coefficients at high pressures. From coefficients, one can notice a friction amplitude variation due to slip velocity (coefficient *B*) of 0.010 and an amplitude variation due to pressure of -0.074 (coefficient *C*). The coefficient *H* of 0.240 shows a smooth pressure dependence decay rate, with a well-defined two plateaus format given by coefficient *N* of 2.000. This trend supports the concept that at low pressures, friction is primarily influenced by the surface oxide layers of the materials. However, as the pressure increases, the metallic asperities come into contact with the raw material, resulting in slightly higher friction coefficients. Figure 102 shows the friction model for Steel – Aluminum contact pair, where the surface is the friction model by regression of data, shown in gray scale according to its residuals.

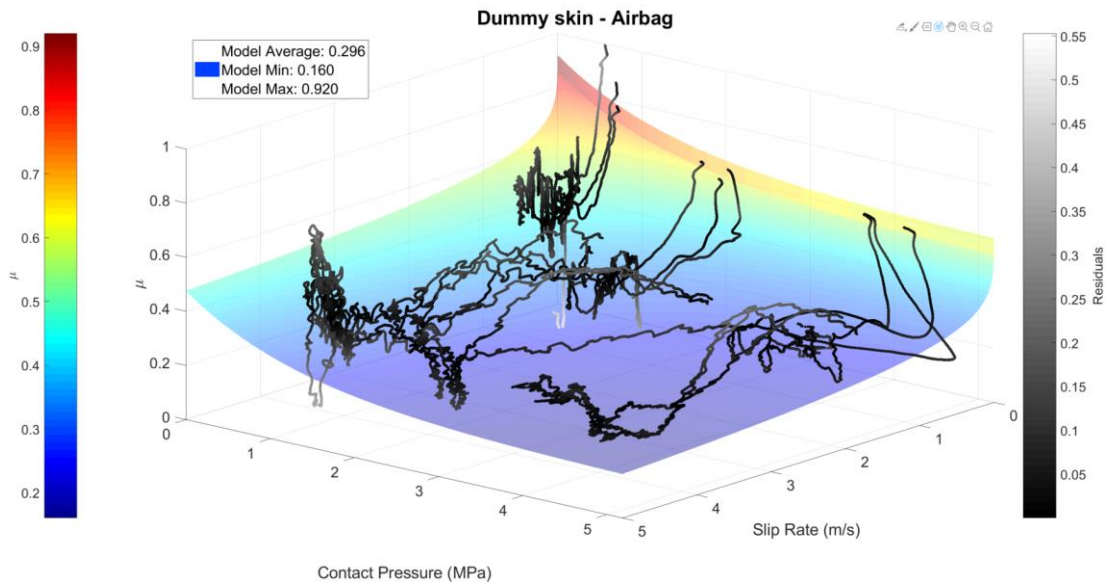
Figure 102 – Steel – Aluminum friction model.



#### 4.2.2. Dummy skin – Airbag

According to the crash test simulations performed in the early stages of this work, Dummy Skin – Airbag is one of the most important contact pairs from the crashworthiness frictional influence standpoint. It governs the stability of the dummy during contact with the airbag, driving the efficiency of this passive safety system. The composition of the Dummy Skin, which is made of vinyl plastisol, introduces potential variability in its tribological properties due to the manufacturing process and selected parameters of its constituents. Its composition has a rubber-like aspect and high friction coefficients are expected from this material. Figure 103 shows the developed model for the friction coefficient between the Dummy skin – Airbag.

Figure 103 – Dummy skin – Airbag friction model.



From the model, one can notice a very high decay amplitude of 0.596 in dependence of slip velocity with coefficient  $B$ , in a smooth shape determined by  $G$  of 0.477. Additionally, there is a clear pressure dependence, with a decay amplitude  $C$  of 0.358 in a smooth shape coefficient  $H$  of 0.905, with higher pressures resulting in smaller friction coefficients. The friction coefficient can be expected to decrease at low slip velocities when samples start from a lying condition, as some adhesion or surface accommodation may occur at this stage. Additionally, the test revealed that higher pressures often led to the development of dummy skin wear, which could explain the lower friction observed at those pressure levels.

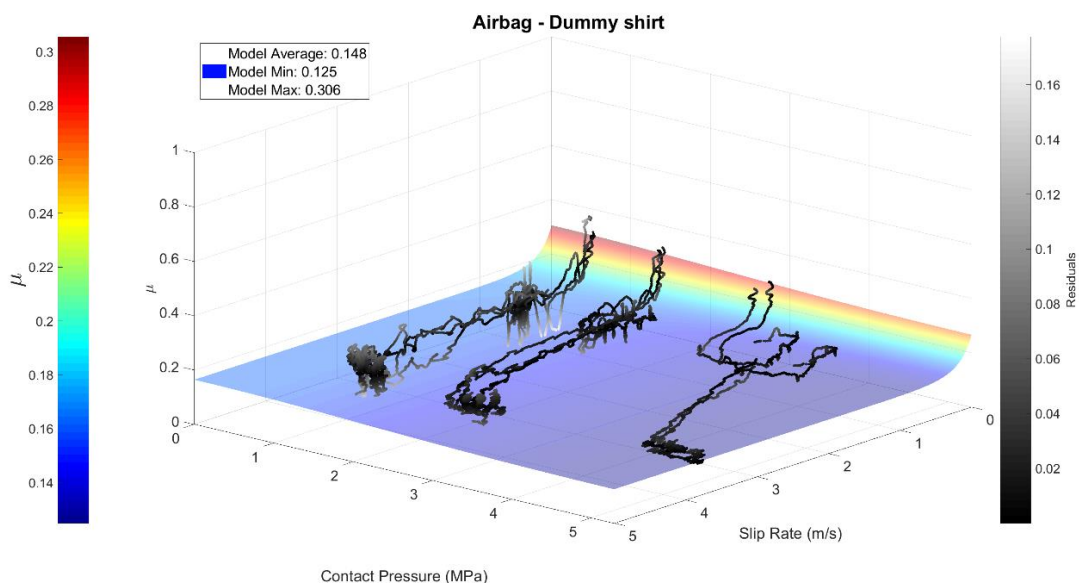
#### 4.2.3. Airbag – Dummy shirt

The frictional interaction between the airbag and the dummy's shirt is an important aspect to consider, as well as the contact with the dummy's face skin. The friction between these two surfaces has been tested, and the resulting model is presented below.

From the equation coefficients, there is a more significant dependence of friction to slip velocity (variation of 0.141 due to amplitude coefficient  $B$ ) than pressure (variation of 0.041 due to amplitude coefficient  $C$ ). This variation is mostly associated with static to dynamic transition, which is evidenced by the

abrupt decrease in friction in low slip velocities (shown by the high value of 5.540 of the decay coefficient  $G$ ). It is also noticeable a smooth transition due to pressure (low value of 0.339 in decay coefficient  $H$ ), which is noticeable in Figure 104.

Figure 104 – Airbag – Dummy shirt friction model.

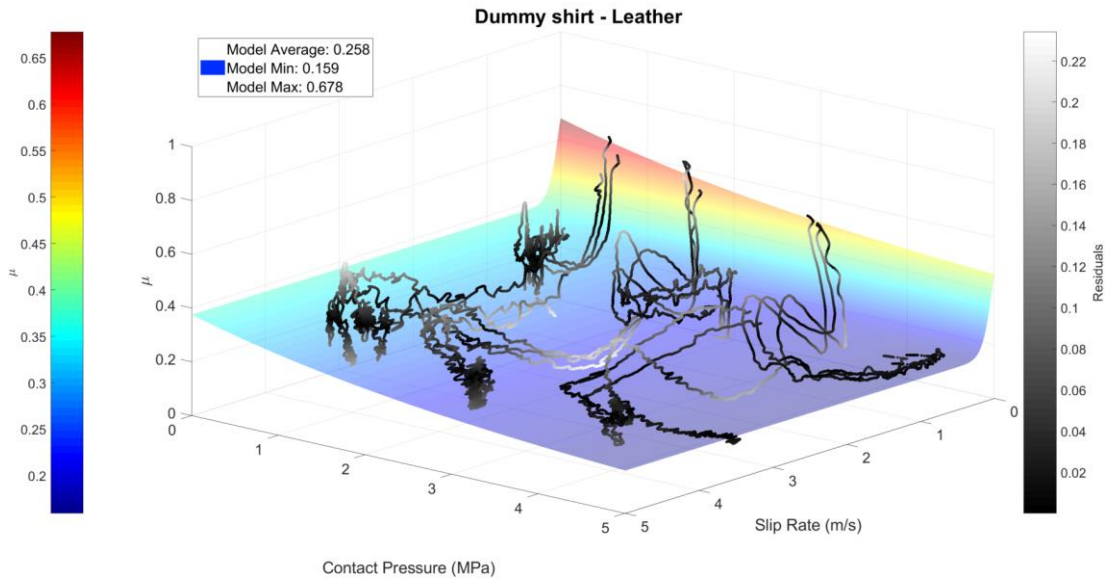


It is important to note that other factors, such as variations in fabric composition, surface roughness, material properties, and the presence of lubricants or coatings could potentially affect the frictional behavior between the airbag and the dummy's shirt.

#### 4.2.4. Dummy shirt – Leather

Leather is a commonly used material for vehicle interiors, especially for seats and door covers. As the dummy interacts with these leather components, the sliding motion between them can significantly impact the dummy's behavior during testing. For example, high values of friction coefficient with seats could induce pelvic rotation (Advisory Group for Aerospace Research & Development, 1996). Therefore, it is important to develop a detailed friction model for leather in contact with the occupant's clothes. Figure 105 shows the results for the considered leather and dummy shirt configuration.

Figure 105 – Dummy shirt – Leather friction model.



The static to dynamic friction coefficient transition was observed across all pressures due to a variation of 0.288 in the amplitude coefficient  $B$  and the high value of the shape coefficient  $G$ . Thus, a decay pressure variation of 0.280 in  $C$  coefficient was also perceived in the model, but in a smoother shape determined by a coefficient  $H$  of 0.299. This can be explained by surface degradation and an increase in the real contact area, which reduces the influence of asperities on the rough surface of the leather.

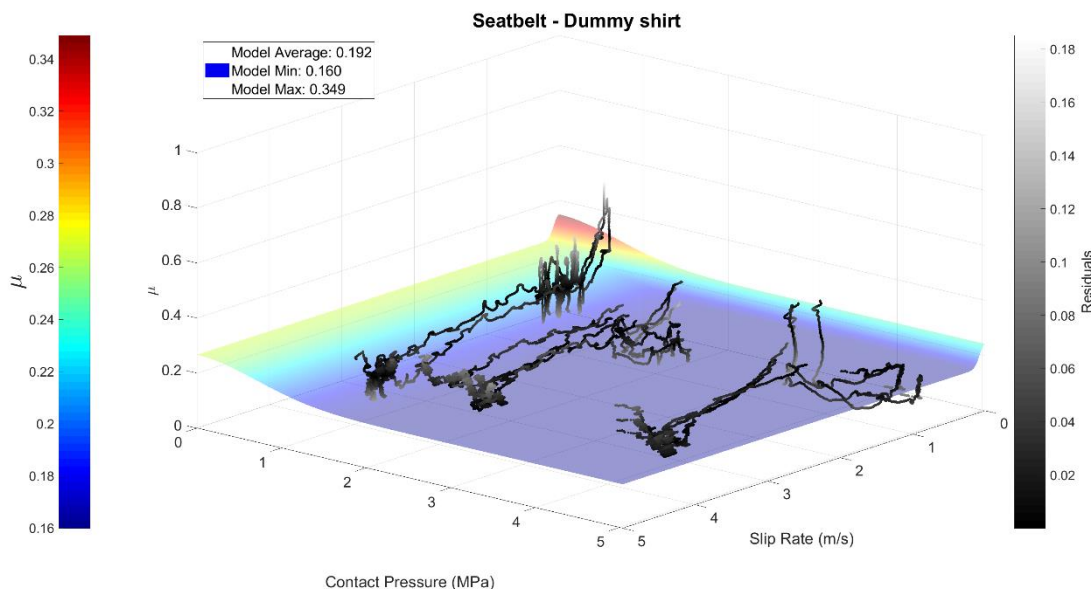
The results agreed with Sulaimany, Algethami e Ali (2011), who have found a maximum value of friction coefficient of 0.6, with slightly decreased with increasing pressure.

#### 4.2.5. Seatbelt – Dummy shirt

The seatbelt is widely recognized as one of the most crucial passive safety systems in vehicles, and its interaction with the dummy has a significant impact on the overall safety performance. Specifically, in terms of friction, crash test simulations have revealed that lack of seatbelt sliding over dummy's chest in high friction scenarios is responsible for a drastic increase in the Chest Severity Index. This accommodation can be influenced by friction, as demonstrated in the crash test simulation developed in this work and by relevant literature (Xiao *et al.*,2016).

Figure 97 shows the measured and modeled friction coefficient of this contact pair.

Figure 106 – Seatbelt – Dummy shirt friction model.



One can observe a modest static to dynamic transition of 0.091 in coefficient  $B$  at the beginning of the tests, with an aggressive shape with coefficient  $G$  of 10.000. There is also a slight pressure dependence of 0.089 in coefficient  $C$ . The overall stability of friction for higher pressures and slip velocities is expected from this contact pair, since no degradation, burning, or shredding marks are observed on the tested samples.

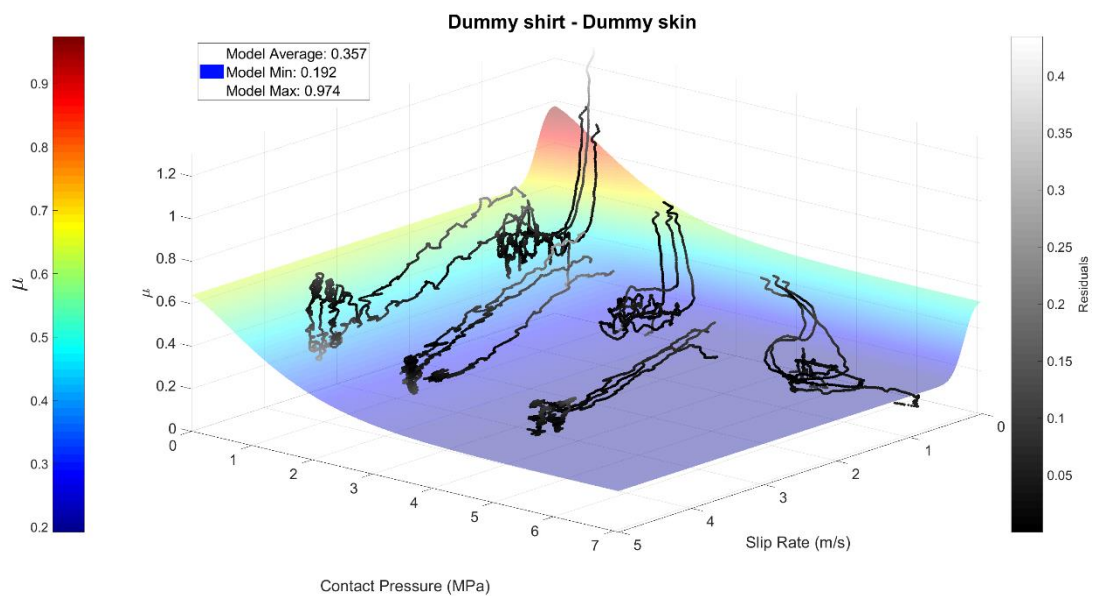
#### 4.2.6. Dummy shirt – Dummy skin

The contact interface between the Dummy Shirt and Dummy Skin is of particular importance, especially in the chest region, as the forces from the seatbelt are primarily transmitted to the dummy shirt and then to the dummy skin. A low friction coefficient could induce a slippery behavior between the occupant and all restraining systems, inducing a non-expected behavior of these. A too high friction coefficient could cause exaggerated shear forces on the dummy skin, which could cause severe burns due to the high pressures applied by the seatbelt.

This contact pair exhibits a significant dependence on slip rate, with an amplitude decay coefficient  $B$  of 0.446, in a sharp shape with coefficient  $G$  of 5.590. Thus, pressure also shows a significant influence on friction, with an amplitude variation of 0.484 in  $C$  coefficient and a smooth transition driven by a coefficient  $H$  of 0.667.

Figure 107 shows the acquired data and generated regression model for the mentioned contact pair friction.

Figure 107 – Dummy shirt – Dummy skin friction model.





## 5. FRICTION COEFFICIENT MODELS ASSESSMENT

This section aims to compare the proposed friction model with an averaged friction coefficient from models, herein called as constant friction model, shown in Table 11. These values are simply the average of surface points shown in the previous section of this work from Figure 102 to Figure 107. This constant friction approach is usually considered on most of the finite element crash test models due to the lack of accurate modeling techniques and the objective is to identify the differences in system response between this approach and the proposed friction modeling technique.

Table 11 – Contact pairs average friction coefficient.

<b>Contact Pair</b>	<b><math>\mu</math></b>
<b>Steel – Aluminium</b>	0.193
<b>Dummy skin – Airbag</b>	0.296
<b>Airbag – Dummy shirt</b>	0.148
<b>Dummy shirt – Leather</b>	0.256
<b>Seatbelt – Dummy shirt</b>	0.192
<b>Dummy skin – Dummy shirt</b>	0.357

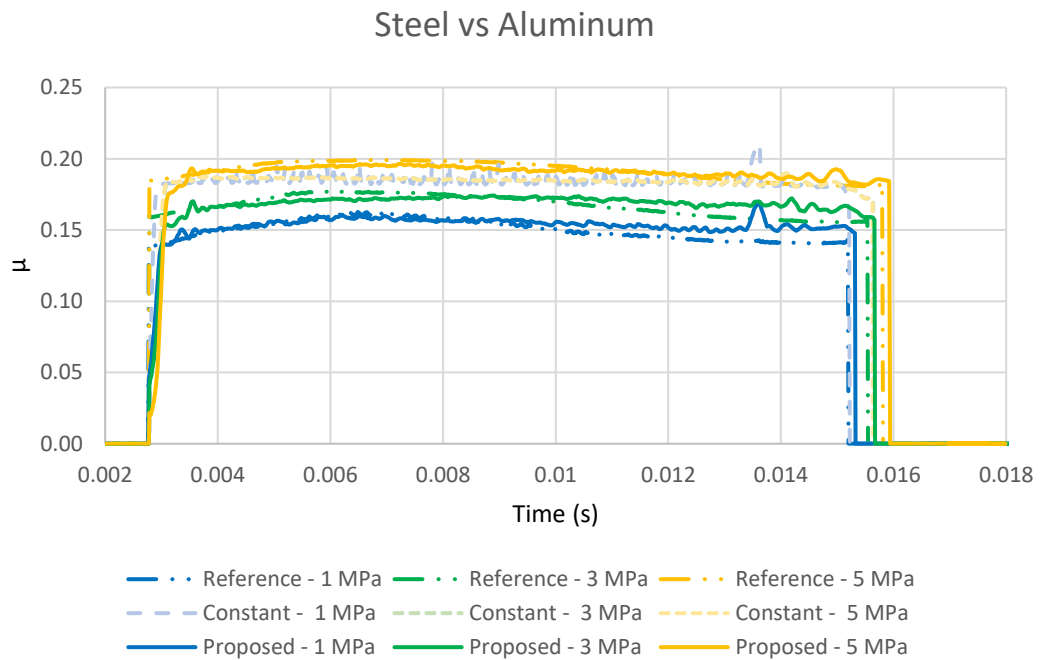
For this study, the impact speed was set at 5 m/s, and the pressures applied were 1, 3, and 5 MPa. Since the developed model is a regression of experimental data and is considered the closest approximation to the test results, it will be taken as the ground truth reference. For that, the contact pressure and sliding velocity will be extracted from the simulation and converted to the respective friction coefficient using Equation (15).

### 5.1. STEEL – ALUMINUM

In this section, it was investigated the frictional behavior between steel and aluminum, which is the first of six contact pairs studied in this research. The stability of the friction coefficient as a function of speed and its dependence on pressure was examined. It was found that higher pressures led to higher friction coefficients, which was in line with the expectations based on the parameters of the constitutive equation. To illustrate these findings, Figure 108

presents a comparison between the simplified constant friction model, a reference friction coefficient value derived from the parameters of the constitutive equation, and the measurement obtained from the simulation using the proposed model.

Figure 108 – Steel – Aluminum friction coefficient comparison.



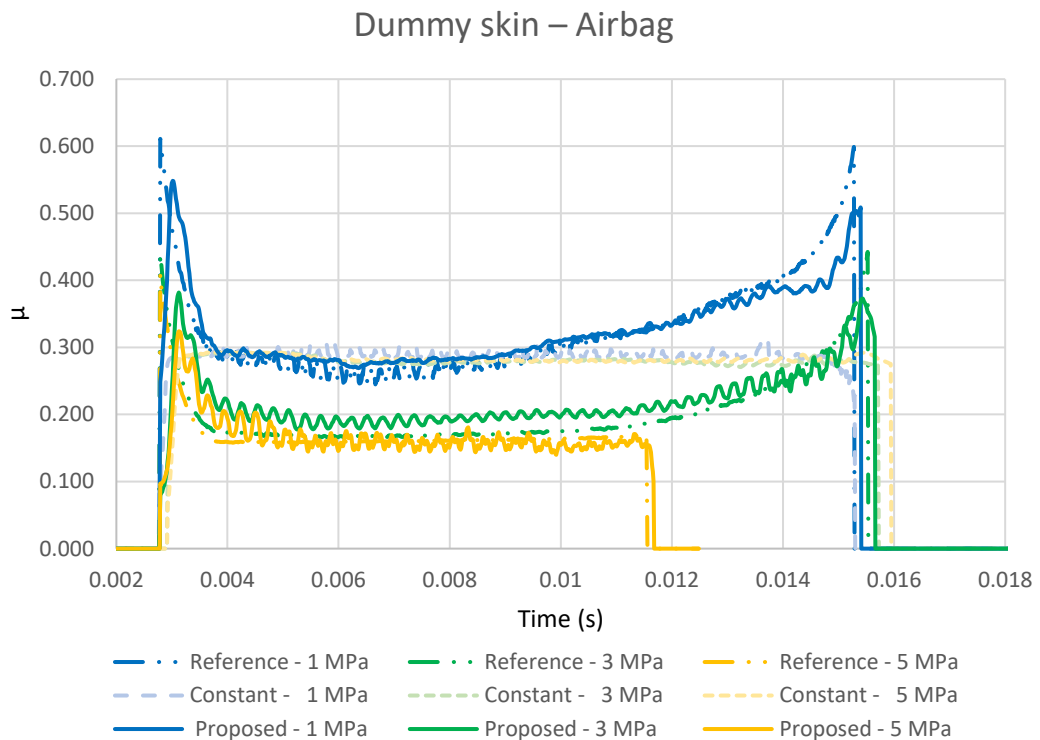
The agreement between the obtained results and the proposed friction model confirms the successful implementation of the friction model within the LS-Dyna software framework. This implementation validates the model's suitability in representing the frictional interactions between steel and aluminum in the simulated system. The demonstrated capability of the friction model to capture such frictional behavior reinforces its potential for conducting more reliable simulations.

## 5.2. DUMMY SKIN – AIRBAG

The contact pair being studied shows a significant dependence on slip velocity and pressure, in contrast to the previous metallic pair. A noticeable transition from static to dynamic friction is observed at the start and end of the test, accompanied by a decrease in the friction coefficient as pressure increases. At 5 MPa, the increasing pressure causes the sample carrier to come to a complete stop, which explains the shorter duration of the yellow curve. Figure

100 compares the theoretical and simulated friction coefficient curves for the Dummy skin – Airbag contact pair. These findings provide insights into the distinctive behavior of this contact pair and confirm the precision of the proposed simulation model in capturing the observed trends.

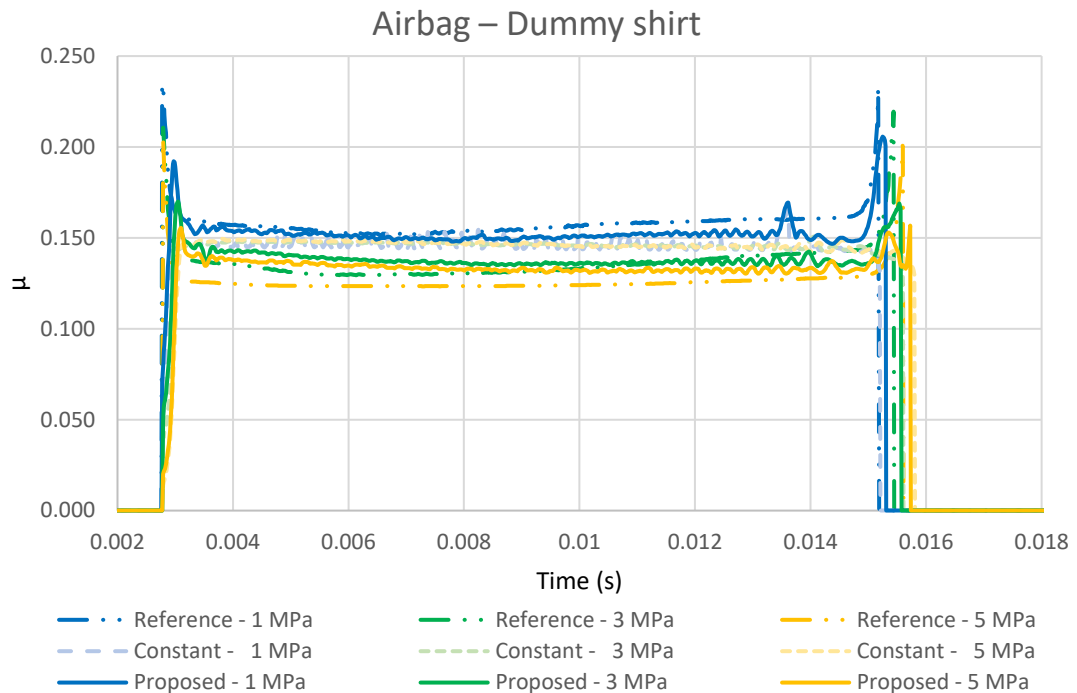
Figure 109 – Dummy Skin – Airbag friction coefficient comparison.



### 5.3. AIRBAG – DUMMY SHIRT

The contact pair between the Airbag – Dummy Shirt showed a transition from static to dynamic friction at the beginning and end of the test. Additionally, it was observed that the friction coefficient was influenced by the applied pressure, as shown in Figure 110. Higher pressures resulted in lower friction coefficients, indicating that the tangential forces were proportionally smaller. Neglecting this influence could lead to inaccurate force responses, as shown by averaged friction coefficient curves.

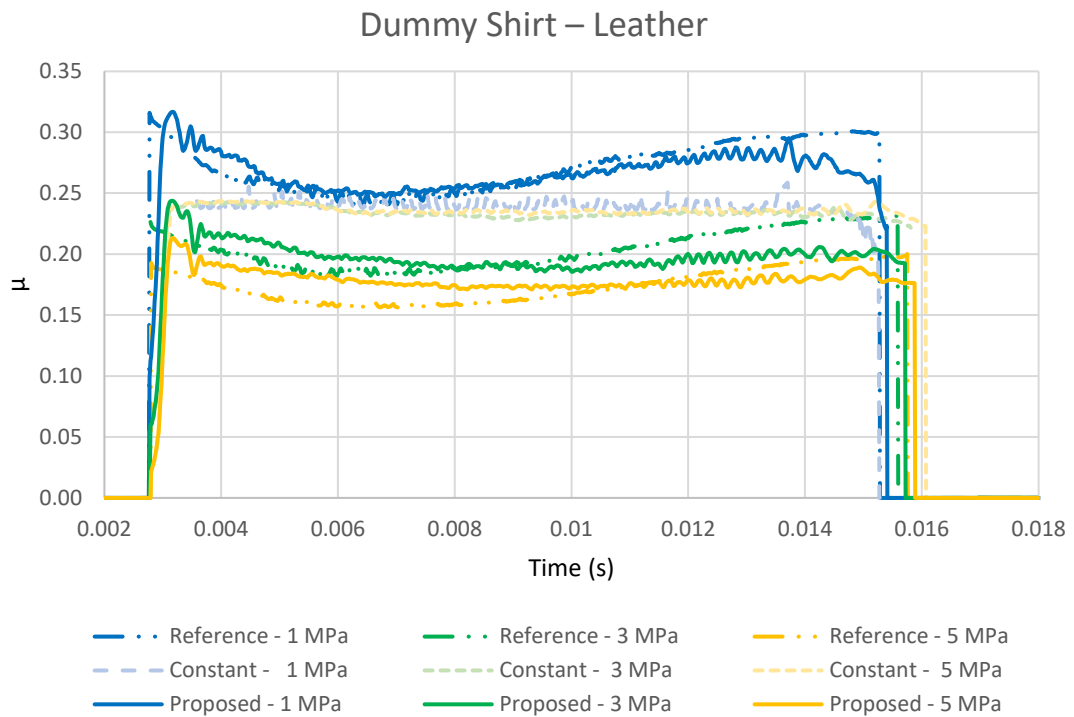
Figure 110 – Airbag – Dummy Shirt friction coefficient comparison.



#### 5.4. DUMMY SHIRT – LEATHER

The friction coefficient in the contact pair between the Dummy Shirt – Leather is significantly influenced by pressure, particularly at lower values. The simulation results closely align with the analytical values, accurately capturing the variations in the friction coefficient with changes in pressure and slip velocity. Figure 111 provides a visual comparison of this contact pair, highlighting the agreement between the simulation and analytical data.

Figure 111 – Dummy shirt leather friction coefficient comparison.

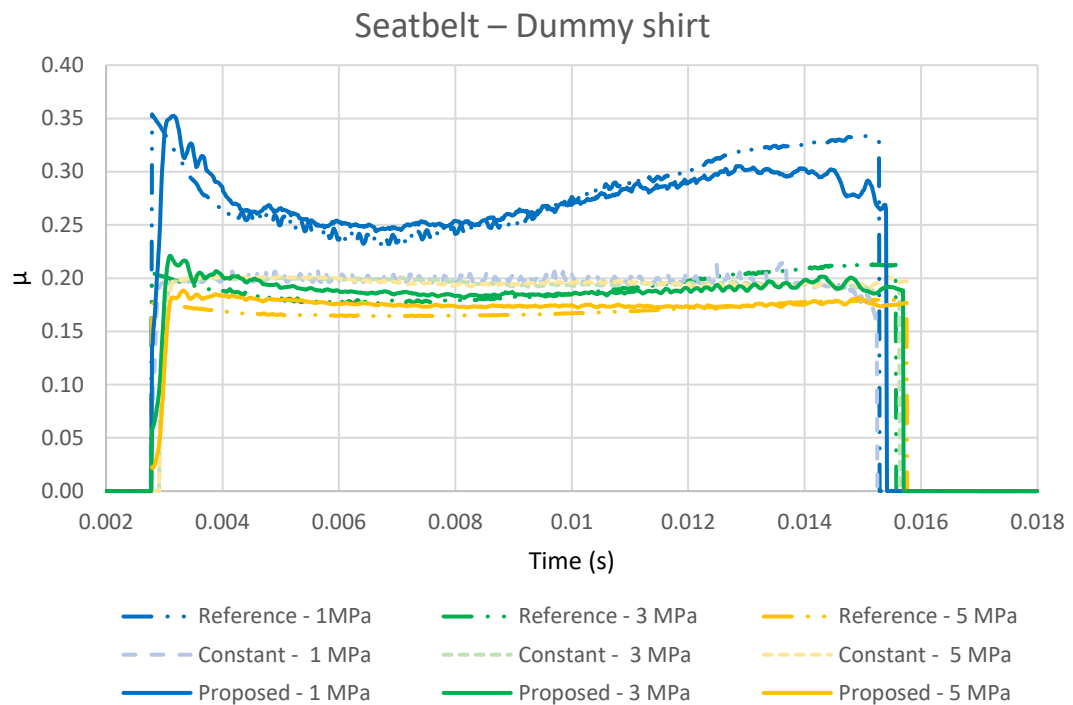


### 5.5. SEATBELT – DUMMY SHIRT

The contact pair between the Seatbelt – Dummy Shirt exhibits a behavior similar to the previous contact pair, with a noticeable effect of pressure, especially at lower pressures. Figure 112 illustrates this behavior. It is important to note that the constant friction coefficient models significantly differed from the proposed constitutive equation.

The observed similarities in behavior between the Seatbelt – Dummy Shirt contact pair and the previous contact pair highlight the consistent influence of pressure on the friction coefficient across different material interactions.

Figure 112 – Seatbelt – Dummy shirt Friction coefficient comparison.

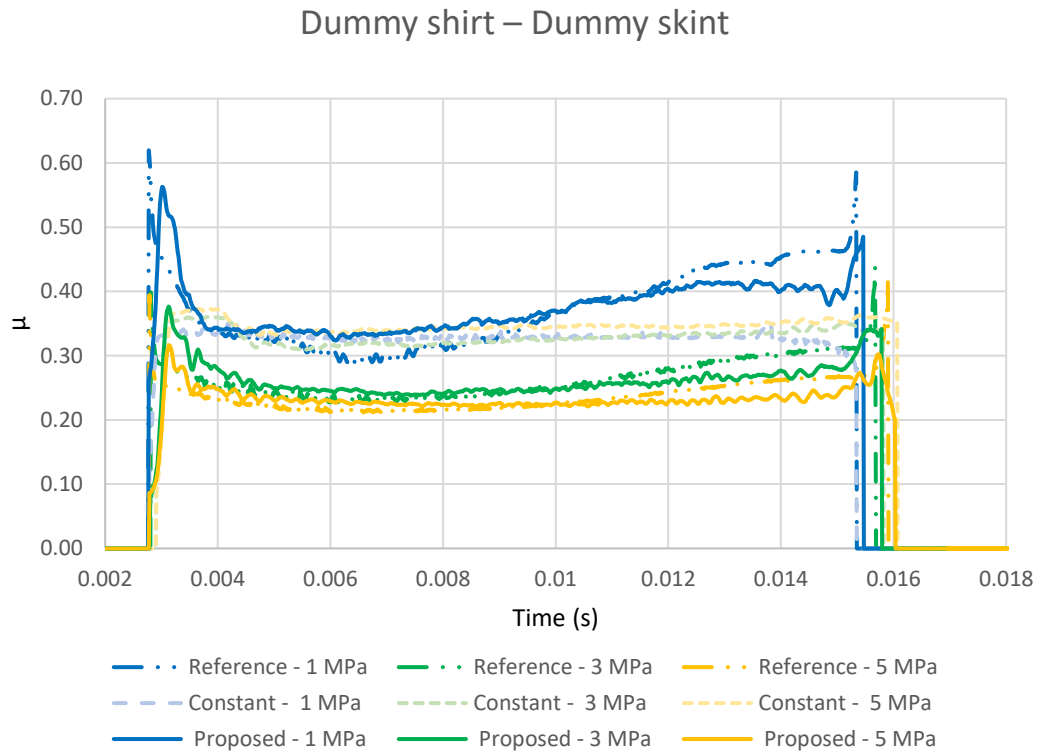


## 5.6. DUMMY SHIRT – DUMMY SKIN

In the final analysis of the contact pair between the Dummy shirt – Dummy skin, a significant decrease in the transition from static to dynamic was observed, as shown in Figure 113. This finding indicates that the transition from static friction to dynamic friction was less pronounced compared to previous contact pairs that were studied.

However, despite the decay in the static-to-dynamic transition, the results showed good agreement with the expected behavior. This agreement suggests that the simulated frictional characteristics of the contact pair between the Dummy skin – Dummy shirt align well with the expected results, based on prior knowledge and understanding of frictional phenomena.

Figure 113 – Dummy skin – Dummy shirt friction coefficient comparison.



To quantify the deviations to reference, the Root Mean Square (RMS) errors between reference and averaged curves are shown in Figure 114, and errors between reference and proposed model are shown in Figure 115. This value is a direct representation of tangential force error between the target and the measured on the simulation and is a simplified manner to assess the accuracy of the friction models.

Figure 114 – RMS Error to reference of constant friction coefficient model.

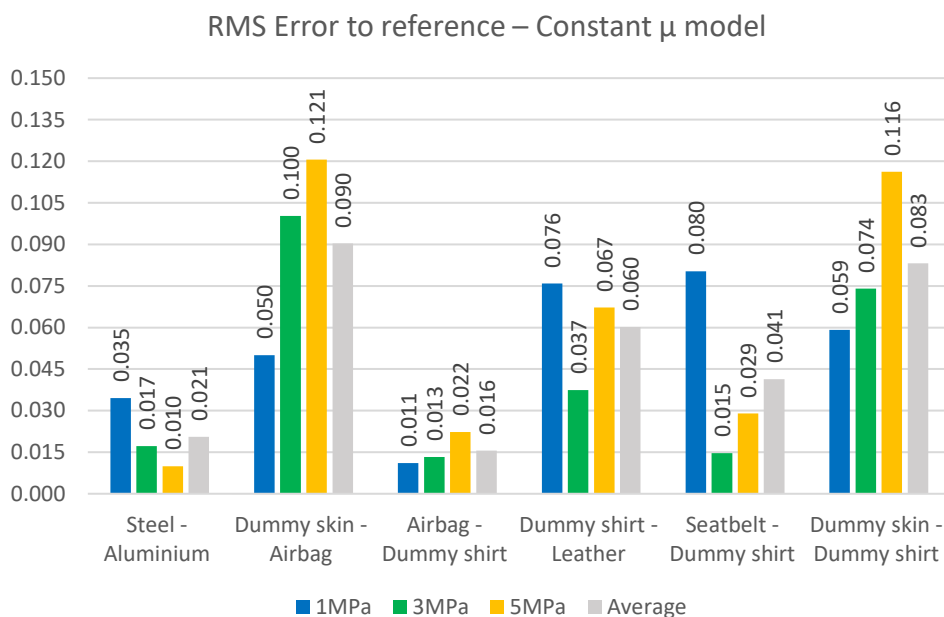


Figure 115– RMS Error to reference of proposed friction coefficient model.

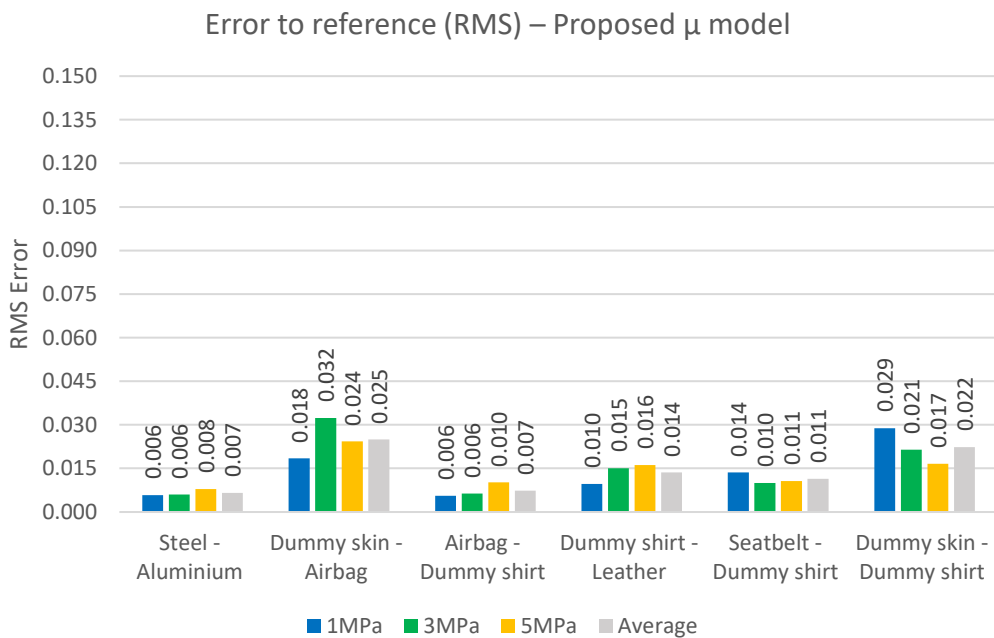




Table 12 shows the RMS error reduction from constant to proposed friction model.

Table 12 – RMS error reduction from constant to proposed friction model.

	RMS error reduction			
	1MPa	3MPa	5MPa	Mean
<b>Steel – Aluminium</b>	83%	65%	21%	68%
<b>Dummy skin – Airbag</b>	63%	68%	80%	72%
<b>Airbag – Dummy shirt</b>	50%	52%	54%	53%
<b>Dummy shirt – Leather</b>	87%	60%	76%	77%
<b>Seatbelt – Dummy shirt</b>	83%	32%	63%	72%
<b>Dummy skin – Dummy shirt</b>	51%	71%	86%	73%
<b>Mean</b>	70%	58%	63%	69%

One can see a significant reduction of up to 87% RMS errors of up to reference on the proposed models, since pressure and slip velocity effects are taken into account, resulting in a 69% error reduction over the tested contact pairs. Interestingly the smaller improvement was in the intermediate pressure 3MPa, since this region tends to be closer to the constant friction coefficient independently to a proportional or inverse relation of friction coefficient to pressure. This error checking approach is similar to Klocke *et al.* (2015), which obtained a 64% error reduction when utilizing pressure, slip velocity and temperature dependent friction coefficient instead of a constant averaged value, as per the data shown in Table 1.

## 6. DISCUSSIONS AND CONCLUSIONS

In accordance with the literature, the numerical simulations of crash events performed in the present work showed that friction plays a crucial role in the overall behavior of a vehicle during a crash test. Although only a small amount of energy is dissipated through friction, it governs the stability of contacts, load paths, and buckling mechanisms of the vehicle's main structural frames, such as the front rail, A column, and Rockwell bar. The results of the three friction coefficient scenarios showed an impressive difference in energy absorption by front rail structural elements of 560%, shown in Figure 90. This was caused by the different energy absorption mechanisms triggered during the impact, where a higher friction coefficient scenario led to a more stable buckling behavior. The low friction coefficient case showed a force peak in the beginning followed by a low mean force and poor energy absorption capability, as also referred by Duddeck (2016) and shown in Figure 6 and Figure 7.

Further, the overall behavior of the vehicle over the barrier during impact was significantly different showing a difference of 26% in average acceleration, in agreement with the findings of Trajkovski, Ambrož, and Kunc (2018) and Stanislawek, Dziejulski, and Kedzierski (2019).

In the biomechanical analysis, the peak head accelerations, chest deflection, and neck moment were found significantly influenced by friction, since this property can trigger mechanisms such as hard contacts, seatbelt, and airbag non-slipping conditions that could potentially harm the occupant during a crash, as pointed by Erikson and Piroti, (2018). In summary, the conducted study agreed with the literature and showed potential trigger mechanisms activated or deactivated by friction variation from a structural and biomechanical point of view during a small overlap crash test.

Various studies (Lai *et al.*, 2012; Klocke *et al.*, 2015; Hu *et al.*, 2017) have highlighted the significance of considering friction pressure and slip velocity dependency in the results of impact tests, emphasizing the challenges of developing sophisticated models, as captured by equation 15. In response to these insights, this study introduces a novel rig and testing methodology,

drawing inspiration from the strip drawing test proposed by Makhkamov (2021) and the rig developed by Lai *et al.* (2012). The approach integrates the best features from these prior works, incorporating a suitable actuation mechanism and sample fixture strategies tailored to the intended materials, as illustrated in Figures 63 to 66. To streamline rig usability and enhance test stability, a single-sided sample approach was taken to facilitate the rig operation and test stability, in the face of two side samples required in the mentioned works. The proposed rig design aims to address various challenges related to robustness, stability in measuring transitions from static to dynamic friction, adaptability to different sample types, usability, and minimizing wear during rigorous testing. Several design options were considered, and the optimal solutions were selected based on decision matrices.

The rig was then manufactured and installed in the impact hammer of the Group of Solid Mechanics and Impact in Structures (GMSIE). Multiple tests were performed for each contact pair under various pressures and slip velocities. The test fixtures were specifically crafted to improve result repeatability, and an approval criterion was implemented to mitigate potential outliers in the test data.

Subsequently, a new friction coefficient modeling equation has been introduced, incorporating an extra degree of freedom compared to the well-known exponential friction model. This modeling technique allows the approximation of distinct friction plateaus in relation to pressure and slip velocity dependencies, as illustrated in Figure 30-b (Hutchings, 2017), Figure 36 (Lim and Ashby, 1987), and Figure 53 (Hu *et al.*, 2017). The incorporation of this additional feature has proven highly effective and a valuable tool in the regression analysis of experimental data in this study, and it has been shown to be applicable in a broader range of friction scenarios with inherent tribological significance.

From the tests, the friction coefficient of Steel – Aluminum contact pair was shown to have almost no influence on slip velocity but showed significant variation with pressure. Javadi and Tajdari (2006) have found a similar pattern

when investigating steel-to-aluminum dry contact, where the friction coefficient was found to be higher at more elevated pressures. The authors concluded that at low normal stresses, the adhesive theory of friction can be used, while for higher normal stresses the junction growth theory must be applied, which agrees with the herein findings.

From the Dummy skin – Airbag contact pair, the results agreed with Dong *et al.* (2020), who found values of friction coefficient up to 1.06 for these materials at low slip rates. Additionally, in most crash tests, the dummy's face is painted with grease, creating a layer that is subsequently removed upon contact with an airbag or any hard surface. This removal of the grease paint can significantly alter the friction behavior of the original contact pair as shown by Erikson and Piroti, (2018). Moreover, a significant question arises regarding the representativeness of the dummy skin (with and without grease paint) compared to human skin in terms of its frictional response to the vehicle's interior. While this study does not aim to answer these questions directly, existing literature (Mihora, Friedman, and Hutchinson, 2011 and Dong *et al.*, 2020) suggests significant differences between these two materials regarding airbag interactions.

Airbag – Dummy shirt have shown a maximum friction coefficient of 0.306 and a minimum of 0.125, according to the model, with significant slip velocity dependence and minimal pressure influence. One interesting finding of this work is that no standard was found to define a specific type of fabric for the dummy shirt. Neoprene, natural cotton, and polyester fabric were found to be used according to the type of crash test and institution responsible for the experiment, and no standard costume material was found to be mandatory, as shown by Xu *et al.*, (2018) and Advisory Group for Aerospace Research & Development (1996). Thus, variations in fabric composition such as surface roughness, material properties, and the presence of lubricants or coatings could potentially affect the frictional behavior between the airbag and the dummy's shirt.

Dummy Shirt – Leather friction coefficient has shown a significant variation of friction coefficient with slip velocity and a slight decrease with increasing pressure, with a maximum value of 0.678 and minimum of 0.159. The results agreed with Sulaimany, Algethami and Ali (2011), who have found a maximum value of friction coefficient of 0.6, with slightly decrease with increasing pressure. This contact pair is specifically important during the dummy sliding over the seat cover, where higher friction values could potentially induce pelvic rotation and significantly change the dummy's behavior during the impact. One more time, the variations in the dummy cloth fabric composition could potentially affect the results of this contact pair frictional behavior.

In the Seatbelt – Dummy shirt model, the friction coefficient was found between 0.349 at low speeds and low pressures and 0.160 at high speeds and high pressures. This dynamic friction coefficient approximates the modeling recommendation of LSTC (2015), and the static value is within the admitted range by Gavelin (2008). According to Dubois, Zellmer e Markiewicz (2009), and Pedrazzi, Elsässer, and Schaub (2001), it was also found that seatbelt friction can influence belt bunching during the impact. This effect can have a negative influence on the restrain function of the seat belt system and lead to increased seat belt forces on the occupant. Despite this phenomenon not being herein detailed, there is an agreement in the literature regarding the multiple effects that friction can play on seatbelt interactions.

Lastly, from Dummy shirt – Dummy skin it was found that the low-speed friction coefficient was very high, up to 0.974. This high friction is much influenced by the rubber-like aspect of vinyl plastisol, which recalls one more time the discussion of the representativeness of this polymer as an appropriate solution for the role. This finding agrees with the high values of friction coefficient over 1.0 found by Yoon and Delevoye (2016) for lower speeds.

An important remark at this point is that all materials herein tested are only an example of the rig capabilities, and other contact pairs shall be tested to ensure that all needed friction models for a crash test are covered. This can be considered a recommendation for further work.

An assessment of the tangential force response was then presented in Chapter 5, where the test rig was simulated under conditions similar to the experiments. By incorporating the suggested friction models into finite element software, one could directly compare the proposed approach to the standard industry method (constant friction coefficient). To establish a baseline, the results were compared against experimentally obtained values corresponding to specific pressure and slip velocity conditions. In a similar fashion to Klocke *et al.* (2015), who found a 64% reduction in the error of numerical-experimental correlation when considering a pressure and slip velocity-dependent friction coefficient, this work found a reduction of 69% in the RMS error to the baseline reference.

Finally, this work proposes as further work an investigation of friction under a different impact scenario. Despite the developed rig and method being shown to be efficient, robust, and reliable in the acquisition process, Oden and Martins (1984) have discussed the standing condition of contact at the beginning of the test and the influence of the time of stationary contact on the value of the static coefficient of friction. The presented methodology considers friction coefficient modeling from a static to a dynamic transition. In a real-world crash test, there are contact pairs initially separated that come into contact with non-zero initial tangential speed. To cover this gap and investigate how friction would behave in such conditions, this work proposes an alternative methodology for the investigation of this scenario in Appendix E, where a new test rig was designed for a small angle oblique impact where the velocity of the test is maximum at the beginning of the contact. This experiment could improve the research on the behavior of the friction coefficient under boundary conditions closer to those found in crash test events.

## 7. REFERENCES

ADVISORY GROUP FOR AEROSPACE RESEARCH & DEVELOPMENT (AGARD), 1996, Neuilly-Sur-Seine. **Anthropomorphic Dummies for Crash and Escape System Testing**. Neuilly-Sur-Seine: North Atlantic Treaty Organization, 1996. Available at: <https://apps.dtic.mil/sti/tr/pdf/ADA313660.pdf>. Accessed: Dec 10, 2023.

ALVES, Marcilio *et al.* Limiting the influence of friction on the split Hopkinson pressure bar tests by using a ring specimen. **International Journal of Impact Engineering**, [S.L.], v. 49, p. 130-141, Nov. 2012. Elsevier BV.

ANDRADE, *et al.* Brazilian Road Traffic Fatalities: a spatial and environmental analysis. *Plos One*, [S.L.], v. 9, n. 1, 30 Jan. 2014. **Public Library of Science (PLOS)**. <http://dx.doi.org/10.1371/journal.pone.0087244>

ASTM G-99: Wear Testing with a Pin-on-Disk Apparatus. **ASTM International**, West Conshohocken, PA, 2000. Available at: <[www.astm.org](http://www.astm.org)>. Accessed: Jul. 14, 2021.

ASTM D1894-00, Standard Test Method for Static and Kinetic Coefficients of Friction of Plastic Film and Sheeting, **ASTM International**, West Conshohocken, PA, 2001. Available at: <[www.astm.org](http://www.astm.org)>. Accessed: Jul. 14, 2023.

ASTM G133-05, Standard Test Method for Linearly Reciprocating Ball-on-Flat Sliding Wear, **ASTM International**, West Conshohocken, PA, 2005. Available at: <[www.astm.org](http://www.astm.org)>. Accessed: Jul 14, 2023.

BENSON, D.J., HALLQUIST, J.O.: A single surface contact algorithm for the post-buckling analysis of shell structures. **Computer Method Applied Mechanics and Engineering** 78, 141–163 (1990)

BRUMBELOW, M. L.; ZUBY, D. S. Impact and Injury Patterns in Frontal Crashes of Vehicles with Good Ratings for Frontal Crash Protection, **Proceedings of ESV Conference**, 2009.

CHO, Dae-Hyun; BHUSHAN, Bharat; DYESS, James. Mechanisms of static and kinetic friction of polypropylene, polyethylene terephthalate, and high-density polyethylene pairs during sliding. **Tribology International**, [S.L.], v. 94, p. 165-175, Feb. 2016. Elsevier BV. <http://dx.doi.org/10.1016/j.triboint.2015.08.027>.

DOMAJNKO, Dora; KRIŽAJ, Dejan. Lagging-Domain Model for Compensation of Hysteresis of xMR Sensors in Positioning Applications. *Sensors*, [S.L.], v. 18, n. 7, p. 2281, Jul. 14, 2018. **MDPI AG**. <http://dx.doi.org/10.3390/s18072281>.

DONG, Sheng *et al.* Experimental Investigation of Friction Between Vehicle Air Bag Material and Head Skin for Humans and Crash Test Dummies. Volume 14: **Safety Engineering, Risk, and Reliability Analysis**, [S.L.], Nov 16, 2020. American Society of Mechanical Engineers. <http://dx.doi.org/10.1115/imece2020-23334>.

DUBOIS, David; ZELLMER, Harald; MARKIEWICZ, Eric. Experimental and numerical analysis of seat belt bunching phenomenon. **International Journal of Impact Engineering**, [S.L.], v. 36, n. 6, p. 763-774, jun. 2009. Elsevier BV. <http://dx.doi.org/10.1016/j.ijimpeng.2008.11.006>

DUDDECK, Fabian. Vehicular Crashworthiness: automotive structures. London: **Queen Mary University of London**, 2016.

ERIKSSON, Jesper.; PIROTI, Shwana. Friction modeling in FE Simulation: identification of friction model parameters in airbag and crash dummy head contact through simulation and experimental data response correlation. 2018. 89 p. Mechanical Engineering, **KTH Royal Institute of Technology**, Stockholm, 2018. Available at: <<http://kth.diva-portal.org/smash/get/diva2:1236998/FULLTEXT01.pdf>>. Accessed: Jul 14, 2023.

EUROSTAT. Road accident fatalities – statistics by type of vehicle. 2020. Available at: <[https://ec.europa.eu/eurostat/statistics-explained/index.php?title=Road\\_accident\\_fatalities\\_-\\_statistics\\_by\\_type\\_of\\_vehicle](https://ec.europa.eu/eurostat/statistics-explained/index.php?title=Road_accident_fatalities_-_statistics_by_type_of_vehicle)>. Accessed: Oct 10, 2021.

GAVELIN, Anders. **Studies on structural and biomechanical responses in seat integrated safety belt configurations**. 2008. 206 f. Thesis (Doctorate) – Mechanical Engineering, Luleå University of Technology, Luleå, 2008. Available at: <https://www.diva-portal.org/smash/get/diva2:999853/FULLTEXT01.pdf>. Accessed: Dec 10, 2023

GUHA, Sarba. **Occupant Modeling Workshop: Dummy Positioning, Sled Modeling, Belt routing and Post processing**. Michigan: LSTC, 2015. 31 p

HAMROCK Bernard., Schmid Steven. and Jacobson Bo. **Fundamentals of fluid film lubrication**. CRC press, 2004.

HOLMBERG, Kenneth *et al.* Friction and wear of coated surfaces — scales, modelling and simulation of tribomechanisms. **Surface And Coatings Technology**, [S.L.], v. 202, n. 4-7, p. 1034-1049, Dec. 2007. Elsevier BV. <http://dx.doi.org/10.1016/j.surfcoat.2007.07.105>.

HU, Yiran. *et al.* Development of an interactive friction model for the prediction of lubricant breakdown behavior during sliding wear. **Tribology International**, [S.L.], v. 110, p.370-377, Jun 2017. Available at: <<http://dx.doi.org/10.1016/j.triboint.2016.11.005>>.

HUTCHINGS, Ian.; SHIPWAY, Philip. Friction and Wear of Engineering Materials. 2nd ed. Butterworth-Heinemann, 2017.

IIHS – Insurance Institute for Highway Safety, “Small Overlap Frontal Crashworthiness Evaluation Crash Test Protocol version VII,” May 2021.

JAVADI, Mehrdad; TAJDARI, Mehdi; Experimental investigation of the friction coefficient between aluminum and steel. **Materials Science-Poland**. Tehran, p. 100-106. Oct. 01, 2006.



JOHNSON, K. L. Contact Mechanics. Cambridge: Cambridge University Press, 1985.

JOHNSON, Norman; KOTZ, Samuel; BALAKRISHNAN, Narayanaswamy. Continuous univariate distributions, volume 2. John Wiley & Sons, 1995.

KAWAKAME.; BRESSAN, J.D.; Atrito e Desgaste em Polímeros. In: **Proceedings of Congresso Brasileiro em Engenharia e Ciência dos Materiais**, 2000, São Pedro – SP; Universidade do Estado de Santa Catarina – Udesc, 2000. p. 53401 – 53412.

KAN, Steve; MARZOUGUI, Dhafer; BEDEWI. Development of a 50th Percentile Hybrid III Dummy Model. **4<sup>th</sup> European LS-Dyna**. Ulm, p. 13-22. May 22, 2003. Available at: <https://lsdyna.ansys.com/wp-content/uploads/attachments/development-of-a-50th-percentile-hybrid-iii-dummy.pdf>. Accessed: Aug 25, 2021.

KLOCKE, Fritz. *et al.* FE-analysis and in situ visualization of pressure, slip-rate, and temperature-dependent coefficients of friction for advanced sheet metal forming: development of a novel coupled user subroutine for shell and continuum discretization. **The International Journal of Advanced Manufacturing Technology**, [S.L.], v. 81, n. 1-4, p. 397-410, May 8, 2015. Springer Science and Business Media LLC. <http://dx.doi.org/10.1007/s00170-015-7184-1>

KRUSE, Moritz *et al.* Investigation of the friction behavior between dry/infiltrated glass fiber fabric and metal sheet during deep drawing of fiber metal laminates. **Production Engineering**, [S.L.], v. 17, n. 1, p. 37-46, 22 jun. 2022. Springer Science and Business Media LLC. <http://dx.doi.org/10.1007/s11740-022-01141-y>

KUMAR, Siva. Experimental Investigations with Crush Box Simulations for Different Segment Cars using LS-DYNA. **International Journal of Current Engineering and Technology**, [S.L.], v. 2, n. 2, p. 670-676, Jan. 1, 2010. Available at: <<http://dx.doi.org/10.14741/ijcet/spl.2.2014.127>>.

LEIMBACH, Frank; KIEBACH, Helge. Reparability and Insurance Ratings in the Development of Cars. **Encyclopedia Of Automotive Engineering**, [S.L.], p. 1-12, Dec. 11, 2013. John Wiley & Sons, Ltd. <http://dx.doi.org/10.1002/9781118354179.auto254>.

LAI, Xinghua *et al.* An experimental method for characterizing friction properties of sheet metal under high contact pressure. **Wear**, [S.L.], v. 289, p. 82-94, jun. 2012. Elsevier BV. <http://dx.doi.org/10.1016/j.wear.2012.04.011>

LIM, Sehchun; ASHBY, Michael. Overview no. 55 Wear-Mechanism maps. [S.L.], v. 35, n. 1, p. 1-24, Jan. 1987. Elsevier BV. [http://dx.doi.org/10.1016/0001-6160\(87\)90209-4](http://dx.doi.org/10.1016/0001-6160(87)90209-4)

LIMA, Anderson de. Desenvolvimento de um veículo urbano seguro utilizando otimização baseada em metamodelos. 2016. 346 f. Thesis

(Doctorate) – Mechanical Engineering, **Universidade de São Paulo**, São Paulo, 2016.

LIN, Liang. *et al.* A technique for measuring dynamic friction coefficient under impact loading. **Review Of Scientific Instruments**, [S.L.], v. 85, n. 9, Sep. 01, 2014. AIP Publishing. <http://dx.doi.org/10.1063/1.4894206>.

LIST, Gautier.; SUTTER, Guy.; ARNOUX, Jean Jacques. Analysis of the high speed sliding interaction between titanium alloy and tantalum. **Wear**, [S.L.], v. 301, n. 1-2, p. 663-670, Apr. 2013 Elsevier BV. <http://dx.doi.org/10.1016/j.wear.2012.11.070>.

LSTC. Livermore Software Technology Corporation. Available at: [http://www.lstc.com/products/models/dummies/H3\\_50th](http://www.lstc.com/products/models/dummies/H3_50th)>. Accessed: Dec. 03, 2015.

MAKHKAMOV, Anvar. Determination of the Friction Coefficient in the Flat Strip Drawing Test. **Engineering**, [S.L.], v. 13, n. 11, p. 595-604, 2021. Scientific Research Publishing, Inc. <http://dx.doi.org/10.4236/eng.2021.1311043>.

MARZOUGUI *et al.* Development & Validation of a Finite Element Model for a Mid-Sized Passenger Sedan. **13<sup>th</sup> Ls-Dyna International Users Conference: Automotive**. Detroit, p. 1-10. Oct 12, 2014. Available at: <https://lsdyna.ansys.com/wp-content/uploads/attachments/development-validation-of-a-finite-element-model-for-a-mid-sized-passenger-sedan.pdf>. Accessed in: Oct. 28, 2021.

MEYER, W. E., and KUMER, H. W. Mechanism of force transmission between tire and road. Tech. rep. **SAE Technical Paper**, 1962.

MIHORA, D.; FRIEDMAN, K.; HUTCHINSON, J. Effect of Friction Between Head and Airbag Fabric on Ejection Mitigation Performance of Side Curtain Airbag Systems. **SAE Technical Paper**, Apr 12, 2011. Available at: <http://dx.doi.org/10.4271/2011-01-0004>>. Accessed: Jul. 14, 2023.

MOHAMMED, Ali Ahmed *et al.* A Review of the Traffic Accidents and Related Practices Worldwide. **The Open Transportation Journal**, [S.L.], v. 13, n. 1, p. 65-83, 30 Jun. 2019. Bentham Science Publishers Ltd. <http://dx.doi.org/10.2174/1874447801913010065>.

MUSSULINI, Bruno Cesar. **Desenvolvimento de um atenuador de impacto para um veículo de fórmula SAE**. 2017. Graduation final work – Escola Politécnica, Universidade de São Paulo, São Paulo, 2017. Available at: <https://repositorio.usp.br/directbitstream/df5c5d0d-c6fd-4636-9c1a-611b60193002/BRUNO%20CESAR%20MUSSULINI%20PME17.pdf>. Accessed: Oct. 30, 2020.

NCAC National Crash Analysis Center. Available at: <http://www.ncac.gwu.edu/vml/models.html>>. Accessed: Nov 20, 2014.

NIA, Saeed. **On Heavy-Haul Wheel Damages using Vehicle Dynamics Simulation**. 2017. 93 f. Thesis (Doctorate) – Mechanical Engineering, KTH Institute of Engineering, Stockholm, 2017.

ODEN, J. T.; MARTINS, J. A. C. (ed.). Models and computational methods for dynamic friction phenomena. **Computer Methods in Applied Mechanics and Engineering**. Austin, p. 527-634. Oct. 22, 1984.

PARENTEAU, Chantal *et al.* Rear-End Impacts – Part 1: field and test data analysis of crash characteristics. **SAE International Journal of Advances and Current Practices in Mobility**, [S.L.], v. 4, n. 6, p. 2106-2119, 29 Mar. 2022. SAE International. <http://dx.doi.org/10.4271/2022-01-0859>.

PEDRAZZI; ELSÄßER; SCHAUB. Aspects of Seat Belt Material Simulation. In: Third European Ls-Dyna Conference, 3., 2001, Paris. **Proceedings of Third European Ls-Dyna Conference**, 2001. p. 56-67

PENNESTRÌ, Ettore; ROSSI, Valerio; SALVINI, Pietro; VALENTINI, Pier Paolo. Review and comparison of dry friction force models. **Nonlinear Dynamics**, [S.L.], v. 83, n. 4, p. 1785-1801, 11 Nov. 2015. Springer Science and Business Media LLC. <http://dx.doi.org/10.1007/s11071-015-2485-3>.

PRASAD, P., DALMOTAS, D., and GERMAN, A., A. An Examination of Crash and NASS Data to Evaluate the Field Relevance of IIHS Small Offset Tests. **SAE International Journal of Transportation Safety**, [S.L.], v. 2, n. 2, p. 326-335, Apr. 01, 2014. SAE International. <http://dx.doi.org/10.4271/2014-01-1989>.

RENISHAW. How optical encoders work. 2018. Available at: <https://www.renishaw.com/en/how-optical-encoders-work--36979>. Accessed: Oct. 23, 2018.

RENISHAW. LA11 absolute magnetic encoder system. Slovenia, 2018. 24 p. Available at: [https://www.rls.si/en/fileuploader/download/download/?d=1&file=custom%2Fupload%2FLA11D01\\_07\\_EN\\_data\\_sheet.pdf](https://www.rls.si/en/fileuploader/download/download/?d=1&file=custom%2Fupload%2FLA11D01_07_EN_data_sheet.pdf). Accessed: Jul. 14, 2023.

STANISLAWEK, S.; DZIEWULSKI, P.; KEDZIERSKI, P. Deterioration of Road Barrier Protection Ability Due to Variable Road Friction. **International Journal of Simulation Modelling**, [S.L.], v. 18, n. 3, p. 432-440, 15 Sep. 2019. DAAAM International. [http://dx.doi.org/10.2507/ijsimm18\(3\)480](http://dx.doi.org/10.2507/ijsimm18(3)480).

SHI, Z. *et al.* A new design of friction test rig and determination of friction coefficient when warm forming an aluminum alloy. **Procedia Engineering**, [S.L.], v. 207, p. 2274-2279, 2017. Elsevier BV. <http://dx.doi.org/10.1016/j.proeng.2017.10.994>.

STATISTA. Registered passenger cars in Europe (EU28) 1990-2017. 2020. Available at: <https://www.statista.com/statistics/452447/europe-eu-28-number-of-registered-passenger-cars/>. Accessed: Oct. 10, 2020.

SULAIMANY; ALGETHAMI; ALI; FRICTION COEFFICIENT BETWEEN CLOTHES AND CAR SEAT COVERS. **Journal Of the Egyptian Society of Tribology**, Al-Taif, v. 8, n. 4, p. 36-47, Oct. 2011.

SUTTER, G.; RANC, N. Flash temperature measurement during dry friction process at high sliding speed. **Wear**, [S.L.], v. 268, n. 11-12, p. 1237-1242, May 2010. Elsevier BV. <http://dx.doi.org/10.1016/j.wear.2010.01.019>.

TABOR, David. Junction growth in metallic friction: the role of combined stresses and surface contamination. **Proceedings Of the Royal Society Of London. Series A. Mathematical and Physical Sciences**, [S.L.], v. 251, n. 1266, p. 378-393, Jun. 09, 1959. The Royal Society. <http://dx.doi.org/10.1098/rspa.1959.0114>.

THK (Brasil). Guia linear com gaiola de esferas. Tokyo, 2018. 24 p. Available at: [https://www.thk.com/sites/default/files/documents/br\\_pdf/product/pamphlet/SHS235-10P.pdf](https://www.thk.com/sites/default/files/documents/br_pdf/product/pamphlet/SHS235-10P.pdf). Accessed: Nov. 10, 2018.

TRAJKOVSKI, Jovan; AMBROŽ, Miha; KUNC, Robert. The Importance of Friction Coefficient between vehicle tires and concrete safety barrier to Vehicle Rollover – FE Analysis Study. **Strojniški Vestnik – Journal of Mechanical Engineering**, [S.L.], Sep. 2018. Faculty of Mechanical Engineering. <http://dx.doi.org/10.5545/sv-jme.2018.5290>

TRIBONET. Pin on Disk Test. 2022. Available at: [https://www.tribonet.org/wiki/pin-on-disk-test/#What\\_is\\_a\\_Pin\\_on\\_Disk\\_Test](https://www.tribonet.org/wiki/pin-on-disk-test/#What_is_a_Pin_on_Disk_Test). Accessed: Mar. 01, 2023.

UNITED NATIONS. Buckling up to save lives: UN celebrates five decades of seat belt laws. 2023. Available at: <https://news.un.org/en/story/2023/06/1137412>. Accessed: Jul. 01, 2023.

VAKIS, A.I. *et al.* Modeling and simulation in tribology across scales: an overview. **Tribology International**, [S.L.], v. 125, p. 169-199, set. 2018. Elsevier BV. <http://dx.doi.org/10.1016/j.triboint.2018.02.005>.

WANG, D., RUI, Y. Simulation of the Stick-Slip Friction between Steering Shafts Using ADAMS. In: **International ADAMS User Conference**, pp. 1–11 (2000).

WRIGGERS, P. Computational Contact Mechanics. 2nd ed. Berlin: Springer, 2006. 518 p.

WWW.800LOADCEL.COM. Load Cell and Strain Gauges Basics. 2018. Available at: <https://www.800loadcel.com/load-cell-and-strain-gauge-basics.html>. Accessed: Jun. 24, 2019.

XIAO, Sen *et al.* Effect of Contact Friction between Seatbelt and Human Body Model on Simulation of Rib Fracture in Frontal Impact. **2016 Eighth International Conference in Measuring Technology and Mechatronics Automation (ICMTMA)**, [S.L.], p. 255-257, mar. 2016. IEEE. <http://dx.doi.org/10.1109/icmtma.2016.69>.

XU, Tao *et al.* Development and Validation of Dummies and Human Models Used in Crash Test. **Applied Bionics and Biomechanics**, [S.L.], v. 2018, p. 1-12, Nov. 13, 2018. Hindawi Limited.  
<http://dx.doi.org/10.1155/2018/3832850>.

YOON, Seokbae; DELEVOYE, Antoine. A Study on the Coefficient of Dynamic Friction between Dummy and Seat by Test Method. **International Research Council on Biomechanics of Injury: IRCOBI**. Seoul, p. 90-91. May 2016.

## APPENDIX A – INJURY CRITERIA

In order to verify potential injuries to occupants, the data obtained from the simulations or tests must be compared to the performance requirements outlined in the European standard ECE R94 for both tests. The following items are checked in the data extracted from the dummy:

### A.1. HEAD INJURY CRITERIA (HIC)

Due to the brain's sensitivity to accelerations, possible head and brain trauma are analyzed using the Head Injury Criteria (HIC) index. The HIC index measures the acceleration level and pulse duration and is defined by Equation (16).

$$HIC = \left\{ (t_2 - t_1) \left[ \frac{1}{t_2 - t_1} \int_{t_1}^{t_2} a dt \right]^{2.5} \right\}_{max} \quad (16)$$

Where:

- $t_1$  and  $t_2$  are the start and end times of the interval that the HIC reaches maximum value (in seconds).
- $a$  is the acceleration, measured in g's (acceleration of gravity at sea level)
- Maximum duration is limited to a value of 36 ms.

Table 13 – HIC allowable values for different dummy models

	Hybrid III 50 <sup>th</sup> Male	Hybrid III 50 <sup>th</sup> Female	Hybrid III 6 years	Hybrid III 3 years	12 Months CRABI
HIC36	1000	1000	1000	900	660

According to the standard, head acceleration cannot exceed 80 g's for more than 3 ms.

### A.2. Chest Severity Index (CSI)

The criterion used by the ECE R94 for maximum chest compression is 76 mm, and the maximum acceleration cannot exceed 60 g's. The Combined Chest Severity Index can be used to determine potential injuries.

$$CSI = \frac{A_{max}}{A_{int}} + \frac{D_{max}}{D_{int}} \quad (17)$$

Where:

- $A_{max}$  is the maximum acceleration on the chest over time;
- $D_{max}$  is the maximum chest deflection over time;
- $A_{int} = 60g$ 's, is the maximum allowable chest acceleration;
- $D_{int} = 76$  mm is the maximum allowable chest deflection.

### A.3. TIBIA AXIAL LOAD

The force transmitted through the tibias due to the contact of the feet with the vehicle floor is a reliable indicator of floor intrusion towards the occupant and is used to analyze potential fractures in the region. This intrusion occurs when the vehicle's front stringers do not properly absorb energy, resulting in an overload on the passenger cabin and causing deformations in areas that should remain intact. The maximum compression value of the tibias should not exceed 35.9 kN.

### A.4. NECK INJURY CRITERIA

During a crash event, the human's neck is vulnerable to impact consequences that can result in paralysis or quadriplegia. The cervical region is critical in cases of vehicular impact, mainly because it is subject to the whiplash effect. This effect involves a rapid movement of the neck, characterized by a sudden transition from extension to flexion at a speed that the human body cannot trigger normal protective muscle reflexes. This effect can cause damage to the soft tissues of the cervical spine, including ligaments, muscles, and intervertebral discs. The Neck Injury Criteria is defined by four combinations of load cases:

- $N_{te}$ : Tensile and extension;
- $N_{tf}$ : Tensile and flexion;
- $N_{ce}$ : Compression and extension;
- $N_{cf}$ : Compression and flexion.

The expression to calculate the neck injury criterion caused by axial load and longitudinal moment, according to ECE R94 standard is given by equation 18

$$N_{ij} = \frac{F_z}{F_{zc}} + \frac{M_{ocy}}{M_{yc}} \quad (18)$$

Where:

- $F_z$  is the axial load;
- $M_{ocy}$  is the longitudinal bending moment at neck;
- $F_{zc}$  is the critical value of axial load and is worth 6806 N for tensile and 6160 N for compression;
- $M_{yc}$  is the critical value of longitudinal bending moment and is 310 Nm for flexion and 135 Nm for extension.

The four values of  $N_{ij}$  must not exceed 1.0 at any time during the test.



## APPENDIX B – COMPONENTS AND SENSORS SELECTION

### B.1. LINEAR GUIDE

The selection of the linear guide for the friction rig was based on the guidelines in the manufacturer's catalog (THK, 2018). Considering the initial design concept, the rig was designed to withstand normal loads of up to 5 kN and achieve slip velocities of up to 5 m/s. These specifications were determined to meet the requirements of the intended testing scenarios.

To ensure the durability and longevity of the rig, a target life of 1 million tests was set as a benchmark. The life calculation for the linear guide was performed based on the supplier's specifications and guidelines, taking into account factors such as load capacity, operating conditions, and expected frequency of usage. By taking these factors into consideration and following the supplier's recommendations, the chosen linear guide is expected to offer the required durability and reliability for the desired number of tests. Equation (19) and Equation (20) refer to the life calculation method indicated by the supplier.

$$L = 50 \left( \frac{f_h f_t f_c C}{f_w P_c} \right) \quad (19)$$

$$L_h = \frac{10^6 L}{2l_s} \quad (20)$$

Where  $f_h$  is the hardness coefficient and is defined as 1.0 as standard,  $f_t$  is the temperature coefficient and is taken as 1.0 once surroundings is at temperature ambient,  $f_c$  is the contact coefficient also taken as 1.0 once a single carrier block is used,  $f_w$  is the load coefficient and taken as 2.0 given the impact scenarios with speeds over 2 m/s

Three candidates were considered for the role, as show in Table 14. Two criteria were taken on selection: the life must stand more than 1 million tests and mass must be the lowest as possible.

Where  $f_h$  is the hardness coefficient, which is defined as 1.0 as standard.  $f_t$  is the temperature coefficient, which is taken as 1.0 when the surroundings are at ambient temperature.  $f_c$  is the contact coefficient, also taken as 1.0 when a

single carrier block is used.  $f_w$  is the load coefficient, which is taken as 2.0 in impact scenarios with speeds over 2 m/s.

Three candidates were considered for the role, as shown in Table 14. The criteria taken into consideration during the selection process are that the product must withstand more than 1 million tests, and the mass must be as low as possible.

Table 14 – Linear guide selection table.

<b>Model</b>	<b>Mass (kg)</b>	<b>C (kN)</b>	<b>L (km)</b>	<b>Lh (# tests)</b>
SHS15	0,23	14,20	26,71	2,67E+05
SHS20	0,46	22,30	103,46	1,03E+06
SHS25	0,72	31,70	297,19	2,97E+06

From Table 14, it was found that SHS20 is the most suitable candidate for attending mass and life constraints.

## B.2. LOAD CELLS

After finalizing the design concept, selecting the appropriate load cells is crucial. Two commonly used methods for constructing load cells are piezoresistive and piezoelectric sensors.

Piezoresistive sensors, also known as strain gauge sensors, operate based on the variation of resistivity in a thin wire bonded to a structure when it is subjected to a load. These sensors consist of resistors connected in a Wheatstone bridge circuit, which allows for the conversion of small changes in resistivity into an output voltage.

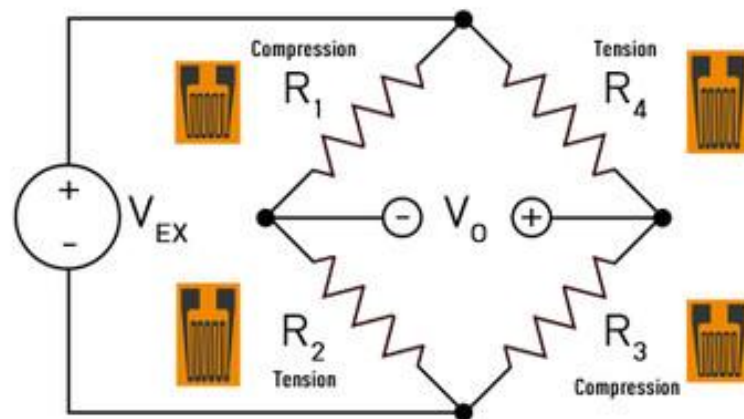
The advantages of piezoresistive sensors include their high sensitivity, excellent linearity, and low power consumption. They are also capable of accurately measuring static and dynamic loads. Moreover, these sensors offer

a wide range of load capacities, making them suitable for a variety of applications.

However, it is important to note that piezoresistive sensors may be sensitive to temperature changes and require compensation techniques to account for temperature variations and minimize their impact on the measurements.

Piezoelectric sensors, on the other hand, operate based on the principle of the piezoelectric effect. This effect occurs when certain materials generate an electric charge in response to mechanical stress or strain. These sensors can effectively measure dynamic loads and are commonly used in high-frequency applications. They offer excellent frequency response and can handle a wide range of load magnitudes.

Figure 116 – full Bridged load cell scheme (800 load cell, 2019).



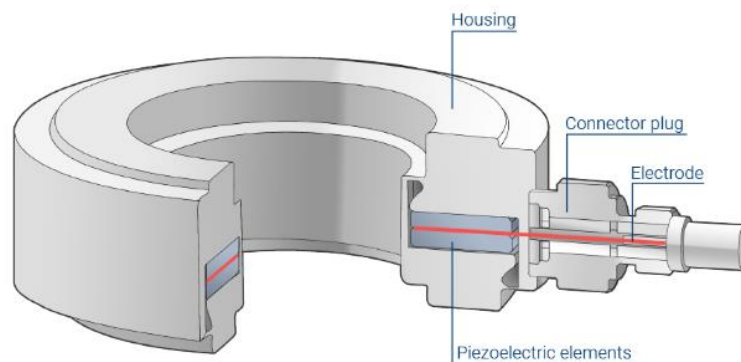
Piezoelectric sensors utilize materials such as quartz crystals or specially formulated ceramics that exhibit the piezoelectric effect. When pressure or force is applied to these materials, they generate a charge across their surfaces. This charge is directly proportional to the applied pressure or force.

To convert the generated charge into a measurable electrical signal, a charge amplifier is typically used. The charge amplifier amplifies the small charge signal from the piezoelectric sensor and converts it into an output voltage

proportional to the pressure variation. This voltage can then be further processed or recorded for analysis.

The advantages of piezoelectric sensors include their high sensitivity, fast response time, and broad frequency range. They are particularly useful for measuring dynamic events and rapid pressure changes due to their ability to detect high-frequency signals accurately. Figure 117 shows a cross section of an annular force measurement piezoelectric sensor.

Figure 117 – Piezoelectric load cell anatomy (source: HBM, 2019)



In the context of this project, the requirement to perform tests at both high and low load rates prompted the evaluation of resistive bridge load cells instead of piezoelectric sensors. While piezoelectric sensors are generally considered ideal for impact conditions, resistive bridge load cells offer the advantage of providing accurate measurements even in static or quasi-static load conditions.

However, one drawback of resistive bridge load cells is their lower natural frequency compared to that of piezoelectric sensors. Piezoelectric sensors typically have natural frequencies exceeding 100 kHz, whereas resistive bridge load cells typically have their first natural frequency below 10 kHz.

To address this issue and ensure accurate measurements, a frequency domain analysis of signal amplitudes needs to be conducted during finite element analysis. This analysis will help identify any significant load components that may be present near the natural frequency of the resistive bridge load cells. By analyzing the signal amplitudes in the frequency domain,

it is possible to evaluate the potential impact of the lower natural frequency and implement necessary measures to minimize any negative consequences.

It is worth noting that resistive bridge load cells still provide reliable and accurate measurements for a wide range of load rates, including both high and low rates. The selection of these load cells was driven by the need to accommodate various load conditions and maintain static loads after bolt tightening.

Considering the design premise of a maximum test pressure of 50 MPa on a sample area of 100 mm<sup>2</sup>, each load cell must be able to support a maximum load of 5 kN. Therefore, for normal load measurements, a 5 kN HBM C9C load cell with a full bridge configuration was selected. For tangential load measurements, a full bridge HBM U93 5 kN load cell was chosen.

Both the HBM C9C and U93 load cells provide reliable and accurate measurements within their specified load range. They are suitable for the intended application and will ensure accurate data acquisition during the tests. This can be seen in Figure 118.

It is important to select load cells that are appropriately rated for the expected loads in order to ensure reliable and accurate measurements. By selecting load cells with the appropriate capacity, the integrity of the test data can be preserved, enabling meaningful analysis and interpretation of the results.

Figure 118 – HBM U93 (left) and C9C (right) Load cells (source: HBM, 2018).



These sensors have an expected error of  $\pm 0.2\%$ , which is the limit used for tests with low pressure levels (or normal force at a scale of 10 N). In this case, the rig shows interchangeability to swap the 5 kN to 0.5 kN sensors, which

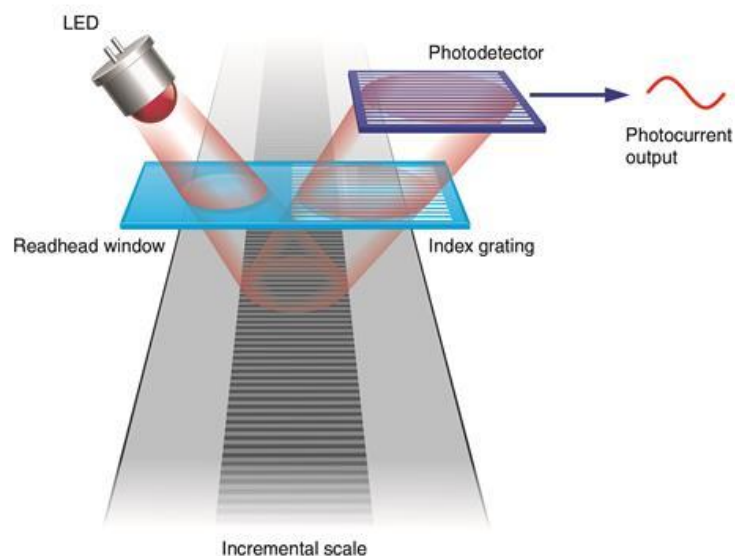
have the same external dimensions as the selected ones. These sensors would be sensitive enough to capture force variations as low as 1 N.

### B.3. LINEAR ENCODER

To ensure highly accurate position and velocity readings with sufficient resolution to capture static-to-dynamic slip transitions, various linear encoder sensors were evaluated. Among the options available in supplier catalogs, four common models were filtered: optical incremental, optical absolute, magnetic incremental, and magnetic absolute.

Optical incremental encoders function by utilizing a laser light that interacts with a striped scale, enabling the counting of displacement increments with each switch of the scale. These sensors are exceptional at detecting even the slightest variations in displacement, often achieving precision levels below 0.1  $\mu\text{m}$ . However, these encoders can be sensitive to certain operating conditions. Factors such as dust, oil, or misalignment may potentially lead to inaccuracies in the reading, affecting their overall precision. Figure 119 shows the working principle of an incremental optical encoder.

Figure 119 – Incremental optical encoder working principle (Renishaw,2019).



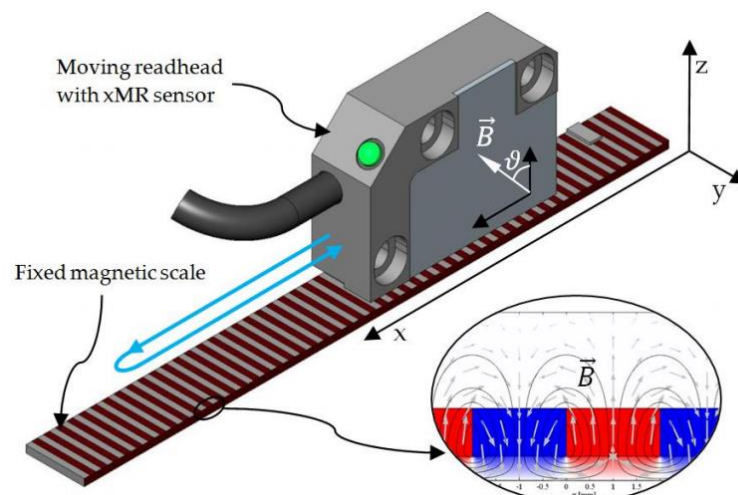
Magnetic sensors, especially those based on the Hall effect, provide improved durability and stability, making them ideal for applications in impact conditions

and harsh environments. These sensors operate by utilizing the Hall effect phenomenon to detect changes in magnetic fields, ensuring reliable and accurate measurements.

One advantage of magnetic sensors, particularly magnetic incremental encoders, is their insensitivity to dust, oil, and other contaminants. As long as there are no metallic particles present between the reader head and the magnetic tape, the performance of the sensor remains unaffected by environmental contaminants. This characteristic makes magnetic sensors a reliable choice in challenging operating conditions where maintaining cleanliness may be difficult.

Magnetic incremental encoders use alternating magnetic fields to detect changes in position. The magnetic tape or scale contains alternating magnetic patterns that the sensor reads in order to determine incremental position changes. This incremental encoding allows for precise position measurements and can provide valuable information for tracking displacement and velocity variations. Figure 120 shows the magnetic orientation in the track of a Hall effect linear encoder.

Figure 120 – Magnetic encoder working principle (Domajnko and Križaj, 2018).

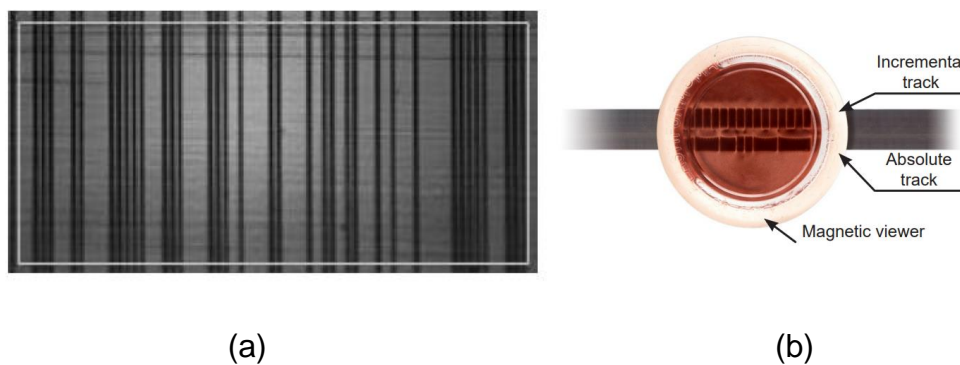


Both magnetic and optical incremental encoders are employed in order to quantify positional changes and determine displacement through signal integration. However, when dealing with long distances, signal drifting can lead

to erroneous measurement. To overcome this challenge, absolute encoders utilize an advanced scale design that allows for direct measurement of absolute position, eliminating the need for signal integration. The scales of absolute encoders incorporate unique binary combinations for different regions, eliminating the need for position referencing. This characteristic allows absolute encoders to provide more precise position information.

Nevertheless, it is important to note that absolute encoders generally offer lower resolution compared to incremental encoders. This limitation arises from the necessity to encode unique binary combinations for each position, which reduces the number of increments or steps available within a given range. Furthermore, absolute encoders tend to be more expensive due to their advanced scale design and enhanced functionality. Figure 121 shows the structure of absolute scales in optical and magnetic encoder systems.

Figure 121 – Incremental optical (a) and magnetic (b) encoder scales (Renishaw, 2018).



To meet the requirements of the rig design, which necessitates high resolution and robustness in a limited reading length, the magnetic incremental sensor Renishaw LM13 was chosen as the best option.

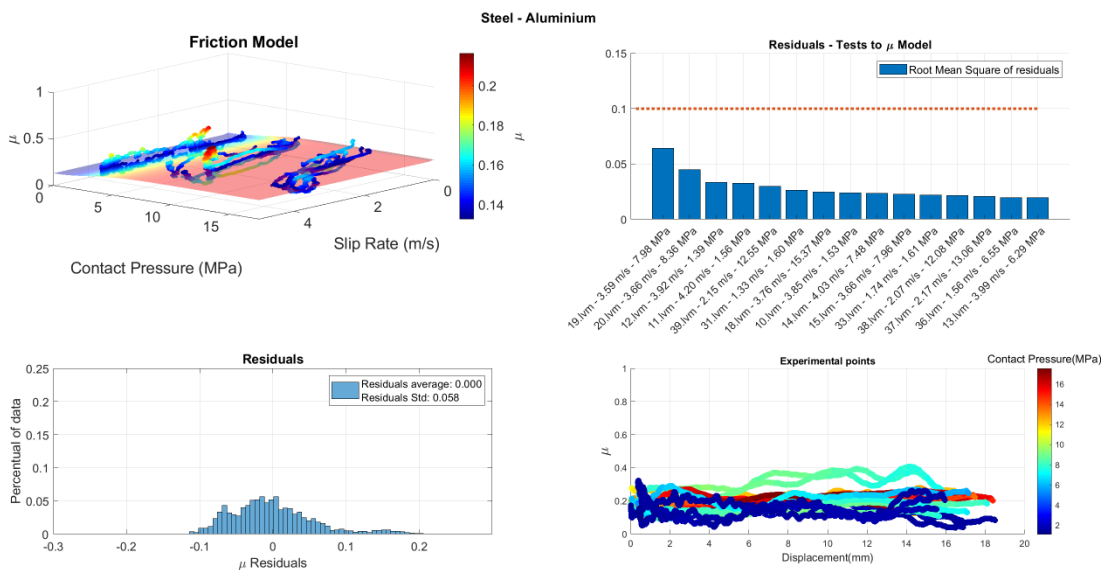


## APPENDIX C – RESULTS METRICS

This section aims to demonstrate the process of data treatment and analysis for each contact pair, including the acceptance ranking criteria of residuals.

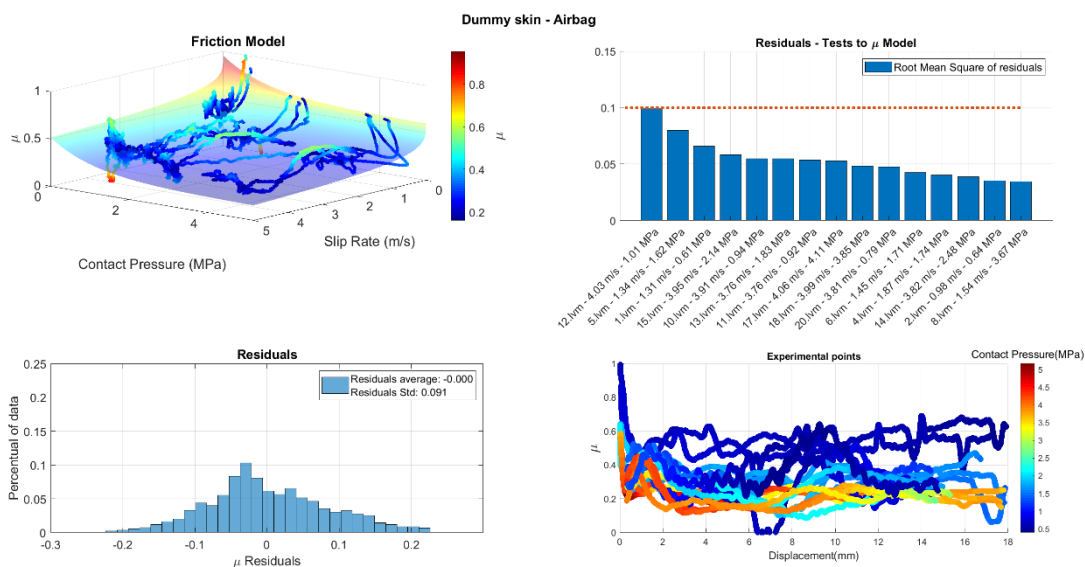
### C.1. STEEL – ALUMINUM

Figure 122 – Steel – Aluminum friction model.



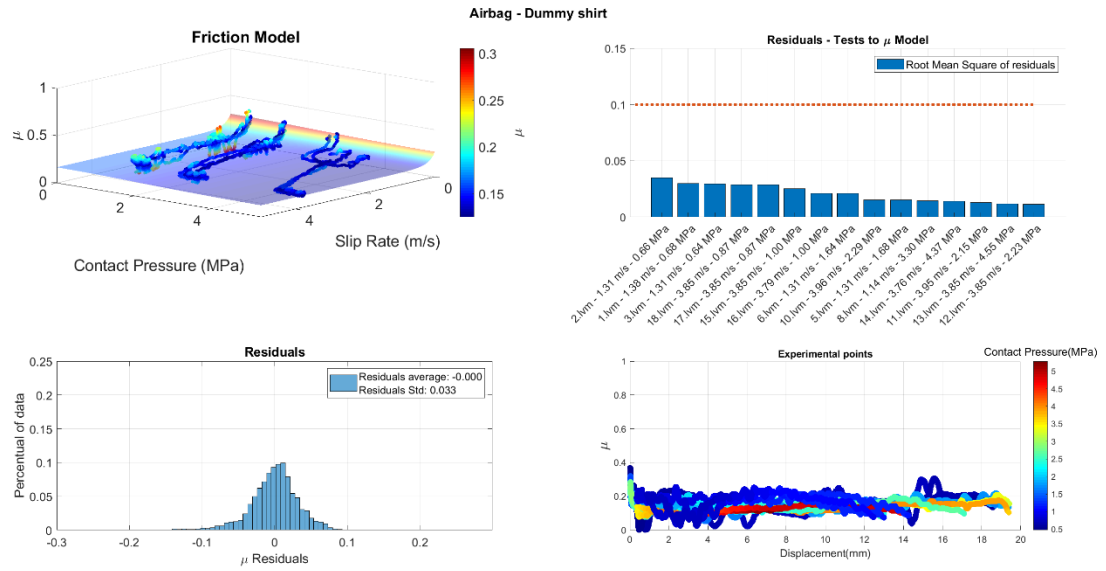
### C.2. DUMMY SKIN – AIRBAG

Figure 123 – Dummy skin – Airbag friction model.



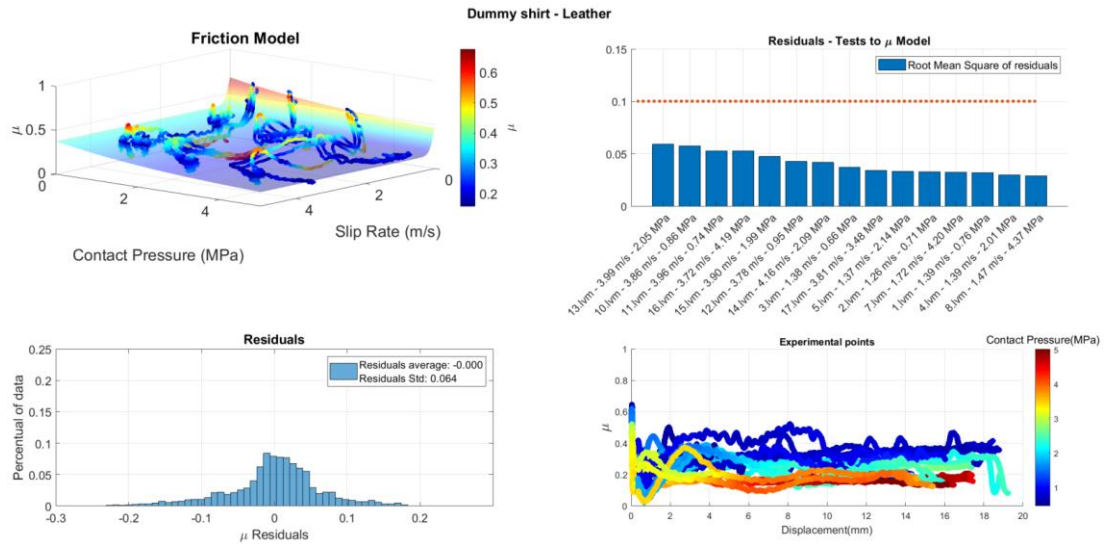
### C.3. AIRBAG – DUMMY SHIRT

Figure 124 – Airbag – Dummy shirt friction model.



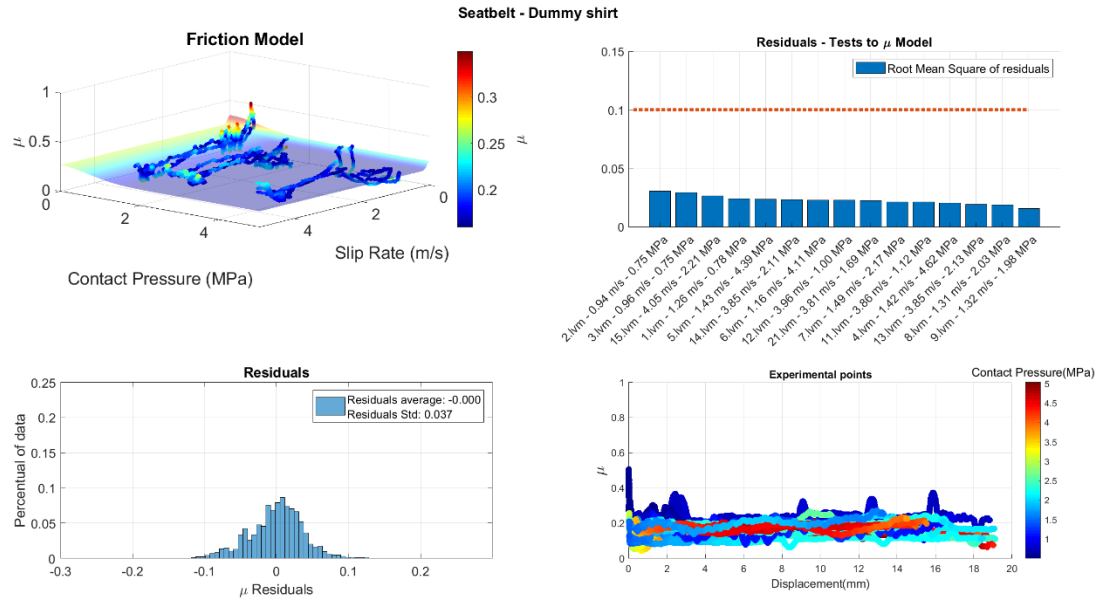
### C.4. DUMMY SHIRT – LEATHER

Figure 125 – Dummy Shirt – Leather friction model.



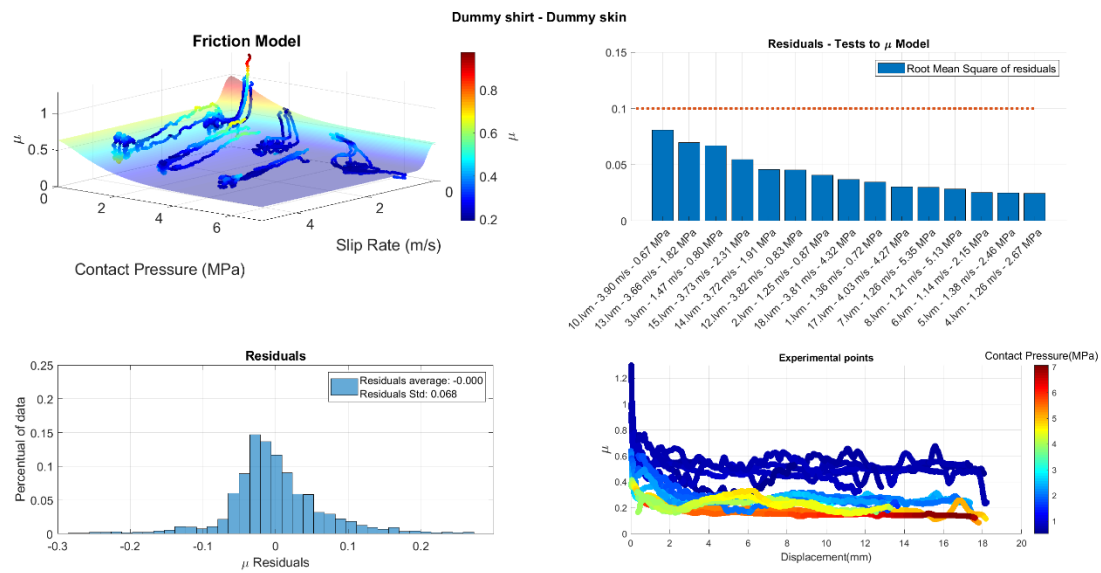
### C.5. SEATBELT – DUMMY SHIRT

Figure 126 – Seatbelt – Dummy Shirt friction model.



### C.6. DUMMY SHIRT – DUMMY SKIN

Figure 127 – Dummy Shirt – Dummy Skin friction model.



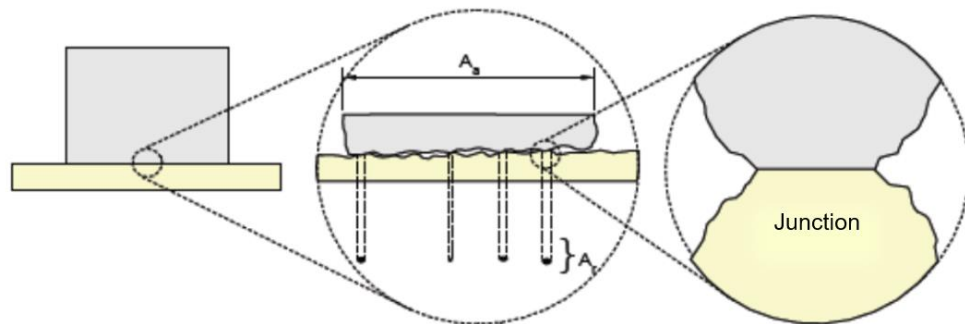
## APPENDIX D – CONTACT MECHANICS COMPLEMENTS

### D.1. CONTACT MECHANICS

When two nominally flat and parallel surfaces are smoothly placed together, apparent mechanical contact occurs across the surface. However, due to surface roughness, the effective contact region initially occurs in only few asperities. These regions are called junctions, and the sum of all regions is called the real contact area. As the normal load increases, the deformation of these regions leads to an increase in the real contact area due to the greater number of touching asperities. (Hutchings, 2017)

Figure 128 illustrates the point contacts (or junctions) for the actual contact area, which is typically much smaller than the apparent contact area.

Figure 128 – Schematic demonstration of real and apparent contact area (Santana, 2009).



The behavior of stress transmission, friction, and wear between two surfaces in contact will depend, among other factors, on the nature of roughness deformations. Such deformations can be elastic or plastic, and this behavior can be determined by the plasticity index. According to Hutchings (2017), the plasticity index is defined by the theory proposed by Greenwood and Williamson. Such a theory describes that the transition from elastic to plastic deformation of surface roughness occurs when certain values are reached, as demonstrated by the Equation (21) and Equation (22).

$$\psi = \frac{E'}{H} \left( \frac{\sigma^*}{r} \right)^{\frac{1}{2}} \quad (21)$$

$$E' = \frac{E_1 E_2}{E_1(1 - \nu_2^2) + E_2(1 - \nu_1^2)} \quad (22)$$

Where  $H$  is the hardness of the softest material,  $E_1$  and  $E_2$  are the modulus of elasticity,  $\nu_1$  and  $\nu_2$  are the Poisson's ratios,  $R$  is the radius of roughness (assuming this is approximately the same for all roughness) and  $\sigma^*$  is the standard deviation of the height of roughness. The indexes 1 and two denotes for the respective materials in contact.

Metallic surfaces produced by conventional engineering methods have values of  $\psi$  between 0.1 e 100, whereas in the case of ceramics and polymers, the factors  $E'/H$  are generally one-tenth of those presented by metals, leading to a proportional reduction in the value of  $\psi$  (Hutchings, 2017).

At the moment of initial contact between two nonconforming solids with smooth surfaces, the geometry in the contact region can be considered as a point or a line. From this point on, any increase in transmitted force will result in an expansion of the contact area due to deformations in the surrounding surfaces. Contact theory is necessary to predict the shape and behavior of this area under normal and possibly tangential loads.

Indeed, one can utilize Hertz's theory of elastic contact, which is based on certain assumptions that validate the equation for pressure distribution across surfaces. The hypotheses are as follows:

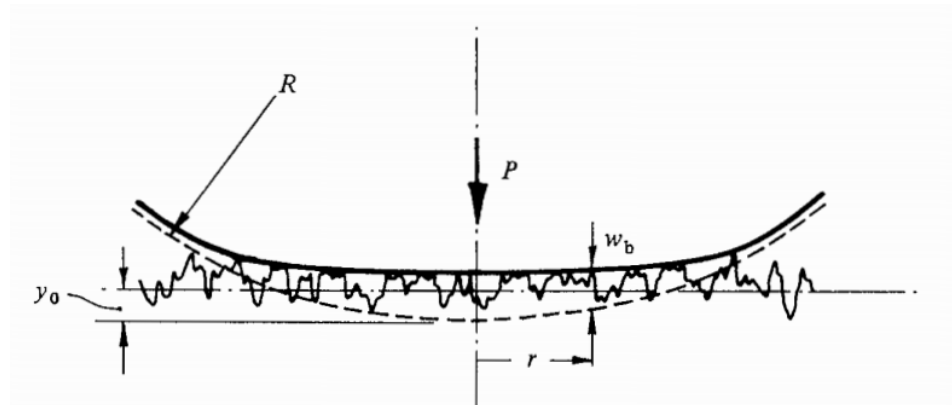
- Surfaces are continuous and non-conforming;
- Stresses are low enough and within elastic limit;
- Surfaces are continuous and much larger than the contact region, and the radius of curvature of the surfaces is much larger than the radius of the contact area.

Any contact that occurs under conditions that do not adhere to the above assumptions is considered non-Hertzian contact, and numerical methods are often necessary to comprehend the phenomenon.

In real world scenarios, the aforementioned circumstances are extremely rare and depend on complex finishing processes to be achieved. For low elasticity materials like some polymers, even without an ideal surface finish, this hypothesis is valid because localized stresses deform the material and contact occurs virtually under ideal conditions. However, for materials with a high elastic modulus, localized stresses may invalidate Hertz's contact theory due to the discontinuity in the application of loads on the actual surface.

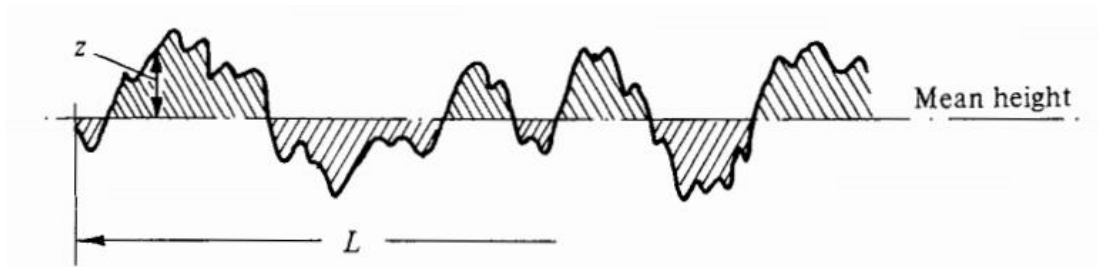
Some of these irregularities exhibit a pattern as a result of manufacturing processes, but the majority of actual surfaces have irregular topography. This makes it impossible to employ a purely analytical approach to determine localized contact stresses, given the random nature of the phenomenon.

Figure 129 – Contact representation between a smooth surface and a rough surface (Johnson, 1985).



The surface texture shown in Figure 129 can be measured using a profilometer. This device slides a small tapered tip under the body to be analyzed and reproduces the topography found along a line in a computer. It obtains statistical data from the surface, indicating the existence of peaks and valleys, as well as their amplitude and statistical distributions. One of the most commonly used data for surface characterization is the average roughness,  $R_a$ , which is the value obtained for the absolute sum of the distances of all points from an average line is set to the smallest possible standard deviation. Figure 130 shows a representation of the average roughness of a surface.

Figure 130 – Representation of the average roughness of a surface (Johnson, 1985).

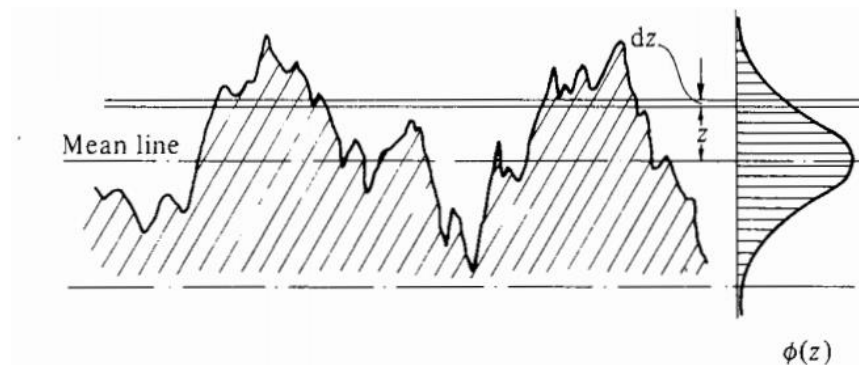


This value can be defined by equation 23.

$$R_a = \frac{1}{L} \int_0^L |Z| dx \quad (23)$$

However, the value of  $R_a$ , does not provide information about the surface profile, specifically the distribution of deviations from the mean and their characteristic dimensions. Then, approaching the problem from a statistical point of view, it was found that on most real surfaces, the distribution of peaks and valleys, as well as their respective amplitudes, follows a distribution close to the Gaussian. The physical representation of this distribution is shown in Figure 131.

Figure 131 – Gaussian distribution of depths of a real surface (Johnson, 1985).



For the contact between two real surfaces, it must be taken into account the roughness present on both faces. Johnson (1985) recommends the expression on Equation (24) for equivalent roughness calculation.

$$R_a^{eq} = \sqrt{R_{a1}^2 + R_{a2}^2} \quad (24)$$

Due to the concentration of surface roughness peaks in very small areas, an increase in the normal force applied during contact leads to deformations of

these peaks, resulting in an increase in the effective contact area. Therefore, increasing pressure may cause variations in the coefficient of friction.

However, as mentioned, not all surfaces adhere to a normal distribution. For example, on rough or polished surfaces, certain asperities are removed, resulting in peaks that are virtually uniform. This means that the resulting surface topography cannot be characterized as being derived from random Gaussian distribution phenomena.

## D.2. FRICTION

### D.2.1. Metallic friction

One of the most important theories for friction between metallic materials was developed by Bowden and Tabor (1950). They state that the frictional force is primarily derived from two phenomena: adhesion and ploughing.

$$F_{total} = F_{adhesion} + F_{ploughing} \quad (25)$$

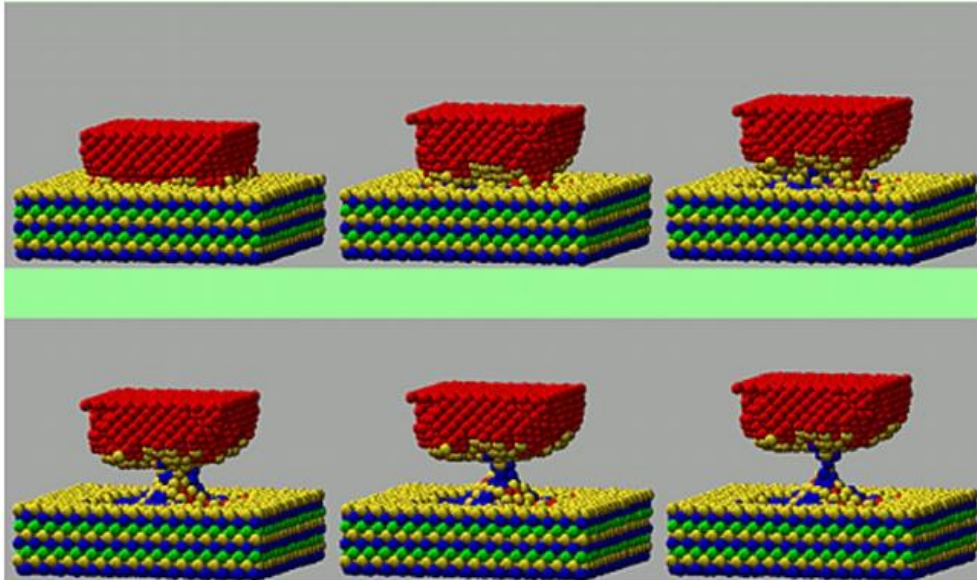
Furthermore:

$$\mu_{total} = \mu_{adhesion} + \mu_{ploughing} \quad (26)$$

Adhesion refers to the joining of the Van der Waals intermolecular forces between surfaces in certain cases, particularly in ductile metals under vacuum conditions where no oxide film is present. This can result in high values coefficients of friction.



Figure 132 – Theoretical modelling of the adhesion effect during contact between a nickel indenter (upper body) and an initially plane gold surface in perfect vacuum (Hutchings, 2017).



In this phenomenon, it is considered that the joint fails by shear in the less resistant material. Thus, considering:

$$F_{adhesion} = W\mu_{adhesion} = A_{real}\sigma_{shear} \quad (27)$$

$$W = A_{real}H \quad (28)$$

Given that  $H$  is the hardness of the material, one finds:

$$\mu_{adhesion} = \frac{\sigma_{shear}}{H} \quad (29)$$

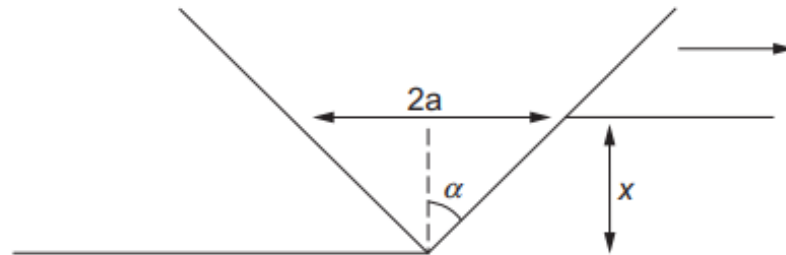
For metals, according to Hutchings (2017) one finds:

$$H \approx 5\sigma_{shear} \quad (30)$$

So, substituting the terms, one finds that  $\mu_{adhesion} \cong 0.2$ .

Ploughing is the process of creating grooves or scratching the softer side of a contact pair. In this case, the mechanical properties of the materials in contact have a predominant influence on the coefficient of friction.

Figure 133 – Model for the ploughing component of friction, in which a conical asperity with a semi-angle  $\alpha$  indents and slides through the surface of a softer material (Hutchings, 2017).



For Hutchings (2017), the deformation component  $\mu_{ploughing}$  is less than 0.1 in most metal cases resulting in a total coefficient of friction  $0.2 \leq \mu_{total} \leq 0.3$ . However, in most cases available in the literature, the values presented differ from the range presented by Bowden and Tabor (1950). Indicating which other effects should be considered in this calculation.

The phenomenon that complements the explanations of adhesion theories and ploughing was presented by the same authors and became known as junction growth.

This phenomenon is characterized by the plastic deformation of contact asperities, which experience high normal and shear stresses. It is important to note that the actual contact area is much smaller than the apparent area. Bowden and Tabor (1950) and Tabor (1959) analytically approached this phenomenon, concluding that for metallic friction with surfaces free of films or contaminants, when the interfacial shear stress is equal to the shear stress of the material, the coefficient of friction would tend to infinity, as presented by the equation 31. The formula is derived from the Tresca criterion.

$$\mu = \frac{F_{max}}{W} = \frac{1}{2 \left[ \left( \frac{\tau_0}{\tau_i} \right)^2 - 1 \right]^{\frac{1}{2}}} \quad (31)$$

However, in most applications, metals are subjected to surface contaminants. As a result, the interfacial shear stress is generally lower than the material stress, leading to lower friction coefficients compared to the unit.

An important analysis of this equation is that one widely used method of reducing friction is to create low shear strength surface films. This results in a high relationship  $\tau_0/\tau_i$  high and consequently,  $\mu$  small. This is the basis of how lubricants work, as they reduce friction by creating a surface layer with very low shear values.

### **D.2.2. Friction in Polymers**

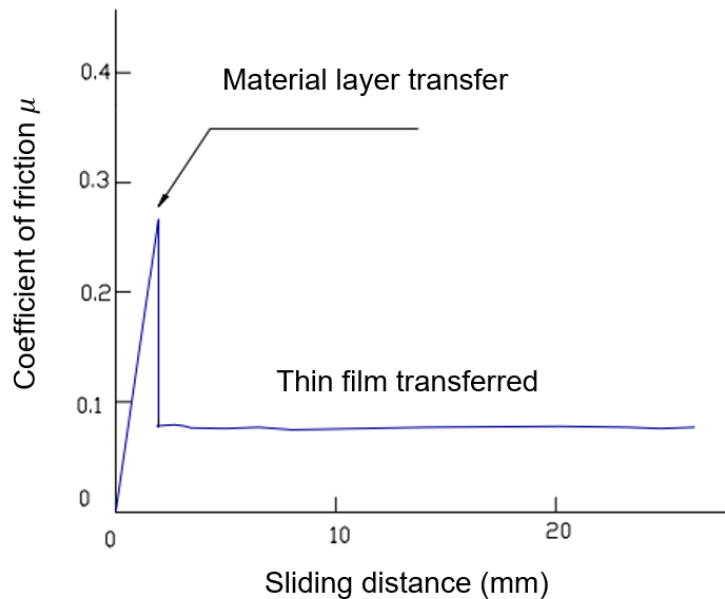
Friction and wear in polymers differ fundamentally from those that occur in metals and ceramics. One of the key differences is its strong dependence on mechanical properties over time, as well as the effects of viscoelasticity and the dependence on the plasticity index. Such effects influence, for example, the so-called dwell time, which refers to the duration that the polymeric surface remains in contact with another surface before sliding. During this period, the actual contact area may grow as a function of the load due to surface deformations. It is possible that objects with identical polymeric surfaces in contact to exhibit different frictional behaviors. This can be attributed to variations in storage times, for example.

Moreover, it has been found in the literature (Cho, Bhushan and Dyess, 2016) that in cases where there are high sliding velocities and, consequently, an increase in the surface temperature, the coefficient of friction of polymers may vary significantly due to the glass transition. The same authors, however, did not find any influence of normal force on the coefficient of friction when studying the friction between different polymers.

Many polymers, when sliding against harder surfaces, transfer thin films to the opposing surface. The formation and behavior of the transferred films are important factors in the friction and wear of these polymers. Once a transfer film is formed, the subsequent interaction occurs between the polymer and a layer of similar material, regardless of the composition of the substrate. Figure

134 shows the behavior of the coefficient of friction between a polymer and glass, highlighting the influence of material transfer.

Figure 134 – Effect of polymer layer transfer on the coefficient of friction of high-density polyethylene (HDPE) against glass (Kawakame and Bressan, 2000).



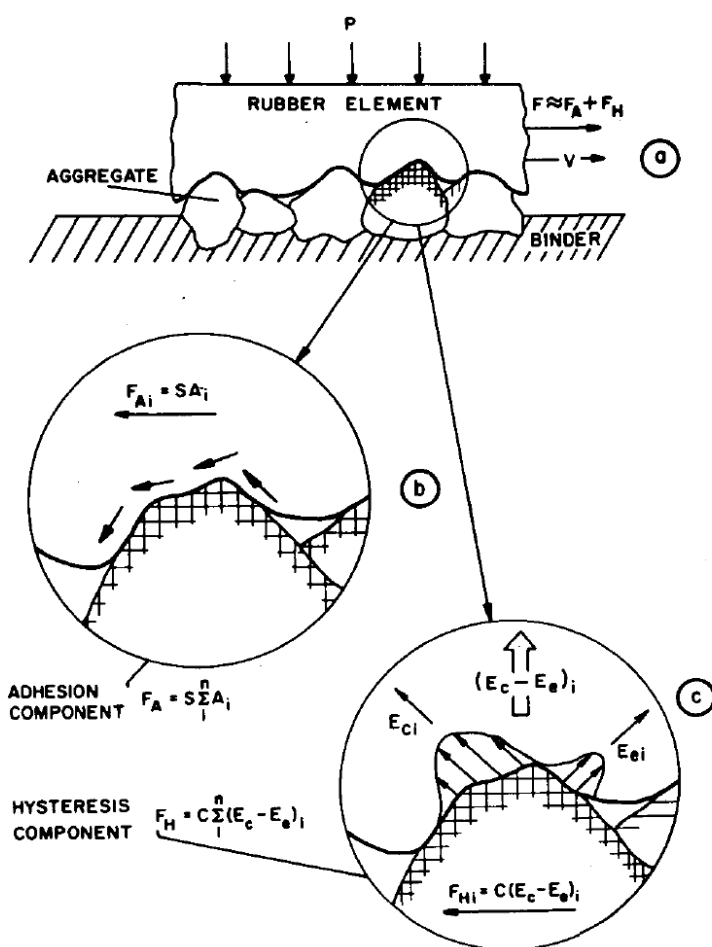
Thus, when dealing with cases where a polymer is likely to slide more than once on the same spot on another surface, one should understand that what is being studied is the friction between the polymer and its deposition on the counter face, not the phenomenon between the polymer and the material of the opposite part.

### D.2.3. Rubber friction

Most studies on the subject of friction are focused on elastic materials such as metals, which have different tribosystems compared to hyperelastic materials like rubber. It was concluded by Meyer and Kummer (1962) that the nature of rubber friction is fundamentally different from that of metals. In its work, a "Adhesion-shear" theory was proposed, in which friction arises from the adhesion shearing of the material and hysteresis losses. The compression of rubber increases the real contact area and results in high localized normal pressures. This, in turn, leads to strong molecular bonds that require a significant amount of shear energy to separate. Additionally, rubber hysteresis

causes heat dissipation during compression and expansion in these regions. The adhesive component of the friction force can be significantly increased by sliding a rubber material over a smooth and clean surface, such as a clean glass plate. In contrast, the hysteresis component dominates when rubber slides over a rough surface. Figure 135 illustrates this phenomenon.

Figure 135 – Adhesion and hysteresis friction mechanisms on rubber block sliding with constant velocity  $v$  over a rough surface (Meyer and Kummer, 1962).



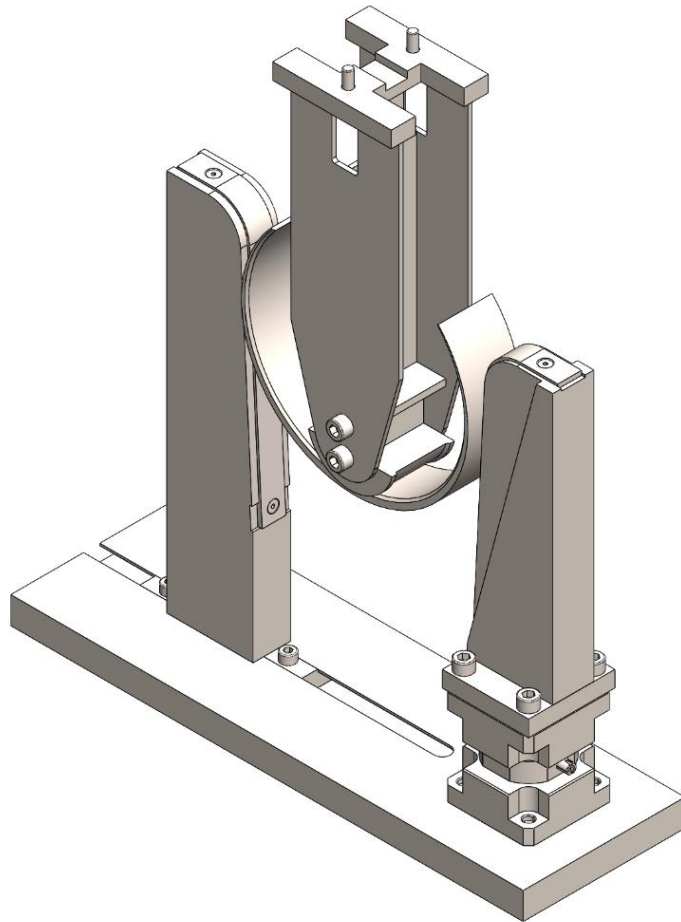
## **APPENDIX E – WEDGE TEST RIG PROPOSAL**

The final appendix of this study introduces a novel concept for a friction test rig aiming the investigation of frictional behavior under a different boundary condition. As previously discussed in this work, the prototyped rig was inspired by the strip drawing test concept, where a normal pressure is applied, and the tangential force initiates sample sliding. However, the proposed concept on this section takes inspiration from crash test events itself, offering a closer approximation to real-world scenarios when parts are not initially in contact. Instead of starting the test from zero velocity and pressure, this rig proposes an oblique impact where the first contact occurs at non-zero tangential speed. This innovative approach promises to provide valuable insights into frictional dynamics under more realistic conditions. The rig can also be used as a validation instrument, correlating the sliding distance with the friction on the contact pair.

Although the manufacturing and testing of this new rig are beyond the scope of this work, all test concepts and calculations will be presented here.

This rig intends to correlate the vertical displacement of a known open profile cylinder indenter (referred as circlip) that impacts low angle oblique faces. If the proposed numerical friction model is accurate enough, the vertical displacement from both numerical and experimental tests should match. Figure 136 shows the design of the validation test rig.

Figure 136 – Design of wedge test rig.



This concept is based on three test samples. One sample is attached to the circlip, while the other two are fixed on wedges through bolts. This rig also allows the use of a biaxial load cell on the base of one of the columns, capturing the friction coefficient during the test.

The circlip is expected to behave as a pressure limiter, ensuring continuous contact between samples. It is designed to operate under a linear elastic regime and can be reused for multiple tests. An eccentric design has been chosen due to better stress distribution.

One counterpoint of this design is that the contact pressure and indent depth depend on the circlip radius and thickness. These parameters must be carefully chosen for different impact speeds and dropping masses.

The contact faces are positioned at a 3° angle in relation to the vertical centerline, and simulations have been conducted for multiple radii and circlip thicknesses.

Since the simulation is static and the structure operates on linear regime, a good approximation of the indent depth values was obtained by solving the energy balance equation.

$$\frac{Mv^2}{2} + Mgh = E_{int} + E_{fric} \quad (32)$$

Considering  $E_{int} \propto h$  and an estimated average value for dynamic friction coefficient  $\mu$ :

$$E_{fric} = 2 \int_0^h \mu F dL = 2\mu Fh, \text{ where } F \propto h \quad (33)$$

And the fact that  $E_{int}$  and  $F$  are simulated for  $h = 0.22$ , one can use proportional relation to the calculation of force reaction  $\bar{F}$  for a given depth indentation  $h$ .

$$\bar{F} = \frac{F}{0.22} h \quad (34)$$

Assuming material linear behavior, the proportional relation can be also assumed for absorbed energy by the circlip  $\bar{E}_{int}$ .

$$\bar{E}_{int} = \frac{E_{int}}{0.22} h \quad (35)$$

Then, the energy balance equation follows as:

$$\frac{Mv^2}{2} + Mgh - \mu \frac{F}{0.22} h^2 = E_{int} \quad (36)$$

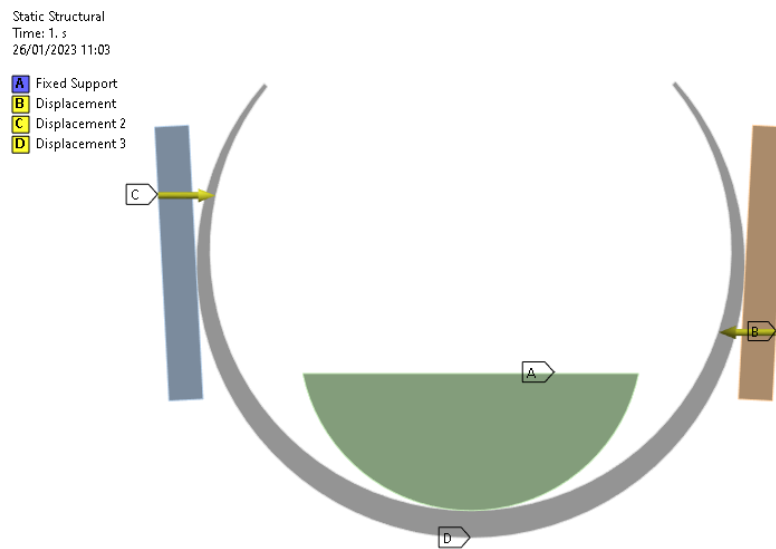
In this case, given the 0.22 m indentation energy  $E_{int}$  and force  $F$  (from previous finite element simulation), one can solve the quadratic equation for  $h$ .

$$h = \frac{-Mg + \frac{E_{int}}{0.22} - \sqrt{\left(Mg - \frac{E_{int}}{0.22}\right)^2 - 4 * \frac{\mu F}{0.22} * \frac{Mv^2}{2}}}{-2 \frac{\mu F}{0.22}} \quad (37)$$



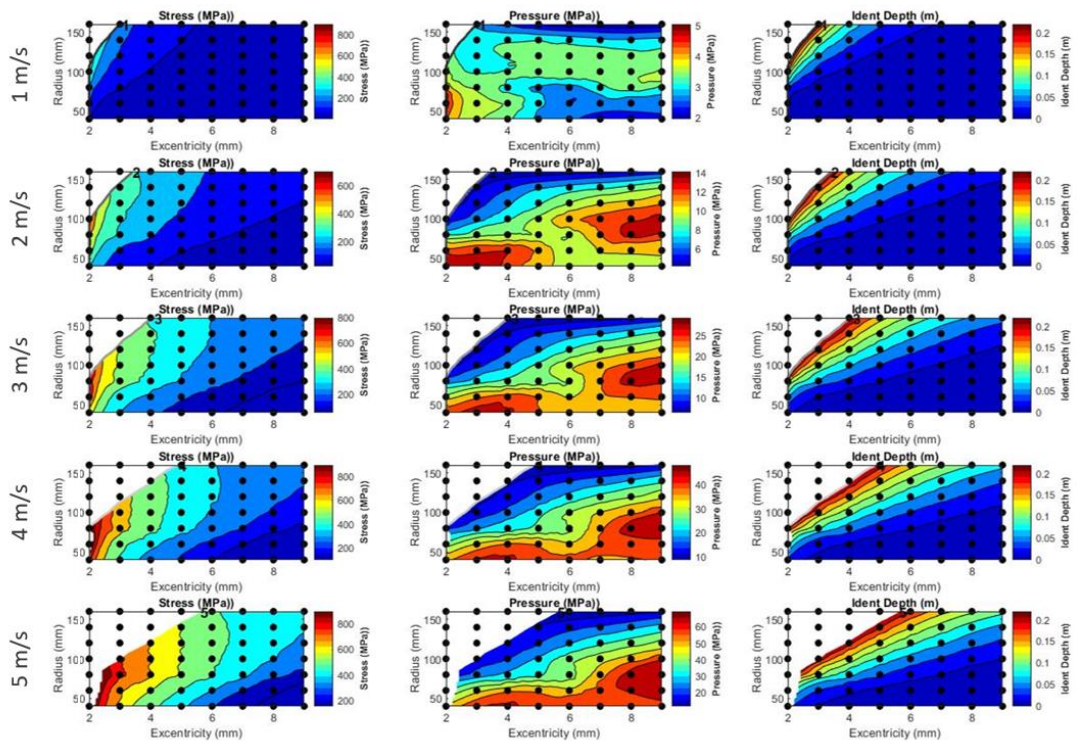
Equation (37) shows the expected indentation depth for a given value of dynamic friction coefficient  $\mu$ , indenter mass  $M$  and impact velocity  $v$ . Also, parameters  $E_{int}$  and  $F$  are necessary to obtain the indentation depth. They are dependent on circlip radius and eccentricity. Thus, a finite element analysis was performed to obtain the values of these variables with multiple combinations of circlip geometries.

Figure 137 – Static analysis on the circlip.



With the aforementioned results, a map of operation of the proposed rig for impact velocities ranging from 1 m/s to 5 m/s, with a 5 kg indenter is shown in Figure 138.

Figure 138– Operation map of the proposed rig.

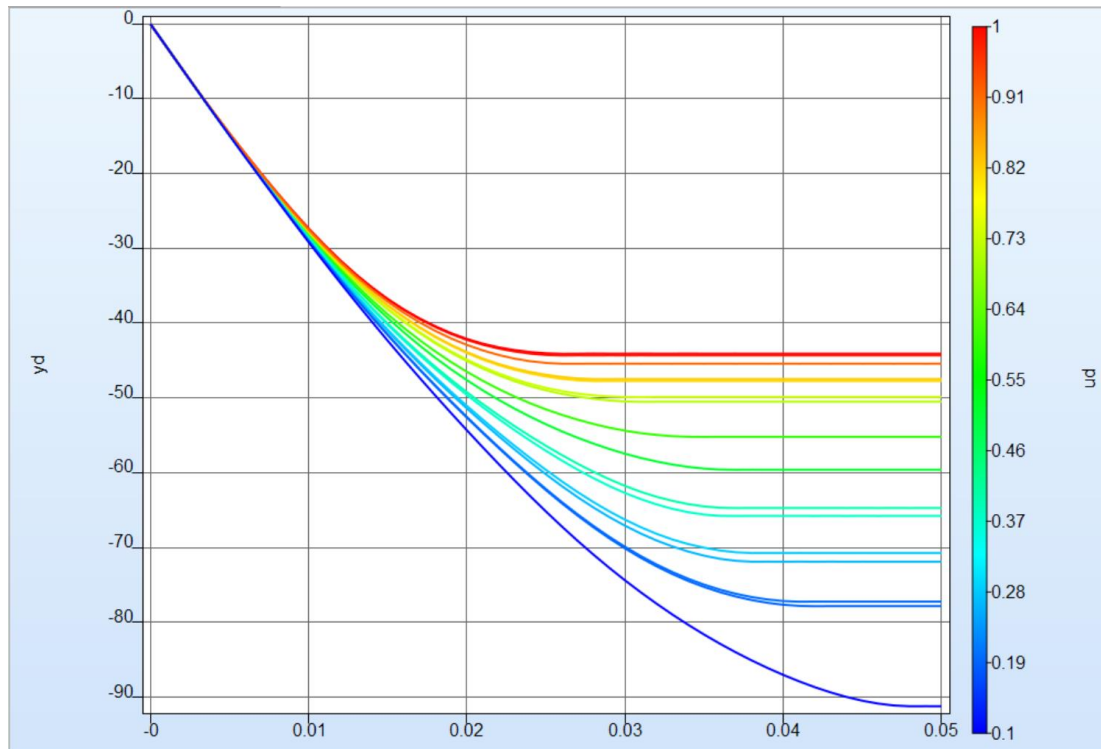


In this figure the response surface was censored on regions where Ident depth was larger than 0.22 m (which is the rig maximum depth) and stress larger than 1000 MPa, from where it was considered the yield limit of the circlip.

Is important to mention that the goal of this formulation is to orient the dimensioning of impact mass and velocity, to ensure the rig will work properly. By using this map of operation, one can properly define the value of  $M$  for a given desired slip velocity  $v$  on the test, and avoid potential issues such as insufficient sliding distance, excessive circlip deformation beyond the yield limit, excessively high pressure, or sliding lengths exceeding the rig's limitations.

Also, a sensitiveness analysis has been done to ensure a smooth and linearly dependence of vertical displacement to friction coefficient on interfaces. This analysis has been performed on LS-Opt varying the dynamic friction coefficient from 0.1 to 1.0 and plotting the vertical displacement of a node on the center of cylinder axis. Results can be seen in Figure 139.

Figure 139 – Sensitiveness analysis of indenter vertical displacement to dynamic friction coefficient.



One can observe a significant sensitivity of vertical displacement to the friction coefficient. The vertical displacement varies from 45 mm to 90 mm within the friction coefficient range of 0.1 to 1.0. This level of variation, exceeding 50% of displacement within the given friction coefficient interval, is considered sufficient to accurately capture the behavior of friction during the tests.

### APPENDIX F – LABVIEW BLOCK DIAGRAM

Figure 140 – Friction rig LabView block diagram of test rig setup

